

Organic-Inorganic Nanomaterial Based Highly Efficient Flexible Nanogenerator for Self-Powered
Wireless Electronics

by

Md. Masud Rana

A thesis

presented to the University of Waterloo

in fulfillment of the

thesis requirement for the degree of

Doctor of Philosophy

in

Electrical and Computer Engineering

Waterloo, Ontario, Canada, 2023

© Md. Masud Rana 2023

Examining Committee Membership

The following served on the Examining Committee for this thesis. The decision of the Examining Committee is by majority vote.

External Examiner	Dr. Peyman Servati Professor, ECE The University of British Columbia
Supervisor	Dr. Dayan Ban Professor, ECE University of Waterloo
Internal Members	Dr. Guo Xing-Miao Professor, ECE University of Waterloo
Internal Members	Dr. Mahla Poudineh Professor, ECE University of Waterloo
Internal-external Member	Dr. Eihab-Abdel Rahman Professor, SYDE University of Waterloo

Author's Declaration

I hereby declare that I am the sole author of this thesis. This is a true copy of the thesis, including any required final revisions, as accepted by my examiners.

I understand that my thesis may be made electronically available to the public.

Statement of Contributions

This thesis contains material from several published journal papers that I authored. Some of these resulted from collaboration with my colleagues in the Ban's group and with professors of other departments at the University of Waterloo and the University of Toronto.

1. Part of the content in Chapter 1 has been published in

Md Masud Rana, Asif Abdullah Khan and Dayan Ban, *Optoelectronic Organic-Inorganic Semiconductor Heterojunctions*, ISBN:9781000325713, CRC Press, **Taylor & Francis**, 2020

Md Masud Rana writing the main draft of the chapter and all co-authors contributed editing of the original draft.

2. Part of the content in Chapter 2 has been published in

Md Masud Rana, Asif Abdullah Khan, Guangguang Huang*, Nanqin Mei, Resul Saritas, Boyu Wen, Steven Zhang, Peter Voss, Eihab Abdel-Rahman, Zoya Leonenko, Shariful Islam, and Dayan Ban, "Porosity Modulated High-Performance Piezoelectric Nanogenerator Based on Organic/Inorganic Nanomaterial for Self-Powered Structural Health Monitoring", **ACS Appl. Mater. Interfaces**, 2020, 12, 42, 47503–12

Md Masud Rana and Asif Abdullah Khan conducted the experiments including device fabrication, characterization and testing. Md Masud Rana drafted the original manuscript and other authors analyzed and discussed the results and provided intellectual input on manuscript drafts. My supervisor Dayan Ban provided guidance during each step of the research and provided feedback on draft manuscripts.

3. Part of the content in Chapter 3 has been published in

Asif Abdullah Khan, **Md Masud Rana**, Guangguang Huang, Nanqin Mei, Resul Saritas, Boyu Wen, Steven Zhang, Peter Voss, Eihab-Abdel Rahman, Zoya Leonenko, Shariful Islam, Dayan Ban, "Maximizing piezoelectricity by self-assembled highly porous perovskite-polymer composite films to enable the internet of things", **Journal of Material Chemistry A**, 2020, 8, 27, 13619-1362

Asif Abdullah Khan, Md Masud Rana and Guangguang Huang conducted the experiments including device fabrication, characterization, testing and drafted original manuscript. All other authors analyzed and discussed the results and provided intellectual input on manuscript drafts. My supervisor Dayan Ban provided guidance during each step of the research and provided feedback on draft manuscripts.

4. Part of the content in Chapter 4 has been published in

Md Masud Rana, Asif Abdullah Khan, Weiguang Zhu, Md Fahim Al Fattah, Sathursan Kokilathanan, Shazzad Rassel, Rozenn Gautheron-Bernard, Soraya Ababou-Girard, Pascal Turban, Shuhong Xu, Chunlei Wang, and Dayan Ban " Enhanced Piezoelectricity in Lead-free Halide Perovskite Nanocomposite for Self-Powered Wireless Electronics" **Nano Energy**, 2022, 101, 107631.

Md Masud Rana conducted the experiments including device fabrication, characterization, testing and drafted original manuscript. All other authors analyzed and discussed the results and provided intellectual input on manuscript drafts. My supervisor Dayan Ban provided guidance during each step of the research and provided feedback on draft manuscripts.

5. Part of the content in Chapter 5 has been published in

Nicolas R. Tanguy*, **Md. Masud Rana***, Asif A. Khan, Xiao Zhang, Nicole Tratnik, Heyu Chen, Dayan Ban, and Ning Yan, " Natural lignocellulosic nanofibrils as tribonegative materials for self-powered wireless electronics." **Nano Energy**, 2022, 98, 107337. (***authors contributed equally**)

Md Masud Rana and Nicolas R. Tanguy conducted the experiments including device fabrication, characterization, testing and drafted original manuscript. All other authors analyzed and discussed the results and provided intellectual input on manuscript drafts. My supervisor Dayan Ban and Prof. Ning Yan provided guidance during each step of the research and provided feedback on draft manuscripts.

Abstract

As the world progresses towards artificial intelligence and the Internet of Things (IoT), self-powered sensor systems are increasingly vital for sensing and detection. Nanogenerators, a new technology in energy research, enable the harvesting of normally wasted energy from the environment. This technology scavenges a wide range of ambient energies, meeting the ever-expanding energy demands as conventional fossil fuel sources are depleted. This research involves designing and fabricating high-performance flexible piezoelectric nanogenerators (PENGs) and triboelectric nanogenerators (TENGs), using novel organic-inorganic hybrid nanomaterials for wireless electronics.

Structural health monitoring (SHM) is crucial in the aerospace industry to enhance aircraft safety and consistency through reliable sensor networks. PENGs are promising for powering wireless sensor networks in aerospace SHM applications due to their sustainability, durability, flexibility, high performance, and superior reliability. This research demonstrated a self-powered wireless sensing system based on a porous PVDF (polyvinylidene fluoride)-based PENG, which is ideal for developing auto-operated sensor networks. The porous PVDF film-based PENG, enhanced output current by ~ 11 times and output voltage by ~ 8 times, respectively, compared to a pure PVDF-based PENG. The PENG device generated sufficient electrical energy to power a customized wireless sensing and communication unit and transfer sensor data every ~ 4 minutes. This PENG could harness energy from automobile vibration, reflecting the potential for real-life SHM systems.

Subsequently, a novel, self-assembled, highly porous perovskite (FAPbBr₂I)/polymer (PVDF) composite film was designed and developed to fabricate high-performance piezoelectric nanogenerators (PENGs). The porous structure enlarged the bulk strain of the piezoelectric composite film, resulting in a 5-fold enhancement of the strain-induced piezo potential and a 15-fold amplification of the output current. This highly-efficient PENG achieved a peak output power density of $10 \mu\text{W}/\text{cm}^2$ and enabled to run a self-powered integrated wireless electronic node (SIWEN). The PENG was applied to real-life scenarios including wireless data communication, efficient energy harvesting from automobile vibrations as well as biomechanical motion. This low-temperature, full-solution synthesis approach could lead to a paradigm shift in sustainable power sources, expanding the realms of flexible PENGs.

One of the remaining concerns is the highly soluble lead component, which is one of the constituents of the PENGs that poses potential adversary impacts on human health and the environment. To address

this concern, lead-free organic-inorganic hybrid perovskite (OIHP) based flexible piezoelectric nanogenerators (PENGs) have been developed. The excellent piezoelectric properties of the FASnBr_3 NPs was demonstrated with a high piezoelectric charge coefficient (d_{33}) of ~ 50 pm/V through piezoelectric force microscopy (PFM) measurements. The device's outstanding flexibility and uniform distribution properties resulted in a maximum piezoelectric peak-to-peak output voltage of 94.5 V, peak-to-peak current of 19.1 μA , and output power density of 18.95 $\mu\text{W}/\text{cm}^2$ with a small force of 4.2 N, outperforming many state-of-the-art halide perovskite-based PENGs. For the first time, a self-powered RF wireless communication between smartphones and a nanogenerator solely based on a lead-free PENG was demonstrated and serves as a stepping-stone towards achieving self-powered Internet of Things (IoT) devices using environment-friendly perovskite piezoelectric materials.

Likewise, triboelectric nanogenerators (TENGs) are also promising energy-harvesting devices for powering the next generation of wireless electronics. TENGs' performance relies on the triboelectric effect between the tribonegative and tribopositive layers. In this study, a natural wood-derived lignocellulosic nanofibrils (LCNF) tribolayer was reported to have high tribonegativity (higher than polytetrafluoroethylene (PTFE)) due to the presence of natural lignin on its surface and its nanofibril morphology. LCNF nanopaper-based TENGs produced significantly higher voltage (160%) and current (120%) output than TENGs with PTFE as the tribonegative material. Assembling LCNF nanopaper into a cascade TENG generated sufficient output to power a wireless communication node to send a radio-frequency signal to a smartphone every 3 mins. This study demonstrates the potential of using LCNF as a more environmentally friendly alternative to conventional tribonegative materials based on fluorine-containing petroleum-based polymers.

Overall, this thesis explores the design and development of highly efficient and flexible nanogenerators for self-powered wireless electronics. By combining highly electroactive nanomaterials with flexible polymer matrix structures, NGs with high electric output performance and flexibility were successfully obtained. The synthesizing process for the electroactive nanomaterials was carefully designed and adopted to sustain the inherent advantages of flexible electronics. The various type of high performance flexible NGs developed in this research work, including ZnO/PVDF porous PENGs, $\text{FAPbBr}_2/\text{PVDF}$ based PENGs, $\text{FASnBr}_3/\text{PDMS}$ based PENGs, and LCNF nanopaper-based TENGs, provide promising solutions for energy harvesting and self-powered sensing.

Acknowledgments

I really would like to start by thanking God Almighty for countless blessings bestowed on me and guidance to achieve my goal in every aspect of life. When I first came to the University of Waterloo, I met many open-minded, brilliant, and supportive people. Here I want to make use of the opportunity to express my gratitude to them and to acknowledge their impact on my academic journey.

I would like to start by thanking my supervisor, Prof. Dayan Ban, for taking me as a graduate student and giving me this wonderful opportunity to conduct my graduate studies with his research team and get valuable experience at the University of Waterloo. I profusely thank Prof. Ban for his excellent guidance, encouragement, providing an interdisciplinary research platform, and freedom in choosing my PhD research topic, and for showing trust in me.

I also want to express my special gratitude to the vibrant group of researchers, especially, Asif Abdullah Khan, Alam Mahmud, Steven Zhang, Guangguang Huang, and Weiguang Zhu those who created the positive and productive environment I got to work in over the last four years.

I am deeply thankful to Prof. Eihab-Abdel Rahman and Prof. Zoya Leonenko for getting me up to speed with the various aspects of measurement and characterization for the experimental work.

I would like to express my special gratitude to Dr. Czang-Ho Lee, Richard Barber, Dr. Sandra Gibson. Likewise, I want to thank Shimco North America Inc. for being our industry partner, NRC, NSERC for the vital funding authorities for our research.

I am grateful to all of my honorable committee members, Prof. Peyman Servati, Prof. Eihab-Abdel Rahman, Prof. Guo Xing-Miao, Prof. Mahla Poudineh for providing their kind consent to evaluate my research despite having their unbelievably busy schedules.

Outside of project and research work, I feel fortunate to find a supportive network and new friends among my fellow PhD students and colleagues, their partners, and my lovely CLV neighborhood.

I would like to express my deep sense of gratitude to my wife Sumaia Saberina, for her love, understanding, tremendous moral support, taking care two of our kids and help she extended to me all the time of my PhD journey.

I would like to end by thanking those who have allowed me to get this far, my beloved parents, parents in law, my brothers and their families, my all relatives, Dr. Rassel and his family, and my friends for their unconditional love and support.

Dedication

This dissertation is dedicated to all of my former teachers from junior school to university. I was the one who love to learn new things and all of you helped to build this. Thank you!

I also dedicate this work to my mother and father, Nazma Begum and Md Anwar Hosen, who first taught me the value of education and helped me to come all the way to where I am today.

Table of Contents

Examining Committee Membership	ii
Author's Declaration	iii
Statement of Contributions	iv
Abstract	vi
Acknowledgments	viii
Dedication	ix
List of Figures	xiv
List of Tables	xxvii
List of Abbreviations	xxviii
Chapter 1 Fundamentals of Nanogenerators and Literature Review	1
1.1 Background	1
1.2 Principles of Nanogenerator	3
1.3 Piezoelectric Nanogenerator (PENG)	5
1.3.1 Basic concept of PENGs and its operating principle	5
1.3.2 Historic outline, advances, and remaining challenges of PENGs	6
1.4 Triboelectric Nanogenerator (TENG)	11

1.4.1	Basic concept of TENGs and its operating principle	11
1.4.2	Historic outline, advances, and remaining challenges of TENGs	13
1.5	Material design and performance enhancement of NG	16
1.5.1	Selection of materials	16
1.5.2	Design of structures	17
1.5.3	Selection of fabrication methods	18
1.5.4	Materials characterization	19
1.6	Research Objectives	19
1.7	Outline of the Thesis	20
Chapter 2	Porosity Modulated High-Performance Piezoelectric Nanogenerator Based on Organic/Inorganic Nanomaterial for Self-Powered Structural Health Monitoring	22
2.1	Introduction	22
2.2	Experiment	24
2.2.1	Fabrication of the porous PVDF thin film	24
2.2.2	The PENG fabrication	25
2.2.3	Characterization and measurements	25
2.3	Results and Discussions	25
2.4	Conclusions	40
Chapter 3	Maximizing Piezoelectricity by Self-assembled Highly Porous Perovskite-Polymer Composite Films for Enabling the Internet of Things	42
3.1	Introduction	42
3.2	Experiment	44

3.2.1	Synthesis of the pure PVDF films	44
3.2.2	Synthesis of the porous PVDF films	44
3.2.3	Synthesis of the FAPbBr ₂ I@PVDF composite films	45
3.2.4	Characterization and measurements	46
3.3	Results and Discussions	46
3.3.1	Device structure and working mechanism of P-PNGs	46
3.3.2	Energy harvesting performance of the P-PNGs	52
3.3.3	Applications of P-PNGs as a sustainable power source in the IoT	57
3.4	Conclusions	61
Chapter 4	Enhanced Piezoelectricity in Lead-free Halide Perovskite Nanocomposite for Self-Powered Wireless Electronics	62
4.1	Introduction	62
4.2	Experiment	65
4.2.1	Materials	65
4.2.2	Synthesis of FASnBr ₃ NPs	65
4.2.3	Growth of FASnBr ₃ @PDMS composite film	65
4.2.4	Fabrication of piezoelectric nanogenerators	66
4.2.5	Characterization of the FASnBr ₃ @PDMS composite film	66
4.2.6	Measurement of device output performance	67
4.3	Results and Discussions	67
4.4	Conclusions	79
Chapter 5	Natural Lignocellulosic Nanofibrils as Tribonegative Materials for Self-Powered Wireless Electronics	80
5.1	Introduction	80
5.2	Experiment	82

5.2.1	Preparation of the nanofibrils	82
5.2.2	Materials characterization	83
5.2.3	Preparation of (L)CNF nanopapers.	84
5.2.4	Assembly of LCNF, PTFE, and CNF-based TENGs	84
5.2.5	LCNF nanopaper cascade TENG assembly and wireless communication node fabrication	85
5.3	Results and Discussions	85
5.3.1	LCNF and CNF nanopaper properties	85
5.3.2	Lignin enhancing surface polarizability of the nanopaper	87
5.3.3	Triboelectric characteristics of LCNF nanopaper in TENGs	89
5.3.4	LCNF nanopaper-based cascade-type TENG for self-powering a wireless communication node	94
5.4	Conclusions	96
Chapter 6	Conclusions and Future Work	98
6.1	Summary of Contributions	98
6.2	Future Work	100
	Letter of Copyright Permission	102
	References	106
	Appendices	128

List of Figures

- Figure 1.1 A tree idea to illustrate Maxwell's displacement current: the first term $\epsilon\partial E/\partial t$ is responsible for the electromagnetic waves' theory; and the second term $\partial P_s/\partial t$ is related to energy and sensor applications, such as nanogenerators. Reproduced with permission [49]. Copyright 2020, Elsevier. 4
- Figure 1.2 Mechanism of piezoelectricity. (a) Atomic model of the wurtzite-structured ZnO. (b) Different piezopotential in tension and compression modes of the PENG. (c) Numerical calculation of the piezoelectric potential distribution in a ZnO nanowire under axial strain. Reproduced with permission [51]. Copyright 2017, Wiley-VCH (d) Band diagram for the charge outputting and flowing processes in the PENG. Reproduced with permission [51]. Copyright 2017, Wiley-VCH. 6
- Figure 1.3 Theoretical models of TENG. (a) Schematic illustration of the first TENG and its operating cycle. (b) The displacement current model of a contact-separation-mode TENG. (c) The equivalent electrical circuit model of TENG. Reproduced with permission [113]. Copyright 2019, Wiley-VCH. 11
- Figure 1.4 Four working modes of TENG. (a) Vertical contact-separation (CS) mode. (b) Lateral-Sliding (LS) mode. (c) Single-Electrode (SE) mode. (d) Freestanding Triboelectric layer (FT) mode. Reproduced with permission [113]. Copyright 2019, Wiley-VCH. 12
- Figure 2.1 Schematic of the wireless sensing system of aircraft structural health monitoring (SHM). (a) schematic illustration of the functional components of piezoelectric nanogenerator (PENG), which is mainly composed of a porous PVDF-based PENG device unit and an integrated circuit unit; (b) an enlarged view of the integrated circuit; (c) an as-fabricated porous PVDF-based PENG device. 26
- Figure 2.2 Step-by-step fabrication process of the Porous PVDF thin film (a) PVDF powder (Sigma Aldrich) is dissolved in N, N-dimethylformamide (N, N-DMF) solvent (10 wt. %). (b) ZnO NPs (35–45 nm, US Research Nanomaterials, Inc.) are mixed within the PVDF matrix solution. and stirred for 4 hours. (c) Ultra-sonication for 30 min to maximize the uniform distribution of ZnO-NPs within the PVDF 27

polymer matrix. (d) The suspension drops cast onto a Si wafer (e) Degassing is done for 30 minutes at 65°C and then annealing at a slightly elevated temperature (75°C) for another 45 minutes. (f)The films peeled off from the Si substrate. (g) Etching with 37 wt. % HCl solution for 4 hours to completely etch off ZnO NPs from the PVDF matrix. (h) Final porous PVDF thin films are ready for device fabrication. (i) Fabricated film (j) large scale fabricated film (15 cm × 15 cm).

- Figure 2.3 Material characterization of as-fabricated porous PVDF-based PENG device: scanning electron microscope (SEM) images of (a) distributed ZnO NPs on the surface of the PVDF matrix before etching (prepared from a mixture 50 wt.% mass fraction of PVDF and ZnO); (b) top view SEM of the porous PVDF film after the etching of the ZnO NPs (Inset is the enlarge view of pore); (c) Elemental composition mapping of Carbon (C), fluorine (F), Zinc (Zn), Chlorine (Cl) in porous PVDF thin film (d) surface morphology characterized by the AFM (e) Fourier transform infrared spectrum (FTIR) of the porous PVDF film to confirm the β phase formation. (f) XRD patterns of pure PVDF, PVDF with ZnO nanoparticles and porous PVDF based thin film. 29
- Figure 2.4 Piezopotential distribution in the porous PVDF with varying porosity under a compressive force of 2GPa (a) with surface pores only, (b) with only inner pores, and (c) a non-porous PVDF. The same scale bar for (a–c) (d) comparison of piezopotential as a function of porosity for surface pores and inner pores. (e) the strain distribution of 50% porous PVDF structure ensembled with both inner and surface pores (f) the piezopotential distribution of 50% porous PVDF structure ensembled with both inner and surface pores. 31
- Figure 2.5 Schematics of the energy generation mechanism from the PENG by considering distributed stress on the film. 33
- Figure 2.6 General setup of the piezoelectric characterization system. The system includes a closed-loop controller, a vibration shaker, a power amplifier unit, an oscilloscope and a self-powered wireless circuit to demonstrate the realization of self-powered wireless electronics. 34

- Figure 2.7 Measured electrical output performance of the porous PVDF-based PENG device: (a) the measured open-circuit voltage of the porous PVDF thin films of almost identical thickness when the ZnO mass fraction increased from 0 wt. % (pure PVDF) to 60 wt. %, with a frequency of 30Hz. (b) peak to peak output voltage at 30 Hz and 2G acceleration when the device was pressed by a standard mass of 138 gram (g) (c) peak to peak output current at 30 Hz and 2G acceleration when the device was pressed by a standard mass of 138 gram (d) polarity switch testing of short circuit current to confirm piezoelectricity (e) polarity switch testing of open circuit voltage to confirm piezoelectricity (f) stability test of the porous PVDF-based PENG device for 36000 cycles (at 30Hz for 20 minutes). 35
- Figure 2.8 Demonstration of high output capability and applications prospect of the porous PVDF-based PENG device (a) comparison of the output voltage at different frequencies of 10 Hz to 50 Hz for the device with 50 wt. % of ZnO-PVDF composition (b) comparison of output current at different frequencies of 10 Hz to 50 Hz for the device with 50 wt. % of ZnO-PVDF composition (c) measured output voltage across the various commercial capacitors of 1 μ F, 2.2 μ F, 4.7 μ F, 10 μ F, 47 μ F, and 100 μ F were charged by the 50 wt. % ZnO-PVDF PENG device at 30 Hz (d) measured peak output power and peak output power density at various loading condition of the PENG at 30 Hz (e) measured output voltage across the input and output capacitor of the EMM, when the PENG is excited with the linear motor shaking at 30 Hz. (f) wireless signal reception by a Bluetooth device (mobile phone) (g) the whole sensing system illustration with the aid of a block diagram. 38
- Figure 2.9 Application of the PENG for SHM (a) Output voltage from a PENG mounted on a automobile car engine for both on and run condition. (b) Corresponding frequency domain distribution via Fast Fourier Transform while the maximum peak occurs at 29 Hz (c) Output charging voltage of a commercial capacitor (1 μ F) by a single PENG by an automobile engine (Mercedes-Benz car); (d) the corresponding digital photo of charging capacitor by engine vibration at stand still. 40

Figure 3.1	Device structure of P-PNGs (a) fabrication process of P-PNGs; (b) XRD patterns of 20 wt. % FAPbBr ₂ I@PVDF composite film; (c) FTIR results of porous PVDF and FAPbBr ₂ I@PVDF composite films (25 wt. %); (d) digital photos of the large area composite film (15 cm * 15 cm) and the fabricated P-PNGs	48
Figure 3.2	(a) Schematic illustration of crystallization process of the PVDF and the FAPbBr ₂ I nanoparticles. The y axis represents the total concentration of PVDF and FAPbBr ₂ I in the solution (b) schematic demonstration shows the interactions between FA ⁺ cations and -CF ₂ - groups. From the FTIR spectrum, this interaction is confirmed by the blue-shift of the infra-red absorption peaks of C-F bond in the wave number range of 1350-1100 cm ⁻¹ .	49
Figure 3.3	Working mechanism of P-PNGs (a) cross-sectional SEM image of the self-assembled highly porous PVDF@FAPbBr ₂ I (20 wt.%) composite films (inset shows the close view of a pore); the corresponding element mapping of (b) fluorine (F) in PVDF and (c) lead (Pb) in FAPbBr ₂ I; (d) calculated stress and (e) piezo potential distribution for a similar area of the pure PVDF, 20% circular porous PVDF and 60% porous FAPbBr ₂ I@PVDF film (porosity induced by 20 wt. % of FAPbBr ₂ I).	50
Figure 3.4	The output performance of P-PNGs (a) Voc and (b) Isc of PNGs made from pure PVDF, porous PVDF (with ZnO nanoparticles) and FAPbBr ₂ I@PVDF composite films. For the porous PVDF, and FAPbBr ₂ I@PVDF composite films, the original mass ratios of nanoparticles inside the final films are 20 wt. %. (c) Polarization verification of the P-PNGs by switching test; (d) relative permittivity of the porous and 20 wt. % FAPbBr ₂ I@PVDF composite films; KPFM images of the (e) porous and (f) 20 wt. % FAPbBr ₂ I@PVDF composite films.	54
Figure 3.5	Self-Powered integrated wireless electronics node (SIWEN) (a) functional block diagram of the SIWEN (b) internal circuit diagram of a LTC 3588-1 module (c) architecture of an RSL-10 system on chip (SoC).	56
Figure 3.6	Framework of the self-powered integrated wireless electronics node (SIWEN) by simultaneously using the P-PNGs as a power -source and a sensor.	58

- Figure 3.7 Application of the P-PNGs for IoT (a) the measured output power of the P-PNG with an applied acceleration of 2 G (30 Hz). The used load was a metal block of 138 g; (b) charging characteristics of the input (1 μ F) and output capacitor (220 μ F) of the SIWEN; (c) the digital photo shows the sensor signal received by the cell phone; (d) SIWEN used for car engine states detection at a parking condition (inset shows the corresponding frequency domain distribution via Fast Fourier Transform); (e) charging of a commercial capacitor (1 μ F) by a single P-PNG while exciting by an automobile engine (Mercedes-Benz car); (f) the corresponding digital photo of engine vibration detection 59
- Figure 4.1 Schematic representation of the PENG device and material structure (a) A pictorial diagram illustrating the structure of FASnBr₃@PDMS composite-based flexible PENG. The FASnBr₃@PDMS based device is inserted between the Cu and ITO coated PET electrode, (b). The cross-sectional SEM image of PENG shows the thickness of the FASnBr₃@PDMS film is approximately 80 μ m and shows better adhesion between each layer. (c) The crystal lattice of the FASnBr₃ perovskite. (d) shows the XRD characteristics peaks of FASnBr₃ nanoparticles. 68
- Figure 4.2 Represents the Scanning Electron Microscopy (SEM) and X-ray photoelectron spectroscopy (XPS) measurements (a) SEM image of pure PDMS and inset shows the enlarged view. (b) SEM images of a composite film of 20 wt. % FASnBr₃ NPs loaded into PDMS matrix. (c) SEM-EDS Electronic image (the approximate size of the NPs is ~250 to 300 nm). (d) (i-vi) shows the elemental composition mapping of different materials inside the FASnBr₃@ PDMS composite film. (e) XPS spectra of Sn3d, (f) XPS spectra of Br3d. 70
- Figure 4.3 Origin of piezoelectricity from the FASnBr₃ NPs: (a) Local longitudinal (vertical) amplitude and phase hysteresis (inset) vs cyclic dc bias loops from -10 to 10 V; (b) Piezoelectric response from the FASnBr₃ and the PPLN sample measured with an ac tip bias from 0.5 V to 8 V; (c) Surface topography; (d) V-PFM amplitude and (e) phase images of the FASnBr₃ NPs; (f) Phase image after poling on the FASnBr₃ NPs. 72

Figure 4.4	Stress (a) and electric potential distribution (b) (close in view) of FASnBr ₃ @PDMS composite. The stress (c) and electric potential distribution (d) along the line XY	73
Figure 4.5	COMSOL model of FASnBr ₃ @PDMS composite and experimentally measured electrical output of PENG device (a) the strain distribution of 20 wt.% FASnBr ₃ NPs in PDMS matrix; (b) the piezo potential distribution of 20 wt.% FASnBr ₃ NPs in PDMS matrix; (c) Voltage; (d) Current at 40 Hz and 2G acceleration. (e) output switching test of short-circuit current (f) measured output voltage and (g) Current at running frequencies from 10 to 50 Hz for the 20 wt. % FASnBr ₃ @PDMS PENG; and (h) Durability test of the PENG device for 48000 cycles (at 40 Hz for 20 minutes).	75
Figure 4.6	Demonstration of energy generation capability and applications prospect of the PENG device (a) Relative permittivity of FASnBr ₃ @PDMS device; (b) demonstrating the direct bandgap property of FASnBr ₃ perovskite NPs with a bandgap of 2.3 eV; (c) measured peak output power of the PENG under various electrical loading conditions at 40 Hz; (d) Output voltage across the capacitors of 1, 2.2, 4.7, and 10 μF were charged by the 20 wt. % FASnBr ₃ @PDMS PENG; (e) charging and discharging output during the LED turns ON and OFF through a full-wave bridge rectifier; (f) Voltage across the 1 μF and 220 μF capacitors during the step-1 and step-2 charging cycles of the EMM when the PENG was operating at 40 Hz and demonstration of the wireless signal transmission; and (g) schematic diagram of the complete sensing system.	77
Figure 4.7	LED lighting by using the power generated from PENG along with charging discharging cycle.	78
Figure 5.1	(a) Schematic depicting lignocellulosic nanofibrils, (b) Deconvoluted XPS C 1 s of LCNF nanopaper, (c) FTIR-ATR spectra of CNF and LCNF nanopapers, (d) TEM image of LCNF, (e) AFM images of LCNF nanopaper and SEM images of the cross-section of the CNF and LCNF nanopaper, (f) Photo of LCNF nanopaper and its water contact angle result.	86

Figure 5.2	(a) Schematic of contact electrification between LCNF (or CNF) nanopaper and aluminum foil and the corresponding CPD values, (b) KPFM surface potential results of CNF and LCNF nanopaper before and after contact electrification with aluminum, (c) Energy band diagram of CNF and LCNF nanopaper during contact electrification with Al.	88
Figure 5.3	(a) Schematic of the LCNF TENG device structure, (b) Steps involved in the power generation of TENGs, (c) Open-circuit voltage output and (d) short-circuit current output of TENGs with LCNF nanopaper compared against that of TENGs with PTFE film as the tribonegative layer, (e) Revised and simplified version of the polymeric triboelectric series according to the test results and literature reference [372], (f) Peak to peak voltage and current of TENGs with either LCNF nanopaper or PTFE film as the tribonegative layer, (g) Effect of contact force on peak to peak open-circuit voltage of TENGs made with LCNF nanopaper and Cu as the two tribolayers, (h) Effect of load resistance on power density of TENGs with LCNF nanopaper and Cu.	90
Figure 5.4	a photograph of the TENG characterization set-up, including Stopper, TENG, Linear motor, and force sensor.	91
Figure 5.5	LCNF@Al-based CTENG for self-powered wireless communication, (a) Schematic of a LCNF-based cascade type (five units) TENG (CTENG) and a wireless communication node (WCN) comprising of an energy management and regulation system for powering up a radio frequency (RF) transmitter, (b) Charging of different capacitors with the CTENG, (c) Charging of the input and output capacitor units of the WCN by the CTENG, (d) Close up view of the measured voltage-controlled charging waveforms in Fig. 5.3c, (e) Discharging of the output capacitor in the WCN to power-up the RF transmitter indicating each RF transmission.	95
Figure A2.1	The characterization of the pure and porous PVDF film. scanning electron microscope (SEM) images of the pure PVDF film (a) Plane view SEM (b) Cross-sectional SEM, annealed at 75°C, the SEM image indicates that the surface of the pure PVDF is uniform for both cases (c) distributed ZnO NPs on the surface of the PVDF matrix. (c) the cross-sectional SEM image of the PVDF mixed with	128

ZnO NPs, The SEM image indicates that nanoparticles are not uniformly distributed rather accumulated in different positions of the PVDF film. This creates pores of different sizes after an etching process. (d) Cross-sectional SEM image of the porous PVDF film after the etching of the ZnO NPs.

Figure A2.2	Element mapping of (a) Carbon (C); (b) fluorine (F); (c) Zinc (Zn); (d) Chlorine (Cl); in porous PVDF thin film for a specific region of interest. (e) compare the quant results of elements in the porous film.	129
Figure A2.3	(a) The selected area of top surface SEM of nanoporous PVDF film; (b) EDS spectrum of the nanoporous PVDF film of image (a); (c) Selected area of cross-sectional SEM of nanoporous PVDF film; (d) EDS spectrum of the nanoporous PVDF film of image (c).	130
Figure A2.4	The characterization of the porous PVDF film (a) the atomic force microscopy (AFM) image of porous PVDF surface (b) measured surface roughness of porous PVDF (~100 nm).	131
Figure A2.5	Strain distribution in the porous PVDF with varying porosity under a lateral bending force of 2GPa (a) pure (0%) PVDF (b) porous PVDF with inner pores only, and (c) porous PVDF with only surface pores. The scale bar is the same for all profiles from (a–c).	132
Figure A2.6	Piezopotential distribution in the porous PVDF model with varying porosity percentages under lateral bending force (a) with surface pores only, (b) with only inner pores, and (c) a non-porous PVDF. Same scale bar for (a–c) (d) comparison of piezopotential as a function of porosity.	133
Figure A2.7	Strain distribution in the porous PVDF with varying porosity under a vertical compressive force of 2 GPa (a) porous PVDF with only surface pores, (b) porous PVDF with inner pores only, and (c) pure PVDF, the scale bar is the same for all profiles from (a–c).	134
Figure A2.8	(a) Stress distribution for pure PVDF film (b) potential distribution for pure PVDF film where the peak output voltage is 10.9 volt, (c) prepared solution of	135

PVDF-ZnO with a ZnO mass ratio of 0 to 60 wt. % (0 and 50 wt. % are not shown here).

- Figure A2.9 Comparison of the electrical output performance for 50 wt. % of ZnO-NP-based PVDF porous and nonporous film. (a) Output voltage (b) output current. 136
- Figure A3.1 The characterization of the pure PVDF film. Scanning electron microscopy (SEM) image of (a) top surface of the pure PVDF (annealed at 75 °C) (b) the cross section of the pure PVDF film. The SEM images indicate that the surface of the pure PVDF is uniform (c) FTIR spectrum of the PVDF film is indicating the β -phase formation (corresponding absorptions at the wavenumbers of 510 cm^{-1} , and 841 cm^{-1}). 139
- Figure A3.2 The characterization of the porous PVDF film (a) top surface SEM image of the PVDF loaded with ZnO nanoparticles (NPs) with a diameter of 35-45 nm (b) cross sectional SEM image of the PVDF loaded with ZnO NPs. The SEM images are indicating that nanoparticles are not uniformly distributed rather accumulated in different positions of the PVDF film. This creates pores of different sizes after an etching process (c) top surface SEM image of the porous PVDF film obtained after the etching of ZnO NPs by 37 wt. % hydrochloric acid (HCl) (d) atomic force microscopy (AFM) image of the porous PVDF surface (e) measured surface roughness of the porous PVDF (~ 100 nm). 140
- Figure A3.3 The morphology of pore structures in the P-PNGs (a) cross-sectional SEM image of the FAPbBr₂I@PVDF film shows that the pores with a length of 20-25 μm are regularly distributed here (b) surface topography of the FAPbBr₂I@PVDF film from the AFM image illustrates that the diameter of the pores are approximately 3-5 μm . 141
- Figure A3.4 The atomic force microscopy (AFM) images of PVDF-FAPbBr₂I film with different mass ratios (wt. %) of FAPbBr₂I precursor in 10 wt. % PVDF solution (a) 5 wt. % (b) 10 wt. % (c) 15 wt. % (d) 20 wt. % (e) 25 wt. % (f) 30 wt. %. This AFM images clearly indicates the gradual increase in the pores size (diameter of up to 7 μm at 30 wt. % FAPbBr₂I) with the increase of FAPbBr₂I concentration. 142

Interestingly the pores are generated almost in the nature of a periodic array throughout the entire film (g) grain boundary topology of FAPbBr₂I NPs.

- Figure A3.5 (a) Finite element simulation of the pure, the circular porous and the highly porous perovskite-polymer films under a compressive pressure of 800 kpa. The mechanical stress is calculated (b) along the horizontal axis (A-F) (c) along the vertical axis, which clearly shows a higher stress in the film with a porous structure than the non-porous (pure) film. The stress distribution is disrupted by the presence of pores inside the film and further increases with the porosity. 143
- Figure A3.6 A comparison of piezo-potential distribution for porous FAPbBr₂I@PVDF (20 wt. %) film with the presence of a single and an array of pore (8 pores) structures. The shape of the pores has been optimized from the observation of cross-section SEM image of the composite film. (a) Mechanical stress distribution of the film with the array of pores (left) and the film with a single pore (right) structure. The arrows are indicating the amplified stress on the sidewall of each pore. (b) The piezo-potential distribution is higher in the film with the presence of a large number of pore structures (left). 144
- Figure A3.7 A characterization system of energy harvester. The controller unit is operated by a workstation interface (Vibration View 9). The controller unit (VR 9500) generates different control signals which are amplified by a power amplifier (Lab Works Inc.'s pa 138) to feed an electrodynamic shaker (ET-126-1) to control its motion. An accelerometer (3055D3) provides the feedback signal from the shaker to the controller unit which can take action if there are any faults. The shaker is mechanically coupled with a metallic hammer to characterize the energy harvesting devices. The output from the devices are measured and viewed by an oscilloscope. 146
- Figure A3.8 The output performance of the P-PNGs. (a) output voltage and (b) current of the P-PNG at 30 Hz and 2G acceleration with an applied load of 138 gram (g). 147
- Figure A3.9 Schematics of energy generation mechanisms of the P-PNGs based on distributed stress profile. 147

Figure A3.10	Variation of output voltage (left) and output current (right) of the P-PNGs with different FAPbBr ₂ I mass ratios (0 wt.%, 10 wt.%, 20 wt.%, 30 wt. %). The maximum output voltage (85 V) and current (30 μA) was obtained for 20 wt. % FAPbBr ₂ I@PVDF composites. The output voltage and current increases up to the mass ratio of 20 wt.%, and then decreases afterwards. The higher mass ratio of FAPbBr ₂ I (> 20 wt. %) will generate very large pores to greatly reduce PVDF per unit volume and create more defects.	148
Figure A3.11	Frequency dependent (10-50 Hz) output voltage (left) and output current (right) of the 20 wt. % FAPbBr ₂ I@PVDF based P-PNGs, when the acceleration is fixed at 2G. The maximum output voltage and output current at 30 Hz frequency was 85 V and 30 μA, respectively. As the frequency increases the strain rate rises and causing the increase in the output voltage and current. The gradual decrease in the output at higher frequencies (> 30 Hz) corresponds to the reduction of impact on the device by the 138-gram (g) proof mass.	148
Figure A3.12	Flexibility test of the P-PNGs at 10 Hz and 2G acceleration when a periodic bending force was applied from an electrodynamic shaker. The generated (a) output voltage (b) output current of 14 V and 0.3 μA, respectively, depicts the performance of the P-PNG during the bending condition.	149
Figure A4.1a	a (i-v) Step by step synthesis process of FASnBr ₃ NPs. (vi-ix) Details of FASnBr ₃ @PDMS composite film preparation.	151
Figure A4.1b	(i) Electrical polling of the composite film at 6kV for 3-4 hours (ii) Schematic of packaged device with different layers (iii) Original fabricated composite film.	152
Figure A4.2	XPS spectra of C1s and N1s.	153
Figure A4.3	Verification of polling effect to confirm the dipole formation inside the composite NPs.	153
Figure A4.4	(a) Lateral PFM amplitude and (b) Lateral phase images of the FASnBr ₃ NPs, the weak signals obtained in the L-PFM images indicates the weak polarization magnitudes in that direction.	154

Figure A4.5	(a) the strain distribution of pure PDMS matrix, (b) the piezopotential distribution of pure PDMS matrix.	154
Figure A4.6	polarity switch testing of open circuit voltage to confirm piezoelectricity.	155
Figure A4.7	Measured electrical output performance of FASnBr ₃ @PDMS PENG device: (a) the measured open-circuit voltage of composite FASnBr ₃ @PDMS PENG when FASnBr ₃ mass fraction increased from 10 wt. % to 30 wt. %, with a frequency of 40Hz.	155
Figure A4.8	Thermal stability of the relative permittivity is measured for one hour at 130 °C, and 200 kHz for the 20 wt. % FASnBr ₃ @PDMS composite film. The relative permittivity showed a negligible change in their values.	156
Figure A4.9	Load resistance dependent voltage and current measurement.	156
Figure A4.10	Energy harvesting from (i) Single finger tapping (ii) Foot stepping (iii) Hand gesture (iv) bending the device (v) device size (vi) charging by using only finger tapping.	157
Figure A4.11	Custom made wireless signal transmission circuit.	158
Figure A4.12	a photograph of the PENG characterization set-up, including mass, PENG, electrodynamic shaker, oscilloscope, shaker controller and the control software.	158
Figure A5.1	a. XPS C 1s deconvoluted spectra of CNF nanopaper, b. XPS survey and c. ATR spectrum, d. TEM image of CNFs, e. AFM results of CNF film.	162
Figure A5.2	DMA results of CNF and LCNF film a. Storage modulus and b. loss modulus, c. photo of CNF film and associated contact angle results.	163
Figure A5.3	Open-circuit voltage and short-circuit current between CNF nanopaper and various materials.	164
Figure A5.4	a. Reliability testing of the output voltage of LCNF nanopaper/Cu TENG (30 Hz, 4.2 N), b. Open circuit voltage of LCNF nanopaper/Cu at different test frequencies.	164

Figure A5.5	Output voltage of LCNF nanopaper/Cu TENG at various %RH levels, a) 27%, b) 40%, c) 50%, d) 60%, e) 70%, f) 80%, g) 90%, h) 95%, and i) TENG voltage outputs plotted against RH levels.	165
Figure A5.6	Output voltage of LCNF nanopaper/Cu TENG at various temperatures, a) 25.6°C, b) 30°C, c) 35°C, d) 40°C, e) 50°C %, f) 64°C, g) TENG voltage outputs against temperature.	166
Figure A5.7	Rectified voltage a. and current b. output of LCNF/Al based cascade-type TENG (CTENG) device.	167

List of Tables

Table 2.1	Performance comparison of various PVDF-based piezoelectric nanogenerators based on different chemical composition and experimental conditions such as the amount of force applied, operation mode, device area, and output load resistance.	36
Table 5.1	LCNF nanopaper/Cu TENG peak to peak voltage outputs at various relative humidity levels.	93
Table 5.2	LCNF nanopaper/Cu TENG peak to peak voltage outputs at various temperatures.	93
Table A2.1	Comparison of percentage increases of piezopotential with porosity.	136
Table A3.1	A Comparison of output performance of the state-of-the-art PNG devices.	150
Table A4.1	output performance comparison of PENGs based on PDMS.	159
Table A5.1	X-ray photoelectron spectroscopy (XPS) peak positions data for C1s line of nanopapers. Band C1s was deconvoluted into five peaks.	167
Table A5.2	X-ray photoelectron spectroscopy (XPS) survey results. Atomic concentration of carbon and oxygen in CNF and LCNF nanopapers.	168
Table A5.3	Comparison of output performances of TENGs using unpatterned metal as the tribopositive layer.	168

List of Abbreviations

Abbreviations	Full Names
<i>NGs</i>	nanogenerators
<i>PENGs</i>	piezoelectric nanogenerators
<i>TENGs</i>	triboelectric nanogenerators
<i>PDMS</i>	polydimethylsiloxane
<i>PMMA</i>	Polymethylmethacrylate
<i>NPs</i>	nanoparticles
<i>PVDF</i>	poly (vinylidene fluoride)
<i>P(VDF-TrFE)</i>	poly (vinylidene fluoride-co-trifluoro ethylene)
<i>CNF</i>	copper-nickel coated polyester fabric (CNF)
<i>LED</i>	light emitting diode
<i>PTFE</i>	polytetrafluoroethylene
<i>SEM</i>	scanning electron microscopy
<i>EDS</i>	energy dispersive spectrometer
<i>PFM</i>	Piezoelectric Force Microscopy
<i>AFM</i>	Atomic Force Microscopy
<i>KPFM</i>	Kelvin probe Force Microscopy
<i>FTIR</i>	Fourier transform infrared spectroscopy
<i>TGA</i>	thermogravimetric analysis
<i>CA</i>	contact angle
<i>ZnO</i>	zinc oxide

<i>PZT</i>	lead zirconate titanate
<i>NWs</i>	nanowires
<i>PET</i>	polyethylene terephthalate
<i>DMF</i>	N, N-Dimethylformamide
<i>HCl</i>	hydrochloric acid
<i>DMSO</i>	Dimethyl sulfoxide
<i>EDX</i>	Energy-dispersive X-ray
<i>XRD</i>	X-ray diffraction
<i>GIXRD</i>	Glancing incidence X-ray diffraction
<i>GPa</i>	Gigapascal
<i>ITO</i>	Indium tin oxide
<i>FASnBr₃</i>	Formamidinium tin bromide
<i>MAPbI₃</i>	Methylammonium lead iodide
<i>UV-Vis</i>	Ultraviolet-visible
<i>Voc</i>	Open-circuit voltage
<i>Isc</i>	Short Circuit current
<i>XPS</i>	X-ray photoelectron spectroscopy

Chapter 1

Fundamentals of Nanogenerators and Literature Review

1.1 Background

Scavenging sustainable power by converting ubiquitously-available unutilized energy to usable electrical energy holds promise to meet ever-expanding energy demands as conventional fossil energy sources are being quickly exhausted. Due to continuous growth in overall energy demand and the related environmental impacts, over the last several decades, an enormous amount of research effort has been devoted to developing eco-friendly sustainable energy storage and conversion systems to replace fast-exhausted fossil fuels. Lately, with the rapid advancement of smart wearable electronics, the demand for corresponding flexible and sustainable power supply units is continuously growing [1]. However, traditional chemical batteries, which are still the most widely used portable energy source so far, cannot meet the requirements of wearable electronics due to their inherent limitations of rigid complex structure, heavy weight, bulky volume, persistent recharging/replacement, and limited lifetime [2]. One of the best routes to mitigate this challenge is to develop self-powered energy harvesters that can scavenge waste biomechanical energy from the surrounding environment, such as human motion, tiny mechanical vibration, car engine vibration, wind, and ocean waves which is ubiquitously available and can be generated continuously and inexhaustibly without ambient environment barrier [3]. Energy harvesting based on nanotechnology [4] is attracting intensive interest and attention for two primary reasons: (i) the potential to realize self-powered electronics [4-7] as portable devices, sensors, and implantable biomedical devices which typically consume very low electrical power [8], and (ii) the potential to reduce global dependency on energy sources based on fossil fuels [9]. Over the past decades, researchers have been investigating different ambient energy harvesting technologies based on electromagnetic [10], electrostatic [11-12], and piezoelectric methods [13-14]. These technologies called nanogenerators (NGs) harvest energy sources in the surrounding environment for driving Internet of Things (IoT) smart electronics [15-17]. Among them, piezoelectric nanogenerators (PENGs) and triboelectric nanogenerators (TENGs) exhibit the excellent capability to efficiently convert different

forms of mechanical energy to electric energy, including human body motion, vehicle movements, water flow, airflow, and acoustic wave, etc. [18-23]. In particular, a variety of flexible NGs with the advantages of low cost, simple configuration, lightweight, environment friendliness, and universal availability have been actively explored [24-27].

The contact electrification effect was first recorded as early as 2600 years ago and the first demonstrated piezoelectric effect was reported by Pierre and Jacques Curie in 1880. Nevertheless, the unprecedented potentialities of these effects in energy harvesting applications had not been fully revealed for a very long time. Following the first demonstration of the piezoelectric nanogenerator in 2006 [28] and the triboelectric (contact-electrification) nanogenerator in 2012 [29], significant efforts have been devoted to accomplishing a brand-new era of self-powered electronics by using organic-inorganic heterojunction nanomaterials to build sophisticated micro-/nano systems [30-39].

Piezoelectric nanogenerators (PENGs), which have compact and flexible working modes, are a very promising alternative solution to the battery. When mechanical stress is applied to a piezoelectric material, the centers of positive and negative charges are separated, thus creating polarization-induced piezo potential. PENG research is focused on manipulating material structures (porous, nanowires, etc.) by lithography, etching, or others to improve stress distribution profiles or growing materials with very high inherent spontaneous polarization. PENG device performance has been improved by a series of structure-driven techniques, such as adopting nanowires [40], aspect ratio tuning, film porosity modulation through a multi-stage etching process [41], cascading multiple devices [42] and reducing charge-screening effects [43]. However, this device still suffers from comparatively lower output performance and operates preferably in higher frequency regimes. A thorough investigation is needed to improve the output performance of the PENG devices.

Triboelectric nanogenerators (TENGs) based on the coupling effect of contact electrification between two different materials and electrostatic induction have emerged as a viable technology to convert ambient mechanical energy into electrical energy. TENGs have numerous advantages, including large power density, high energy conversion efficiency, versatile options for material selection, lightweight, low cost, etc. They have been successfully used as self-powered sensors in wind speed sensing, micro liquid biological and chemical sensing, vibration monitoring, transportation, and traffic management, motion tracking, and powering biomedical microsystems, among others [44-46]. The contact electrification-induced surface charge density is defined as the key figure of merit for TENGs, which originates from the different work functions between two materials. Therefore, increasing surface area

by creating nanostructures, designing nanomaterials with high energy storing capabilities, or having dense surface states are the efficient routes towards a highly-efficient TENG. A state-of-the-art TENG can produce a power density of up to 500 W/m² [47]. However, in contact separation-triggered TENGs, the air breakdown effect can significantly limit the surface charge density on triboelectric surfaces [48]. So, a detail understanding of the underlying physics is needed to improve the output performance of the TENG devices.

1.2 Principles of Nanogenerator

Nanogenerators efficiently transform mechanical energy into electrical power/signal, which has broad applications in energy science, environmental protection, wearable electronics, self-powered sensors, medical science, robotics, and artificial intelligence [49]. TENGs are generally based on contact electrification. When two dissimilar materials are brought into contact, electrostatic charges are created on the material surfaces due to the different electron affinities of the materials. When the two materials are subsequently separated, the developed voltage forces the electrons to flow between two electrodes, generating an alternating current in the TENG. When mechanical stress is applied, a piezoelectric material is polarized, creating a piezo potential. The physics behind nanogenerators (NGs) can be explained using Maxwell's equations.

Ampere's circuital law with Maxwell's addition is

$$\nabla \times H = J + \frac{\partial D}{\partial t} \quad (1.1)$$

where H is the magnetic field and D is the displacement field.

$$D = \epsilon_0 E + P \quad (1.2)$$

Here P is the polarization field and E is the electric field. Therefore, Maxwell's displacement current can be defined as:

$$J_D = \frac{\partial D}{\partial t} = \epsilon_0 \frac{\partial E}{\partial t} + \frac{\partial P}{\partial t} \quad (1.3)$$

The first part on the right of equation (1.3) gives the birth of electromagnetic waves. The second part relates to the output of the nanogenerator. If the surface charge density of a piezoelectric nanogenerator is σ_p , and there is no external electric field, the displacement current is reduced to [50]

$$\frac{\partial D}{\partial t} = \frac{\partial P}{\partial t} = \frac{\partial \sigma_P}{\partial t} \quad (1.4)$$

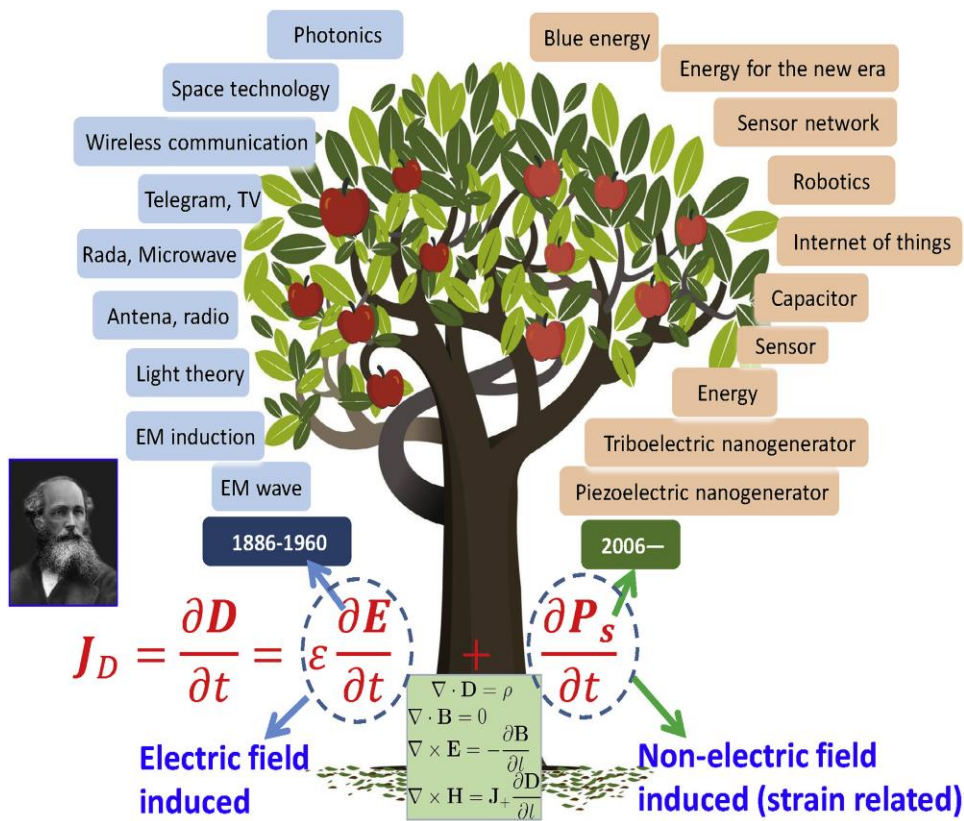


Figure 1.1. A tree idea to illustrate Maxwell's displacement current: the first term $\epsilon \partial E / \partial t$ is responsible for the electromagnetic waves' theory; and the second term $\partial P_s / \partial t$ is related to energy and sensor applications, such as nanogenerators. Reproduced with permission [49]. Copyright 2020, Elsevier.

Equation (1.4) denotes the observed output current in PENGs. In TENGs, the electrostatic field built by the triboelectric charges (with a surface charge density of σ_c) drives the electrons to flow through an external load, resulting in an accumulation of free electrons in the electrode $\sigma_1(z, t)$. $\sigma_1(z, t)$ is a function of the gap distance $z(t)$ between the two dielectrics. The corresponding displacement current is [50]

$$\frac{\partial D}{\partial t} = \frac{\partial \sigma_1(z,t)}{\partial t} = \sigma_c \frac{\partial z}{\partial t} \quad (1.5)$$

This is the observed current for TENG. $\partial z / \partial t$ depicts the speed at which two triboelectric layers contact each other. This basic theoretical understanding of nanogenerator operation is vital to further modeling and analysis, which unveils enormous potentialities for meeting future energy demands as shown in **Figure 1.1**.

1.3 Piezoelectric Nanogenerator (PENG)

1.3.1 Basic concept of PENGs and its operating principle

Originating from Maxwell's displacement current, the piezoelectric nanogenerator concept was coined by Prof. Wang in 2006 [28], where an array of zinc oxide (ZnO) nanowires (NWs) grown on a metallic substrate was bent by a conductive atomic force microscope (AFM) cantilever probe, as shown in **Figure 1.2**. The tetrahedrally coordinated Zn^{2+} and O^{2-} were accumulated layer-by-layer along the c-axis (**Figure 1.2a**). At its original state, the charge center of the anions and cations coincide with each other. Once an external force is applied, the ZnO nanowire structure is deformed and stretched on one side while compressed on the other side, which accumulates negative and positive charges on the respective sides. Therefore, the negative and positive charge centers are separated and form an electric dipole leading to a piezoelectric potential (**Figure 1.2b**). If an external load is connected to the deformed material, the free electrons are driven to partially screen the piezoelectric potential and flow through the external circuit to realize a new equilibrium state [51-52]. The resultant piezopotential is observed through the formed Schottky barrier between the AFM probe tip and semiconducting ZnO NW, which forces the electrons to flow between the electrodes, through an external circuit (**Figure 1.2c-d**).

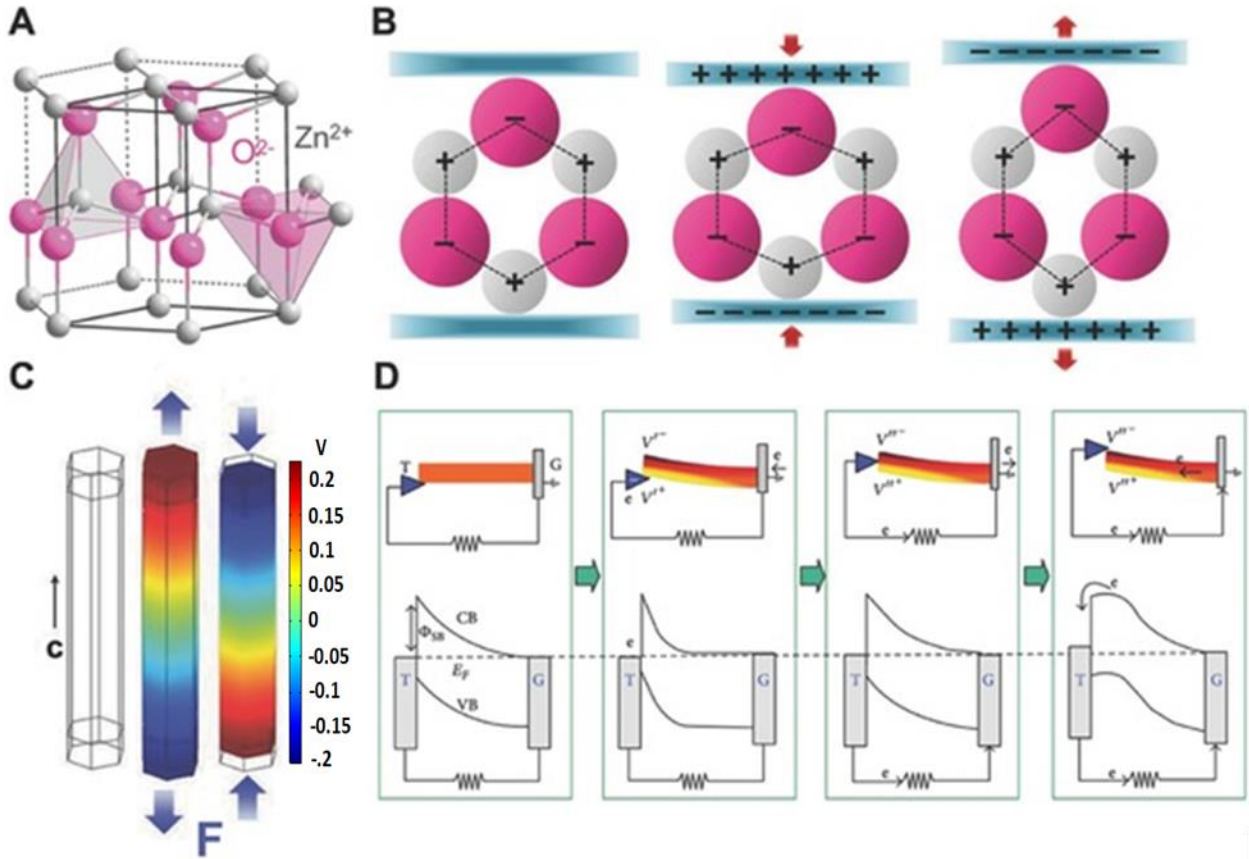


Figure 1.2. Mechanism of piezoelectricity. (a) Atomic model of the wurtzite-structured ZnO. (b) Different piezopotential in tension and compression modes of the PENG. (c) Numerical calculation of the piezoelectric potential distribution in a ZnO nanowire under axial strain. Reproduced with permission [51]. Copyright 2017, Wiley-VCH (d) Band diagram for the charge outputting and flowing processes in the PENG. Reproduced with permission [51]. Copyright 2017, Wiley-VCH.

Since this pioneering work, intensive research efforts were made to enhance output power generation from ZnO NW-based PENGs as it is environmentally friendly, easy to grow at low temperatures, and is self-poled. In contrast, most of the ferroelectrics require high-temperature processing conditions [32].

1.3.2 Historic outline, advances and remaining challenges of PENGs

Over the past few decades, piezoelectric based energy harvesters have been evolving rapidly. Unlike many conventional harvesters, they have the capability of transforming small mechanical vibration in the environment in to useful electrical energy.

The mechanical energy density available in the free environment can reach to up to an order of 10 mW/cm² which is the second highest after solar energy (10-100 mW/cm²) [53]. Scientists have used numerous piezoelectric materials including ZnO [51], CdS [54], GaN [55], NaNbO₃ [56], PVDF [57], BaTiO₃ [58], PZTs [59], and InN [60] for this purpose.

The first reported piezoelectric energy harvester which was used vertically aligned arrays of ZnO nanowires was developed by Z. L. Wang in 2006 [28]. The working mechanism of the device is already presented in **Figure 1.2**. This demonstration paved a way to develop “self-powered” nano-devices that can generate electrical energy under the action of external forces using nanometer-scale piezoelectric materials [61].

Although the quantity of electric output of a single strained nanowire is promising, but for practical applications the amount of power is still very limited and therefore it is essential to collect the power from an array of nanowires. In the following year, Z. L. Wang group developed the first ever piezoelectric nanogenerator excited by ultrasonic waves which could drive AC current through an external load uninterruptedly [62]. This work demonstrated a route toward resolving the fundamental engineering issues associated with effective usage of nanogenerators. The physical configuration of the device allows for the bending of the nanowires and in turn generation of piezoelectric voltage when a sound pressure is applied to the top electrode. A number of other devices were fabricated using the same zigzag electrode configuration such as those formed by gold-coated ZnO nanowires [63-66].

While the first-ever energy harvester based on piezoelectric nanowires in 2006 could only generate up to 9 mV output, it opens the route towards more efficient devices with enhanced output performance. Yang et al. in 2009, designed and developed a flexible PENG based on a single horizontal ZnO “Fine wire” with a length and diameter of 200 μm and 4 μm, respectively. The device is able to generate up to 65 mV output voltage at bending state [67]. Later in 2014, Zhou et al. developed a flexible nanocomposite PENG consisting of hydrothermally grown freestanding PZT nanowires and a polydimethylsiloxane (PDMS) matrix. The configuration of the device made full use of piezoelectric properties of the inorganic nanowires and the flexibility of the organic polymer matrix. The output open circuit voltage and short circuit current of the PENG device was reported to be up to 7 V and 120 nA, respectively [68].

In early 2017, Alluri et al. designed and demonstrated a piezoelectric device, which is composed of BTO and PDMS for scavenging biomechanical energy. The reported open circuit voltage and short

circuit current were as high as 126.3 V and 77.6 μA , respectively [69]. This outstanding performance allowed for powering portable electronic devices with a continuous power supply. After that the following year, Malakooti et al. used a 3D printing method to construct a piezoelectric nanocomposite PENG with controlled alignment using the direct-write method. They demonstrated that by using this technique, they can incorporate highly aligned BTO nanowires in polylactic acid (PLA) polymer and enhance the output of the device by aligning the nanowires in the direction of applied stress. The output of the device demonstrated that using the direct write method can improve the performance by about 400% compared to that of randomly oriented nanowires [70]. All the results demonstrated clearly that the design of the PENG has evolved from a single nanowire with an output of mV range to more than 100 V in about a decade or so, therefore empowering self-powered portable electronic devices to replace battery operated sensors.

To a continuation, recently, Yuan et al. presented a cascade type 6-layer rugby-ball-shaped PENG and improved the output performance to 88.62 V and 353 μA , setting a record value for multilayer PENGs [71]. Although piezoelectricity can be enhanced by these strategies, optimally unifying appropriate mechanical and electrical properties in a single piezoelectric film remains a challenge. Growing organic-inorganic molecular perovskite solution, or synthesizing an organic-inorganic perovskite single-crystal have recently achieved record d_{33} coefficients (~ 185 pC/N) [72] by surpassing their inorganic counterparts, e.g. lead zirconium titanate (PZT), lead magnesium niobate lead titanate (PMN-PT) and Barium titanate (BTO). By dispersing highly piezoelectric nanoparticles (NPs) in a flexible polymer, composite films can be developed, which has been proven as an attractive, easier approach in terms of fabrication scalability, device flexibility, improved mechanical strength, and enhanced electrical output and stability. Nanowire (NW) arrays' unique advantages, such as enhanced surface area, relatively high mechanical flexibility, and high sensitivity to small forces, make them an ideal candidate for piezoelectric nanogenerator (NG) applications [73-75]. Such NGs produce piezoelectric potential (piezopotential) under external dynamic strain and drive electrons to flow in an external load [76-77]. III-nitrides NWs such as AlN, AlGa_{1-x}N_x, GaN, and InN are noted for their tunability, direct bandgap, high chemical stability and strong resistance to atmospheric moisture, and their unique piezoelectric property arising from their non-centrosymmetric wurtzite crystal structures [78-79]. The large dislocation density that is often observed in InN planar structures grown on lattice-mismatched substrates, can be substantially minimized in InN nanowire structures. This is attributed to highly efficient strain (and thermal) relaxation in nanowire lateral surfaces [80-83]. In addition, by adding p-

dopants into InN nanowires, the piezoelectric device performance is significantly improved compared to intrinsic InN NW-based devices. A systematic study on the p-type InN nanowire material and devices for piezoelectric NG applications has been conducted and the experimental results demonstrate excellent reproducibility and reliability of p-type InN NW-based nanogenerator devices [84]. Using radiofrequency plasma-assisted molecular beam epitaxy (MBE), intrinsic and magnesium (Mg)-doped (p-type) InN NWs have grown on Si (111) substrates under nitrogen-rich conditions, respectively, using the InN NW-growth procedure detailed by others [85-86]. After the first demonstration of PENGs based on ZnO nanowire arrays [28], researchers continue to design and fabricate new device structures, to improve device performance. Many PENGs are based on ZnO NWs or nanorods because one-dimensional (1D) ZnO nanostructures with a high aspect ratio exhibit better piezoelectric performance. However, 1D ZnO nanostructures suffer from mechanical fragility and instability. On the contrary, two-dimensional (2D) ZnO nanosheets can generate direct current-type piezoelectric output, which is attributed to their buckling behavior and formation of a self-formed anionic nano clay layer. A PENG based on the integration of 1D and 2D ZnO nanostructures on the same substrate was demonstrated for the first time, which was synthesized using a simple, low-temperature, and low-cost hydrothermal method [87].

Recently, organic-inorganic halide perovskites have received significant attention as materials for various electronic applications such as photovoltaic cells, photodetectors, light-emitting diodes, and sensors, owing to their outstanding and unique properties such as high-power conversion efficiency, tunable bandgap, solution-based processability, and high absorption coefficient [88]. These materials retain a general perovskite crystal structure with stoichiometry ABX_3 , in which A represent an organic cation such as $CH_3NH_3^+$ (MA) or $CH(NH_2)_2^+$ (FA), B represents a metal cation with a different oxidation number than A, such as Pb^{2+} or Sn^{2+} , and X is an anion such as Cl^- , Br^- , or I^- [89]. Although initial studies of OIHPs focused on photovoltaic applications, the applications of their piezoelectric phenomena continue to attract research interest [90-94].

The OIHPs combine the advantages from both the organic molecular part and inorganic octahedron of the perovskite structure at a microscopic level, have been the focus of research for quite some time as a potential alternative to ceramics [95, 90]. Besides their distinct optoelectronic properties, OIHPs exhibit great advantages in terms of their compositional variability, structural flexibility, and room-temperature and solvent-based synthesis process [90-92]. Organic-inorganic halide perovskites materials exhibit structural phase transition that is similar to other inorganic perovskite materials

leading to ferroelectric polarization [96]. Also, halide perovskites have shown excellent piezoelectric and ferroelectric properties comparable to those of conventional inorganic piezoelectric materials. The ferroelectric polarization switching and piezophototronics properties of $\text{CH}_3\text{NH}_3\text{PbI}_3$ (MAPbI_3) perovskite were demonstrated by Coll et al. in 2015 [93]. The following year another study by Kim et al. showed that the PENGs fabricated with MAPbI_3 thin films give an output voltage of 2.7 V and a current of 140 nA/cm² [94]. Potential piezoelectric application of OIHPs became more feasible after the invention of piezoelectric composite films which exhibited superior flexibility and sustainability by introducing perovskite nanoparticles within different soft polymer materials. Perovskite NPs examined in the literature to date include FAPbBr_3 , Fe-doped MAPbI_3 , and FASnI_3 [95, 97-104].

However, a major concern and obstacle to commercialization related to traditional lead-based perovskite materials is the environmental toxicity of these materials. After exposure to water, the lead-based materials can easily form a solution containing the life-threatening lead, which may be released to the environment where it can accumulate in the food chain and impose deleterious impacts on ecosystems and human health [105]. In recent years, scientists are devoted to finding the solution to the stability and toxicity problem present in the lead-based system by replacing Pb^{2+} in perovskites [106] with other divalent cations, such as Sn^{2+} , Ge^{2+} , Mg^{2+} , Ca^{2+} , Sr^{2+} , or Ba^{2+} [107-109, 95]. Due to the ion size effects and lone pairs of electrons, Sn^{2+} and Ge^{2+} are among the best candidates for the replacement of Pb^{2+} . Moreover, Sn-based OIHPs exhibit robust photovoltaic performance because of their high electronic dimensions and unique electronic configuration [110]. However, Sn^{2+} in Sn-based OIHPs can easily be oxidized to Sn^{4+} . One solution to address this challenge would be to engineer the composite material structure to effectively prevent the migration of external oxygen and moisture through the material and to suppress internal ion diffusion inside the devices [106]. In this context, the PENG design strategy whereas the OIHPs scaffolded by an insulating polymer has drawn much attention for large-scale application [97].

Nevertheless, despite the development of various halide perovskite materials with excellent piezoelectric properties, an understanding of piezoelectricity in halide perovskites is still further required to realize practical piezoelectric applications. Part of this research also aims to find the fundamental understanding of the energy harvesting property of various halide perovskite materials and the factors to be considered for the development of high-performance energy harvesters.

1.4 Triboelectric Nanogenerator (TENG)

1.4.1 Basic concept of TENGs and its operating principle

Founded on the omnipresent but detrimental contact-electrification effect, triboelectric nanogenerators (TENGs) are originally developed for scavenging the mechanical energy from impacts, sliding, and rotations [111-112], producing higher output voltages than other harvesters. Tribo electrification/contact electrification creates static polarized charges on two material surfaces, whereas electrostatic induction on the electrodes by the tribo-charges converts the applied mechanical energy to electrical energy by changing the separating distance and hence creating potential differences [113]. According to the lump circuit model of TENG, it is a variable capacitor type voltage generator in which the device output is associated with the separation distance between the electrodes (**Figure 1.3(c)**).

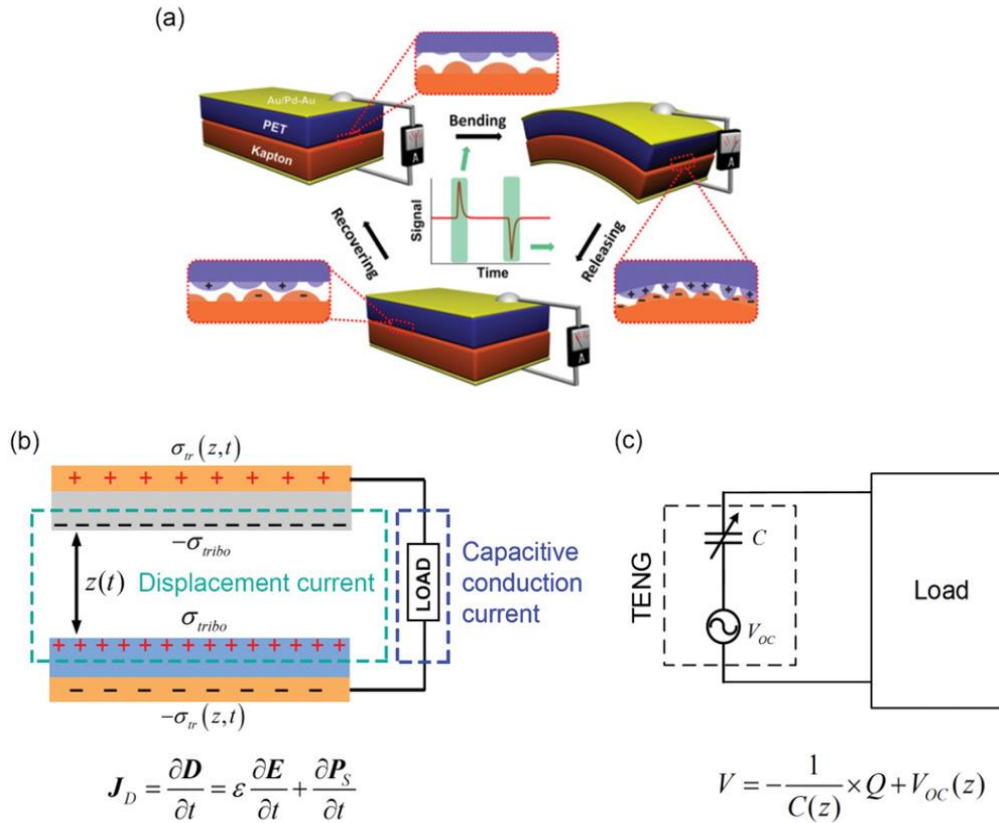


Figure 1.3. Theoretical models of TENG. (a) Schematic illustration of the first TENG and its operating cycle. (b) The displacement current model of a contact-separation-mode TENG. (c) The equivalent electrical circuit model of TENG. Reproduced with permission [113]. Copyright 2019, Wiley-VCH.

TENGs offer advantages such as more flexible material choices, easy fabrication, lightweight, and low cost. In 2012, Prof. Wang's group first introduced the TENG model in energy harvesting device fabrication, exhibiting unprecedented energy generation potentialities at low frequency. As demonstrated in **Figure 1.3(a)**, the TENG device structure is composed of Au/Kapton/Air gap/PET/Au. Periodic contact-separation between PET and Kapton can generate sufficient output power. From there onwards, significant research progress has been made and a maximum output power density of 500 W/m² has been reported recently [47]. Depending on the direction of the polarization change and electrode configuration, four different operation modes of the TENG have been proposed [29] including vertical contact-separation (CS) mode, lateral-sliding (LS) mode, single-electrode (SE) mode, and freestanding triboelectric-layer (FT) mode, as shown in **Figure 1.4**. These can scavenge almost all types of mechanical energy from the environment. The vertical CS mode uses relative motion perpendicular to the interface and the potential change between electrodes, and thus external current flow is dictated by the gap distance between material surfaces.

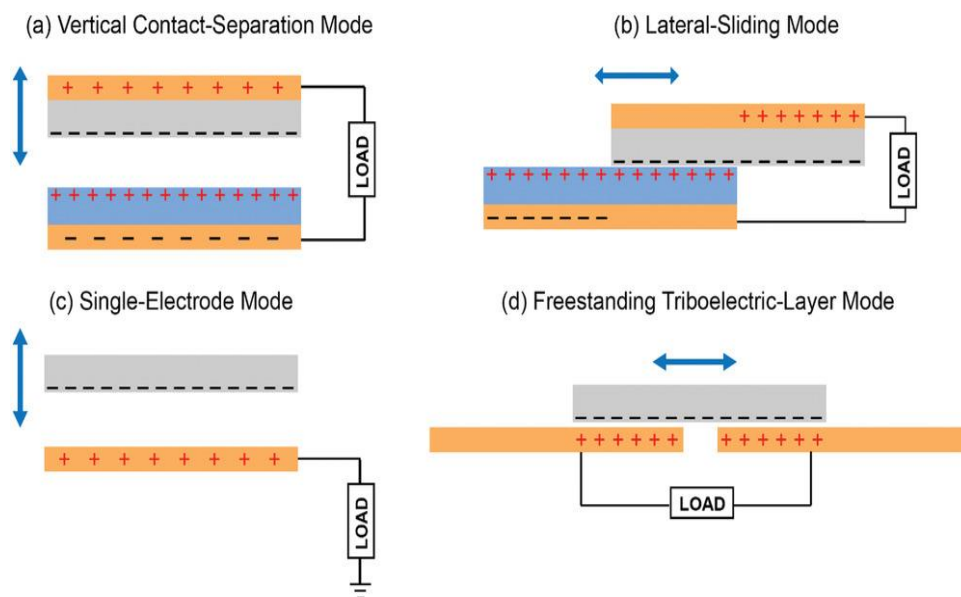


Figure 1.4. Four working modes of TENG. (a) Vertical contact-separation (CS) mode. (b) Lateral-Sliding (LS) mode. (c) Single-Electrode (SE) mode. (d) Freestanding Triboelectric layer (FT) mode. Reproduced with permission [113]. Copyright 2019, Wiley-VCH.

The lateral-sliding mode uses the relative displacement in the direction parallel to the interface, and it can be implemented in a compact package via rotation-induced sliding. The single-electrode mode takes the ground as the reference electrode and is versatile in harvesting energy from a freely moving object without attaching an electric conductor, such as a hand typing, human walking, and moving transportation. The freestanding triboelectric-layer mode is developed upon the single-electrode mode, but instead of using the ground as the reference electrode, it uses a pair of symmetric electrodes and electrical output is induced from asymmetric charge distribution as the freely moving object changes its position [113]. One thing worth noting is that the practical application of TENG is not limited to one single-mode but relies more on the conjunction or hybridization of different modes to harness their full advantages.

1.4.2 Historic outline, advances and remaining challenges of TENGs

Triboelectric nanogenerators (TENGs) work on the combined principle of triboelectrification and electrostatic induction. In definition, triboelectrification is the process of charge generation on the surface of two dissimilar materials when they are brought into contact. Whereas the electrostatic induction is an electricity-generating phenomenon in which electrons flow from one electrode to another electrode through an external load to equalize their difference in potential [29]. The mechanism behind the formation of charges on the surface of the triboelectric material was not defined clearly and remain highly debated [114-115]. A fundamental physical model was formed only in the year 2017, in which the triboelectrification mechanism that has been known for thousands of years was traced back to Maxwell's Displacement current.

The first flexible TENG was invented in 2012 by Z. L. Wang's group by sandwiching polyester (PET) and Kapton thin films, which produced an open-circuit voltage of 3.3 V and current of 0.6 μA at a power density of $\sim 10.4 \text{ mW/cm}^3$ [88]. Not far along in the same year, Zhu et al. gave a suitable explanation for the TENG-based power conversion utilizing polymethylmethacrylate (PMMA) and Kapton as triboelectric materials [116]. These new forms of vigorous nanogenerators produce an open circuit voltage of 110 V, and the instantaneous power density could reach up to 31.2 mW/cm^3 . Later in the same year, Z. L. Wang et al. designed and developed an arc-shaped triboelectric nanogenerator using polymer thin film and a thin metal film along with the explanation using finite element analysis. The unique arc-shaped designed TENG [116] reached an output of 230 V, $15.5 \mu\text{A/cm}^2$, and 128 mW/cm^3 . Polydimethylsiloxane (PDMS) is considered as one of the suitable materials for TENG

applications because of its distinct properties like flexibility, transparency, high negative polarity, and easy fabrication. In the year 2013, Zhu et al. designed a TENG using nanoparticle-enhanced PDMS and gold (Au) thin film, based on contact separation mode. The device generated a record high voltage of ~1200 V, instantaneous power output of 1.2 W, power density of 313 W/m², with an average output power of 132.1 mW [117]. In the following year, Yun et al., exposed the PDMS to ultraviolet-ozone followed sprinkled with NaOH solution to get a triboelectric voltage of 49.3 V and 1.16 μA, respectively [118]. This output is recorded to be 15 times larger than the TENG using pure PDMS. In 2013, Hu et al. developed a vertical contact TENG integrated with a 3D spiral structure that can produce a maximum output power output of 2.76 W/m² on a resistive load of 6 MΩ at a resonant condition [119]. Recently, a TENG has been designed based on harmonic resonator for an active vibration sensor, and coupled with nanomaterials modifications. When a vibration with the variable frequency of 2 to 200 Hz with a considerable working frequency of 13.4 Hz was applied, it generates a uniform output of 284.7 V, a current of 76.8 μA, and a peak power density of 726.1 mW/m² [120].

Normally, the nanogenerator produce high output voltage but low output power. In order to improve the instantaneous power output of the TENG, Cheng et al. developed a nanogenerator based on a contact switching mode during the mechanical triggering which largely decreases the duration of charging/discharging process. That's how the pulse of the instantaneous power output improves without compromising the output voltage. The output current and power reaches as high as 0.53 A and 142 W at a resistive load of 500 Ω [121]. The recorded current and power density reach as high as 1325 A/m² and 3.6 × 10⁵ W/m², respectively. Another approach to solve the lower power output in TENGs were designed later in 2014 by Yang et al. They designed a 3D integrated multilayered TENGs, where the output of individual TENGs are synchronized to achieve a maximum value [122]. This 3D TENG has a multilayered structure with acrylic supporting substrates. PTFE nanowires are used as triboelectric materials, and aluminum and copper are used as electrodes and contact surfaces. The synchronized 3D TENG produces a short circuit current of 1.14 mA and an open-circuit voltage of 303 V with a power density of 104.6 W/m². Lin et al. [123] studied the relationship between the motion of a single water drop on to the water TENG and proposed a sequential contact-electrification and electrostatic-induction process to understand the working mechanism of it. The TENG is made out of nanostructured PTFE thin film and PMMA as substrate layer coated with Cu electrode. The TENG is based on a single electrode mode. When a 30 μL water drop hits the TENG, it can achieve a peak voltage of 9.3 V and a peak current of 17 μA. A maximum power output of 145 μW is obtained when the generator is

connected to a resistive load of 5 M Ω . The study also proved that the superhydrophobic nature of the PTFE film is responsible for the high output.

It is always challenging to improve TENGs output performance and which also hindrance the progress of TENG. Although some research theoretically showed the energy conversion of TENG is 85%, but in practice, it has not yet been achieved [114,124]. Based on the electron affinity of different materials, the triboelectric series has been created to quantify the figure of merits of TENG design. The displacement current model, the capacitive model, and the figure of merits of TENG all suggest that its output current and voltage are proportional to the triboelectric surface charge density (SCD) and that the output power is proportional to the square of the surface charge density [113]. A recent study demonstrated that designing a new working mode and enlarging the frictional triboelectric surface area and the frequency can significantly influence the output performance of the TENGs [125]. Based on this theory, in the year 2018, Feng et al. came up with an innovative TENG based on biodegradable leaf and leaf powder, which gives 15 μ A current and 430 V under 5 Hz contact mode [114]. Later, poly-L-lysine (PLL) is applied in the same device to modify the leaf powder, which enhances the output performance as high as 60 μ A and 1000 V. A conductive double-sided carbon tape composed of carbon powder was proposed as electrodes for TENGs by Shi et al. [126] in 2019 for higher output power density.

Lu et al. showed that the performance of a PTFE-based TENG and its electrical output decreased with increasing temperature in the range of -20 to 20 $^{\circ}$ C, remained stable from 20 to 100 $^{\circ}$ C and then dropped subsequently [127]. This temperature-dependent change in output charge density is attributed to the change in material permittivity and temperature-induced surface defects such as surface oxidation or defluorination. Wang et al. enhanced the triboelectric charge density of a basic Cu-PTFE-based TENG to a record-high value of 660 μ C/m 2 by simply operating the device in a high vacuum to prevent air breakdown, which is the biggest performance-limiting factor of TENG [116, 128]. Besides the aforementioned three approaches, high dielectric constant materials such as BaTiO $_3$ and SrTiO $_3$ have been widely used as fillers, (P(VDF-TrFE)) as the matrix material for charge-attracting, and high-dielectric barium titanate (BTO) nanoparticles for charge-trapping to enhance TENG performance [129-131]. Adding a carbon nanotube (CNT) charge transport layer between the triboelectric and dielectric material can effectively increase triboelectric charge density by facilitating the charge accumulation process [132].

Particularly, polytetrafluoroethylene (PTFE) has become the most widely used tribonegative material [133]. To date, PTFE and other fluorinated polymers accounted for negative tribolayers in more than 50% of reported TENGs in the literature [134].

However, there are growing global interests in replacing petroleum-based non-biodegradable plastics by green natural materials to attain a higher sustainability and a lower environmental impact. As a result, (ligno)cellulose, ubiquitous as a low-cost, renewable, biocompatible, and biodegradable material, has attracted significant attentions. Cellulosic materials have become a top choice for making more sustainable electronic devices, including transistors, [135-136] supercapacitors [137-138] batteries [139-140] sensors,[141] and antennas [142-143] that are green, flexible, and disposable or recyclable [144]. Recently lignocellulosic composite (composed of lignin, starch, glycerol and NaOH) revealed tribopositive capabilities when paired with nylon [145]. However, cellulosic materials were rarely explored as tribonegative layers because pure cellulose exhibited weak intrinsic tribopositivity. The few studies that investigated cellulosic materials as tribonegative layers yielded TENG devices with only modest power output performances. The best TENG devices with cellulosic tribonegative layers reported so far involved the use of nitrated cellulose nanofibrils (CNF) nanopapers (Nitro-CNF) and disulfide-containing regenerated cellulose films (cellophane). The integration of nitro functionalities altered the surface charge density of the CNF nanopapers due to good electron withdrawing properties of the nitro group. Nevertheless, the Nitro-CNF (-) @copper (+) pair only produced 70% of the power output of the TENG using fluorinated ethylene propylene as the tribonegative layer [146]. Recently, a fully cellulose-based TENG was fabricated by integrating regenerated cellulose film as the tribopositive layer and cellophane as the tribonegative layer.

Therefore, the quest for new device design, material innovation, and underlying fundamental physics investigation by considering the ambient parameters, such as temperature, humidity, ambient pressure, is important to realize an era of self-powered TENG-based micro/nanosystems.

1.5 Material design and performance enhancement of NG

1.5.1 Selection of materials

For flexible PENGs design, the frequently used piezoelectric inorganic semiconductors and piezoelectric ceramics are unable to meet the demand of adequate flexibility because of their inherent brittleness [147]. On other hand, due to their excellent flexibility and easy fabrication process, piezoelectric polymers such as PVDF and P(VDF-TrFE) show promising potential in flexible and

wearable applications [148]. Nevertheless, the output of such polymer based PENGs are relatively small because of their intrinsic low polarization [149]. Therefore, novel nanocomposite device containing inorganic piezoelectric nanoparticles and flexible polymers has been developed for improving the piezoelectric output performance of polymeric PENGs, taking advantages of the high piezo response of the inorganic part and the flexibility of the polymer [150]. Among all the piezoelectric polymers, PVDF and its copolymer P(VDF-TrFE) is attractive due to its enhanced spontaneous polarization. For the piezoelectric nanofillers, inorganic ZnO, organic/inorganic perovskite nanoparticles have been used to enhance the piezoelectric property of polymers because of their high piezoelectric coefficient [151].

Selection of material for flexible TENGs are mainly depend on triboelectric series. It is obvious that the choices for triboelectric materials are huge, but the selection of suitable friction pair materials with reverse triboelectric polarities is still consider a crucial factor to obtain enhanced electrical output performance. In addition, the flexibility of triboelectric materials should also be carefully considered to achieve flexible and wearable TENGs.

1.5.2 Design of structures

The key points for better device performance have been attributed to the higher aspect ratios of NWs, Schottky barrier formation between the top electrodes and ZnO due to the higher work function of a PdAu electrode than other commonly used metals, and reduced charge-screening effects. As the tensile stress and compressive stress induces negative and positive piezopotential, respectively, an approach stems from creating pn junction ZnO NWs rather than intrinsic ones, to reduce local charge screening effects inside the NWs [152]. However, the lower piezoelectric coefficient ($d_{33} \sim 12$ pC/N) and the fragile nature of ZnO NWs, nanobelts, or nanorods are limiting their applications as a high-performance renewable power source. On the contrary, polymer materials like PVDF (Polyvinylidene fluoride) and PVDF-TrFE (Polyvinylidene fluoride trifluoro-ethylene) are promising piezoelectric materials that have higher flexibility, piezoelectric coefficients, and long-term reliability. Altering the microstructures of such piezoelectric films to enhance strain-dependent piezoelectric polarization has proven to be an effective energy-harnessing mechanism. Film porosity modulation through a multi-stage etching process, aspect ratio tuning, and cascading multiple devices are remarkable structure-driven techniques, further pushing the piezoelectricity limit. For example, by using random and highly porous (50%) polyvinylidene fluoride (PVDF) structures (through etching process), Mao et al. enhanced the output

voltage and current of PENG to ~ 11.1 V and $9.7 \mu\text{A}$, respectively, which is higher than lithography assisted porous PVDF nanowire array [153].

Design of flexible TENGs is relatively easy as most of the used materials are polymeric nanomaterials. The flexible multilayer stacking structured TENG made from biodegradable LCNF nanopaper fabrics has been investigated to take both advantages of the green functional materials and inherent characteristics of tribonegativity. Subsequently, the TENG with multilayer performance has been confirmed to run a self-powered electronic sensor.

1.5.3 Selection of fabrication methods

For the preparation of flexible PENGs, easy approach of one step drop casting and modified LARP techniques are realized followed by HCL etching where required. Due to the enhancement of mechanical stretching for porous structure and electric poling together with surface modification of nanoparticles, as well as ultrasonication induced adsorption process, high output performance of PENG is anticipated in this study.

On the other hand, for developing high-performance TENGs, constructing micro/nanostructure on the surface of triboelectric materials has been demonstrated as an effective strategy to enlarge the effective contact area and improve the triboelectric charge density. The displacement current model, the capacitive model, and the figure of merits of TENG all suggest that its output current and voltage are proportional to the triboelectric surface charge density (SCD) and that the output power is proportional to the square of the surface charge density [113]. That is why the underlying mechanism concerning the origin of the triboelectric charge still requires further investigation. The improvement of SCD can be classified into three major approaches: material composition modification, enhancement of effective contact area, and adjustment of environmental conditions. The material modification strategy can be further divided into chemical surface functionalization and bulk composition manipulation. In chemical surface functionalization, the triboelectric material is modified by changing the functional groups exposed on the surface so that its charge capture capability is enhanced [114-116]. For example, Wang et al. demonstrated the use of self-assembled monolayers, thiols, and silanes, to modify the surfaces of the conductive material Au and dielectric material SiO_2 , respectively [115]. The results show that the output of the Au-based TENG is enhanced by the largest scale when the more triboelectrically positive function group, amine ($-\text{NH}_2$) is introduced on the Au surface, while its performance deteriorates when

the triboelectrically negative group (-Cl) is used. This approach eludes the change in bulk material and their properties and still possesses long-term stability with experimental validation.

Secondly, the SCD can be improved by increasing the surface contact area through surface engineering. The active contact area of two solid materials is generally small due to surface roughness, and thus by simply improving the contact effectiveness, the total amount of triboelectric charges will increase. Some forthright and widespread approaches such as surface texturing and nanostructure preparation can be adopted through lithography assisted nanofabrication techniques, which elevates the SCD to several times higher for the same material.

The third approach is the control and tuning of environmental conditions such as temperature and pressure.

1.5.4 Materials characterization

To investigate the morphologies, element compositions, and other characteristics of the materials, scanning electron microscopy (SEM) equipped with energy dispersive spectrometer (EDS), Piezoelectric Force Microscopy (PFM), Atomic Force Microscopy (AFM), Kelvin Probe Force Microscopy (KPFM), X-ray photoelectron spectroscopy (XPS), X-ray diffraction (XRD), Fourier Transform Infrared Spectroscopy (FTIR), Ultraviolet–visible spectroscopy (UV-Vis), Piezoelectric Coefficient (d_{33}), thermogravimetric analysis (TGA), contact angle (CA), measurements have been conducted in this study.

1.6 Research Objectives

This research mainly focuses on design and developing high performance piezoelectric/triboelectric nanomaterials based flexible NGs. The efficient material synthesis, device fabrication and characterization, and structure designs are also explored and studied in detail.

The comprehensive objectives of this research are summarized as follows:

- Explore, design, and demonstrate a self-powered wireless sensing system based on a porous PVDF PENG
- Synthesize a novel, self-assembled, highly porous perovskite/polymer composite film to fabricate high-performance piezoelectric nanogenerators

- Develop lead-free flexible piezoelectric nanogenerators as a substitute for lead-based energy harvesters
- Study a natural wood-derived lignocellulosic nanofibrils tribolayer to construct and assemble a multilayer TENG with high output electrical voltage and current

Overall, this thesis will explore the design and development of highly efficient and flexible nanogenerator for self-powered wireless electronics. By combining highly electroactive nanomaterials with flexible polymer matrix structures, NGs with high electric output performance and flexibility will be attained. The synthesizing process for the electroactive nanomaterials will be carefully designed and adopted to sustain the inherent advantages of flexible electronics.

1.7 Outline of the Thesis

This thesis consists of six chapters and organized as follows:

Chapter 1 presents research background on organic-inorganic nanomaterials based nanogenerators (NGs). It also reviews the literatures on the recent progress of flexible self-powered PENGs and TENGs, including working principles, materials selections, fabrication methods, as well as structural designs.

Chapter 2 demonstrates a self-powered wireless sensing system based on a porous PVDF-based PENG, which is prominently anticipated for developing auto-operated sensor networks. The fabricated porous PVDF-based PENG demonstrates ~ 11 times and ~ 8 times enhancement of output current and voltage, respectively, compared to a pure PVDF-based PENG. By harnessing energy from minute vibrations, the fabricated porous PVDF-based PENG device (area of $A = 11.33 \text{ cm}^2$) can generate sufficient electrical energy to power up a customized wireless sensing and communication unit, and transfer sensor data every ~ 4 minutes.

Chapter 3 presents a novel, self-assembled, highly porous perovskite/polymer (polyvinylidene fluoride (PVDF)) composite film for fabricating high-performance piezoelectric nanogenerators (PENGs). The macroscopic porous structure can significantly enlarge the bulk strain of the piezoelectric composite film, which leads to a 5-fold enhancement in the strain-induced piezo potential and a 15-fold amplification of the output current. Efficient energy harvesting from automobile vibrations and biomechanical motions was demonstrated.

Chapter 4 presents an organic-inorganic hybrid perovskites (OIHP) PENG, which is a combination of lead-free Formamidinium tin (Sn) halide perovskite ($\text{CH}(\text{NH}_2)_2\text{SnBr}_3$ (FASnBr_3)) nanoparticles (NPs) and polydimethylsiloxane (PDMS) polymer matrix. Piezoelectric force microscopy (PFM) measurements unveiled the excellent piezoelectric properties of the FASnBr_3 NPs with a high piezoelectric charge coefficient (d_{33}) of ~ 50 pm/V.

Chapter 5 reports the discovery of a natural tribonegative material, LCNFs, wherein the lignin bound on the surface of the cellulose nanofibrils possess strong tribonegative properties by acting as an electron-withdrawing component. The experimental results show that LCNF nanopaper (as a highly tribonegative layer in TENGs) out-performs PTFE and other conventional petroleum-based plastic tribonegative materials. The research illustrates great potential of using lignocellulosic materials as green alternatives to replace fluorine-containing polymers in TENGs for developing green self-powering wireless disposable electronics.

Chapter 6 summarizes the research results, points out the current limitations and presents the future work of organic-inorganic nanomaterials based highly efficient flexible nanogenerators.

Chapter 2

Porosity Modulated High-Performance Piezoelectric Nanogenerator Based on Organic/Inorganic Nanomaterial for Self-Powered Structural Health Monitoring

2.1 Introduction

Self-powered structural health monitoring (SHM) can be used to monitor the in-service conditions of aerospace systems [154]. Such an SHM system can overcome the failure modes of traditional deficient time-based, high-cost scheduled maintenance, and thus enhance the safety, consistency, and efficiency of military and civilian aircraft [155]. Currently, wired sensor networks are still the industry standard for aircraft SHM [156-157]. Nevertheless, the installation of the wired network can be an error-prone process requiring a significant workforce and costs. Alternatively, a wireless sensor network system can effectively eliminate wiring problems [158]. For such a wireless system, a reliable and long-lasting power supply becomes critical. One emerging and promising technology is to use an energy-harvesting device, which harvests energy from the ambient environment and makes the system self-operating [159-160].

To date, numerous approaches have been adopted to harvest widespread ambient energies, such as from vibration, wind, raindrops, ocean waves, etc. These technologies include but are not limited to triboelectric [161] or piezoelectric [162-163] nanogenerators, and devices based on electromagnetic [164-168] and electrostatic methods [169-171]. Triboelectric nanogenerators (TENGs) demonstrate adequate energy conversion efficiency, high output voltage, flexible material selection, lightweight, and low cost [161, 172-184]. However, lack of durability and compactness are the two important bottlenecks limiting their SHM applications, particularly for aircraft. On the contrary, piezoelectric nanogenerators (PENGs) exhibit mechanical robustness, excellent environmental adaptability, and better sensitivity, showing a good fit for SHM applications [185-188]. Numerous materials have been used to fabricate PENGs such as inorganic lead zirconate titanate (PZT) [189-190] barium titanate (BaTiO_3), [191-192] ZnO , Na/KNbO_3 , and ZnSnO_3 nanoparticles, [193-196] which have large

piezoelectric coefficients and high energy conversion efficiencies. Organic piezoelectric polymers, such as polyvinylidene fluoride (PVDF), [197] and their copolymers hexafluoropropylene [P(VDF-HFP)], [198] trifluoroethylene (P(VDF-TrFE)), [199] and poly (vinyl acetate) (PVAc), [200] have also attracted significant attention because of their high flexibility, biocompatibility, simple material synthesis process and the presence of energy-efficient β -phase [201]. However, intrinsic PVDF-based PENGs yield lower electrical energy outputs compared to their inorganic counterparts. To address these issues, numerous approaches have been used such as incorporating nanofillers of piezoelectric materials or replicating micro/nanostructures to further enhance the piezoelectricity [202-210]. By using ZnO nanowire templates Cha et al. fabricated a nanoporous PVDF array which can generate a piezoelectric output voltage of 2.6 V and output current of 0.6 μ A under an ultrasonic excitation power of 100 dB at 100 Hz [211]. In this similar way, an AAO template (200 nm pore diameter) assisted PVDF-TrFE nanowire arrays [199] exhibited a peak output voltage and current of 3 V and 5.5 nA, with a strain rate of 0.1% s^{-1} ; PVDF-TrFE nanotubes delivered a voltage output of 4.8 V and power output of 2.2 μ W/cm² at a dynamic compression pressure of 0.075 MPa at 1 Hz which is 36 times higher than of its bulk PVDF-TrFE counterparts [212]. The reason for this high output is mainly attributed to the efficient strain-confinement in the direction of applied mechanical excitation, as a result of the alteration of the microstructure of these ferroelectric polymers. The above-mentioned PENGs have demonstrated an excellent output performance, however, there remains a distinct gap to deploy them as a sustainable compact power source in real-life applications. Mao et. al. developed a simple yet efficient approach to fabricate mesoporous PVDF PENGs by the etching of embedded ZnO nanoparticles (NPs) from the PVDF polymer and raised the output voltage and current to 11 V and 9.8 μ A at 40 Hz due to its higher energy conversion efficiency [213] Such type of porous PVDF based PENGs can be used as an implantable power-sources for biomedical applications [214-215] and promising for next-generation self-powered electronics. Two main problems limit the use of mesoporous PVDF PENGs in many piezoelectric applications. Firstly, due to the improper etching of the NPs from the PVDF creates an electrical breakdown during the high voltage poling to align the PVDF dipoles and cannot reach to its saturated polarization. Secondly, the presence of moistures, defects and pinholes may create short-circuit between the electrodes.

In this chapter, a high-performance porous PVDF-based PENGs based on a one-step etching of ZnO NPs was presented, and with this high energy conversion efficiency successfully demonstrated a self-powered wireless sensing platform. I also develop a model to explain the experimentally observed

performance enhancement in the fabricated porous PVDF-based PENG. Experimental measurements show that with applied mechanical stress of only 2 kPa (corresponding proof mass of 138 gram (g)) the device can produce a peak to peak short-circuit current (I_{sc}) of 22 μA , an open-circuit voltage (V_{oc}) of 84.5 V, the peak power of 0.46 mW, and areal peak power density of 41.02 $\mu\text{W}/\text{cm}^2$. Compared to similar pure PVDF-based PENG, the I_{sc} and V_{oc} are enhanced by ~ 11 times and ~ 8 times, respectively, and are better than those of many previously reported PVDF composite based nanogenerators (**Table 2.1**). The fabricated porous PVDF-based PENG can produce sufficient electrical energy to drive a wireless sensing unit or to light up LEDs. This porous PVDF-based PENG is successfully integrated with a custom-made Bluetooth compatible wireless sensing unit and can send out mimic sensor signals to a remote receiver every ~ 4 minutes. The PENG can also generate sufficient electrical energy from an automobile car vibration, which reflects the scenario of potential real-life SHM systems. The results demonstrate the great potential of porous PVDF-based PENG for practical applications.

2.2 Experiment

2.2.1 Fabrication of the porous PVDF thin film

PVDF powder (Sigma Aldrich) is dissolved in N, N-dimethylformamide (N, N-DMF) solvent (10 wt. %) at 70°C for 24 hours. Then ZnO NPs (35–45 nm, US Research Nanomaterials, Inc.) are mixed within the PVDF matrix solution and the mass ratio between ZnO NPs to PVDF is adjusted to create different porosities. This solution is stirred for another 4 hours on a hot plate with a temperature of 45°C followed by extended ultra-sonication for 30 min to maximize the uniform distribution of ZnO-NPs within the PVDF polymer matrix. The suspension then drops cast onto a Si wafer and degassing is done for 30 minutes at 65°C in a vacuum oven purged with N_2 to suppress potential bubble formation during the curing process. After that, the annealing is done in the same vacuum oven at a slightly elevated temperature (75°C) for another 45 minutes. The films are then peeled off from the Si substrate with cares and immersed in a 37 wt. % HCl solution for 4 hours to completely etch off ZnO NPs from the PVDF matrix. After HCl etching, the films are washed by deionized (DI) water, dried with N_2 gas, and put in a vacuum oven overnight at 60°C for better drying. Finally, porous PVDF thin films are ready for device fabrication.

2.2.2 The PENG fabrication

A high voltage electrical poling of the porous PVDF film is performed with an electric field of 120 V/ μm for 5-6 hours with a DC voltage of 0-6 kV. The films are stable throughout the entire poling process. No short circuit or noticeable voltage fluctuation is detected up to the maximum voltage of 6 kV. Then the poled porous PVDF composite films are inserted between two copper electrodes. For the characterization purpose, the electrical connections are made from both of the top and bottom electrodes by very thin and flexible copper conductors. Finally, the layered structure of polyester/copper/porous PVDF film/copper/polyester film is inserted and passed through a commercial thermal laminator tightly to eliminate any air gaps to secure uniform adhesion.

2.2.3 Characterization and measurements

A JSM-7200F Field-emission scanning electron microscope is used to characterize the morphology and structural properties of the PVDF thin films. Fourier transform infrared spectroscopy (FTIR) is performed by Nicolet iS50 to confirm the piezoelectric β - phase formation inside the porous PVDF film by measuring characteristic absorbance peaks in a wavenumber range from 400 to 1000 cm^{-1} . Atomic force microscopy (AFM) images are captured by using JPK Nanowizard II, configured in intermittent-contact mode (scan rate 0.3 Hz).

2.3 Results and Discussions

The self-powered wireless structural health monitoring system (SHM) consists of an energy generation unit (the porous PVDF-based PENG device), an energy management circuit, and a radio frequency (RF) data transmission module. In the sketched SHM shown in **Figure 2.1a**, the porous PVDF-based PENG device is placed between two metal sheets to reflect the scenario of a PENG operating inside a mechanical joint. The device is composed of a porous PVDF piezoelectric thin film ($\sim 50 \mu\text{m}$ in thickness) which is sandwiched between two copper electrodes and encapsulated with polyester substrates. For wiring purposes, very thin and flexible copper wires ($\sim 100 \mu\text{m}$ of diameter) are connected to both electrodes. Finally, the layered structure of polyester/copper/porous-PVDF film/copper/polyester is compressed tightly by a commercial thermal laminator to eliminate any air gaps by confirming uniform adhesion between each layer. A custom-made wireless sensing circuit as shown in **Figure 2.1b** is placed inside a central groove of the metal sheets (**Figure 2.1a**), which includes functions of energy management, storage, signal conditioning, and wireless data transmission. The high-performance porous PVDF-based PENG, used as a sustainable power supply for the SHM system, is based on a mesoporous thin-film structure.

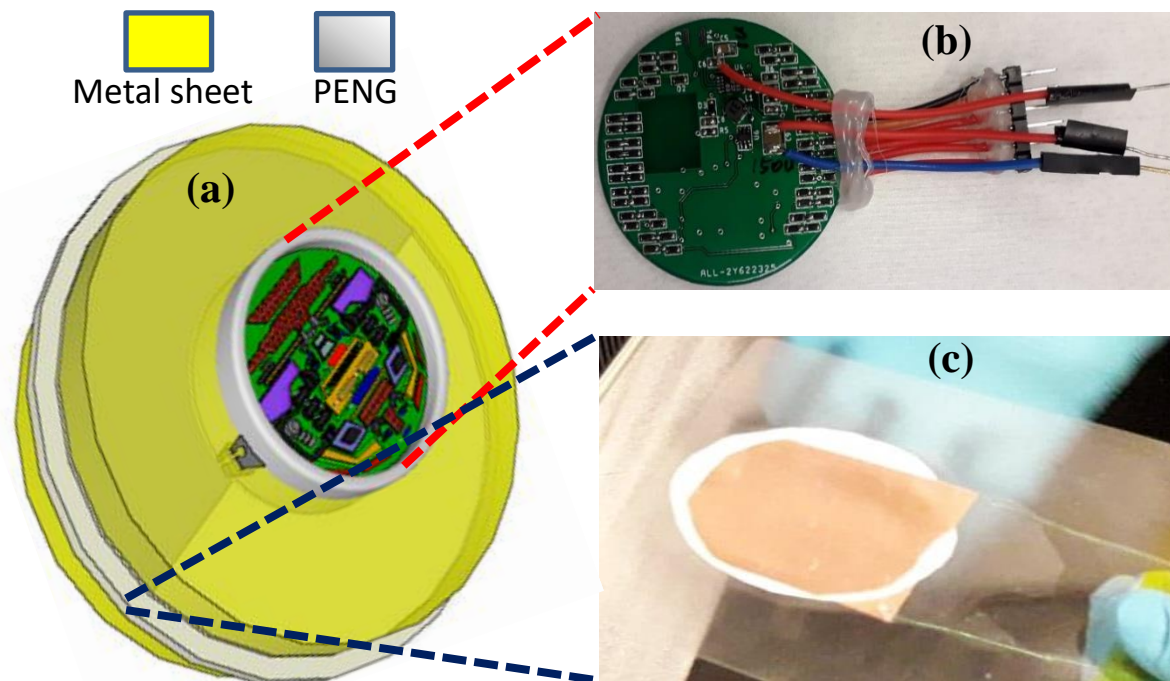


Figure 2.1. Schematic of the wireless sensing system of aircraft structural health monitoring (SHM). (a) schematic illustration of the functional components of piezoelectric nanogenerator (PENG), which is mainly composed of a porous PVDF-based PENG device unit and an integrated circuit unit; (b) an enlarged view of the integrated circuit; (c) an as-fabricated porous PVDF-based PENG device.

As to be revealed shortly, the built-in pores in the porous PVDF film substantially elevate the stress distribution inside the film and thus boost strain-induced piezo potential. PVDF powder is first dissolved in N, N-dimethylformamide (N, N-DMF) solvent and then mixed with ZnO NPs. The mass ratio between the ZnO NPs (35-45 nm of diameter) to the PVDF solution is adjusted, yielding different porosity of the films. To maximize the uniform distribution of ZnO-NPs within the PVDF polymer matrix, the solution is stirred on a hot plate followed by extended ultra-sonication for half an hour. The whole process of porous PVDF thin film preparation and porous PVDF-based PENG device fabrication has been described in detail in the experimental section (2.2.1 & 2.2.2) and illustrated in **Figure 2.2**. The schematic illustration of a fabricated porous PVDF-based PENG device with proper packaging and electrical connection is shown in **Figure 2.1c**. By adopting the aforementioned thin-film synthesis approach, a scalable and industry-viable porous PVDF film (area of 15 cm × 15 cm) is also fabricated and demonstrated in **Figure 2.2**.

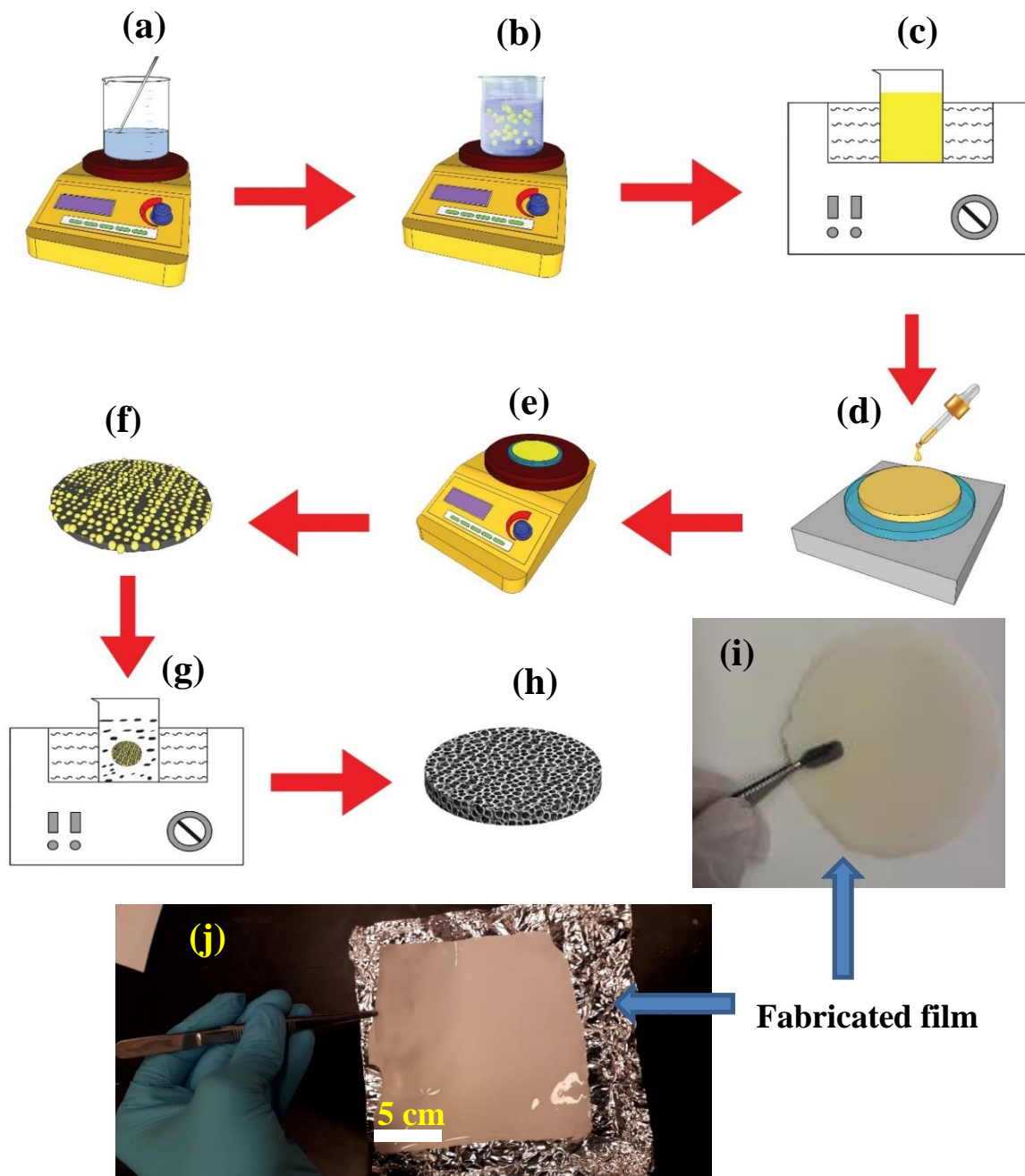


Figure 2.2. Step-by-step fabrication process of the Porous PVDF thin film (a) PVDF powder (Sigma Aldrich) is dissolved in N, N-dimethylformamide (N, N-DMF) solvent (10 wt. %). (b) ZnO NPs (35–45 nm, US Research Nanomaterials, Inc.) are mixed within the PVDF matrix solution. and stirred for 4 hours. (c) Ultra-sonication for 30 min to maximize the uniform distribution of ZnO-NPs within the PVDF polymer matrix. (d) The suspension drops cast onto a Si wafer (e) Degassing is done for 30 minutes at 65°C and then annealing at a slightly elevated temperature (75°C) for another 45 minutes. (f) The films peeled off from the Si substrate. (g) Etching with 37 wt. % HCl solution for 4 hours to completely etch off ZnO NPs from the PVDF matrix. (h) Final porous PVDF thin films are ready for device fabrication. (i) Fabricated film (j) large scale fabricated film (15 cm × 15 cm)

Figure A2.1a, Appendix shows the top surface scanning electron microscopy (SEM) image of a pure PVDF film, indicating that the surface topography is homogenous without wrinkles, grains, voids, cracks, and deformation. **Figure 2.3a** shows the top surface scanning electron microscopy (SEM) image of a thin film prepared from the mixture of 50 wt.% mass fraction of PVDF and ZnO. The ZnO nanoparticles (NPs) are distributed into the PVDF matrix which shows that the ZnO NPs are accumulated in the PVDF film like a cluster, which is mainly due to their different molecular weight (M_w) (M_w of ZnO NPs are higher than that of the PVDF molecule). The main purposes of introducing ZnO-NPs to the PVDF matrix are (1) to create porosity (by HCl etching) in the PVDF film for manipulating its mechanical property, and (2) to promote the formation of porous PVDF film piezoelectric β -phase through the dipolar interaction between ZnO's Zn^{2+} cations and PVDF's $-CF_2^-$ anion groups. Moreover, ZnO NPs have several unique advantages over inorganic (e.g. SiO_2) or organic (e.g. polystyrene) NPs for the fabrication of similar porous nanostructures ZnO NPs mixed PVDF, which include cost-effectiveness, non-toxicity, good scalability, and facile removal by acidic solution [216-220]. Similar phenomena are observed inside the composite film for both pure PVDF and ZnO NP-mixed PVDF, which is distinguishable as revealed by cross-sectional SEM images (**Figure A2.1b-c**). SEM image of **Figure 2.3b** shows the top surface of a porous PVDF thin film after removing ZnO NPs by HCl etching. I envision that during the etching process, hydrochloric acid (HCl) starts to react firstly with the inorganic ZnO NPs on the surface, and then gradually infiltrates to the bulk of the PVDF film. As ZnO NPs are distributed throughout the film, pores are not only formed on the surface but throughout the whole film and the size of the pores should be larger than the actual nanoparticle size. It is seen that the pore sizes are 60 nm with those of the clustered ZnO NPs whereas the average NPs sizes are 35–45 nm. The ZnO-NP are interconnected inside the film allowing completely removed via HCl etching. **Figure 2.3c** explains the energy-dispersive X-ray spectroscopy (EDS) element mapping of the top surface porous film. These results confirm the percentage of detected Zn is negligible compared to the percentage of C and F elements detected on the top surface of the porous film. The corresponding individual element mapping of **Figure A2.2a-e** in porous PVDF thin film for a specific region of interest confirms the percentage of detected elements in the porous film. The top surface and cross-sectional SEM images of the porous PVDF film along with the corresponding EDS spectrum in **Figure A2.3a-d** further confirm the dominating peak of C and F compare to Zn and Cl. The atomic force microscope (AFM) image in **Figure 2.3d** is a 3-dimensional surface topology of the porous PVDF film. The surface roughness of the top surface of the porous PVDF film is confirmed and measured to

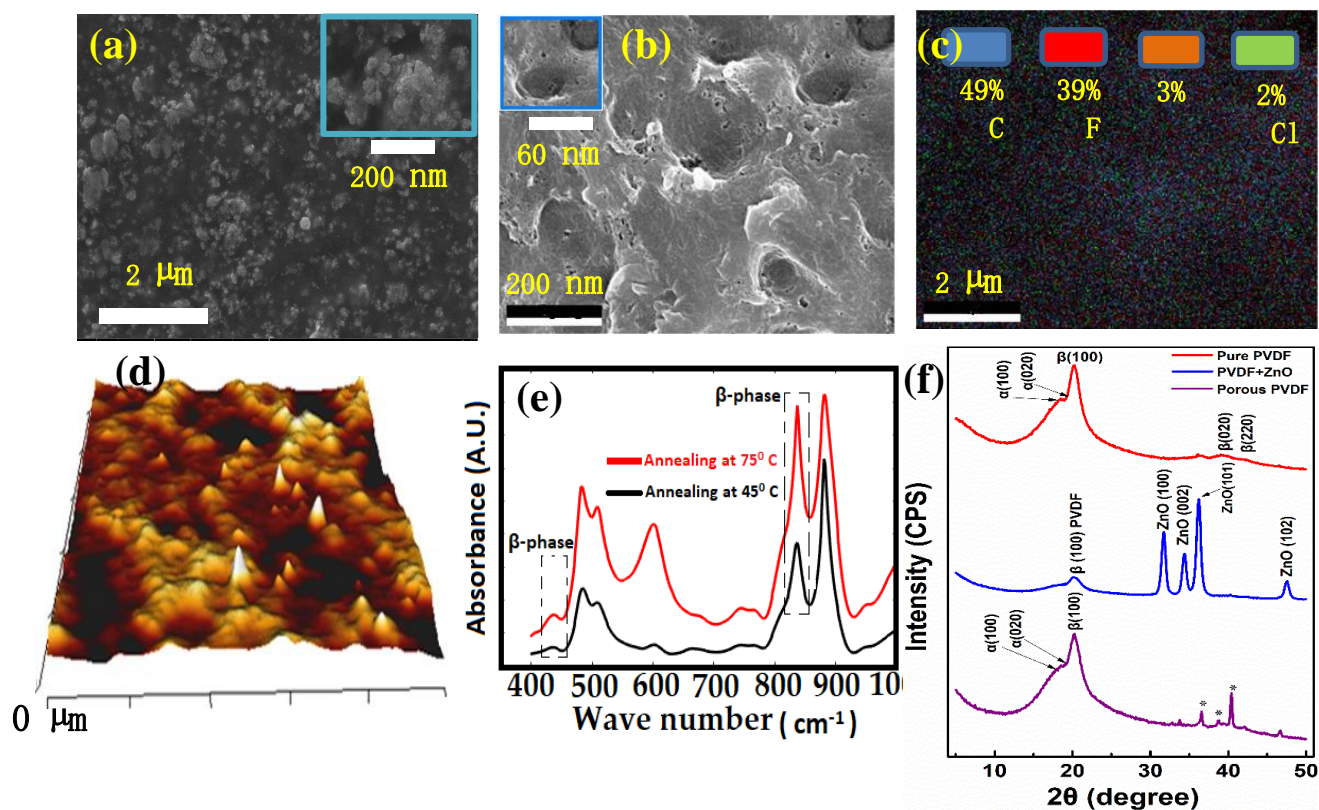


Figure 2.3. Material characterization of as-fabricated porous PVDF-based PENG device: scanning electron microscope (SEM) images of (a) distributed ZnO NPs on the surface of the PVDF matrix before etching (prepared from a mixture 50 wt.% mass fraction of PVDF and ZnO); (b) top view SEM of the porous PVDF film after the etching of the ZnO NPs (Inset is the enlarge view of pore); (c) Elemental composition mapping of Carbon (C), fluorine (F), Zinc (Zn), Chlorine (Cl) in porous PVDF thin film (d) surface morphology characterized by the AFM (e) Fourier transform infrared spectrum (FTIR) of the porous PVDF film to confirm the β phase formation. (f) XRD patterns of pure PVDF, PVDF with ZnO nanoparticles and porous PVDF based thin film.

be ~ 100 nm (**Figure A2.4a, b**). In addition to creating porosity, promoting the β -phase crystallinity of the PVDF film is crucial, as it possesses the highest spontaneous polarization than the other polymorphic phases of the PVDF (α , γ , δ). To confirm the β -phase formation of porous PVDF thin film, Fourier transform infrared (FTIR) spectrum analysis in the wavenumber range of $400\text{--}1000\text{ cm}^{-1}$ is performed. The characteristic peaks of the β -phase at 431 and 840 cm^{-1} can be observed in the FTIR spectrum (**Figure 2.3e**) [221-222]. The formation of the β -phase in the PVDF matrix is assisted through the interactions between the dipoles of PVDF and the surface charges on ZnO-NPs. The positively charged Zn^{2+} cations (0001 surfaces) and O^{2-} terminated anions ($000\bar{1}$ surfaces) interact with the $-\text{CF}_2^-$

or CH_2^+ groups of the PVDF that have negative and positive charge densities respectively, resulting in the β -phase nucleation. Upon applying a high electric poling field, the dipoles of the PVDF are aligned in the direction of the field. The XRD pattern of three different films of pure PVDF, PVDF with ZnO NPs, and porous PVDF are shown in **Figure 2.3f**. These results demonstrate that the piezoelectric β -phase is well-preserved both for pure PVDF and porous PVDF along with other characteristics peak of PVDF and some unknown peaks. Whereas, the XRD pattern of the PVDF film combined with ZnO shows the dominating ZnO characteristics peak compare to the PVDF peaks. This is because the XRD for the organic ZnO is much more profound than the polymer PVDF. It is noteworthy to mention that these results also confirmed the etching of ZnO from the film, helping to enhance the mechanical properties, which is more suitable for the PENG device fabrication. To understand the porosity effect on material piezoelectric properties, a PENG model based on finite element simulations (**COMSOL Multiphysics 5.3**) is developed. A PVDF piezoelectric polymer is used to study the simple cases of a porous structure, where a square (100 nm \times 100 nm) two-dimension (2D) model is employed. Three device models are simulated and compared, including a non-porous (pure) PVDF, a porous PVDF with surface pores, and a porous PVDF with inner pores only, with a pore size of 5 nm in radius and different porosity percentages. To study the piezoelectricity of the porous structure, two independent scenarios—a compressive force and laterally bending force of 2 GPa are uniformly applied on the side and top surface respectively. **Figure 2.4a-c** shows the simulation results of the effect of porosity on piezopotential under compressive force, which demonstrated clearly that pores modify the relative magnitude of the piezopotential. Accordingly, the piezopotential increased proportionally with the degree of porosity, which is represented by the brightness of color grading. The potential is raised by 5.79 % (46.6 V to 49.3 V) when the porosity increases from zero to 3.9 % if pores are on the surface, and the potential is raised by 13.73 % (46.6 V to 53 V) when the porosity increases from zero to 7.85 % if pores are inside (**Figure 2.4d**). (Detail calculations provided in **Table A2.1**). It is also explored that the porous PVDF film will remarkably boost the piezoelectric potential by forming stress concentration centers around the pores. To verify this phenomenon, the strain distribution with lateral bending force is compared between pure PVDF, PVDF with inner pores, and surface pores as shown in **Figure A2.5a-c**. It is clearly shown from the figures that, under the lateral bending force of 2 GPa, the displacement induced of the three different models of the same film thickness of 100 nm is drastically different. The deformation of the porous PVDF film is higher than the pure PVDF film. It is also obvious that the pore position and size influence the mechanical stress distribution, which results

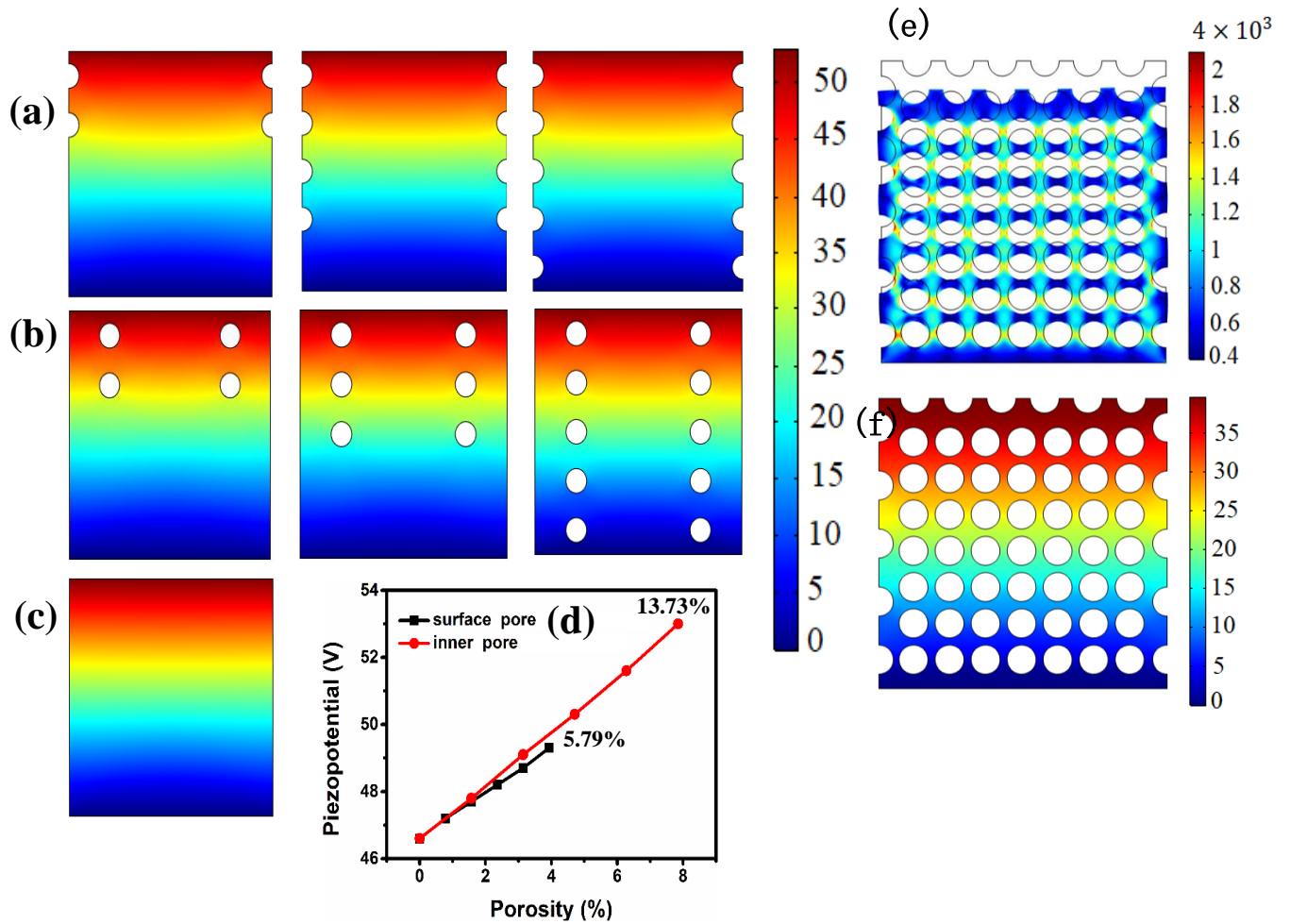


Figure 2.4. Piezopotential distribution in the porous PVDF with varying porosity under a compressive force of 2GPa (a) with surface pores only, (b) with only inner pores, and (c) a non-porous PVDF. **The same scale bar for (a–c)** (d) comparison of piezopotential as a function of porosity for surface pores and inner pores. (e) the strain distribution of 50% porous PVDF structure ensembled with both inner and surface pores (f) the piezopotential distribution of 50% porous PVDF structure ensembled with both inner and surface pores.

in large deformation for surface pore structure than the inner pore structure and so as the potential with lateral bending force. As shown in **Figure A2.5a-c**, the local strain around each pore has a much higher magnitude than the bulk strain in the pure PVDF. This localized strain of higher magnitude induces higher potential, which adds up and enhances the bulk piezopotential. Similarly, the simulated piezopotential results are shown in **Figure A2.6a-d** when a lateral bending force is applied to the side surface of the PVDF structure and described briefly in the **Supporting note A2.1**. As expected, the output potential increases linearly with the applied force, but an important point to be noted that the potential for the equal amount of force is smaller for lateral bending force compare to vertical

compressive force. This is clarified by the fact that the piezoelectric coefficient along the vertical axis of PVDF has the highest value. Consequently, a compressive force applied along the c-axis (vertically), will produce higher output piezopotential compared to a lateral bending force. Then the strain distribution phenomenon for the vertical compressive force is compared between pure PVDF, PVDF with inner pores, and with surface pores in **Figure A2.7a-c**, and systematically investigated (**Supporting note A2.2**). These results conclude that the local strain distribution around the pores, with compressive force and a lateral bending force, leads to a much higher piezopotential enhancement. The strain-induced piezopotential benefits from the stress concentration behavior through enhanced piezoelectric polarization and is crucial for determining the piezopotential distribution [219]. Based on the above discussion, a device model similar to the fabricated device in which pores are distributed both on the surface and in the bulk is built. The simulation result of 50 wt. % of porous PVDF films are compared to that of pure PVDF films. **Figure 2.4e-f** shows the stress distribution and output voltage of the porous PVDF films under uniaxial compressive stress of 800 kPa whereas **Figure A2.8a, b** shows the result of pure PVDF. It is evident that the induced displacement and output of the two PENG models for the same film thickness is remarkably different- the porous PVDF film experiences much larger deformation and thus produces higher voltage output compared to the pure PVDF. This phenomenon can be attributed to the position of pores and size influence. Finally, experimentally investigate the effect of porosity on practical PENG device performance. The electricity generation mechanisms from the poled porous PVDF-based PENG device is demonstrated in **Figure 2.5a-e**. In the beginning, the net dipole moment inside the film is zero with the absence of externally applied force (**Figure 2.5a**). Then dipoles are aligned by applying a high electric field of (120 V/ μm) for 2-3 hours, to the direction of the electric field (**Figure 2.5b**). After that when a vertical compressive force is applied on the device, the net polarization within the PENG device will change, thus resulting in a piezoelectric potential (**Figure 2.5c**). This forces free electrons to move from one electrode to another. After releasing the force, the piezoelectric potential diminishes and electrons move back (**Figure 2.3d**). Finally, the PENG film shows an additional damping cycle, which leads to the observation of an alternative output current pulse due to the formation of porous structures, (**Figure A2.5e**). The fabricated porous PVDF-based PENG device is integrated into the SHM system and evaluated. An electrodynamic shaker is employed for mechanical excitation. The porous PVDF-based PENG device is placed between the shaker hammer and a block of stainless steel (138 g), producing piezoelectric output upon the application and releasing of mechanical stress.

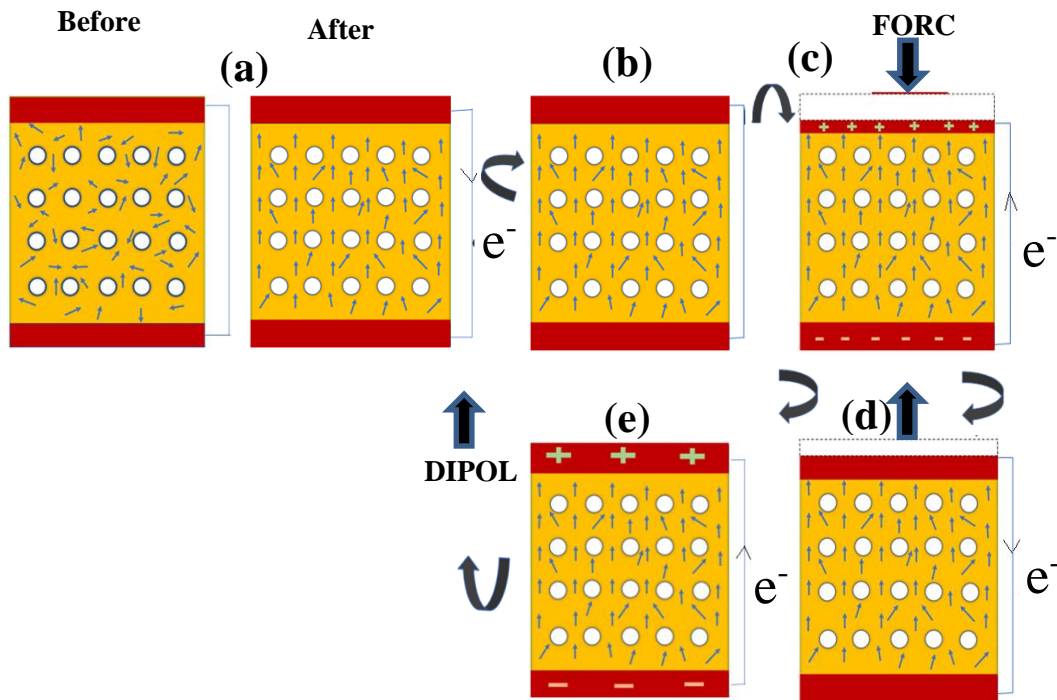


Figure 2.5. Schematics of the energy generation mechanism from the PENG by considering distributed stress on the film

The porous PVDF-based PENG device and the weight system can be treated as a free vibration spring-mass system with damping. The practical setup including all the necessary equipment for the measuring purpose is shown in **Figure 2.6** [216]. PVDF thin films of different porosities are prepared from the mixture of ZnO NPs with different mass ratios (from 0 wt. % to 60 wt. %) (**Figure A2.8c**). As shown in **Figure 2.7a**, the device output voltage increases from 18 V(p-p) to 84.5 V(p-p) when the ZnO NP mass ratio increases from 0 wt. % to 50 wt. %. However, a further increase in the ZnO mass ratios (60 wt. %) results in a decrease of the output voltage to 60 V (p-p). This is because the porosity dependent output is related to the amount of β -phase of PVDF, which is increased with the increase of ZnO mass ratio to PVDF from 10% to 50%. Further increase of ZnO causes a decrease in the total amount of PVDF per unit volume in the mixture, which results in lowering the β -phase. So, the porous PVDF film made from the mixture of 50 wt.% of ZnO possessed the highest β -phase quantity, exhibits the highest output performance, which is attributed to enhanced strained-induced piezo potential due to amplified

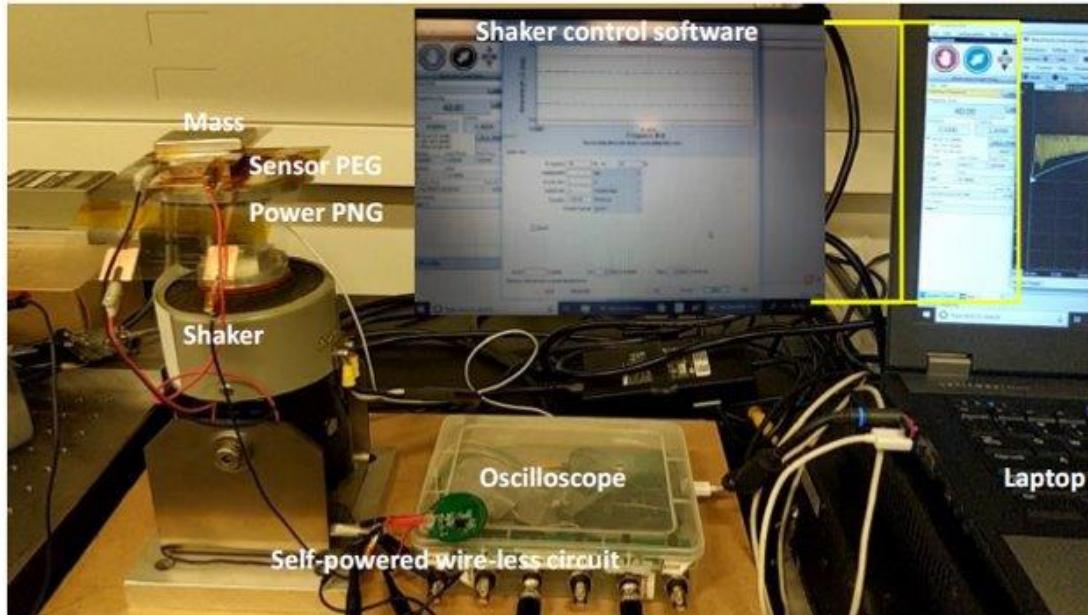


Figure 2.6. General setup of the piezoelectric characterization system. The system includes a closed-loop controller, a vibration shaker, a power amplifier unit, an oscilloscope and a self-powered wireless circuit to demonstrate the realization of self-powered wireless electronics. [216].

mechanical displacement inside the porous film, as revealed in the modeling. The measured peak-to-peak output open-circuit voltage (V_{oc}) and short circuit current (I_{sc}) at 30 Hz frequency is about 84.5 V and 22 μ A, respectively from an active device area of 11.3 cm² for a 50 wt. % ZnO@ PVDF device (**Figure 2.7b, c**). This porous PVDF composite based PENG shows a drastic increase in the output current and voltage performance of ~ 11 times ($\sim 22 \mu$ A (p-p)), and ~ 8 times (~ 84.5 V (p-p)), respectively, compared to a pure PVDF-based PENG (ZnO NP mass ratio: 0 wt. %). It is noteworthy to mention that in the experimental studies; there are other factors in porous PVDF PENG, e.g., a higher amount of the β Phase formation, higher porosity due to the etching of randomly distributed ZnO nanoparticles, which further enhance the PENG output. None of these factors was considered in the simulation studies. As a result, the PENG voltage output is enhanced by ~ 8 times which is much higher than the predicted simulation results. It also shows better performance compared to many previously reported PVDF composite based nanogenerators (**Table 2.1**).

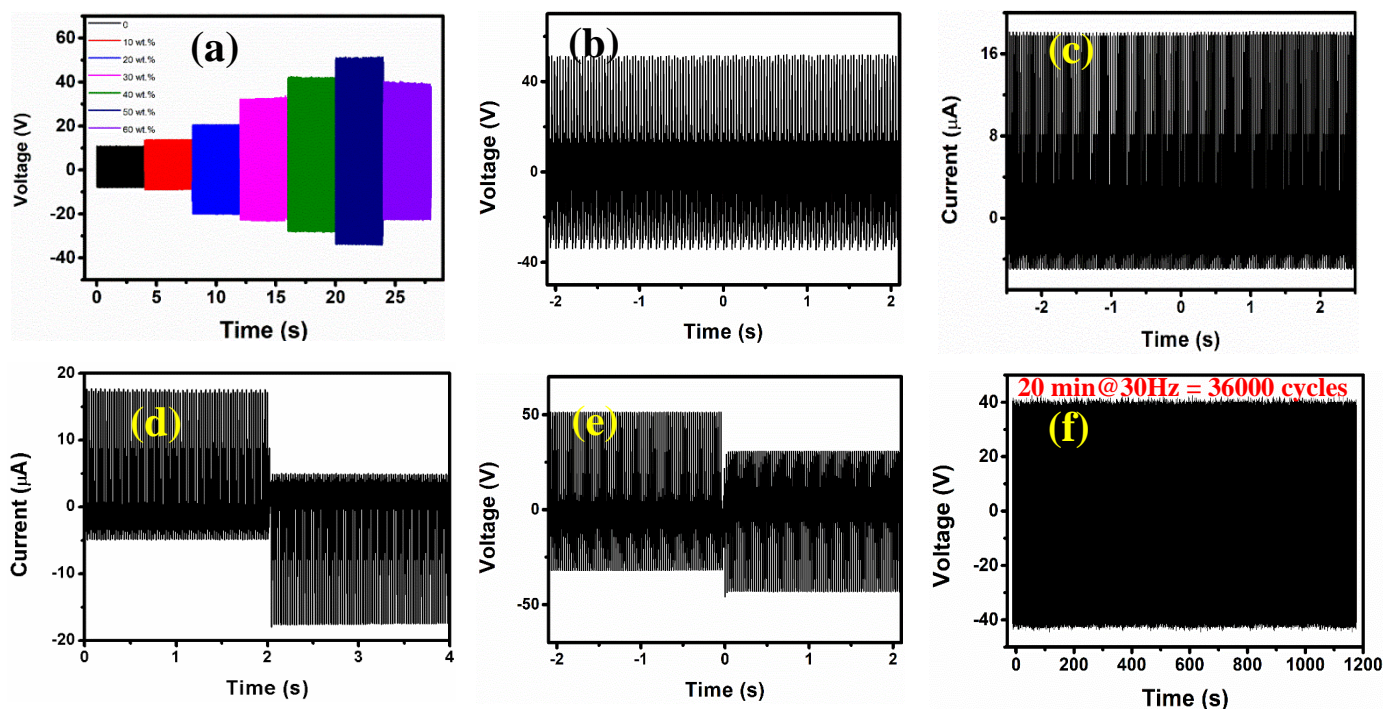


Figure 2.7. Measured electrical output performance of the porous PVDF-based PENG device: (a) the measured open-circuit voltage of the porous PVDF thin films of almost identical thickness when the ZnO mass fraction increased from 0 wt. % (pure PVDF) to 60 wt. %, with a frequency of 30 Hz. (b) peak to peak output voltage at 30 Hz and 2G acceleration when the device was pressed by a standard mass of 138 gram (g) (c) peak to peak output current at 30 Hz and 2G acceleration when the device was pressed by a standard mass of 138 gram (d) polarity switch testing of short circuit current to confirm piezoelectricity (e) polarity switch testing of open circuit voltage to confirm piezoelectricity (f) stability test of the porous PVDF-based PENG device for 36000 cycles (at 30 Hz for 20 minutes).

I have also studied the electrical characterization of film that contains 50 wt.% of ZnO NP inside the PVDF matrix in both porous and non-porous conditions (**Figure A2.9a, b**). It is seen from the result that the output voltage and current both are enhanced due to the porosity of the film. A polarity-switching test is carried out. When the connection is reversed, the reversal in the open-circuit voltage (**Figure 2.7d**) and the short circuit current (**Figure 2.7e**) revealed identical amplitude with reversed polarization, which confirm the inherent piezoelectricity originated from the high-performance porous PVDF PENG [213]. The fabricated PENG is capable of sustaining over a distance future under a constant oscillation without notable degradation in the output signal for 36000 cycles (30 Hz for 20 minutes) (**Figure 2.7f**), showing excellent long-term stability.

Table 2.1: Performance comparison of various PVDF-based piezoelectric nanogenerators based on different chemical composition and experimental conditions such as the amount of force applied, operation mode, device area, and output load resistance.

Materials	Fillers	Structures	Open-circuit voltage	Short-circuit current	Power	References (appendix)
P (VDF-TrFE)	—	Flat film	7 V	58 nA	—	[1]
P (VDF-TrFE)	—	Curved film	120 V	700 μ A	3.9 mW/cm ²	[2]
PVDF	3D Nanofillers	Flat film	11 V @ 729 μ ϵ (strain)	—	72 μ W/cm ³	[3]
PVDF/Ba (Ti _{0.9} Zr _{0.1})O ₃	Nanocubes	Flat film	11.99 V @ 11 N	1.36 μ A @ 11 N	—	[4]
PVDF/ZnO	Nanoparticles	Flat film	24.5 V @ 28 N	1.7 μ A @ 28 N	—	[5]
PVDF/SnO ₂	Nanosheets	Flat film	42 V	6.25 μ A/cm ²	4900 W/m ³	[6]
PVDF/AlO-rGO	Nanoparticles	Flat film	36 V @ 31.19 kPa	0.8 μ A @ 31.19 kPa	27.97 μ W	[7]
PVDF/ZnO	Nanowires	Flat film	6.9 V	0.96 μ A	6.624 μ W	[8]
PVDF/BaTiO ₃	Nanowires	Flat film	14 V	4 μ A	1.5 μ W	[9]
PVDF/BaTiO ₃	Nanoparticles	Flat film	10 Vp-p @ 2 N	2.5 μ Ap-p @ 2 N	5.8 μ W	[10]
PVDF	—	Electrospun membrane	48 V @ 8.3 kPa	6 μ A @ 8.3 kPa	51 μ W	[11]

PVDF	—	Fabric	14 V @ 0.1 MPa	29.8 μ A @ 0.1 MPa	5.1 μ W/m ²	[12]
PVDF/NiO @ SiO ₂	Nanoparticles	Flat film	53 V @ 0.3 MPa	0.3 μ A·cm ⁻² @ 0.3 MPa	685 W/m ³	[13]
PVDF/NKNS-LT- BZ	Nanoparticles	Flat film	18 V @ 50 N	2.6 μ A @ 50 N	—	[14]
PVDF/ZnO	Nanorods	Electrospun membrane	85 V	2.2 μ A	—	[15]
PVDF/ZnO	Nanoparticles	Flat film (Porous)	84.5V @ 2KPa	22 μA @ 2KPa	0.46 mW	This work

The open-circuit voltage (**Figure 2.8a**) and short circuit current (**Figure 2.8b**) of the PENG device are measured within a frequency range from 10 Hz to 50 Hz by turning the frequency of the VR9500 shaker. The piezoelectric output voltage (V_{oc}) peaks at 30 Hz, corresponding to the resonant frequency of the porous PVDF-based PENG device [213]. The harnessed energy is stored in commercial capacitors through a full-wave bridge circuit and the charging characteristics are plotted in **Figure 2.8c**. As expected, the charging time gradually increases with the capacitance (1.0 μ F, 2.2 μ F, 4.7 μ F, 10 μ F, 47 μ F, and 100 μ F). It takes 140 seconds to charge the 100 μ F capacitors to 3 V. The output power from the porous PVDF-based PENG device is measured as a function of load resistance (**Figure 2.8d**). The peak output power ($P_{out} = I_L^2 \times R_L$) (where I_L is the load current and R_L is the load resistance) measured to be 78 μ W at a load resistance of 7 M Ω , corresponding to a peak power density of 12 μ W/cm². This is sufficient for driving the entire wireless SHM system. A two-stage charging system, in which the input capacitor is 1 μ F and the output capacitor is 220 μ F), is employed to improve electrical energy collection efficiency. The porous PVDF-based PENG device produces electrical energy by harvesting mechanical energy from the vibration of the VR9500 shaker operated at 30 Hz. **Figure 2.8e** shows the charging/discharging characteristics of the input (black curve) and output (red curve) capacitors. The whole operation of the custom-designed wireless sensing node is described in detail in **Figure 2.8g**. Herein, the electrical output from the porous PVDF-based PENG is used for two purposes: for sensing and powering up the data transmission unit. The alternating electrical output collected from the porous PVDF-based PENG device is first rectified by a bridge rectifier unit and then

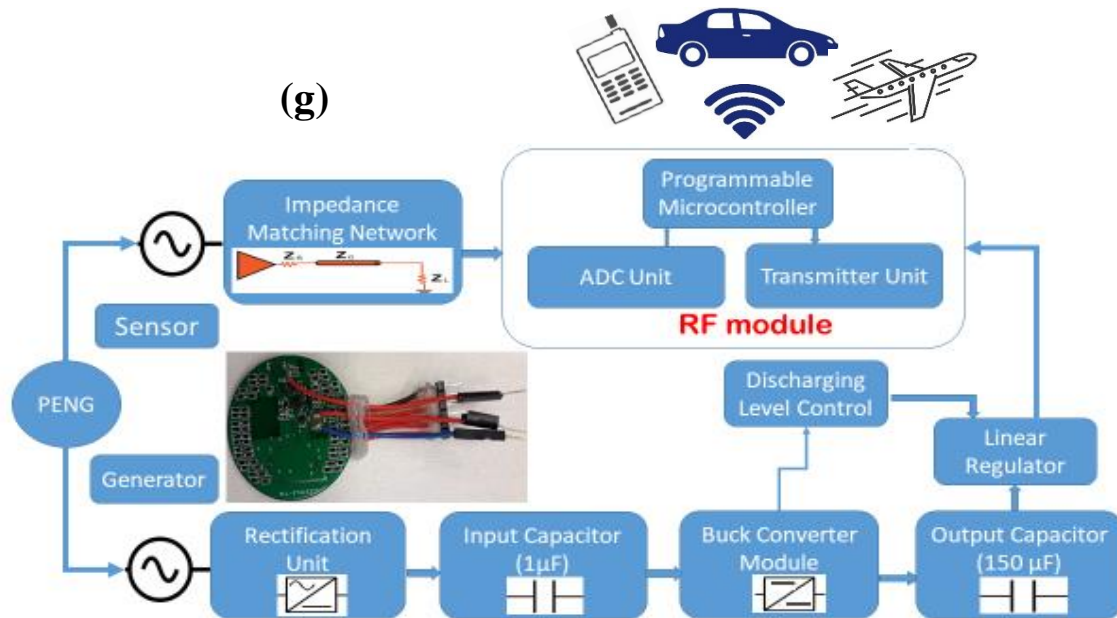
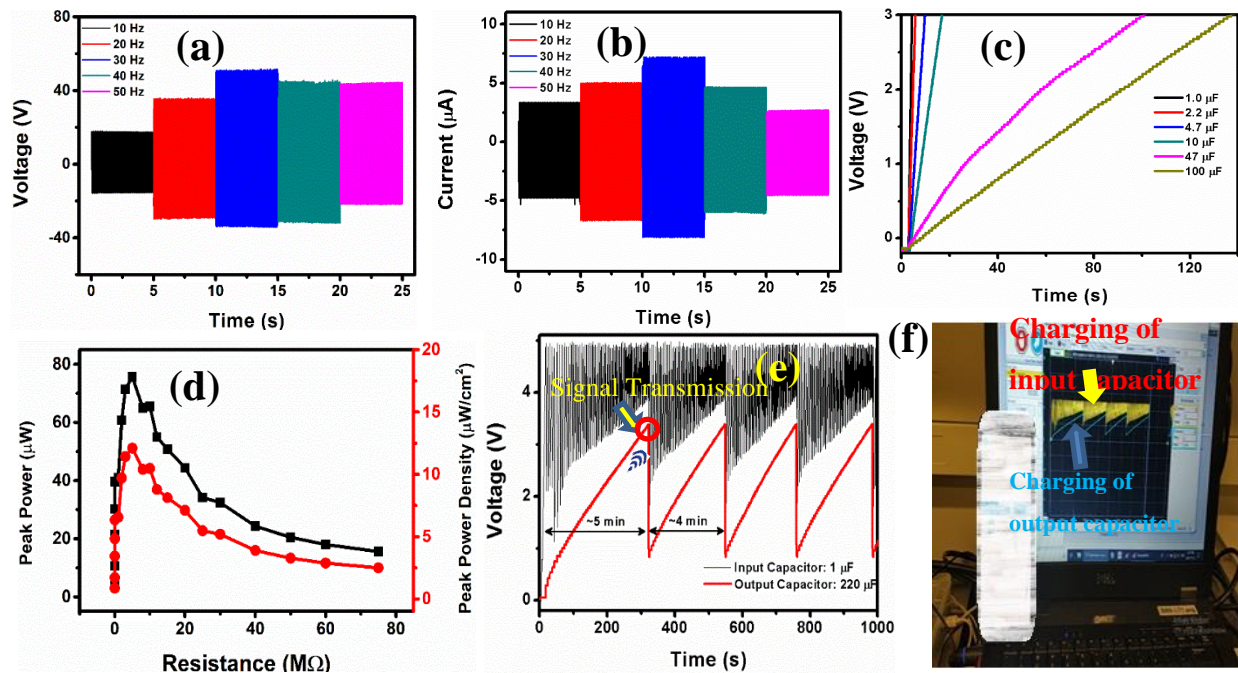


Figure 2.8. Demonstration of high output capability and applications prospect of the porous PVDF-based PENG device (a) comparison of the output voltage at different frequencies of 10 Hz to 50 Hz for the device with 50 wt. % of ZnO-PVDF composition (b) comparison of output current at different frequencies of 10 Hz to 50 Hz for the device with 50 wt. % of ZnO-PVDF composition (c) measured output voltage across the various commercial capacitors of 1 μF , 2.2 μF , 4.7 μF , 10 μF , 47 μF , and 100 μF were charged by the 50 wt. % ZnO-PVDF PENG device at 30 Hz (d) measured peak output power and peak output power density at various loading conditions of the PENG at 30 Hz (e) measured output voltage across the input and output capacitor of the EMM, when the PENG is excited with the linear motor shaking at 30 Hz (f) wireless signal reception by a Bluetooth device (mobile phone) (g) the whole sensing system illustration with the aid of a block diagram.

fed to the energy management module (EMM). As a result, the voltage of the input capacitor drops down to a regulated voltage of $\sim 2\text{-}3$ V. The output capacitor ($220\ \mu\text{F}$) is then disconnected from the input capacitor by the MOSFET switches of the buck converter. The input capacitor is charged up again to continue this charging-discharging cycle. The charging-discharging cycle continues until the output capacitor is charged up to ~ 3.1 V, by when the output capacitor releases its stored energy to drive the wireless data transmission system. For sensing purposes, the alternating output from the PENG is fed to the RF module via an impedance matching network (IMU), which contains a diode and an operational amplifier (Op-Amp) as shown in **Figure 2.8g**. The RSL-10 system on chip (SoC) of the RF module is programmed to operate for a pre-set ~ 1 second/data transmission cycle, during which the measured sensor signal from the PENG device is digitized and transmitted wirelessly to remote receivers (mobile phones). A discharging level controller of the output capacitor based on a delay circuit is introduced as well to control the data transmission frequency. The whole system including the rectifier, the EMM, the RF module, and the impedance matching unit are integrated on a circular printed circuit board (PCB) of a diameter of 3cm as shown in **Figure 2.1b**. The full operation of energy harvesting, energy-storing, data collecting, and wireless transmitting is demonstrated and recorded. This application scenario is demonstrated in **Figure 2.8f** where the Bluetooth receiver of the smartphone is receiving and decoding the mimic sensor signals simultaneously. To demonstrate versatile applicability, the PENG is used in harnessing vibration from an automobile car engine. **Figure 2.9a** represents the measured output voltage from the PENG mounted on the car engine during the off and running condition of the engine. The output peak-to-peak voltage of 8.5 V was measured at the running condition, while there was no voltage recorded at the off condition. Corresponding fast Fourier transform (FFT) (**Figure 2.9b**) of the output voltage was performed, which reveals the major contribution of the device output produced from the vibration components of approximately 29 Hz, which is close to the resonance frequency (30 Hz) of the PENG. The deviation in the FFT signal obtained by the PENG from different structural vibration conditions is critical to monitor structural health. Therefore, the PENG has great potential to SHM application with a wide range of vibrational energy harnessing capabilities. The harnessed energy from the engine vibration can charge a $1\ \mu\text{F}$ commercial capacitor of up to 2.2 V within 60 seconds, as shown in Figure A2.11c. The scenario of energy storing in the commercial capacitor is demonstrated in **Figure 2.9d**.

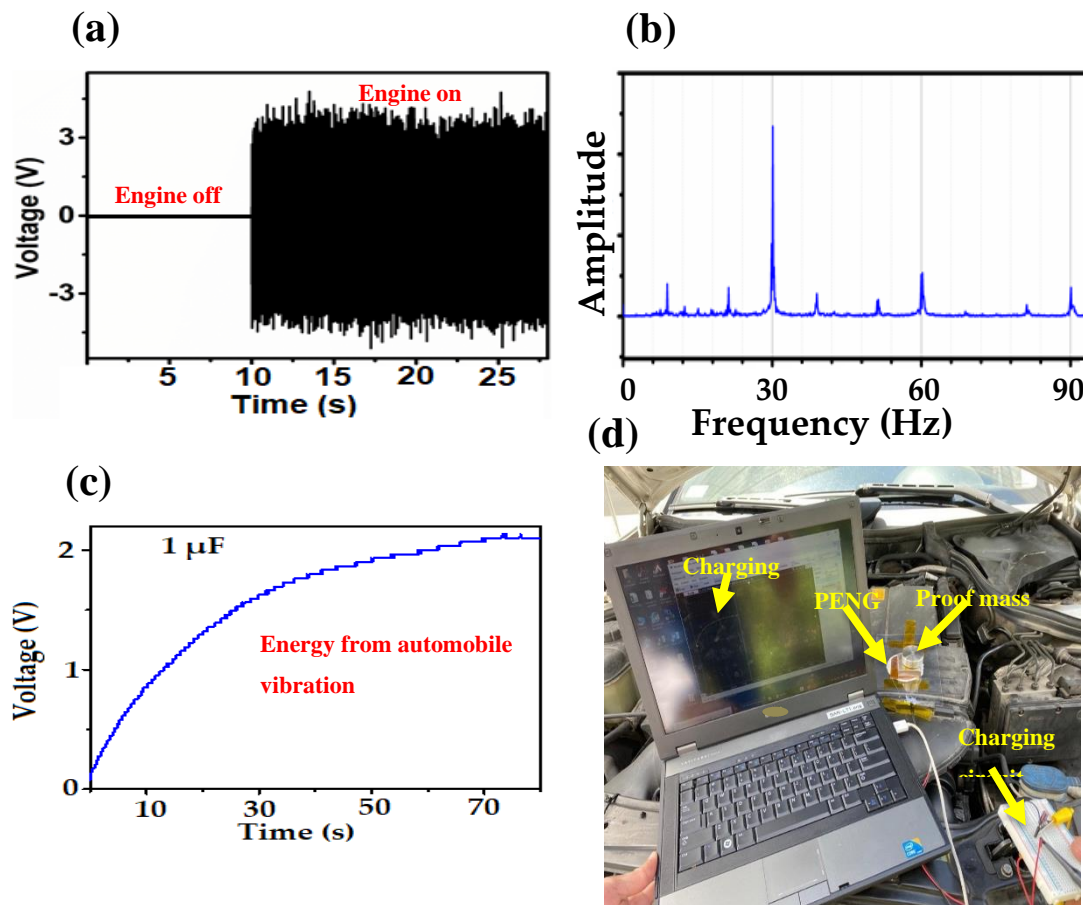


Figure 2.9. Application of the PENG for SHM (a) Output voltage from a PENG mounted on a automobile car engine for both on and run condition. (b) Corresponding frequency domain distribution via Fast Fourier Transform while the maximum peak occurs at 29 Hz (c) Output charging voltage of a commercial capacitor (1 μF) by a single PENG by an automobile engine (Mercedes-Benz car); (d) the corresponding digital photo of charging capacitor by engine vibration at stand still.

2.4 Conclusions

In conclusion, this section successfully demonstrates a high-performance porosity modulated robust PENG device that can generate electrical energy by reaping mechanical vibration energy. The developed PENG exhibits a high output current of 22 μA (p-p), a voltage of 84.5 V (p-p), the peak output power of 0.46 mW, and a power density of 41.02 $\mu\text{W}/\text{cm}^2$ from a single device of area 11.33 cm^2 , outperforming other recently-reported NGs (**Table 2.1**) The control of porosity empowers the adaptable mechanical property of the PENG device, which is inimitable merits critical for harvesting ambient mechanical energy and developing practical self-powered electronic systems. The very simple and effective fabrication method also enhances the formation of piezoelectric β -phase with an applied electric field of 120 V/ μm instead of a large mechanical strain. The as-fabricated PENG allows forced

oscillation to operate in a wide range of frequencies (10 to 50 Hz) apart from its resonant frequency with promising outputs, which unlocks another route toward broadband energy harnessing. The PENG can also generate sufficient electrical energy by harnessing automobile vibrations. With these outstanding performances from PENG discussed above, this chapter successfully demonstrates several auspicious applications such as self-powered SHM for remote sensing which is promising at inconsistent environments for modern IoT based applications and charging commercial capacitors that can power LED devices. It is expected that the achieved noteworthy evolution of porous PVDF film-based PENG provides a promising solution for scavenging energy from the surroundings of the real-world, which reveals new prospects for environment-friendly self-powered technology.

Chapter 3

Maximizing Piezoelectricity by Self-assembled Highly Porous Perovskite-Polymer Composite Films for Enabling the Internet of Things

3.1 Introduction

Developing increasingly compact structures and high performing sustainable power sources have constantly become the important area of research focus to help in the deployment of self-powered electronics. Piezoelectric nanogenerators (PNGs), composed of flexible and compact structures, have emerged as a promising candidates for this purpose [223]. To name a few applications, PNGs have found importance in self-powered nanoelectromechanical systems (NEMS), electronic/piezotronics devices, and implantable medical devices and remote sensing [224-230]. Altering the microstructures of piezoelectric films to enhance the strain-dependent piezoelectric polarization has proven to be an effective energy-harnessing mechanism. For instance, adopting nanowires, [231-234] aspect ratio tuning, film porosity modulation through a multi-stage etching process, [235-240] cascading multiple devices, [241-244] and reducing charge screening effects [244-249] are remarkable structure-driven techniques, further pushing the piezoelectricity limit. By creating pores in ZnO nanowires, [235] Su et al. demonstrated ≈ 23 -fold boosted output current in the PNGs (27.7 nA), with an elevated porosity percentage of 5.4%. By using random and highly porous (50%) polyvinylidene fluoride (PVDF) structures [236] (through etching process), Mao et al. enhanced the output voltage and current of the PNG to 11.1 V and 9.7 μ A, respectively, which is higher than those of a lithography assisted porous PVDF nanowire array [231]. Recently, Yuan et al. presented a cascade-type 6-layer rugby-ball-shaped PNG structure and improved the output performance to 88.62 V_{P-P} and 353 μ A, which is a new record value for multilayer PNGs [241]. Although piezoelectricity can be enhanced by these strategies, optimally unifying appropriate mechanical and electrical properties in a single piezoelectric film still remains to be a challenge. Among the piezoelectric materials, the single crystals such as lead zirconium titanate (PZT), $(1-x) \text{Pb}(\text{Mg}_{1/3}\text{Nb}_{2/3})\text{O}_3-x \text{PbTiO}_3$ (PMN-PT) [250] are highly desirable as it possess very high piezoelectric coefficient (d_{33}). But the high temperature material synthesis, brittleness, and

the presence of toxic lead are the major limiting factors to be used in the PNGs. Thus, developing lead-free piezoelectric materials is an alternative and promising route for fabricating environment-friendly PNG, but the output performance of such materials still remains modest [251]. By dispersing highly piezoelectric NPs in a flexible polymer, composite films can be developed, which is proven to be an attractive, yet easier approach in terms of fabrication scalability, device flexibility, improved mechanical strength, and enhanced electrical output [252-256]. Nevertheless, nanoparticle (NP) dispersion promoters had to be employed to improve the homogeneous dispersion of the NPs in a polymer scaffold (such as PVDF), [257-262] which adversely impacts device performance. As a trade-off, this issue was addressed by functionalizing the surface of piezoelectric NPs before mixing with polymer [263] or replacing NPs with organic-inorganic metal halide perovskites (OMHPs) [264]. By mechanically reinforcing a polymer scaffold (PVDF) with the homogeneously dispersed Formamidinium lead halide (FAPbBr₃), Ding et al. recorded (the highest output of this type) a piezopotential of 30 V and current density of 6.2 $\mu\text{A}/\text{cm}^2$, incorporating an applied pressure of 0.5 MPa [265]. By optimally quantifying the content of uniformly distributed methylammonium lead iodine (MAPbI₃) in the PVDF matrix, a cost-effective solution approach for the MAPbI₃-PVDF piezoelectric composites was also introduced as a result [266]. In this process, a similar approach stems from changing the polymer to polydimethylsiloxane (PDMS), but it still possesses a detrimental brittleness issue [267]. Moreover, substituting the atomic constituents of the OMHP, the piezoelectric and ferroelectric properties can be tuned, and exciting experimental investigations are underway to reliably implement them in practical PNG applications.

In this chapter, a novel self-assembled highly porous perovskite/polymer composite film via the simultaneous control of film structure and material design, which can be used for the PNG applications is reported. The composition of a polymer (PVDF) with a novel hybrid halide perovskite - FAPbBr₂I, can significantly enlarge the bulk film strain by forming self-assembled high-density and ordered pores, and can reduce the film impedance due to the high relative permittivity of FAPbBr₂I. Consequently, the output voltage and current of the developed P-PNG device dramatically increased by ≈ 5 times (to ≈ 85 V peak to peak), and ≈ 15 times (to ≈ 30 μA peak-to-peak), respectively over pure PVDF-based PNGs, with an acceleration of 2G and proof mass of 138 g. Notably, the composite film can be prepared in a one-step manner as the incorporation of multiple nanostructure building blocks, the NP surface functionalization, and follow-up chemical etching all become unnecessary, greatly simplifying the film preparation process and as a result lowering the cost at the same time. The PNG-driven SIWEN

demonstrated in wireless communication between the P-PNG sensors and personal electronics (mobile phones), which is significant for the applications such as self-powered IoT devices, health monitoring of aerospace structures, and implantable biomedical devices. The demonstrated applications also include harnessing tiny mechanical vibrations from a running automobile car engine to efficiently charging up energy storing capacitors and monitoring the engine states by the P-PNG, as well as harvesting energy from biomechanical energy sources (e.g., human hand-tapping) to directly drive light-emitting diodes (LEDs).

3.2 Experiment

3.2.1 Synthesis of the pure PVDF films

To prepare the PVDF solution, PVDF was purchased as a powder form (Sigma Aldrich) and was dissolved in N, N-DMF (N, N-dimethylformamide $\geq 99\%$, Sigma Aldrich) solvent (10 wt. %) by stirring for 12 hours at 40°C. The temperature was maintained at 40°C and was used to prevent agglomeration and achieve better dissolution. To prepare the PVDF film, the solution was drop cast on a standard glass wafer that was placed on a very flat hotplate. The sides of the glass substrates were covered with polyamide tape, to prevent the solution from flowing outwards. Before starting the annealing process, the solution was kept under ambient conditions for 30 minutes for degassing. To form the spontaneous electroactive β - phase in the PVDF, the curing temperature was adjusted carefully and kept at 80°C for 1 hour. Then as grown thin film ($\approx 40\text{-}50\ \mu\text{m}$) was peeled off from the glass substrate. The formation of the β -phase in the PVDF was confirmed by FTIR spectrum analysis (**Figure A3.1c, Appendix**) and the surface morphology was investigated by using a scanning electron microscope (SEM) (**Figure A3.1a-b**). Finally, a high voltage electrical poling (50-120 V/ μm) was performed for 2-4 hours to align the electric dipoles. For the high-voltage poling purpose- two gold coated copper electrodes were prepared via the electroplating method. To minimize the negative influence of the ambient moistures or the dust particles, the electrical poling was performed in a vacuum box. After that, to make the PNG, the films were placed between two copper tapes, and thermally laminated between two polyester substrates.

3.2.2 Synthesis of the porous PVDF films

PVDF powder was dissolved in N, N-dimethylformamide (DMF) by stirring the solution for 12 hours at 40 °C. To create different porosities, zinc oxide (ZnO) nanoparticles (NPs) (35–45 nm, US Research Nanomaterials, Inc.) were dispersed into the PVDF solution and again stirred at 40 °C for 24 hours. The

mass ratios between the PVDF and ZnO NPs (20 wt. % for this experiment) were adjusted to create different pores inside the PVDF. To achieve a uniformly mixed PVDF-ZnO composite solution, it was further treated in an ultrasonic bath for 1 hour. Then the uniform solution was drop casted onto a glass substrate and degassed for 30 minutes. The solution was cured at 75 °C inside a vacuum oven for 30 minutes. Afterward, the PVDF-ZnO composite film was peeled off from the glass substrate (**Figure A3.2 a-b** for the surface and cross-sectional morphology). To obtain the porosity inside the PVDF, one-step etching of the ZnO NPs was performed in an ultrasonic bath by immersing the PVDF-ZnO composite film in a 37 wt. % HCl solution for 4 hours. Then the porous film was cleaned with DI water, and dried in a nitrogen filled oven at 60 °C for 3 hours (**Figure A3.2 c-e** for the surface morphology). Finally, high-voltage electrical poling (50-120 V/ μm) was performed for 2-4 hours to align the dipole. Then the films were placed between two copper tapes and thermally laminated to encapsulate them between the polyester substrates.

3.2.3 Synthesis of the FAPbBr₂I@PVDF composite films

The FAPbBr₂I precursor solution was prepared by dissolving FAI (Formamidinium iodide $\geq 99\%$, Sigma-Aldrich) and PbBr₂ (lead (II) bromide $\geq 98\%$, Sigma-Aldrich) at an equal molar ratio (0.5:0.5) in an N, N- DMF (N, N-dimethylformamide $\geq 99\%$, Sigma-Aldrich) solvent, followed by stirring at 60 °C for 12 hours. The PVDF solution was dissolved in N, N DMF with constant stirring at 50 °C for 24 hours. The final concentrations of FAPbBr₂I and PVDF in DMF were kept at 20 wt. % and 10 wt. %, respectively. Then, the FAPbBr₂I@PVDF composite precursor solutions were prepared by homogeneously mixing 20 wt. % FAPbBr₂I and 10 wt. % PVDF. To optimize the concentration, the 10 wt. %, 20 wt. %, and 30 wt. % composite solutions were synthesized. Then the mixed solution was drop-casted onto a glass substrate and stored for approximately 1 hour for the degassing process. Immediately followed by annealing at 120 °C, the highly crystalline composite films were obtained after 2-3 hours.

To align the dipoles in the FAPbBr₂I@PVDF film, high-voltage electrical poling was completed with an electric field of 50-120 V/ μm for 2-3 hours. After the poling, the films were sandwiched between two copper electrodes. Finally, the sandwiched structure of the polyester/copper/FAPbBr₂I-PVDF/copper/polyester film was pressed through thermal lamination, which eliminates air gaps and provides uniform adhesion between the copper electrodes and the piezoelectric film.

3.2.4 Characterization and measurements

To investigate the crystallinity of the hybrid halide into the ferroelectric PVDF scaffold an X-ray diffraction (XRD) analysis was performed. A Bruker D8 DISCOVER was used with a Cu K α radiation source ($\lambda = 1.54 \text{ \AA}$) to scan the optimized thin film samples (25 wt. % FAPbBr₂I-PVDF) from an angular range of zero to seventy degrees. Fourier transform infrared spectroscopy (Nicolet iS50) was employed to confirm the ferroelectric β -phase formation inside the porous PVDF and hybrid halide-embedded PVDF film by measuring the characteristic absorbance peak in a wavenumber range from 400 to 1000 cm^{-1} . The dielectric properties of the samples (C-V characteristics) were measured using a Keithley-4200 semiconductor parameter analyzer. JSM-7200F field-emission scanning electron microscopy tools were used to obtain surface morphologies and nanoparticles distributions inside PVDF were mapped by analyzing energy dispersive X-rays in a cleanroom environment (Class-100). The AFM and KPFM images were captured using a JPK Nanowizard II, configured in intermittent-contact mode (a scan rate of 0.3 Hz). For the KPFM imaging, a cantilever probe (spring constant 42 N/m) with a platinum-coated tip (radius < 20 nm) was used to probe a grounded sample. A constant tip-sample interaction with a phase-locked loop and the internal reference of the lock-in amplifier was an applied AC voltage (3 kHz) to the sample surface is maintained. To study the electrical output performance of the P-PNGs an electrodynamic shaker (Lab Works Inc.) was used, controlled by a power amplifier and a controller. A digital oscilloscope (Tektronix 2004 C) and a low-noise current preamplifier (SR 570, Stanford Research Systems Inc.) were used to measure the electrical signal output from the nanogenerators.

3.3 Results and discussions

3.3.1 Device structure and working mechanism of P-PNGs

The piezoelectric potential is critically affected by the internal pores, as they can redistribute the mechanical strain profile inside the film. By mixing FAPbBr₂I perovskite with PVDF, a new class of piezoelectric films are developed, which takes advantage of the enhanced strain from the internal pore microstructures and the beneficial properties of the novel hybrid lead halide perovskite. A FAPbBr₂I perovskite precursor solution (20 wt. %) was synthesized at 60 °C from a homogeneous mixture of Formamidinium iodide (FAI) and lead (II) bromide (PbBr₂) powder in N, N-dimethylformamide (N, N-DMF). The FAPbBr₂I precursor solution was diluted in 10 wt. % PVDF, and drop casted on a glass substrate followed by a one-step annealing at 120 °C. Moreover, to align the dipoles a high voltage

electrical poling was performed for 2-3 hours with an electric field of 50-120 V/ μm by sandwiching the film between two gold electrodes placed inside a vacuum box. **Figure 3.1a** depicts a schematic illustration of the final device fabrication step, where the composite film is sandwiched between two copper electrodes and is encapsulated between polyester substrates, through a thermal lamination process. To elucidate the perovskite crystal formation inside PVDF, XRD scans over a wide range (diffraction angle 2θ ranging from 10 to 50 degrees) were conducted. The major diffraction peaks appear in **Figure 3.1b** at diffraction angles (2θ) of 14.64, 29.43, 33, 42.12 and 44.39 can be assigned to the (100), (220), (222), (224) and (300) crystal planes of a cubic perovskite structure, respectively. It is noteworthy to mention that replacement of MA with FA cation in the FAPbBr₂I crystal, greatly enhance the structural stability, which is more suitable for the PNG device fabrication. Since it is well known that semi-crystalline PVDF polymer has four distinct phases (α , β , γ , and δ) where β -phase is the only one that possess the highest spontaneous polarization, the existence of β -phase can be confirmed by the Fourier Transform Infrared (FTIR) spectrum. The FTIR spectrum in **Figure 3.1c** demonstrates that, compared with the conventional pure porous PVDF, [268-269] the coherently grown films of FAPbBr₂I crystals with polymer PVDF, have a higher intensity at a wavenumber of $\approx 475 \text{ cm}^{-1}$, and a similar intensity at 840 cm^{-1} . This result is attributed to the improved β -phase crystallinity of the PVDF, due to the existence of dipolar interactions between the FA⁺ cations of FAPbBr₂I and the anionic fluorine (-CF₂-) groups of the PVDF [270-271]. The piezoelectric coefficient (D_3) of the composite films can be written as

$$D_3 = \alpha_1 L_E \phi d_1 + \alpha_2 (1 - \phi) d_2 \quad (3.1)$$

where α_1 and α_2 are the poling rate, d_1 , and d_2 are the piezoelectric coefficients of different materials in the composite film, respectively, L_E is the local field coefficient and ϕ is the mass fraction. Assuming organic and inorganic phases are fully poled, i.e., $\alpha_1 = \alpha_2 = 1$, and $\phi = 0.2$, the piezoelectric coefficient D_3 can be estimated. The local electric field ($L_E = 3\epsilon / (2\epsilon + \epsilon_c)$) is related to the relative permittivity of the FAPbBr₂I nanoparticles (ϵ_c) as well as the composite film (ϵ). A previous report suggested that the ϵ_c can reach to 1000, which is much larger than ϵ . Therefore, L_E is estimated to be approximately 0.1-0.3 [272]. It has been identified that the piezoelectric coefficients of the PVDF and FAPbBr₂I phases are opposite. The approximated D_3 is calculated to be -23 pm/V when taking $d_1 \approx 25 \text{ pm/V}$ and $d_2 \approx -29 \text{ pm/V}$ [265].

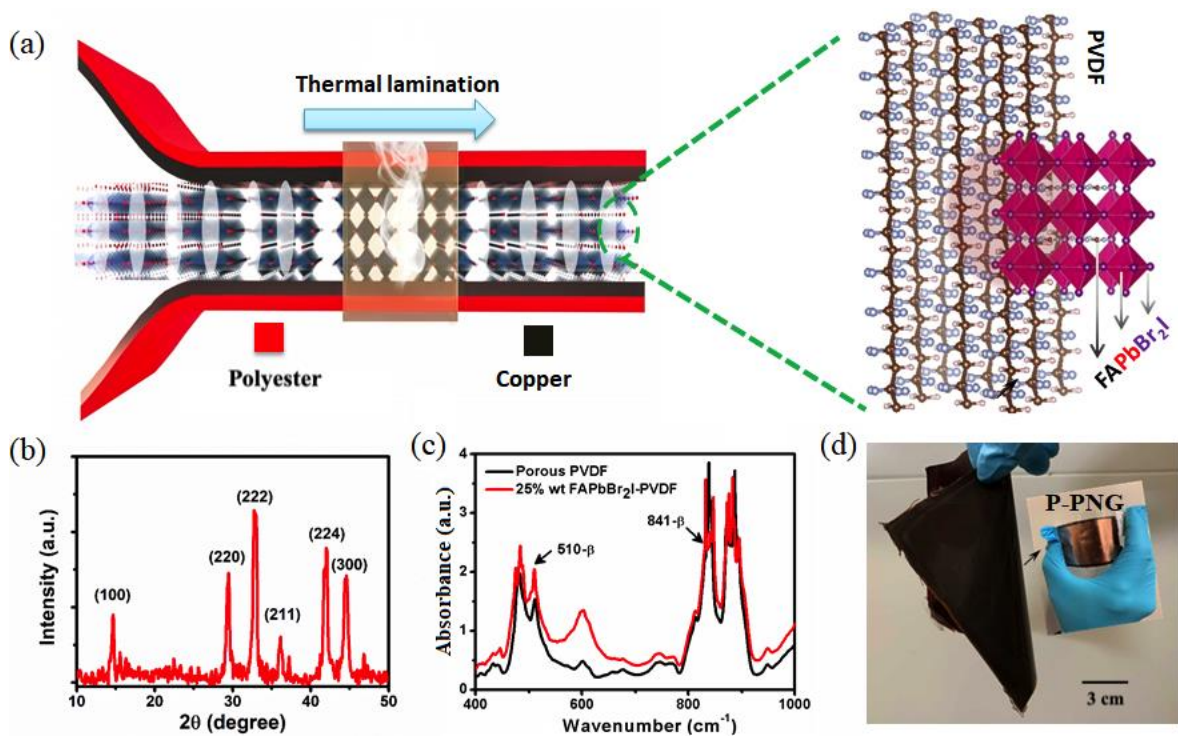


Figure 3.1. Device structure of P-PNGs (a) fabrication process of P-PNGs; (b) XRD patterns of 20 wt. % FAPbBr₂I@PVDF composite film; (c) FTIR results of porous PVDF and FAPbBr₂I@PVDF composite films (25 wt. %); (d) digital photos of the large area composite film (15 cm × 15 cm) and the fabricated P-PNGs.

Moreover, other predominant factors such as the nanoparticles distribution and film geometry also significantly influence the piezoelectricity of this complex hybrid composite material system. The scalable FAPbBr₂I@PVDF composite film (15 cm × 15 cm) and a fabricated flexible P-PNG device are shown in **Figure 3.1d**. During the crystallization process, phase separation usually plays an important role in the formation of the porous structures in the composite film. As a result, the crystallization process of PVDF@FAPbBr₂I can be divided into the following two stages [273]. During the first stage (schematic illustration in **Figure 3.2a**) (i) while heating up the solution at 60 °C, the N, N-DMF solvent starts to evaporate and the PVDF crystallizes due to its relatively lower solubility. Then it transforms into a colorless film and remains in an intermediate state. (ii) After that, the FAPbBr₂I solution begins to approach its supersaturated concentration (C_0) and then forms into nanoparticles, which is indicated by the change in color from colorless to red. The keys to the self-assembly process

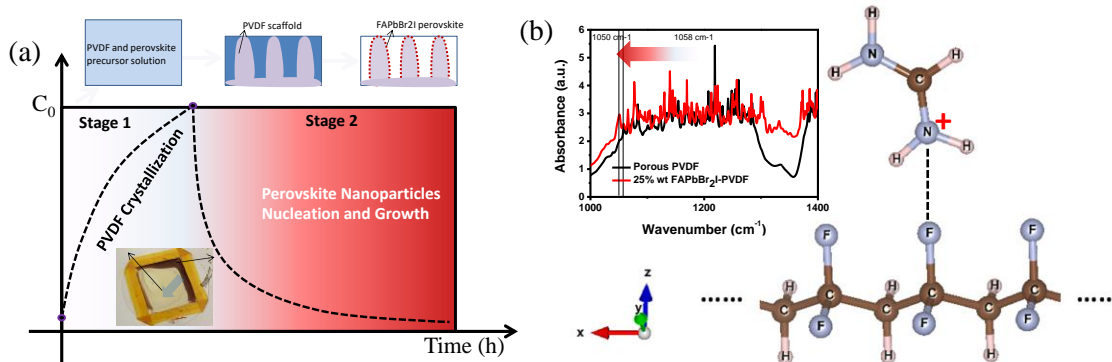


Figure 3.2. (a) Schematic illustration of crystallization process of the PVDF and the FAPbBr₂I nanoparticles. The y axis represents the total concentration of PVDF and FAPbBr₂I in the solution (b) schematic demonstration shows the interactions between FA⁺ cations and -CF₂- groups. From the FTIR spectrum, this interaction is confirmed by the blue-shift of the infra-red absorption peaks of C-F bond in the wave number range of 1350-1100 cm⁻¹.

of FAPbBr₂I nanoparticles embedded into the PVDF scaffold are two different crystallization processes of the PVDF and the FAPbBr₂I. During the second stage, the strong interactions between NH₃⁺ in the Formamidinium (FA) cations of the FAPbBr₂I and -CF₂- groups of the PVDF, the perovskites nanoparticles tend to anchor on the PVDF scaffold. This interaction is reflected by the blue-shift of the infrared absorption peaks of the C-F bond in the wave number range of 1350-1100 cm⁻¹ (FTIR spectrum in **Figure 3.2b**) due to the decreased force constant according to the expression of $(\nu=1304\sqrt{(k/u)} \text{ (cm}^{-1}\text{)})$, where ν is the frequency, k the force constant (N/m) and u the effective mass. From the cross-section of the film, demonstrated by the scanning electron microscopy (SEM) image in **Figure 3.3a**, an array of almost periodic vertical pores was observed. In contrast to a solid and conventional porous PVDF film (**Figure A3.1 & Figure A3.2**), uniquely self-assembled and highly porous structures were found in the FAPbBr₂I@PVDF composite film (material synthesis are described in the experimental sections **3.2.1, 3.2.2 & 3.2.3**). The pores are $\approx 20\text{-}25 \mu\text{m}$ in length (SEM image in **Figure A3.3a**) and approximately $\approx 3\text{-}5 \mu\text{m}$ in diameter (atomic force microscopy (AFM) image in **Figure A3.3b**). In addition, this interaction can also be observed from the mapping of the fluorine (F) atoms and lead (Pb) atoms which correspond to the PVDF polymer chain (**Figure 3.3b**) and the FAPbBr₂I crystal (**Figure 3.3c**). The perovskite clusters (in **Figure 3.3c**) are attached to the PVDF polymer because of their

common solubility in the DMF solvent (two materials can grow in one step) and the dipolar interactions between NH_3^+ in FA (perovskite) and $-\text{CF}_2-$ groups of the PVDF. The porosity and size of the pores can be well controlled via tuning the mass ratios (wt. %) of the hybrid halide perovskites with the polymer. The corresponding surface morphologies revealed in the AFM images (**Figure A3.4f**) show that the pore diameter gradually increases to approximately $\approx 7 \mu\text{m}$ at 30 wt. % of FAPbBr_2I . During the crystallization process, the increase in mass ratios should be led to the agglomeration of FAPbBr_2I NPs. The reason should be the aforementioned strong dipolar interactions between the FA^+ cations and the anionic fluorine ($-\text{CF}_2-$) groups of the PVDF [270-271].

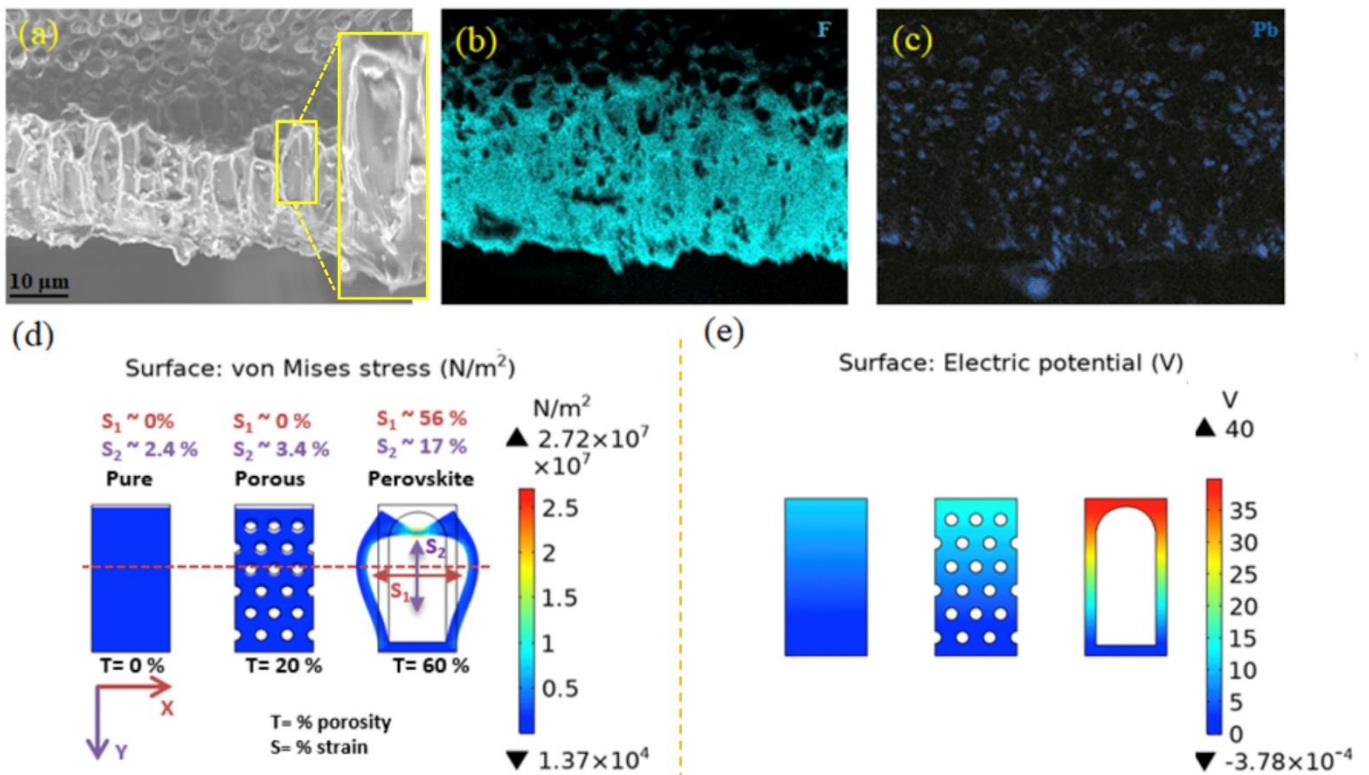


Figure 3.3. Working mechanism of P-PNGs (a) cross-sectional SEM image of the self-assembled highly porous PVDF@FAPbBr₂I (20 wt.%) composite films (inset shows the close view of a pore); the corresponding element mapping of (b) fluorine (F) in PVDF and (c) lead (Pb) in FAPbBr₂I; (d) calculated stress and (e) piezo potential distribution for a similar area of the pure PVDF, 20% circular porous PVDF and 60% porous FAPbBr₂I@PVDF film (porosity induced by 20 wt. % of FAPbBr₂I).

It has been investigated that the porosity in ferroelectric polymers will remarkably boost the piezoelectric potential by forming stress concentration centers around each pore. A PNG model for the perovskite/polymer composite was constructed to reveal the effects of self-assembled highly-porous characteristics on the output piezo- potential, and simulated using COMSOL Multiphysics 5.3. The simulation results were compared with those of pure (solid without pores) PVDF films and 20% circular-shaped porous PVDF films (circular shapes were adopted from the ZnO NPs. **Figure 3.3d** clearly shows that, under uniaxial compressive stress of 800 kPa, the induced displacement of the three different PNG models (the same film thickness of 30 μm) is drastically different. The pure PVDF film is the least deformed, whereas the hybrid halide-induced porous PVDF is the most deformed. It is evident that the pore position and size, influence the mechanical stress distribution, which is attributed to the increase in the average stress distribution profiles inside the films. From the finite element calculation (along the cut lines in **Figure A3.5b-c**), the stress inside the pure PVDF film is quite uniform under uniaxial vertical stress. In contrast, in the circular porous PVDF structure, the stress distribution is asymmetric in nature. Compared to the pure PVDF the stress distribution in the circular porous PVDF model is extremely disrupted by the presence of pores. In such circular porous structures (the middle model of **Figure 3.3d**), the stress is mainly confined around each pore but is particularly higher along the direction of the applied force, namely, at the top and bottom pore sides. Therefore, the localized compressive strain of each pores results in a bulk film strain mainly in the vertical direction (x-direction strain $S_1 \approx 0\%$, y-direction strain $S_2 \approx 3.4\%$) and modifies the internal coupling. Excitingly, unlike the uniform and circular porous PVDF (the deformation mainly occurred in the vertical direction), the highly ordered porous structure (the right-most model of **Figure 3.3d**) of the $\text{FAPbBr}_2\text{I@PVDF}$ film is not only deformed along the vertical direction ($S_2 \approx 17\%$) but also significantly elongated along the horizontal direction ($S_1 \approx 57\%$). The stress concentration spots at the top exert a pushing force on the pores of the perovskite/polymer composite, inducing a relaxing strain on the two sides. **Figure A3.5b** (the right most model) shows the linear stress-enhancing characteristics of this larger pore to the sidewall of the structure. This phenomenon is similar to the flex-tensional mechanism, [274-275] which underlines the structural modification of the mechanical body that could further amplify the applied vertical stress into the horizontal direction. Since the strain-induced piezo potential is a collective outcome from the strains around each of the pores, the piezoelectric potential in the circular porous PVDF structure is therefore higher (**Figure 3.3e**) than that in the non-porous PVDF piezoelectric films. The vibration-induced electric displacement D_3 (charge per unit area) is calculated by

$$D_3 = e_{333}S_{33} + |e_{331}|S_{31} \quad (3.2)$$

where e_{331} and e_{333} are the piezoelectric constants [276] and S_{31} and S_{33} are induced strains along the horizontal and vertical directions, respectively (**Supporting note A3.1**). It is clear that the D_3 of the FAPbBr₂I@PVDF composite film is synergistically influenced by the bidirectional (horizontal and vertical) strains S_1 ($\approx 57\%$) and S_2 ($\approx 17\%$). Therefore, the proposed novel P-PNG structure greatly increases the strain-induced piezo-potential or voltage output (according to the parallel plate capacitor model, $V = Q/C$, where Q is the total induced charge and C is the device capacitance), which was confirmed by the finite element simulation in **Figure 3.3e**. It demonstrates the maximum piezoelectric potential of ≈ 40 V for FAPbBr₂I@PVDF composite films, which is ≈ 11 V and ≈ 15 V for pure and 20% porous PVDF films, respectively (with the same applied stress of 800 kPa). It should be noted that an array of such a highly ordered pores (**Figure A3.6a**) in the P-PNG, would generate even higher potential than a structure having a single of such pores (the right most model in **Figure A3.6b**). In the array with such a larger pore, the wall of the inner pore structures is highly compressed due to the bidirectional stress (indicated by the arrows in **Figure A3.6a**). Between the interpore distance, the boosted stress is further improving the piezoelectric potential of the film. Yuan *et al.* also enhanced the total piezo potential of a 6-layer PVDF-TrFE (trifluoro ethylene) based PNGs by 2.2 times, by making a rugby-ball-shaped PNG structure to utilize this flex-tensional strain effect [241]. This approach is another promising way to develop new PNGs based on the amplified mechanical strain of a particular composite piezoelectric film and to realize a compact and flexible power source for next-generation micro/nanodevices.

3.3.2 Energy harvesting performance of the P-PNGs

The highly porous FAPbBr₂I@PVDF film provides an excellent platform for developing scalable PNGs, which only need two thin metal electrodes (copper) on both sides. Exploiting the unique microstructure features along with the formation of beneficial FAPbBr₂I nanocrystals, I investigated the effect on practical PNG performance. The device was placed on a hammer of an electrodynamic shaker and sandwiched by a 138 g metal block (stainless steel) on top (schematic illustration of testing set-up in **Figure A3.7**). The generated output voltage and current were measured from the periodic mechanical vibration produced by the electrodynamic shaker at various frequencies (10-50 Hz) and accelerations (1-2.5G). I found an output voltage of ≈ 85 V (peak to peak) and short-circuit current of

$\approx 30 \mu\text{A}$ (peak to peak), respectively, from an active device area of $3.8 \text{ cm} \times 3.8 \text{ cm}$ at 30 Hz and 2G (results are presented in **Figure A3.8a-b**). In **Figure A3.9a-e**, the electricity generation mechanisms of this P-PNG device are schematically illustrated from the stress mapping by employing finite element simulation (COMSOL Multiphysics 5.3). When there is no applied electric field, the net dipole moment inside the film is almost zero (**Figure A3.9a**). By applying a high electric field ($50\text{-}120 \text{ V}/\mu\text{m}$) for 2-3 hours, dipoles are aligned to the direction of the electric field (**Figure A3.9b**). Now, if a compressive force is applied to the device, the net polarization changes in the composite film due to the flex-tensional strain, thus producing piezoelectric potential (**Figure A3.9c**). It is predicted that due to rapid change in the net dipole moment by the flex-tensional mechanism will promote a polarization change in the poled P-PNG, yielding an even higher potential [277-278]. If the two electrodes are connected to each other, then an electric current will flow to balance this piezo potential. While releasing the force, the piezo potential returns to zero because of the diminished film strain, and then the accumulated electrons will flow back (**Figure A3.9d**).

Due to the formation of larger porous structures, the piezoelectric film could undergo an additional damping cycle, leading to the observation of a second output current pulse (**Figure A3.9e**). As discussed earlier that the pore size (and thus porosity) in the $\text{FAPbBr}_2\text{I@PVDF}$ composite film increases with the concentration of FAPbBr_2I precursors, which plays an important role in the PNG device performance. An interesting trend is found, that the output voltage and current increase with the composition of FAPbBr_2I (up to $\approx 85 \text{ V}$ and $\approx 30 \mu\text{A}$ at 20 wt. %) and decrease afterward (**Figure A3.10a-b**). The possible reasons are: Firstly, PVDF per unit volume is greatly reduced due to the very high porosity. Secondly, the film impedance is reduced by higher mass ratios ($> 20 \text{ wt. \%}$) of FAPbBr_2I , as a result, causing the earlier dielectric breakdown before maximum polarization charges are achieved by electrical poling. Thirdly, the defects generated by the agglomeration of FAPbBr_2I NPs. Therefore, the device with 20 wt. % of FAPbBr_2I demonstrated the highest output performance, and after a certain threshold margin, the device performance starts to degrade with further addition of excess FAPbBr_2I NPs. The highest measured output voltage and current of the P-PNG with 20 wt. % FAPbBr_2I was compared with the pure and 20% circular porous PVDF based PNG devices (**Figure 3.4a** and **Figure 3.4b**). Notably, the output voltage and current of the 20 wt. % P-PNGs are boosted by ≈ 5 times and ≈ 15 times, respectively, compared to those of the pure PVDF based PNG model ($\approx 17 \text{ V}$, and $\approx 2 \mu\text{A}$). They are also substantially higher than those of the 20 % circular porous PVDF PNG ($\approx 40 \text{ V}$, $\approx 6 \mu\text{A}$). The generated electricity of the P-PNG originated from the inherent piezoelectric polarization [279-

286] was verified from the output polarity switching (**Figure 3.4c**) clearly showing the expected output reversal. I sought further evidence by investigating the intrinsic material properties to explain the sharp enhancement in the output current of the P-PNG device. The relative permittivity of the porous PVDF and 20 wt. % FAPbBr₂I@PVDF films were measured in a frequency range of 1 kHz to 1 MHz (**Figure 3.4d**). For both of the films, at the lower frequency regime, permittivity is high at the beginning due to the interfacial polarization effect [287] between the nanoparticles and polymer interface, which arises from the free carriers in the polymer material. However, with an increase in the applied electric field frequency, the interfacial polarization cannot cope up with the frequency change, which results in the decreased permittivity. Lastly the increasing pattern of the relative permittivity could be correlated with the arising of a high frequency stray capacitance during the measurements.

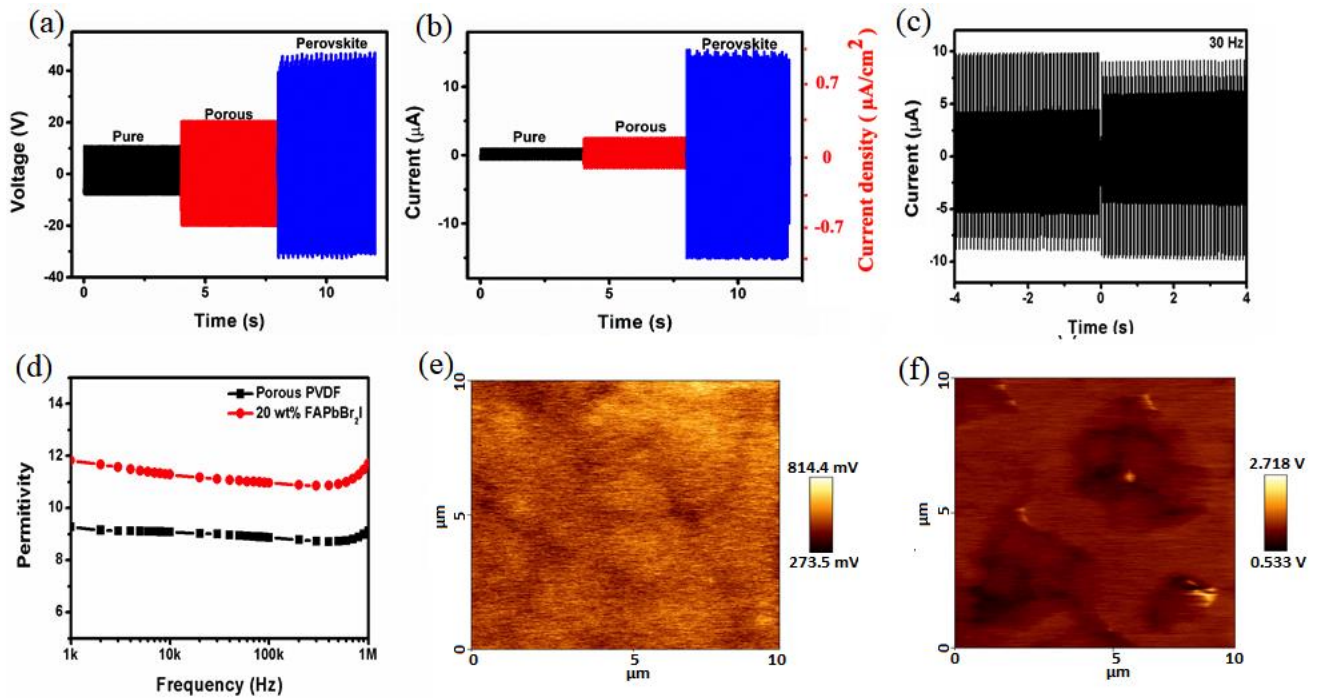


Figure 3.4. The output performance of P-PNGs (a) V_{oc} and (b) I_{sc} of PNGs made from pure PVDF, porous PVDF (with ZnO nanoparticles) and FAPbBr₂I@PVDF composite films. For the porous PVDF, and FAPbBr₂I@PVDF composite films, the original mass ratios of nanoparticles inside the final films are 20 wt. %. (c) Polarization verification of the P-PNGs by switching test; (d) relative permittivity of the porous and 20 wt. % FAPbBr₂I@PVDF composite films; KPFM images of the (e) porous and (f) 20 wt. % FAPbBr₂I@PVDF composite films.

The higher permittivity of the FAPbBr₂I@PVDF film (≈ 12 at 1 KHz) enhances the piezoelectric performance, as it increases the piezoelectric coefficient (D_3) [288-290]. In addition, the enhanced permittivity of FAPbBr₂I perovskites give rise to the output current by reducing the internal impedance (Z) of the film-

$$Z = R - j \frac{d}{2\pi A \epsilon_0 \epsilon_r} \quad (3.3)$$

where, R is the film resistance, d the thickness, A the area, ϵ_0 the vacuum permittivity and ϵ_r the relative permittivity. The charges due to the internal polarization are also affected by the relative permittivity of FAPbBr₂I. The surface potential of the FAPbBr₂I@PVDF film was measured by employing Kelvin probe force microscopy (KPFM). The relationship between the permittivity and polarization can be expressed as [291]

$$\vec{P} = \epsilon_0(\epsilon_r - 1)\vec{E} \quad (3.4)$$

where, \vec{P} is the electric polarization within the material, ϵ_0 the permittivity of free space ($8.854 \times 10^{-12} \text{ F m}^{-1}$), ϵ_r the relative permittivity and \vec{E} the electric-field. From equation (3.4), the higher permittivity of the composite film due to the presence of perovskite will certainly change the strain induced electric field inside the composite film, and as a result the magnitude of the surface potential will be different. In general, for perovskite PNGs, the surface potential is of particular interest because it affects band bending and carrier transport at the interfaces [292-296]. By measuring the contact potential difference using a platinum (Pt) KPFM tip (20 nm radius) in intermittent contact mode, the average surface potential of FAPbBr₂I@PVDF was found to be 1.1 V, which is more than twice that of porous PVDF (**Figure 3.4e & Figure 3.4f**). The observed variation in the average surface potential in FAPbBr₂I@PVDF film was very small (<100 mV), which eliminates possible surface contamination by the remnant precursors-formamidinium iodide (FAI), or lead bromide (PbBr₂).

The combination of high permittivity and the porosity mediated spongy type mechanical property made the FAPbBr₂I@PVDF thin film a promising candidate for harvesting mechanical energy from a wide range of environmental vibrations. The ambient vibration dependent output voltage and current of the P-PNGs (**Figure A3.11**) were measured. By keeping the force constant, the frequency of the electrodynamic shaker was varied from 10-50 Hz by a controller unit (Vibration Research's VR 9500 Revolution). Maximum output was obtained at 30 Hz, corresponding to the resonant condition in which

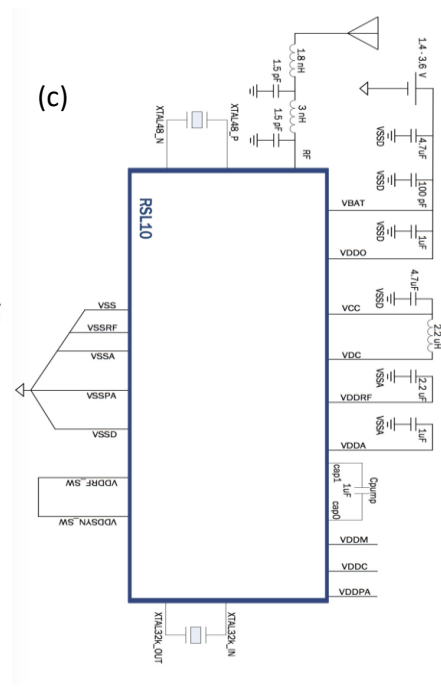
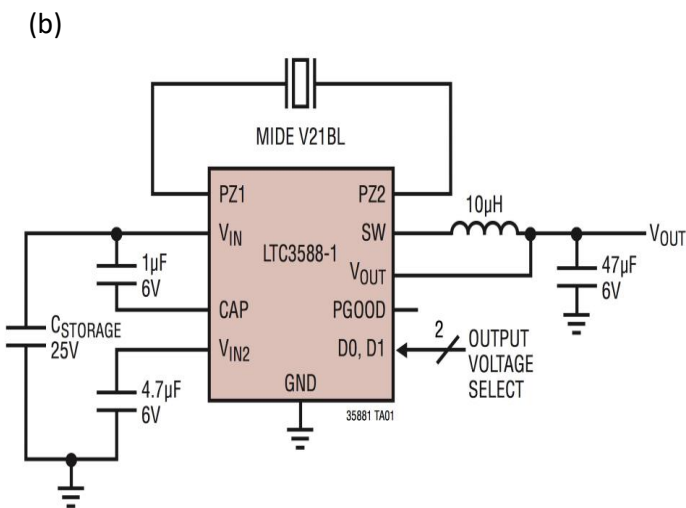
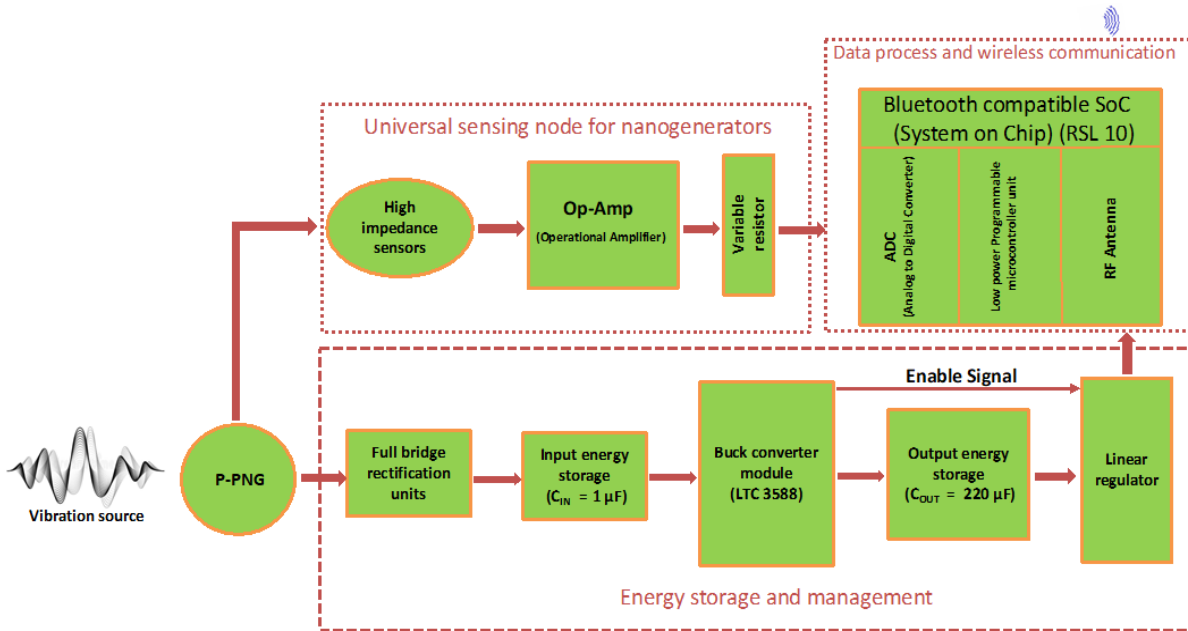


Figure 3.5. Self Powered integrated wireless electronics node (SIWEN) (a) functional block diagram of the SIWEN (b) internal circuit diagram of a LTC 3588-1 module (c) architecture of an RSL-10 system on chip (SoC).

the electromechanical coupling is the greatest. To evaluate the flexibility of the device, a periodic bending force was applied at a constant strain rate (15.5 cm/s) and measured the output voltage and current. The peak-to-peak output voltage was 14 V, and the current was 0.3 μA (**Figure A3.12a-b**), which can be enhanced further by increasing the bending radius [262].

3.3.3 Applications of P-PNGs as a sustainable power source in the IoT

Despite vast efforts in the past decade, the implementation of composite PNGs, especially in real-time applications, is still limited. To address these limitations, this work employed a novel flexible P-PNGs as a power source to implement a true SIWEN for the distributed IoT network. This SIWEN can remotely communicate with any Bluetooth-compatible personal electronics to transfer data from many distributed sensors. The functional block diagram of the SIWEN is shown in **Figure 3.5**. The SIWEN incorporates a rectification unit, two-stage energy transfer system, regulated switches, and a low-power system on chip (SoC) for conditioning the sensor signal and transmitting it to a remote end receiver. To store and manage the energy harnessed by the P-PNGs, two-stage energy transfer mechanism was adopted. Following the rectification of the P-PNG output by using a Schottky diode based full-bridge rectifier unit (**Figure 3.5a**), rectified output was stored in an input capacitor of 1 μF . The output level of the input capacitor was regulated to $\approx 5\text{ V}$. After the voltage level of the input capacitor reaches to 5 V, the stored electrical energy was transferred to the output capacitor of 220 μF (permanent storage) through a buck converter module (LTC 3588-1). The buck converter module operates at undervoltage-lockout mode (UVLO), which allows a certain portion of energy from the input storage to be transferred to the permanent storage. While transferring the energy through an inductor (10 μH) (**Figure 3.5b**) to the output capacitor, a PMOS switch (p-type metal-oxide-semiconductor) inside the LTC-3588-1 module is used to ramping up the output current and a NMOS switch (n-type metal-oxide-semiconductor) is used to bring it down. This switching strategy provides a high output current to store electrical charges to the output capacitor. When the input capacitor's voltage falls below the UVLO threshold, the buck converter is turned off and input capacitor starts to store the charges again. The output voltage of the permanent storage capacitor is monitored by a V_{OUT} pin (circuit diagram in **Figure 3.5b**) and compared with a pre-set regulation point ($\approx 3\text{ V}$) of a comparator (PGOOD). After reaching the output voltage level of the permanent storage to the set point, the buck converter generates a control signal (enable) through the PGOOD pin in **Figure 3.5b** while entering into a sleep mode ($\approx 100\text{ nA}$ of load current).

The enable signal in **Figure 3.5a** switches a linear regulator (a digital switch), and energy from the output capacitor is transferred to an RSL-10 (architecture in **Figure 3.5c**) system on chip (SoC). In the RSL-10, sensor's output signal is continuously sampled by an ADC (analog to digital converter), and the signal is processed to capture the peak value of the output and to transmit it to the remote receiver through a radio frequency link. As the nanogenerator based sensors (e.g., the P-PNG) possesses a high internal impedance (of megaohm range), it is challenging to integrate them with an existing commercial electronics node (e.g., RSL-10). Nevertheless, an Op-Amp (operational-amplifier) which operates at unity gain was designed as an interfacing unit between the sensor and RSL-10. When the magnitude of the enable signal reaches $\approx 92\%$ of its peak value, linear regulator turns off, and buck- converter is disconnected from the output energy storage and input energy storage unit start to charge again by the P-PNG. In **Figure 3.6** a P-PNG is exemplified both as an electrical power source and sensor, which is capable of harnessing mechanical energy from wide range of vibration sources (e.g., human motion, vibration of aircrafts and automobiles). However, during the experiment, an electrodynamic shaker was used to generate mimic vibrations at 30 Hz and 2G. Before integrating the P-PNG with SIWEN, a practical load-driving capability was confirmed.

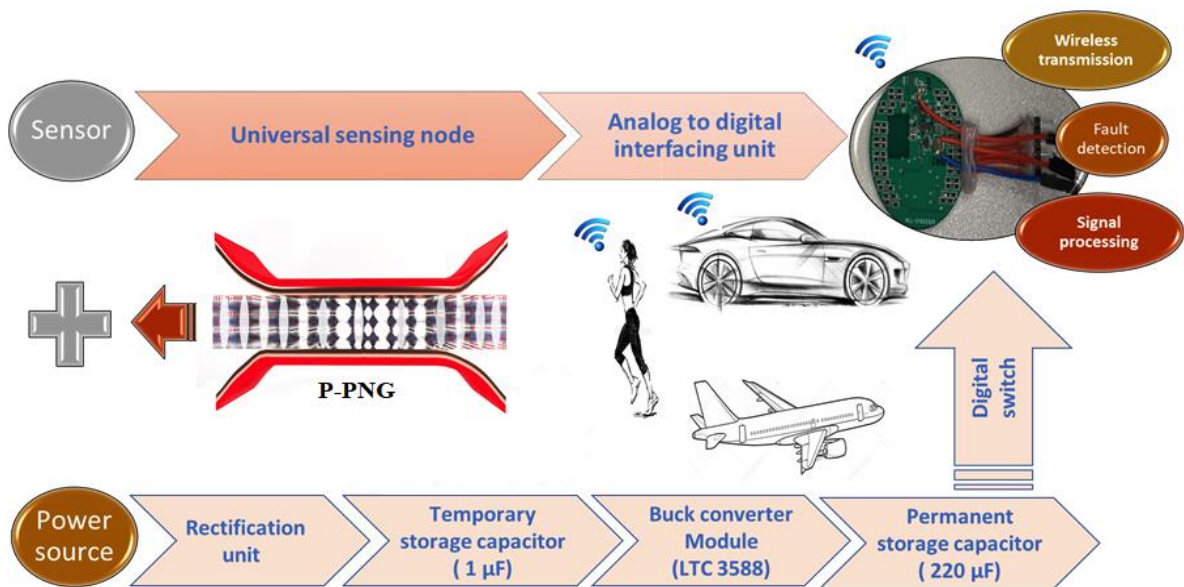


Figure 3.6. Framework of the self-powered integrated wireless electronics node (SIWEN) by simultaneously using the P-PNGs as a power -source and a sensor.

The maximum instantaneous power delivered to the load was measured from the output currents of the P-PNG with a wide range of external load resistances (100 K Ω to 80 M Ω). A peak output power of $\approx 105 \mu\text{W}$ and a power density of $10 \mu\text{W}/\text{cm}^2$ were obtained at a load resistance of 7 M Ω (**Figure 3.7a**). The energy harnessed by the P-PNG is being stored to powering up the SIWEN to initiate data transfer. The measured charging characteristics of the two-stage energy transfer system enabled by two capacitors (C_p) are shown in **Figure 3.7b**. When the voltage of an input capacitor (1 μF) reaches $\approx 5\text{V}$, which is regulated by a Zener diode, it discharges energy through a buck converter module to an output capacitor (220 μF).

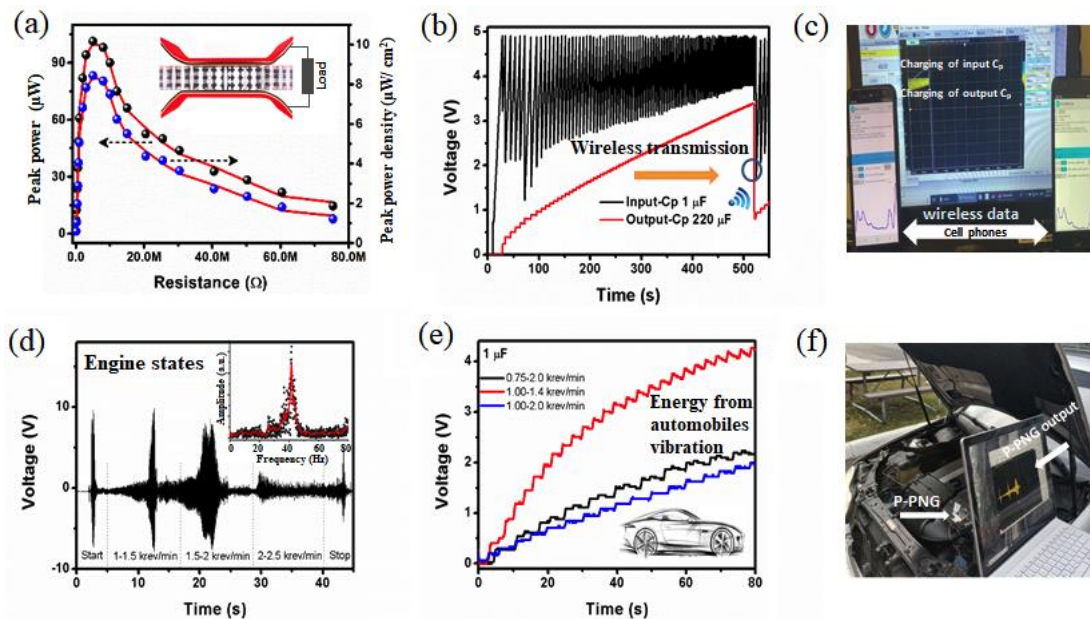


Figure 3.7. Application of the P-PNGs for IoT (a) the measured output power of the P-PNG with an applied acceleration of 2 G (30 Hz). The used load was a metal block of 138 g; (b) charging characteristics of the input (1 μF) and output capacitor (220 μF) of the SIWEN; (c) the digital photo shows the sensor signal received by the cell phone; (d) SIWEN used for car engine states detection at a parking condition (inset shows the corresponding frequency domain distribution via Fast Fourier Transform); (e) charging of a commercial capacitor (1 μF) by a single P-PNG while exciting by an automobile engine (Mercedes-Benz car); (f) the corresponding digital photo of engine vibration detection

The buck converter module consists of two metal oxide semiconductor field-effect transistor (MOSFET) switches. After the output voltage of the 1 μF input capacitor dropped down to a regulated voltage of $\approx 2\text{-}3\text{V}$, the 220 μF output capacitor is disconnected from it by the MOSFET switches and the input capacitor stops discharging and starts to be charged. In this manner, the output capacitor is charged until $\approx 3.1\text{ V}$ with high energy transfer efficiency, and can power up any electronics node. Another P-PNG (P-PNG sensor) incorporated in the SIWEN as a sensing unit is connected with an analog-to-digital converter (ADC) of the SoC via an impedance-matching bridge. Immediately after reaching the output voltage of the 220 μF capacitor to 3.1 V, a trigger signal turns on a switch through which the output capacitor discharges energy to power-up the SoC and transmits the digital sensor data from the P-PNG sensor to a remote receiver. The full operation of energy harvesting, energy storing, data collecting and wireless transmitting were demonstrated and recorded. **Figure 3.7c** shows, two smartphones receiving the transmitted data from the SIWEN and decode the mimic sensor signals (obtained from the P-PNG sensor). To assess more versatile applicability, the P-PNGs were used in harnessing vibration from an automobile vehicle. **Figure 3.7d** depicts the measured output voltage from the P-PNG, mounted on the car (while the engine is running), where device output reflects the acceleration and rotational speed-dependent vibration pattern of the engine. After the engine is turned on, the rpm (revolutions per minute) was varied from a range of 1-1.5, 1.5-2, 2-2.5 kilo revolutions per minute (Krev/min) while maintaining a constant acceleration between each rpm regime. Initially, a peak-to-peak voltage of $\approx 13\text{ V}$ was measured, which is attributed to the abrupt engine vibration when getting started. Later, the P-PNG output dropped, due to a gradual decrease in the vibration magnitude in the higher rpm regimes. We also performed a fast Fourier transform (inset of **Figure 3.7d**) revealing the major contribution of the device output produced from the vibration components of approximately 40 Hz, which is close to the resonance frequency of the P-PNG. By harnessing energy from such minute engine vibrations, a commercial capacitor of 1 μF was charged up to 4 V in ≈ 1 minute (**Figure 3.7e**). The capacitor was continuously charged up by switching the car rpm back and forth between 1–1.4 krpm (red curve), 1–2 krpm (blue curve) and 0.75–2 krpm (black curve). The best charging performance at 1–1.4 krpm is attributed to the highest acceleration and more frequent excitation (due to lower rpm switching time) to the capacitor. For the other two wider rpm regimes, acceleration is lower and their longer rpm switching time allows the capacitor to further discharge its energy.

3.4 Conclusions

To summarize, a novel self-assembled highly porous phenomenon in a composite piezoelectric polymer film by employing new hybrid halide perovskites (FAPbBr₂I) precursors, is discovered. This chapter discussed a successful fabrication of an efficient, flexible and all-solution processed perovskite-piezoelectric nanogenerator (P-PNGs). Because of the enlarged film strain of the self-assembled highly ordered porous scaffold (PVDF) and the enhanced relative permittivity of the novel perovskite FAPbBr₂I, the composite material's piezoelectricity was dramatically boosted, yielding a strain-induced piezo potential of 85 V (\approx 5 times greater than PVDF PNGs) and a current of \approx 30 μ A (\approx 15 times more than PVDF PNGs), with an applied load of 138 g. A very high peak output power density of 10 μ W/cm² (across a resistance of 7 M Ω) was recorded to implement the novel P-PNGs in a broad range of practical applications. The experimental results were supported by the numerical simulation of three different PNG device models (pure PVDF, circular porous PVDF and the perovskite-polymer composite film). A self-powered universal wireless electronics node (SIWEN) capable of communicating remotely with personal electronics was demonstrated by using the P-PNG as an alternative means of a battery. The P-PNG could also generate electricity by harnessing energy from automobile vibrations and biomechanical motion which can be easily extended to many applications as well. This research reveals the underlying mechanisms for the performance enhancement observed in the P-PNGs based on the novel perovskite/polymer composite film. This in return shows that the results pave a way to achieve the practical implementation of self-powered technologies.

Chapter 4

Enhanced Piezoelectricity in Lead-free Halide Perovskite Nanocomposite for Self-Powered Wireless Electronics

4.1 Introduction

In the modern era of thriving inventions, energy sources play a vital role. Conventional fossil fuel-based energy sources are gradually being replaced by unconventional ones to address imminent challenges, such as inadequacy of resources, environmental pollution, and global warming [297-298]. Alongside large-scale conventional energy harnessing sources, many unconventional systems including solar [299], thermoelectric [300], triboelectric [301-302], electrostatic [303], piezoelectric [304], meta-triboelectric [305-306], electromagnetic [307] and hybrid nanogenerators by integrating different types of harvesters in a single unit [308-309] were developed to convert the energy available in the ambient environment into usable electrical energy for self-powered electronic applications. Since after the discovery in 2006, piezoelectric nanogenerators appeared/considered as a remarkable energy-harnessing technology to convert useful electrical energy from available mechanical energy, and were implemented in self-powered electronics [310-312]. Following the first reported development of PENGs based on zinc-oxide nanowires in 2006 [313], numerous piezoelectric nanostructures were utilized to construct nanogenerators, such as gallium-nitride nanorods [314], lead zirconate-lead titanate (PZT) nanofibers [315], porosity control PZT ceramic structure [316] polyvinylidene fluoride polymer (PVDF) nanofibers [317], and patterned ion-gel electrolyte on ZnO nanowire (NW) [318]. In piezoelectric materials, an induced electric dipole moment can be generated upon the application of vertical or parallel mechanical force. Due to the application of unidirectional stress, the dipole moment induced can be in-plane or out-of-plane to the applied stress, which is ascribed to the two most common piezoelectric phenomena, namely longitudinal and transverse respectively [319]. Piezoelectric materials can be deformed by introducing an external force along a parallel and/or perpendicular direction. This inverse piezoelectric effect is quantified by material piezoelectric coefficients (d_{33} and d_{31}) [319].

Owing to their high d_{33} value, inorganic perovskite piezoelectric crystals, such as $\text{Pb}(\text{Zr,Ti})\text{O}_3$ (PZT), BaTiO_3 (BTO), and PbTiO_3 (PT), were extensively investigated and explored for their energy-harvesting applications [320-323]. However, the inherently brittle and rigid nature, and requisite high temperature synthesis of these ceramic materials often limit their applications [324-327].

The OIHPs combine the advantages from both the organic molecular part and inorganic octahedron of the perovskite structure at a microscopic level, have been the focus of research for quite some time as a potential alternative to ceramics [319, 328]. Besides their distinct optoelectronic properties, OIHPs exhibit great advantages in terms of their compositional variability, structural flexibility, and room-temperature and solvent-based synthesis process [328-330]. These materials retain a general perovskite crystal structure with stoichiometry ABX_3 , in which A represent an organic cation such as CH_3NH_3^+ (MA) or $\text{CH}(\text{NH}_2)_2^+$ (FA), B represents a metal cation with a different oxidation number than A, such as Pb^{2+} or Sn^{2+} , and X is an anion such as Cl^- , Br^- , or I^- [327]. Although initial studies of OIHPs focused on photovoltaic applications, the applications of their piezoelectric phenomena continue to attract research interest [328-330, 332-333].

The ferroelectric polarization switching and piezophotonics properties of $\text{CH}_3\text{NH}_3\text{PbI}_3$ (MAPbI_3) perovskite were demonstrated by Coll et al. in 2015 [332]. The following year another study by Kim et al. showed that the PENGs fabricated with MAPbI_3 thin films give an output voltage of 2.7 V and a current of 140 nA/cm^2 [333]. Potential piezoelectric application of OIHPs became more feasible after the invention of piezoelectric composite films which exhibited superior flexibility and sustainability by introducing perovskite nanoparticles within different soft polymer materials. Perovskite NPs examined in the literature to date include FAPbBr_3 , Fe-doped MAPbI_3 , and FASnI_3 [319, 334-341]. However, a major concern and obstacle to commercialization related to traditional lead-based perovskite materials is the environmental toxicity of these materials. After exposure to water, the lead-based materials can easily form a solution containing the life-threatening lead, which may be released to the environment where it can accumulate in the food chain and impose deleterious impacts on ecosystems and human health [342].

In recent years, scientists are devoted to finding the solution to the stability and toxicity problem present in the lead-based system by replacing Pb^{2+} in perovskites [343] with other divalent cations, such as Sn^{2+} , Ge^{2+} , Mg^{2+} , Ca^{2+} , Sr^{2+} , or Ba^{2+} [316–319]. Due to the ion size effects and lone pairs of electrons, Sn^{2+} and Ge^{2+} are among the best candidates for the replacement of Pb^{2+} . Moreover, Sn-based OIHPs

exhibit robust photovoltaic performance because of their high electronic dimensions and unique electronic configuration [344]. However, Sn^{2+} in Sn-based OIHPs can easily be oxidized to Sn^{4+} . One solution to address this challenge would be to engineer the composite material structure to effectively prevent the migration of external oxygen and moisture through the material and to suppress internal ion diffusion inside the devices [343]. In this context, the PENG design strategy whereas the OIHPs scaffolded by an insulating polymer has drawn much attention for large-scale application [334].

This work discussed in this chapter, for the first time successfully demonstrated an efficient composite film-based NGs by using organic-inorganic Sn-halide perovskite, in which NPs of $\text{CH}(\text{NH}_2)_2\text{SnBr}_3$ (FASnBr_3) were incorporated in polydimethylsiloxane (PDMS) polymer matrix. Remarkably, these NPs were uniformly distributed inside the PDMS polymer to form high-quality composite piezoelectric films, which have high mechanical flexibility and can be bent upon externally applied mechanical stress. This high-performance, flexible composite film was used to demonstrate a PENG for self-powered wireless communication.

The room temperature synthesis of FASnBr_3 NPs were done by using a modified ligand-assisted reprecipitation (LARP) technique reported by Zhang et al. [319, 346-348]. The composition was prepared by adding the FASnBr_3 NPs into the PDMS matrix with mass ratio of 20wt%. Finally, a consistent and chemically stable piezoelectric composite film of $\text{FASnBr}_3@PDMS$ was fabricated successfully by the solution drop-casting method on a polyethylene terephthalate (PET) substrate coated with conductive Indium tin oxide (ITO). In this design, the ITO coated PET also serves as a flexible bottom electrode of the PENG. The fabricated PENGs produced peak to peak open circuit voltage (V_{oc}) of 94.5Vp-p, peak to peak short-circuit current (I_{sc}) of 19.1 μA p-p, and power density of 18.95 $\mu\text{W}/\text{cm}^2$, by applying a minute's force (4.2 N/4.66 kPa). This performance is substantially surpassing the reported PENGs of the similar type in terms of their output power density such as $\text{FAPbBr}_3@PDMS$ (12 $\mu\text{W}/\text{cm}^2$ at 0.5 MPa), Sm-PMN-PT@PDMS (11.5 $\mu\text{W}/\text{cm}^2$ at 0.35 MPa), and $\text{BaTiO}_3@PDMS$ (0.12 $\mu\text{W}/\text{cm}^2$ at 0.002 MPa) in **Table A4.1** [319]. The composite PENG device has excellent electromechanical energy conversion capability to run the SoC and successfully transfer data wirelessly to a Bluetooth compatible smart device every ~6 minutes. This study demonstrates the great potential of lead-free OIHPs materials in next-generation high-performance PENG applications.

4.2 Experiment

4.2.1 Materials

FABr (Formamidinium bromide, 98 %, Sigma-Aldrich), SnBr₂ (Tin (II) bromide, ≥98%, Sigma-Aldrich), Toluene (99.9%, Sigma-Aldrich), DMF (N, N-dimethylformamide, ≥99%, Sigma-Aldrich), PDMS (Sylgard 184, Dow Inc.), OTA (Octylamine, 99%, Sigma-Aldrich).

4.2.2 Synthesis of FASnBr₃ NPs

1 mmol FABr and 1 mmol SnBr₂ were dissolved in 10 mL of DMF to grow FASnBr₃:



Then 70 μL octylamine (OTA) was added into the solution followed by constant stirring at 60 °C for 60 minutes. The role of another additive octylamine (OTA) in the above reaction is to control the preferential growth of the perovskite nanostructures.¹ More specifically, controlling the amount of the OTA would favor the growth of different perovskite microstructures [224] whereas a lower concentration of OTA would partially cover the surface of the perovskite nuclei and would favor the growth of FASnBr₃ NPs type structure.

The as-prepared precursor solution was slowly dropped into 200 mL (20 times of the precursor solution) of toluene under vigorous stirring at room temperature (25 °C). Along with the mixing, the color of the solution turned from clear to slight white, indicating the formation of NPs. The NPs were purified via centrifuging at 6500 rpm for 2-3 minutes and then re-dissolved in 2 mL toluene for the composite film growth.

4.2.3 Growth of FASnBr₃@PDMS composite film

the piezoelectric composite film was prepared via dispersing the above FASnBr₃ NPs into the PDMS matrix with the mass ratios from 0 to 40 wt. %. After stirring 30 minutes, a curing agent was added into the mixture with a weight ratio of 1:10 with the PDMS matrix. Then the as-prepared solution was drop-casted onto PET/ITO substrate. Before curing the film at 150 °C for 2 hours, the degassing was needed inside a vacuum chamber for few hours to remove the residual bubbles.

4.2.4 Fabrication of piezoelectric nanogenerators

a copper (Cu) electrode was attached to the top surface of the FASnBr₃@PDMS film as the top electrode. Finally, the sandwiched structure of PET/ITO/FASnBr₃@PDMS/copper was put in a pouch bag and then pressed firmly by a commercial thermal laminator. In this process, a uniform adhesion was obtained between each layer of the PENGs. To improve the device performance, the dipoles need to be aligned at a high electrical poling voltage of 6.0 kV for 2-3 hours operated inside a vacuum chamber.

4.2.5 Characterization of the FASnBr₃@PDMS composite film

X-ray powder diffraction (XRD) investigations were carried out by using the Bruker D8-Discover diffractometer with Cu K_α radiation ($\lambda=1.5418 \text{ \AA}$). The scanning electron microscope (SEM) and element mapping test were performed by using JSM-7200F electron microscope. The attenuated total reflection Fourier-transform infrared spectroscopy (ATR-FTIR) was carried out by TENSOR 27, Bruker, USA.

The vertical and lateral piezoelectric force microscopy (PFM) was recorded via Bruker AFM (Dimension Icon). The probe used for the PFM is an n-doped (Antimony) silicon probe coated with reflective Pt/Ir on the back and a conductive tip coating, having a nominal stiffness of 3 N/m. The sample for the PFM was prepared by drop-casting the diluted NPs solution on the n-doped silicon wafer. The piezoelectric response curves were collected via applying a sequence of direct current (dc) voltages from -10 to 10 V with a superimposed alternating current (ac) voltage of 2 V to probe tip. To verify the accuracy of the PFM measurements, several control experiments were performed on a standard n-type silicon wafer using a similar approach as described above. The resonance frequency of the probe was around 305 kHz and the drive frequency were set at 304.45 +/- 0.03 kHz for all the images taken. The relative permittivity (ϵ_r) of the composite film, was also measured by using the Keithley 4200 semiconductor characterization system with the frequency from 1 kHz to 1 MHz. The efficient piezoelectric coefficient of the composite film was measured via the quasi-static method (Polyk d₃₃ meter).

4.2.6 Measurement of device output performance

To measure the electrical output from the PENGs, an electrodynamic shaker system (ET-140, Lab works Inc.) was used to create periodic mechanical excitation. The generated output voltage from the device was recorded by a digital oscilloscope (Tektronix 2004C) with a 100 M Ω probe, and the short-circuit current was measured by a low-noise current preamplifier (SR570, Stanford Research Systems, Inc.). Fixed resistances were used in a range from 100 K Ω to 75 M Ω to optimizing the output power density. To remove any external artifact signals, the measurement was performed on an electrically grounded platform and turning off nearby mechanical machinery in the laboratory.

4.3 Results and Discussions

The sequential steps from the synthesis of the FASnBr₃ NPs to the PENG device fabrication are illustrated in **Figure A4.1a, Appendix**: (i-v) FASnBr₃ NPs were synthesized using the LARP technique (see **details explanation in section 4.2**); (vi) the precursor for the composite film was prepared by mixing the FASnBr₃ NPs with PDMS matrix with certain wt. %; (vii) the composite film was fabricated by simply drop-casting the precursor prepared in step (vi) onto a conductive ITO-coated PET substrate, which was also used as the bottom electrode; and (viii) the solution was then cured at 130 °C for 2 hours. Thereafter, (ix) a conductive tape of copper (Cu) was added to the top of the film to serve as another electrode and subsequently, a dc voltage of 6.0 kV was used to do the poling for several hours to maximize the alignment of dipoles in the piezoelectric film (see details fabrication method in the supporting information). Finally, the device was encapsulated with a polyester package and thermally laminated to get better adhesion of the individual layers and minimize the contact-induced triboelectric charges (**Figure A4.1b**). A typical schematic representation of the final fabricated FASnBr₃@PDMS PENGs is illustrated in **Figure 4.1a** where the film was encapsulated between a Cu and PET/ITO electrode. **Figure 4.1b** illustrate the SEM (cross-section) image of the fabricated PENG. It is clearly visible from the SEM image that the composite film was prepared with a mass ratio of 20 wt. % FASnBr₃ NPs having a thickness of ~ 80 μ m and is encapsulated compactly between the electrodes. The SEM micrographs also demonstrate that there were no significant gaps between constituent layers, which alleviate unwanted triboelectric effects. The crystal structure of FASnBr₃ developed using 3D visualization for structural models (VESTA) is shown in **Figure 4.1c**. The detailed structural analysis was indexed with a cubic lattice (space group: Pm3m) mainly adopted at room temperature according to previous experiments [349].

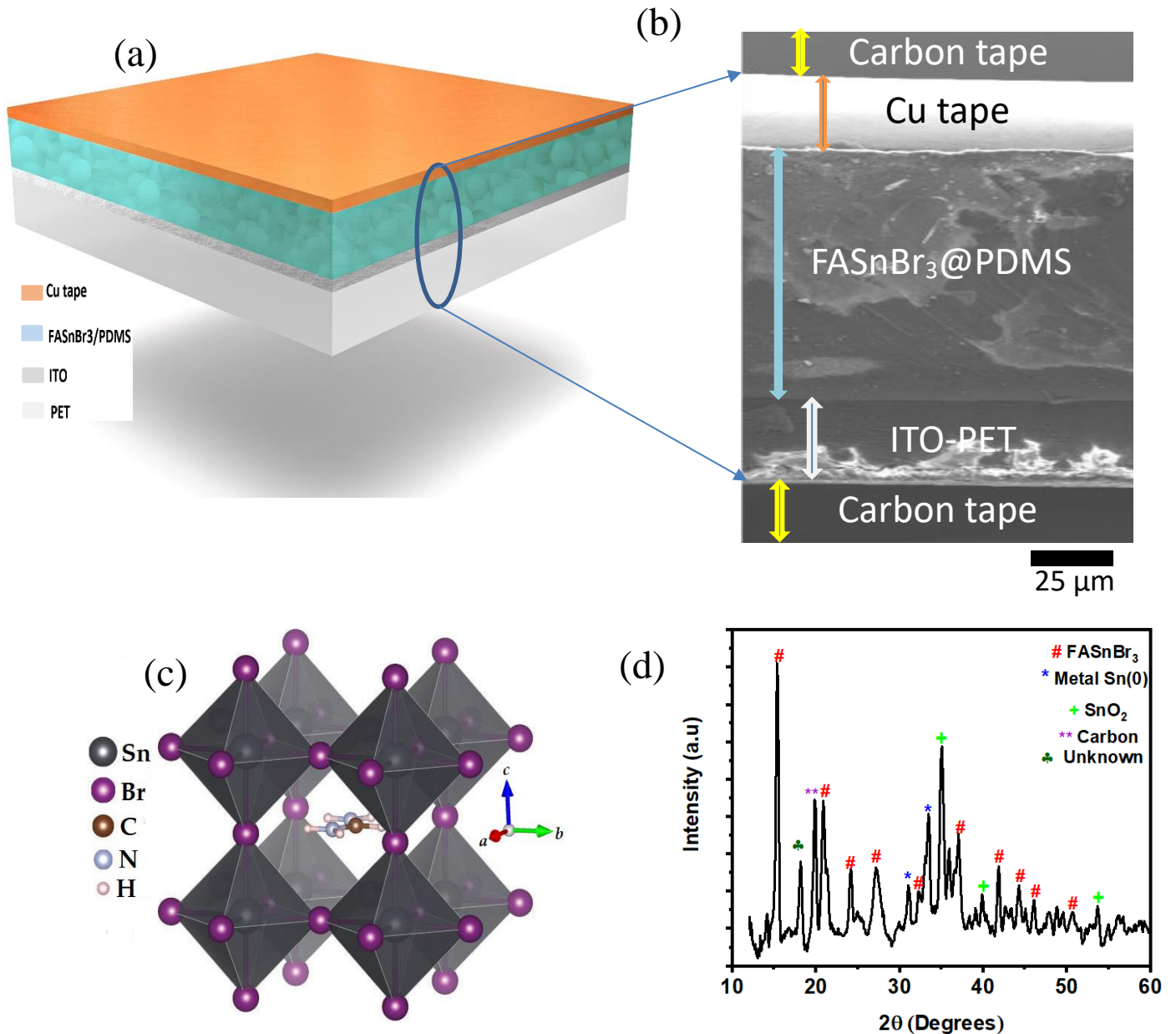


Figure 4.1. Schematic representation of the PENG device and material structure (a) A pictorial diagram illustrating the structure of FASnBr₃@PDMS composite-based flexible PENG. The FASnBr₃@PDMS based device is inserted between the Cu and ITO coated PET electrode, (b). The cross-sectional SEM image of PENG shows the thickness of the FASnBr₃@PDMS film is approximately 80 μm and shows the better adhesion between each layer. (c) The crystal lattice of the FASnBr₃ perovskite. (d) shows the XRD characteristics peaks of FASnBr₃ nanoparticles.

The morphology of the FASnBr₃ NPs was studied via X-ray diffraction pattern (XRD) (**Figure 4.1d**). The significant diffraction peak characteristic of the synthesized FASnBr₃ NPs at 2θ degree of 15.36°, 20.85°, 37.05°, 41.85°, and 44.25°. The distinct diffraction angles are the indication of the lattice planes of cubic perovskite crystal structures, with a space group of Pm3m, and is expected according to previous reports [350-353]. **Figure 4.2a** is the surface SEM image of pure PDMS film and the top right corner shows a zoomed-in SEM image, as expected, these images confirmed the absence of any particles prior to the addition of FASnBr₃ NPs. **Figure 4.2b** confirms the homogeneous distribution of FASnBr₃ NPs inside the PDMS. **Figure 4.2c** shows the SEM-EDS electronic image, from where it can estimate the approximate size of the NPs as 250-300 nm and demonstrates homogenous distribution inside the polymer matrix. The energy-dispersive X-ray spectroscopy (EDS) mapping over the surface of the fabricated PENG device (i.e., elemental mappings of Sn, Br, Si, Au, N, and O, are shown in the **Figure 4.2d** (i-vi)). The SEM-EDS images demonstrate that the FASnBr₃ NPs (corresponding to the elemental mapping of Sn, Br, and N) were distributed uniformly inside PDMS (corresponding mapping of Si and O). The elemental mapping distribution for N and O does not provide useful information on the spatial distribution of elements. The reason is for most of the SEM-EDS setup, elements with the atomic number below 11 (Na) [354] cannot be realistically detected, even if it is possible to detect their presence, however cannot be quantified reliably. The SEM sample is coated by gold to avoid the charging effect and for better conductivity. Uniform NP distribution inside the composite is crucial to get optimal performance because the NPs are considered as the mechanical load carrier of the film; furthermore, the homogeneous NP distribution will prevent the film from high voltage-poling breakdown. To obtain the surface chemical elements and valence states of the NPs, X-ray photoelectron spectroscopy (XPS) measurements were achieved (**Figure 4.2e-f**). In **Figure 4.2e**, the three peaks deconvoluted from the Sn3d_{5/2} peak at binding energies of 484.24 eV, 485.90 eV and 486.95 eV corresponded to Sn (0), Sn²⁺, and Sn⁴⁺ respectively, whereas the three significant peaks from the Sn3d_{3/2} at 492.38 eV, 494.30 eV and 496.10 eV corresponded to Sn (0), Sn²⁺, and Sn⁴⁺ respectively. The peaks at 68.74 eV in the Br3d XPS spectra in **Figure 4.2f** also established the existence of Br inside the composite films. XPS spectra of C1s and N1s are illustrated in **Figure A4.2**. The XPS results are in well compliance with a previous report [346] and confirm the chemical states of FASnBr₃ NPs. The synthesized FASnBr₃ NPs were spin-coated on an aluminum-coated silicon substrate to make a homogenous and uniform film of about 1-2 μm to investigate the local polarization state using PFM.

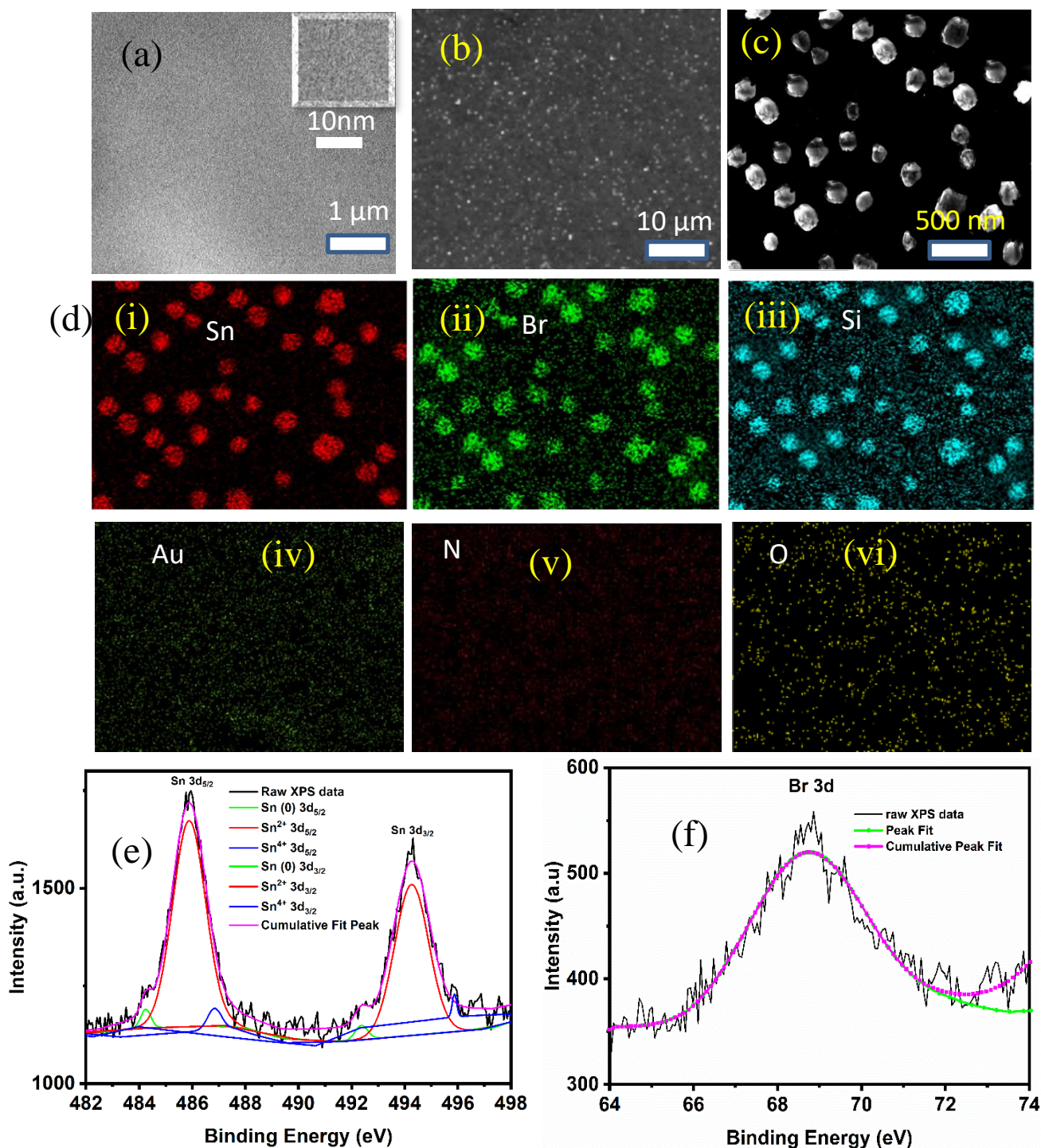


Figure 4.2. Represents the Scanning Electron Microscopy (SEM) and X-ray photoelectron spectroscopy (XPS) measurements (a) SEM image of pure PDMS and inset shows the enlarged view. (b) SEM images of a composite film of 20 wt. % FASnBr₃ NPs loaded into PDMS matrix. (c) SEM-EDS Electronic image (the approximate size of the NPs is ~250 to 300 nm). (d) (i-vi) shows the elemental composition mapping of different materials inside the FASnBr₃@ PDMS composite film. (e) XPS spectra of Sn3d, (f) XPS spectra of Br3d.

The piezoelectric polarization phenomenon in the FASnBr₃ NPs was studied in both the vertical (i.e., longitudinal) and lateral (i.e., transverse) PFM modes. In the vertical PFM measurement (V-PFM) mode, z-axis displacement resulted due to the perpendicular bending movement of the tip. In V-PFM analysis, a series of dc voltages from -10 to +10 V was applied perpendicularly to the FASnBr₃ film surface ([001]) from a conductive AFM tip coated with metal by keeping the ac voltage constant at 2V. Ideally, the electric domain inside a ferroelectric material can be reversed by applying an electric field. As ferroelectric material possesses dipole-switching properties and has a residual polarization without bias, so applying a cyclic bias to the film during the PFM measurements produced a phase and a butterfly amplitude loop. It is clearly showed a 180° change in the phase-hysteresis loop at the time of V-PFM measurements (inset in **Figure 4.3a**), and also observed a characteristic butterfly feature in the amplitude curve in **Figure 4.3a**. The polarization switching voltages both in the amplitude and phase hysteresis loop were found at $\sim \pm 1$ V, respectively, similar to the typical ferroelectric like materials [355-356]. The amplitude and phase measurements in the V-PFM strongly indicate that the FASnBr₃ NPs have an out-of-plane piezo response which is originated from its out-of-plane polarization [334]. Moreover, to determine the piezoelectric charge coefficient (d_{33}) of the FASnBr₃ NPs, a periodically poled lithium niobate (LiNbO₃) (PPLN) film (Oxford Instruments, USA) was used as a standard sample for V-PFM analysis. As depicted in **Figure 4.3b**, the measured slope of amplitude vs. drive voltage of FASnBr₃ ($K_1 = .25$) is nearly 3.5 times higher than the standard PPLN sample ($K_2 = .07$) [44]. Consequently, the d_{33} of FASnBr₃ is estimated at ~ 50 pm/V, which is quite fascinating compare to traditional organic-inorganic metallic perovskites and other molecular materials (**Table A4.1**). The surface topography, piezoelectric amplitude, and phase image of the FASnBr₃ thin film was unveiled by the V-PFM mode and presented in **Figure 4.3c-e**. There was a clear 180° phase reversal in the PFM phase image in **Figure 4.3e**; although noise was present in both amplitude (**Figure 4.3d**) and phase images which was caused by the smaller bias voltage (~ 2 V) used for the measurements. In the V-PFM, surface charges could create electrostatic responses which are similar to the electromechanical response of a piezoelectric material [357]. While comparing to the surface topography image (**Figure 4.3c**) the phase image is quite dissimilar, which discards any topographic cross-talking in the V-PFM measurements. **Figures A4.3** and **Figure 4.3f** show the effect of poling on the FASnBr₃ thin film, whereas the dc bias of -10 V and +10 V was applied alternatively on the surface and simultaneously the PFM amplitude and phase images were recorded.

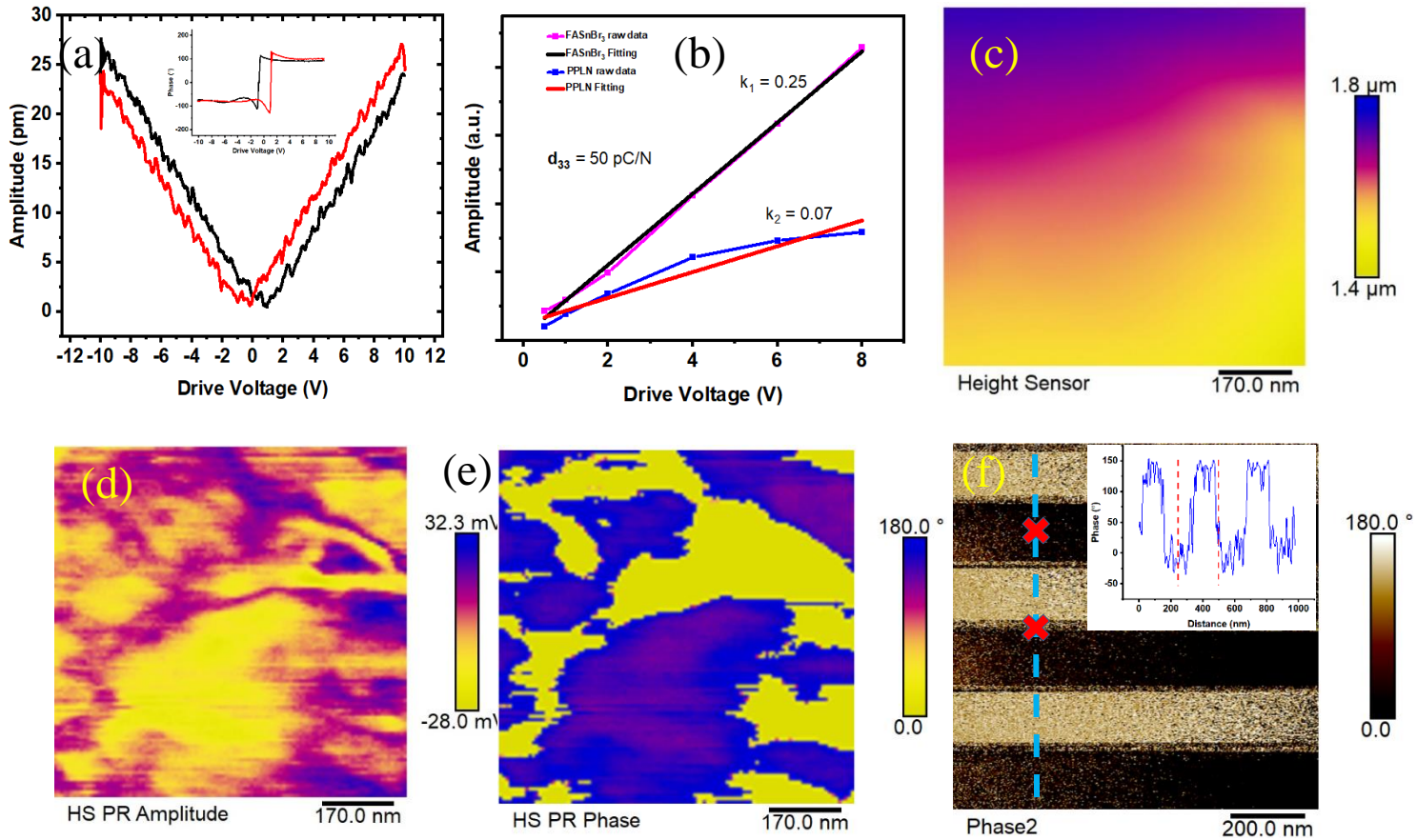


Figure 4.3. Origin of piezoelectricity from the FASnBr₃ NPs: (a) Local longitudinal (vertical) amplitude and phase hysteresis (inset) vs cyclic dc bias loops from -10 to 10 V; (b) Piezoelectric response from the FASnBr₃ and the PPLN sample measured with an ac tip bias from 0.5 V to 8 V; (c) Surface topography; (d) V-PFM amplitude and (e) phase images of the FASnBr₃ NPs; (f) Phase image after poling on the FASnBr₃ NPs.

The PFM phase images in **Figure 4.3f** clearly shows domain switching from 0 to 180° by forming two different striped regions on the surface visualized from the clear color contrast between them. The inset of **Figure 4.3f** is denoting the 180° phase contrast between two adjacent striped regions across the surface of the film which again confirms that polarization in the FASnBr₃ is switchable. The lateral PFM technique (L-PFM), which depicts the shear force among the PFM tip and sample results in in-line displacement, and corresponding laser glance in the horizontal axis is measured. The L-PFM results did not show a noticeable phase change (**Figure A4.4a**) also the piezoresponse magnitude (**Figure A4.4b**) was negligible than that observed in the V-PFM. To verify the real-life energy harnessing scenario of the FASnBr₃ NPs, finite element simulation was conducted for the PENG-model by using the COMSOL (Multiphysics 5.3). An adapted piezoelectric material using the parameters of

CH(NH₂)₂SnBr₃ was used to simulate a PENG, in which a two-dimensional (2D) model was employed for a square (100 μm × 100 μm) sized PDMS. Two models were simulated and compared, which includes a pure PDMS-based PENG, and a composite device in which 20 wt. % of NPs (at which the maximum output is achieved experimentally) was added to the PDMS matrix. The size and distribution of piezoelectric nanoparticles inside the PDMS matrix will significantly influence the stress and stress-induced piezo potential. Ideally, due to the difference in stiffness between the nanoparticles and the PDMS, the distribution of stress will mainly encompass the stiffer nanoparticle (close in view of **Figure 4.4a**). In this simulation model, (**Figure 4.4b**) top surface was chosen as the boundary load whereas the bottom surface was fixed. Due to the applied force on the top surface, higher stress will be developed near the top of the film. From the positive correlation between the stress and piezo potential, the calculated piezo electric potential will be higher at the top of the composite film model.

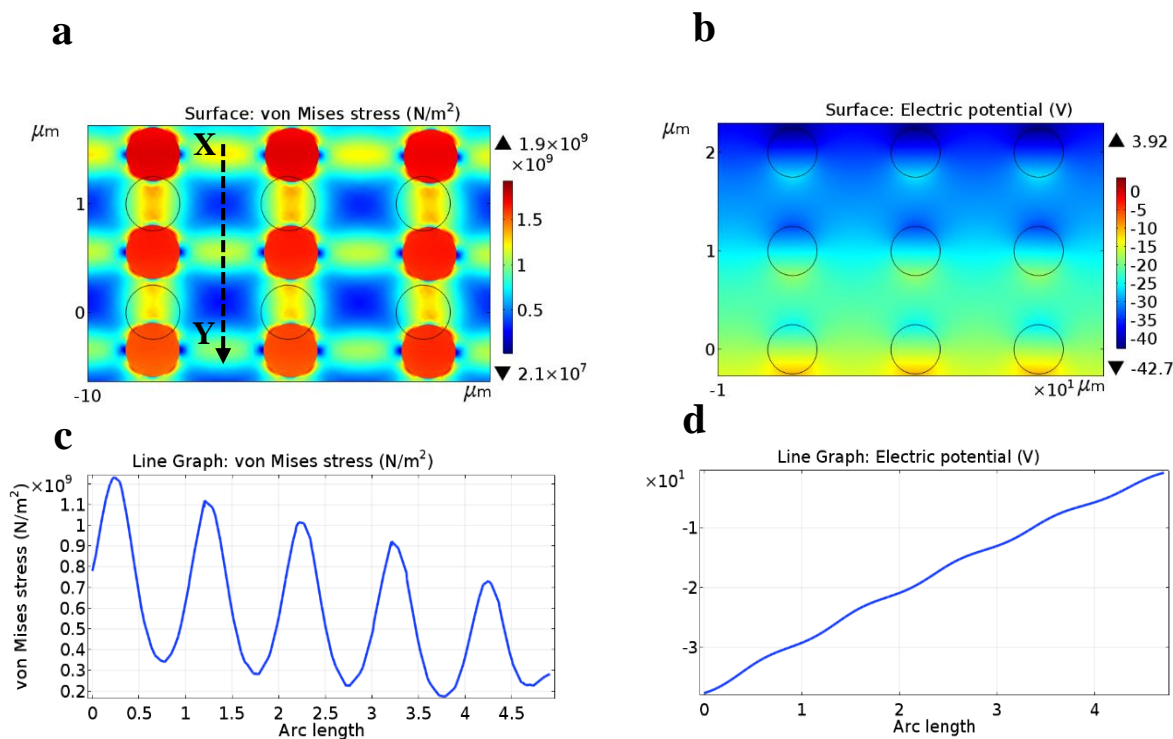


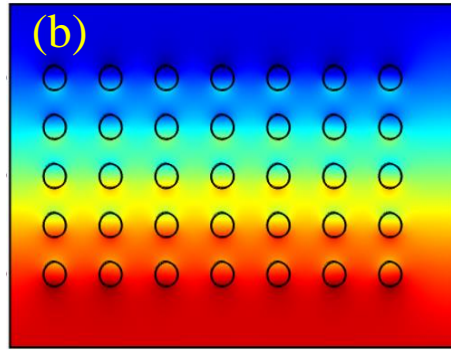
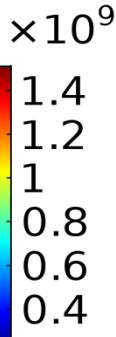
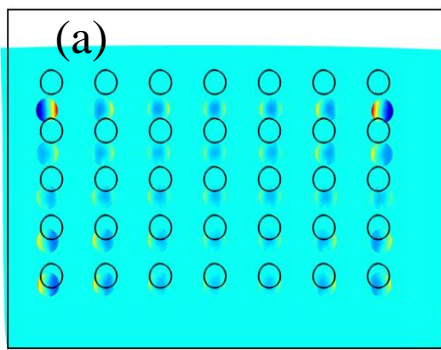
Figure 4.4. Stress (a) and electric potential distribution (b) (close in view) of FASnBr₃@PDMS composite. The stress (c) and electric potential distribution (d) along the line XY

A line (XY) was drawn across the top to bottom surface to further explain the stress distribution profile. The stress was gradually reducing to the bottom of the surface (**Figure 4.4c**), causing a proportionate change in the piezo potential (**Figure 4.4d**). The stress distribution follows an amplitude modulated sinusoidal functions-like characteristics along the XY line. It is to be mentioned that during the applied force on the top surface, the nanoparticles are also compressing each other, hence the stress amplified region is found between them compared to the less stressed regions without the nanoparticles. That is to say, the nanoparticles loading and their homogeneous distribution inside the polymer is important to maximize the piezoelectricity in a composite film.

To study the piezoelectricity of the structures, the top surface of the modeled PENG was uniformly compressed with the stress of 1 GPa. **Figure 4.5a-b** illustrates the consequence of the addition of NPs on the stress distribution and piezo potential. In contrast to the results obtained for the pure PDMS (**Figure A4.5a-b**), the addition of NPs to the PDMS matrix drastically enhanced the piezo potential. Then the effect of introducing FASnBr₃ on real-world PENG device performance was investigated. The maximum recordable peak to peak voltage and current at 40 Hz were 94.5 V_{p-p} and 19.1 μA_{p-p}, respectively, from an effective area of 6.25 cm² device a 20 wt. % FASnBr₃@PDMS composite and illustrated in **Figure 4.5c-d**. The PENG (20 wt. % mixture of NPs) showed a dramatic increase in the output current and voltage by ~ 11 times (~ 19.1 μA_{p-p}, and ~ 10 times (~ 94.5 V_{p-p}, respectively, in comparison to pure PDMS device. An output-switching test was also carried out; when the electrical connection was switched in terms of its polarity, the voltage (**Figure A4.6**) and current (**Figure 4.5e**) were found reversed, and also their amplitudes were conserved. This is further confirming the piezoelectric phenomena of the FASnBr₃@PDMS device [358]. The output voltage (**Figure 4.5f**) and current (**Figure 4.5g**) of the PENG was also recorded across a range of frequencies from 10 to 50 Hz by using an electrodynamic shaker (VR9500). The piezoelectric voltage and current peaked at 40 Hz, corresponding to the resonant condition of the device system [358]. These results also demonstrated the broadband energy-harvesting capability of the PENG device. The fabricated PENG was able to sustain over an extended period under a continuous alternation without a noticeable change in the outcome for 48000 cycles (i.e., 40 Hz for 20 minutes) (**Figure 4.5h**), proving its excellent reliability.

von Mises stress (N/m²)

Electric potential (V)



▲ 3.92



▼ -42.7

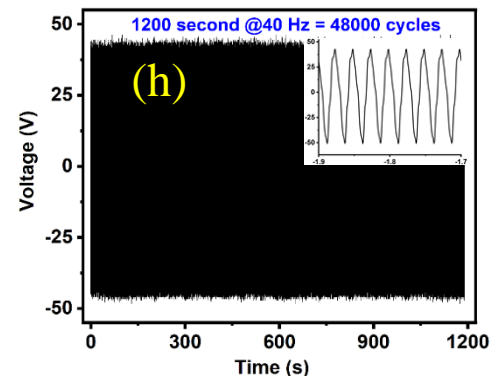
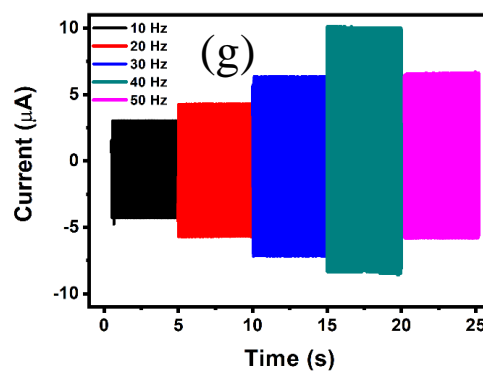
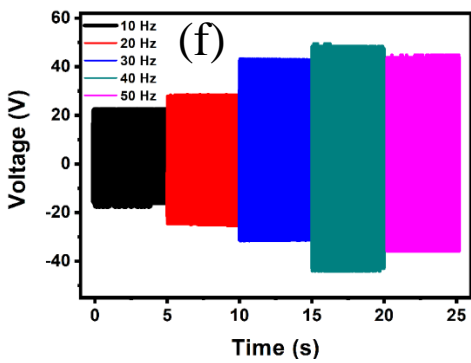
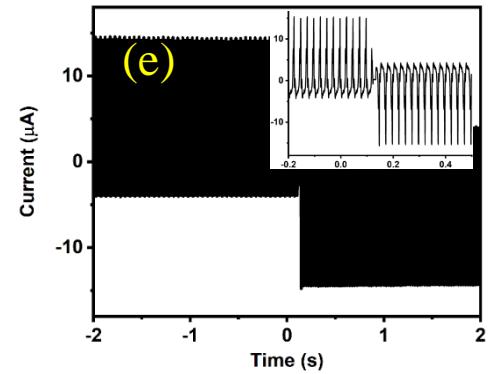
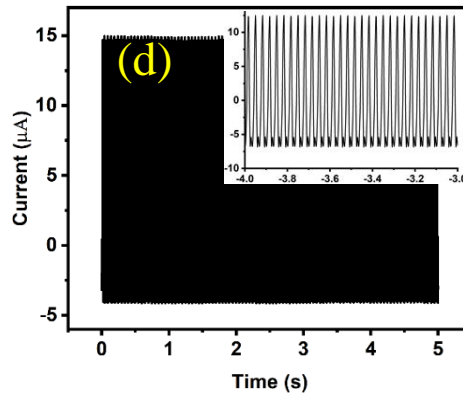
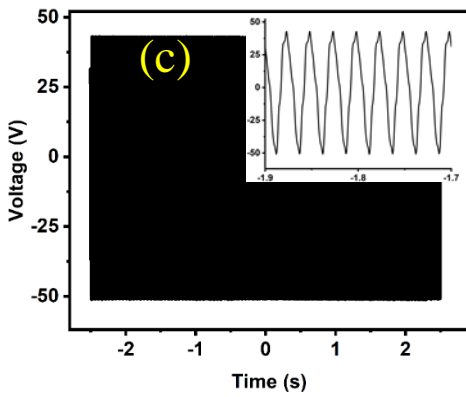


Figure 4.5. COMSOL model of FASnBr₃@PDMS composite and experimentally measured electrical output of PENG device (a) the strain distribution of 20 wt.% FASnBr₃ NPs in PDMS matrix; (b) the piezo potential distribution of 20 wt.% FASnBr₃ NPs in PDMS matrix; (c) Voltage; (d) Current at 40 Hz and 2G acceleration. (e) output switching test of short-circuit current (f) measured output voltage and (g) Current at running frequencies from 10 to 50 Hz for the 20 wt. % FASnBr₃@PDMS PENG; and (h) Durability test of the PENG device for 48000 cycles (at 40 Hz for 20 minutes).

The relative permittivity (ϵ_r) of the FASnBr₃ film was measured to be ~ 6.2 - 4.1 from 1 kHz to 1 MHz (**Figure 4.6a**); this permittivity was considerably smaller than most other widely-used piezoelectric perovskite ceramics reported in the literature, such as BTO or PZT (both of which have ϵ_r values two orders of magnitude higher than the present film) [359]. In addition, these results indicated that increasing the percentage of NPs in the PDMS matrix increased the relative permittivity of the film (which behaved in an inversely proportional manner to the piezoelectric voltage coefficient (g_{33})). This explains the maximum output was measured with the 20 wt. % FASnBr₃@PDMS devices (**Figure 4.5c-d**), and the output became lower when FASnBr₃ NPs exceeded 20 wt. % due to the percolation threshold. Furthermore, it experimentally investigated the effect of adding FASnBr₃ NPs of different mass ratios with PDMS (from 10 wt. % to 30 wt. % with a step of 5 wt.%) (**Figure A4.7**). The result clearly demonstrated that the 20 wt.% gives the highest output. The relative permittivity of the 20 wt. % FASnBr₃@PDMS composite film was also stable with temperatures, measuring for 60 minutes continuously with the temperature set at 130°C, and frequency was 200 kHz (**Figure A4.8**). Permittivity values were recorded every 10 minutes for a time span of 1 hour; a negligible variation of ± 0.03 in permittivity was noticed, which reflects the very stable phase of FASnBr₃ inside the PDMS and thus would be promising for harnessing energy in adverse environments. **Figure 4.6b** shows the direct bandgap of 2.3 eV, which is responsible for high absorption and is equally important for optical applications, such as solar cells. The deliverable output power from the PENGs to the electrical loads was measured across a range of resistances from 100 k Ω to 75.4 M Ω (**Figure 4.6c**). From the measurements, the highest output power density of 18.95 $\mu\text{W}/\text{cm}^2$ was calculated across a resistor of 9 M Ω (testing conditions were fixed at 40 Hz and 4.2 N). Notably, the measured PENG outputs of 94.5 V_{p-p}, 19.1 μA_{p-p} , and 18.95 $\mu\text{W}/\text{cm}^2$ with a small mechanical force (4.2 N) were competitive to the previously reported PENGs, which were based on the same PDMS matrix (**Table A4.1**). The voltage and current were also measured across various resistances (**Figure A4.9**). The results show that voltage increased proportionally, whereas the current behaved in an opposite manner with increasing the load, as anticipated according to Ohm's law. The generated energy of PENGs was stored in different commercial capacitors after rectifying with a full-wave bridge rectifier circuit and the charging curves are shown in **Figure 4.6d**. As anticipated, the charging time gradually rose with the capacitance (1.0 μF , 2.2 μF , 4.7 μF , and 10 μF). It only took around 20 seconds to accumulate enough charges in the 10 μF capacitors to elevate its output voltage to 3 V, and the device was able to light a red LED (**Figure 4.7**) and also demonstrated the charging and discharging behavior curve in **Figure 4.6e**.

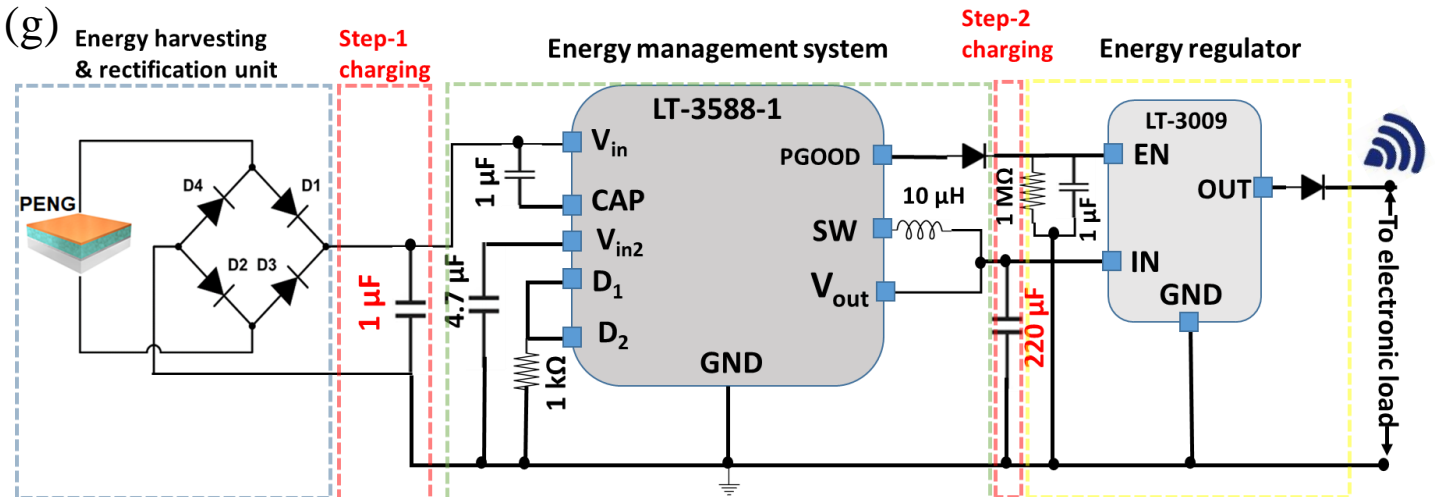
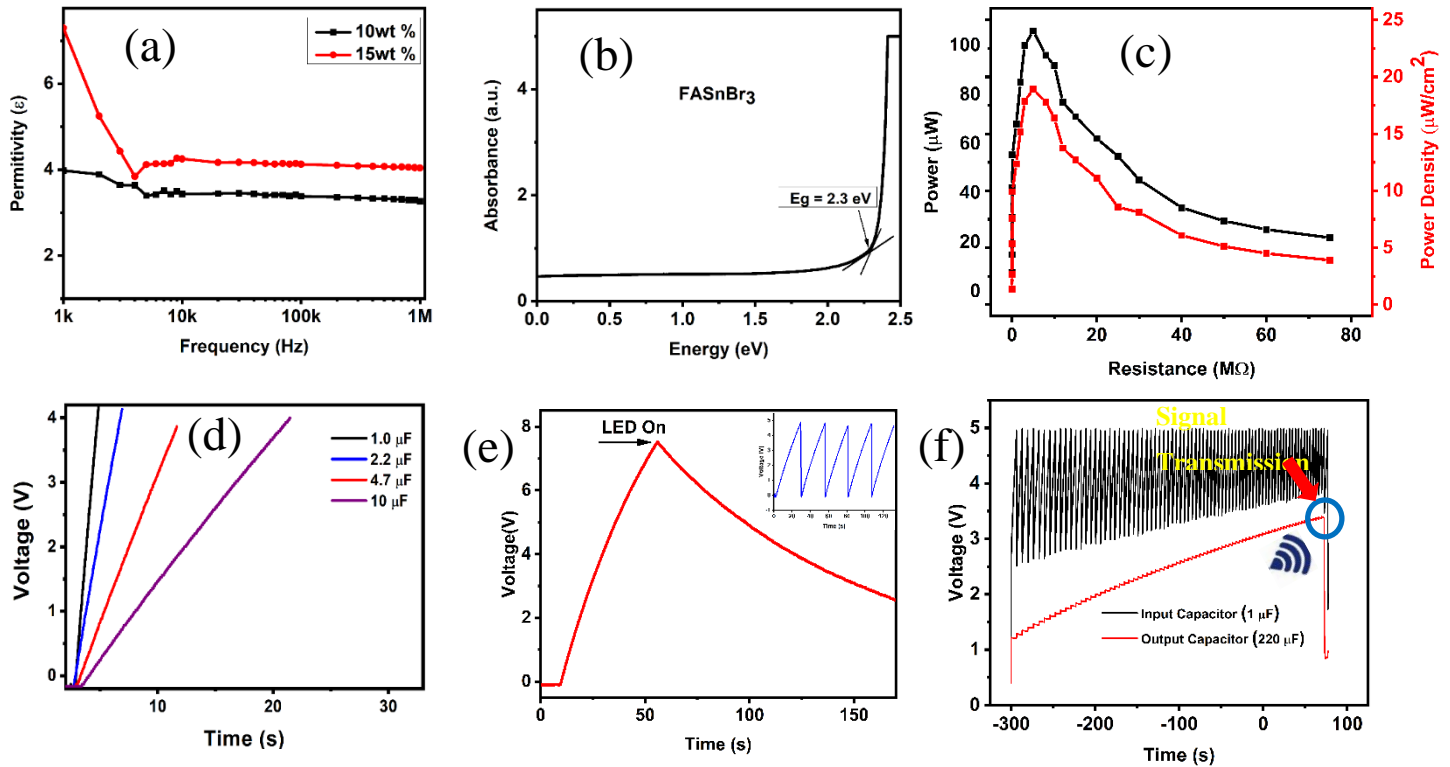


Figure 4.6. Demonstration of energy generation capability and applications prospect of the PENG device (a) Relative permittivity of FASnBr₃@PDMS device; (b) demonstrating the direct bandgap property of FASnBr₃ perovskite NPs with a bandgap of 2.3 eV; (c) measured peak output power of the PENG under various electrical loading conditions at 40 Hz; (d) Output voltage across the capacitors of 1, 2.2, 4.7, and 10 μF were charged by the 20 wt. % FASnBr₃@PDMS PENG; (e) charging and discharging output during the LED turns ON and OFF through a full-wave bridge rectifier; (f) Voltage across the 1 μF and 220 μF capacitors during the step-1 and step-2 charging cycles of the EMM when the PENG was operating at 40 Hz and demonstration of the wireless signal transmission; and (g) schematic diagram of the complete sensing system.

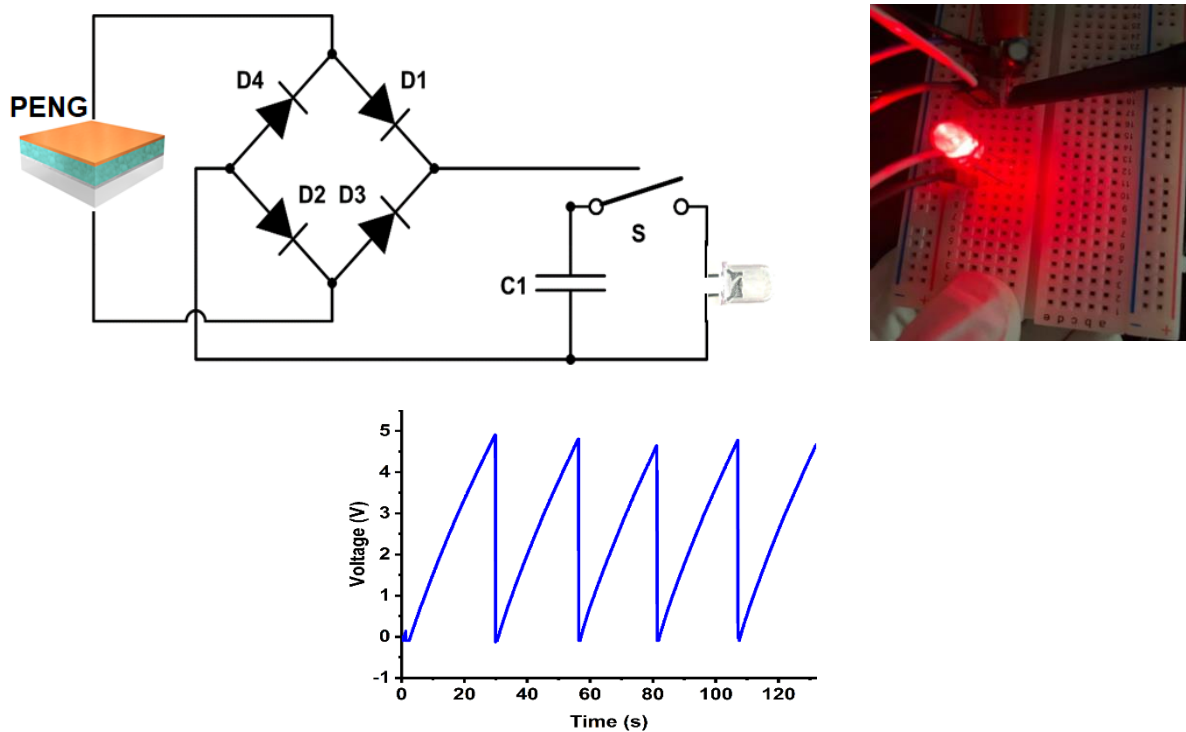


Figure 4.7. LED lighting by using the power generated from PENG along with charging discharging cycle

To realize real-life application, the PENG successfully demonstrated biomechanical energy harvesting from real-life body movement, and the results are provided in **Figure A4.11**. Finally, to demonstrate the wireless communication capability an energy-efficient charging circuit was developed which functions in two different steps (**Figure 4.6f**). In this process, the rectified electrical output from the PENG was stored to a smaller capacitor (1 μF) (step-1 charging). A commercial LTC-3588-1 unit was used to regulate the maximum charging level of this capacitor to 5 V (black curve in **Figure 4.6g**). As soon as the output voltage of this capacitor reaches 5 V, the step-2 charging cycle begins and it transfers a portion of the stored electrical energy to a larger capacitor of 220 μF (voltage increase in the red curve of **Figure 4.6g**) and its voltage-level drops from 5 V to 3 V. By using an inductor (10 μH) and two metal oxide semiconductor field-effect transistor (MOSFET) switches in the LT 3588-1 module, the current can be raised to mA level to charge the 220 μF capacitor in step-2 charging. After the step-2 charging cycle, the 220 μF capacitor is disconnected and step-1 charging begins again. Given the

periodic mechanical excitation to the PENG this charging-discharging cycle persists till the output voltage of the 220 μF capacitor increases to ~ 3.1 V, at which point the LT-3009 switch is activated to yield the stored energy to the RF transmitter in the SoC. The SoC was set to operate for a very short time (1 second/data transmission cycle) to reduce the energy consumption of the circuit. During this time window sensor signal was digitized and transmitted wirelessly to remote receivers (mobile phones). In this periodic manner, electronic or wireless circuits can be repeatedly powered up using stored energy from the PENG, thus yielding potential to realize self-powered wireless sensing [361-365], structural health monitoring, self-powered implantable biomedical devices, and other critical sensor technologies. The whole system was designed and manufactured on a circular printed circuit board (PCB) with a diameter of 3 cm (**Figure A4.12**). The practical setup, including all the necessary measuring equipment, is shown in **Figure A4.13** [360].

4.4 Conclusions

In conclusion, this work successfully developed and demonstrated a performance-enhanced and flexible piezoelectric nanogenerator based on a FASnBr_3 @PDMS composite film. The out-of-plane (i.e., along the y-axis) ferroelectric properties with a piezoelectric coefficient (d_{33}) of ~ 50 pm/V and a switchable polarization in the well-developed FASnBr_3 NPs were confirmed. The piezoelectric composite film was prepared by dispersing the FASnBr_3 NPs in the PDMS polymer matrix. An optimal ratio of 20 wt. % FASnBr_3 NPs was determined after rigorous experimental trial and verification. The maximum piezoelectric output peak to peak open-circuit voltage (V_{oc}), peak to peak short circuit current (I_{sc}), and power density (P/A) of 94.5 Vp-p, 19.1 μA p-p, and 18.95 $\mu\text{W}/\text{cm}^2$, respectively, were obtained from the nanogenerator with a small compressive force of only 4.2 N. The outputs are considerably higher than previously reported organic-inorganic metal halide perovskite-PDMS-based devices (**Table A4.1**), which supports the successful fabrication of an efficient PENG in the present study. In addition, the PENG is able to operate sustainably across a broad frequency range from 10 to 50 Hz apart from its resonant frequency, which unlocks its potentialities to be used as a broadband mechanical energy harvester. The outstanding performance of this fabricated PENG was used to successfully demonstrate a customized self-powered wireless power communication for remote sensing, and charging commercial capacitors that can power LED devices. It is anticipated that this work will innovatively expand the scope of lead-free perovskite-based PENGs for use in next-generation sensing and actuating applications.

Chapter 5

Natural Lignocellulosic Nanofibrils as Tribonegative Materials for Self-Powered Wireless Electronics

5.1 Introduction

Triboelectric nanogenerators (TENGs) are a transformative energy harvesting technology owing to their high-power output, simple architecture, small size, and low cost. They are highly promising to provide embedded powering capabilities to next-generation of disposable wearable electronics (i.e., as part of glasses, shoes, or fabrics) that are completely autonomous [366-367]. TENGs generate electrical energy by harvesting chaotic and low-frequency mechanical energy from environmental or human motions (i.e., waves, wind, walking, running) through the coupling of the triboelectric effect and electrostatic induction [368–370]. The contact between two materials with different electron-donating/withdrawing tendencies causes electrification due to the triboelectric effect, which then drives an electrical current by electrostatic induction when separated. Hence, it is critical to select suitable materials as tribo- negative and positive layers (i.e., work function and polarizability) to achieve high power outputs [371–373]. Fluorine-containing polymers, with their high strength, thermal stability, inertness, and electron-withdrawing properties, are well suited for application as the tribonegative layer in TENGs [372]. Particularly, polytetrafluoroethylene (PTFE) has become the most widely used tribonegative material [374]. To date, PTFE and other fluorinated polymers accounted for negative tribolayers in more than 50% of reported TENGs in the literature [375]. However, there are growing global interests in replacing petroleum-based non-biodegradable plastics by green natural materials to attain a high sustainability and a lower environmental impact. As a result, (ligno)cellulose, ubiquitous as a low-cost, renewable, biocompatible, and biodegradable material, has attracted significant attention and has become a top choice for making more sustainable electronic devices, including transistors [376-377], supercapacitors [378-379], batteries [380-381], sensors [382], and antennas [383-384], that are green, flexible, and disposable or recyclable [385]. Previous studies demonstrated the potential of using renewable lignocellulosic materials as the tribopositive layer replacing other common tribopositive substrates (such as metals, metal oxides, and petroleum-based polymers) [386–390]. Among all

cellulosic systems tested, regenerated cellulose films demonstrated remarkable tribopositive performances, with an electron surface charge density more than three-times higher than that of Buna-N rubber ($+10.05 \mu\text{C m}^{-2}$ vs. $+2.95 \mu\text{C m}^{-2}$) [391]. Similarly, a lignocellulosic composite (composed of lignin, starch, glycerol, and NaOH) revealed tribopositive capabilities when paired with nylon [392]. However, cellulosic materials were rarely explored as tribonegative layers because pure cellulose exhibited weak intrinsic tribopositivity. The few studies that investigated cellulosic materials as tribonegative layers yielded TENG devices with only modest power output performances. The best TENG devices with cellulosic tribonegative layers reported so far involved the use of nitrated cellulose nanofibrils (CNF) nanopapers (Nitro-CNF) and disulfide-containing regenerated cellulose films (cellophane). The integration of nitro functionalities altered the surface charge density of the CNF nanopapers due to the good electron withdrawing properties of the nitro group. Nevertheless, the Nitro-CNF (-) @copper (+) pair only produced 70% of the power output of the TENG using fluorinated ethylene propylene as the tribonegative layer [393]. Recently, a fully cellulose-based TENG was fabricated by integrating regenerated cellulose film as the tribopositive layer and cellophane as the tribonegative layer [391]. Despite tribonegative properties induced by the disulfide bonds in cellophane, the cellophane (-) @regenerated cellulose (+) pair only produced 40% of the output when PTFE was used as the tribonegative layer. In an attempt to derive the triboelectric series of a wide range of materials, it was recently suggested that a derivative of cellulose, referred to as “clear cellulose”, could be more tribonegative than PTFE [372], however, the chemical composition of this material was not given. Neither was the performance of the TENG constructed using this material reported in that study. Moreover, since chemical modification processes are usually chemical and energy intensive, they are not ideal for making sustainable disposable triboelectric energy harvesting devices. Meanwhile, other unmodified natural materials have been shown to mostly exhibit intrinsic tribopositive properties (such as silk, starch, cellulose, chitosan) [375, 394–396]. Identifying natural tribonegative materials for TENGs that can produce superior power output than conventional fluorine-containing polymers is highly desirable. The natural tribonegative materials would enable the fabrication of a new generation of low-cost, disposable, biocompatible, biodegradable, and efficient mechanical energy harvesting devices that will have a lesser impact on the environment. Nature imparted plants with remarkable strength through the precise assembly of the complex components of the cell wall into hierarchical macrostructures [397]. The systematic and careful layering of cellulose nanofibrils that are bonded to lignin via lignin-carbohydrate complex together with the lignin gluing the cell walls together ensures

the plant has high stiffness and strength. Generally, the production of nanocellulose (cellulose nanofibrils (CNF) and cellulose nanocrystals) [398] requires pure cellulose that is obtained by removing lignin (a significant mass fraction) from the original natural feedstock [399]. However, our group has recently developed lignocellulosic nanofibrils (LCNF) from tree barks with lignin remaining as an integral part of the nanofibrils, retaining the natural assembly structure of the original cell wall, thereby considerably reducing environmental footprint and cost while increasing production yield from the starting raw materials [400-401]. Due to the covalently bound more hydrophobic lignin on the surface of the cellulose nanofibrils, LCNFs had lower water permeation and absorption, higher water contact angle, and wet mechanical strength than CNFs [401-406]. In particular, it is shown that the naturally occurring quinone moieties in lignin biomolecules imparted the LCNF nanopapers with intrinsic redox capabilities that boosted the electrochemical capacitance when used as a flexible electrode in supercapacitors [406]. Thus, LCNFs are promising for applications in electronic devices to provide improvements not only in mechanical properties (strong and flexible) and sustainability but also in electrochemical performances. Here, this section reports the discovery of a natural tribonegative material, LCNFs, wherein the lignin bound on the surface of the cellulose nanofibrils possesses strong tribonegative properties by acting as an electron-withdrawing component. Specifically, the LCNF nanopaper performed as a highly tribonegative layer in TENGs, outperforming PTFE and conventional petroleum-based plastic tribonegative materials as demonstrated. When LCNF nanopaper was combined as the tribonegative layer with aluminum as the tribopositive one in a zigzag structure to form a cascade type of TENG, it could be used as a power source to run a wireless communication node, which had never been achieved before by any reported TENGs containing a natural material as the tribonegative layer. The results of this work illustrated the excellent promise of using lignocellulosic materials as green alternatives to fluorine-containing polymers in high power output TENGs for developing green self-powering wireless disposable electronics.

5.2 Experiment

5.2.1 Preparation of the nanofibrils

LCNF and CNF were prepared from Red Cedar bark (Terminal Forest Products, CA). Small pieces of bark were placed in 1% NaOH solution, weight ratio 1:10, at 90 °C for 2 h to remove extractives. The residues were washed until a clear liquor (no extractives in bark) could be observed with excess water. 2 wt% of the bark residues were soaked in distilled water for 48 h and placed in a super mass colloidier (MKZA10-15 J, Masuko Sangyo Co., Ltd., Japan) for a fibrillation step at 1500 rpm for 20 passes for

obtaining LCNF. CNF were fabricated with an additional bleaching step prior to fibrillation. The bleaching step was conducted by placing 100 g of the alkali-extracted bark residues in distilled water (3200 mL), glacial acetic acid (10 mL), and reagent-grade sodium chlorite (30 g). The reaction was heated up to 70–80 °C for 4 h with adding sodium chlorite (30 g) every hour. The obtained yellow pulp was washed with excess distilled water until reaching a neutral pH and white color. The pulp was then fibrillated using the same steps as the ones for the fabrication of LCNF.

5.2.2 Materials characterization

X-ray photoelectron spectroscopy (XPS) was performed using a K-Alpha XPS spectrometer (ThermoFisher Scientific, E. Grinstead, UK) with a monochromatic Al K α X-rays of 400 μm nominal spot size. XPS results first were acquired to determine the atomic composition of LCNF and CNF. The films were placed on carbon tape to collect a survey spectrum, obtained at low energy resolution with a pass energy of 25 eV. The relative atomic% was estimated using the sensitivity factors provided with the equipment (C1s: 1 and O1s: 2.881). Then, high resolution (pass energy–25 eV) spectra were recorded for Cs, and O1s regions. Instrument operations and further data processing were completed using the Avantage v. 5.962 software. CNF and LCNF nanofibrils were imaged using transmission electron microscopy (TEM) (TM-1000, Hitachi, Japan). The morphology of the LCNF and CNF nanopapers was studied via scanning electron microscopy (SEM) (S-5200, Hitachi, Japan). First, the nanopapers were soaked in liquid nitrogen and snapped before being carbon-coated using a carbon evaporator. The coated samples were then mounted on a custom-made holder and placed in the SEM. Mechanical properties of LCNF and CNF nanopapers were studied in tension mode by dynamic mechanical analysis (DMA, TA Instruments, USA). The samples were tested using a multifrequency strain mode at a frequency of 1 Hz and an amplitude of 15 μm . The films were cut in a rectangular shape, mounted on a clamp, and studied from room temperature to 350°C (ramp of 3°C.min⁻¹) The storage and loss modulus as a function of temperature were recorded. Chemical signatures of CNF and LCNF nanopapers were collected using a Bruker FTIR spectrometer (model Tensor 27) equipped by an attenuated total reflectance accessory (ATR) from 4000 to 400 cm⁻¹ by averaging 64 scans at a resolution of 4 cm⁻¹. The microscopic surface roughness (Rq) of the samples was measured by an Atomic Force Microscope (AFM, XE-100, Park Systems, Korea) adopting non-contact mode. Rq of the films was achieved by scanning a 5 μm * 5 μm area. KPFM measurements were taken using a Bruker Dimension Icon system and a SCM-PIT-V2 probe (Reflective PtIr,F: Conductive PtIr coated; Bruker Corporation, Billerica, MA, USA).

5.2.3 Preparation of (L)CNF nanopapers

LCNF nanopapers were prepared by mixing LCNF nanofibrils suspension in water (0.7 wt%) overnight (**Supporting note A3.1**). The homogeneous suspension was filtered using a membrane of polyvinylidene fluoride (PVDF, 0.22 μm pore size, Millipore GVWP14250, Bedford, USA). A second membrane of PVDF was placed on top of the wet film after filtration. The sandwiched wet film was placed in between blotting papers and pressed for 6 min at 345kPa. The wet blotting papers were replaced by dry ones, and the films were left to air-dry under the pressure of approximately 20kPa for 4 days. CNF nanopapers were prepared following a similar protocol by incorporating additional water prior to mixing overnight (1 mg per 10 mL final concentration).

5.2.4 Assembly of LCNF, PTFE, and CNF-based TENGs

An Al tape was attached as a back electrode of the LCNF and CNF nanopapers, and PTFE was placed on an acrylic substrate. The other triboelectric test materials (copper, aluminum, indium-tin-oxide, Kapton, polyethylene terephthalate) were placed on the opposite end of the device and were separated by an air gap of 6 mm from the reference materials (LCNF nanopaper and PTFE film). The acrylic substrate with the reference was fixed on a metallic stopper. The test materials were fixed on another acrylic substrate with Al as an electrode and connected to a hammer driven by a linear motor that allowed to control impact force and frequency. The experiments were performed under a relative humidity (%RH) condition of $\sim 27\%$. To measure the humidity-dependent output voltage, a transparent commercial glove bag, a humidifier (Honeywell), and a humidity sensor (ThermoPro) were used. The CTENG device was attached at the fixed positioned stopper of the linear motor. Then the CTENG, stopper, and humidity sensor were all covered by the air-tight glove bag. A humidifier was used to input the moisture inside the glove bag by using a vacuum hose pipe to change and control the humidity. The humidity level was recorded by the humidity sensor which was placed near the CTENG to get the actual humidity condition surrounding the CTENG device. To measure the temperature-dependence of the output voltage, a commercial hot plate (Fairweather & Co, USA), and an infrared thermometer (ETEK CITY, China) (50 to 550°C) were used. The hot plate had two parts, the control unit, and the base/plate. The base/plate was directly attached to the stopper of the linear motor and put the CTENG device on top of the base/plate. Then the temperature was controlled by the control unit of the hot plate and measured by an infrared thermometer.

5.2.5 LCNF nanopaper cascade TENG assembly and wireless communication node fabrication

A cascade-type TENG (CTENG) was fabricated on a flexible Kapton substrate by using the LCNF as the tribonegative layer and the Al as the tribopositive layer. Double-sided copper tape was used as the back electrode for the LCNF layer, and each TENG unit was repeated in a zigzag structure by the Kapton substrate (128 μm thick). The CTENG with five units of LCNF@Al TENGs was connected in a parallel electrical connection by full-bridge rectifier circuits to be integrated into a wireless communication node (WCN). The WCN was composed of an energy management (EM) and a regulation unit. The energy regulator unit was a controlled digital switch which connected the output capacitor to the RF transmitter as soon as its output voltage level reached ~ 3.1 V (common voltage level standard for commercial electronics). Before driving WCN, CTENG was used to directly charge different capacitors (1 μF , 2.2 μF , and 4.7 μF) to verify the energy-storing capabilities. To power up the RF module, the CTENG was excited at 20 Hz, and the harvested electrical energy was stored initially in a 1 μF input capacitor.

5.3 Results and Discussions

5.3.1 LCNF and CNF nanopaper properties

LCNF containing a high lignin content (31.1 wt.%) (**Figure 5.1a**) were prepared following a previously reported protocol [382]. The presence of lignin on the surface of the cellulosic nanofibrils was demonstrated by the dominant C-C bonds in the deconvoluted XPS spectra of LCNF nanopaper (**Figure 5.1b**, **Figure A5.1a-b**, **Table A5.1**, **Table A5.2**, **Appendix**). Moreover, these results indicated that lignin was the primary component on the nanopaper surface considering the relative percentage of C-C, C-OH, and COOH moieties, and the carbon/oxygen balance of the dominant monomers in lignin (*p*-coumaryl alcohol, coniferyl alcohol, and sinapyl alcohol) and cellulose (glucose) [407]. The chemical signature of LCNF (**Figure 5.1c**, **Figure A5.1c**) agreed well with previously reported FTIR results for technical lignin [408], with bands at 1570 cm^{-1} representing aromatic skeletal vibrations, 1400–1500 cm^{-1} representing C–H deformations in $-\text{CH}_3$, and $-\text{CH}_2-$, and 1232 cm^{-1} representing C–O stretching in the syringyl ring. Lignin could be clearly observed as a dark mass extending across several nanofibrils (**Figure 5.1d**, **Figure A5.1d**).

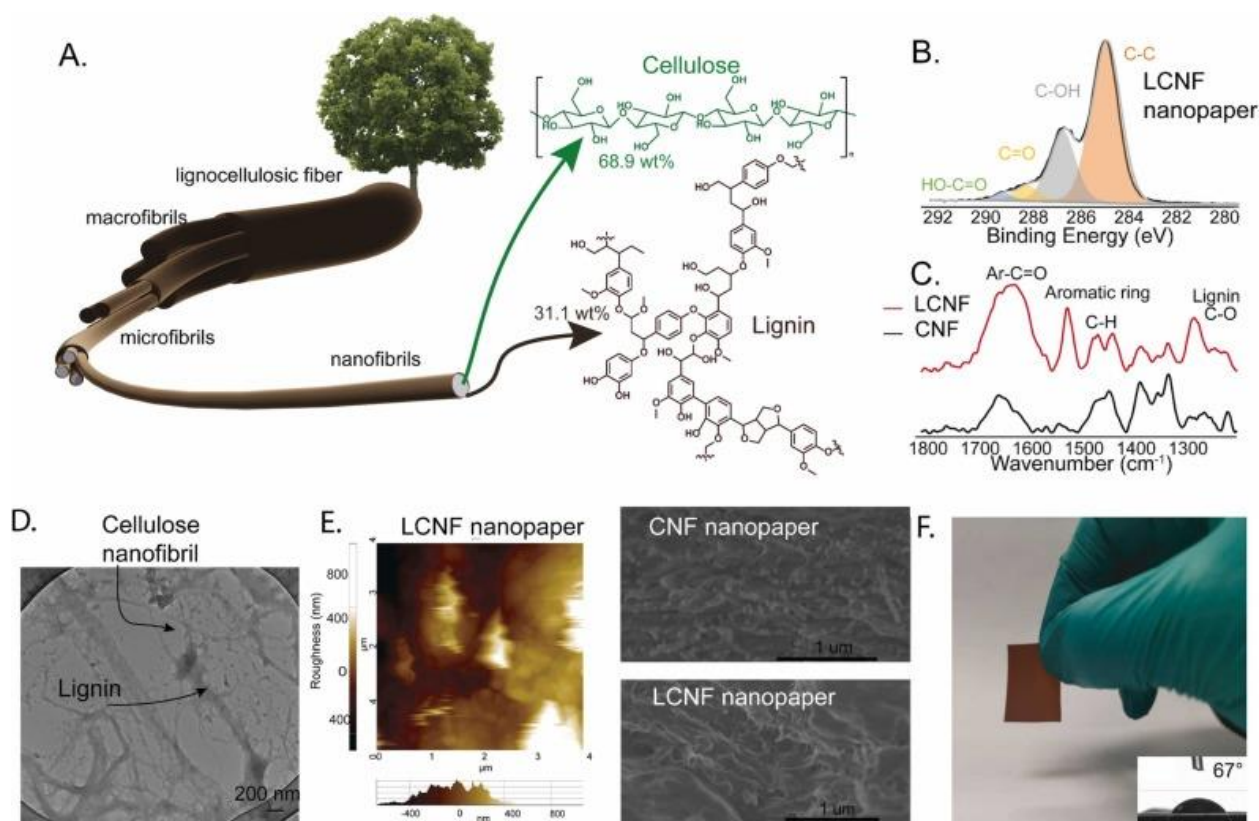


Figure 5.1. (a) Schematic depicting lignocellulosic nanofibrils, (b) Deconvoluted XPS C 1 s of LCNF nanopaper, (c) FTIR-ATR spectra of CNF and LCNF nanopapers, (d) TEM image of LCNF, (e) AFM images of LCNF nanopaper and SEM images of the cross-section of the CNF and LCNF nanopaper, (f) Photo of LCNF nanopaper and its water contact angle result.

This was coherent with the role of lignin in plant cell walls, where it exists as a stiff and amorphous polymer binding cellulosic fibrils together. The cross-section of LCNF nanopaper resembled that of a porous thermoplastic matrix, suggesting that the high lignin content yielded a nanopaper with the nanofibrils almost covered entirely by lignin (**Figure 5.1e**). These results marked a striking difference from previous literature observations of lignin as small nanoparticles on cellulose nanofibrils when the lignin content was not as high (from 12.5 wt% to 21.8 wt%) [405, 409-410]. Compared to CNF, LCNF nanopaper had a rougher surface (**Figure 5.1e, Figure A5.1e**) (RMS ca. 49.97 for CNF nanopaper, and ca. 85.25 for LCNF nanopaper), which might be due to a smoother surface with a higher level of interlocking and tighter packing in CNF nanopaper in general, the LCNF nanopaper exhibited

mechanical properties consistent with previously reported values (**Figure A5.2a-b**) [406]. Even though lignin was more hydrophobic than cellulose, LCNF nanopaper showed a relatively low water contact angle (67°) (**Figure 5.1f, Figure A5.2c**).

5.3.2 Lignin enhancing surface polarizability of the nanopaper

It is known that selecting a pair of tribolayers with dissimilar work functions and a large difference in their surface charge potentials will produce a higher electrical power output in TENGs. To investigate the influence of lignin in the nanofibril, the surface potential of LCNF and CNF nanopaper was characterized before and after contact electrification with an aluminum foil (**Figure 5.2a-b**). The values for the contact potential difference (CPD) (i.e., the surface potential) of LCNF and CNF nanopaper after undergoing friction with an aluminum foil were + 0.425 V and + 0.081 V, respectively. Since aluminum is inherently highly tribopositive, these results indicated that both nanopapers behaved as tribonegative materials. However, the high CPD value of LCNF nanopaper after friction against aluminum foil implied that lignin endowed the nanopaper with more pronounced polarizability. In contrast, pure cellulose (CNF) nanopaper was only weakly polarized, which could be explained by the slight tribopositivity endowed by the abundant oxygen-containing moieties and electron-donating carboxy groups in CNF produced during the nanofibrillation process [393, 411]. It is attributed lignin for improving the triboelectric properties of LCNF nanopaper by creating additional lower energy electron unoccupied states due to its π -electron rich aromatic moieties (**Figure 5.2c**) [412]. These additional electron unoccupied states in LCNF could enhance the charges received by the nanopaper during frictional contact contributing to its increased performance as a negative tribolayer. Typically, electrically insulating materials have a high band gap and contain partially localized electron trap states at their surface between the lowest unoccupied molecular orbital level and the highest occupied molecular orbital level. During frictional contact between the metal layer and the nanopaper insulator layer, the compression of the metal and the nanopaper reduced the atomic distance between the two materials that resulted in a larger overlap of electron clouds and electronic charge transfer between frontier orbitals [373, 413]. The short atomic distance helped to overcome the energy barrier between the two materials to favor the donation of electrons from the tribopositive layer to the tribonegative one.

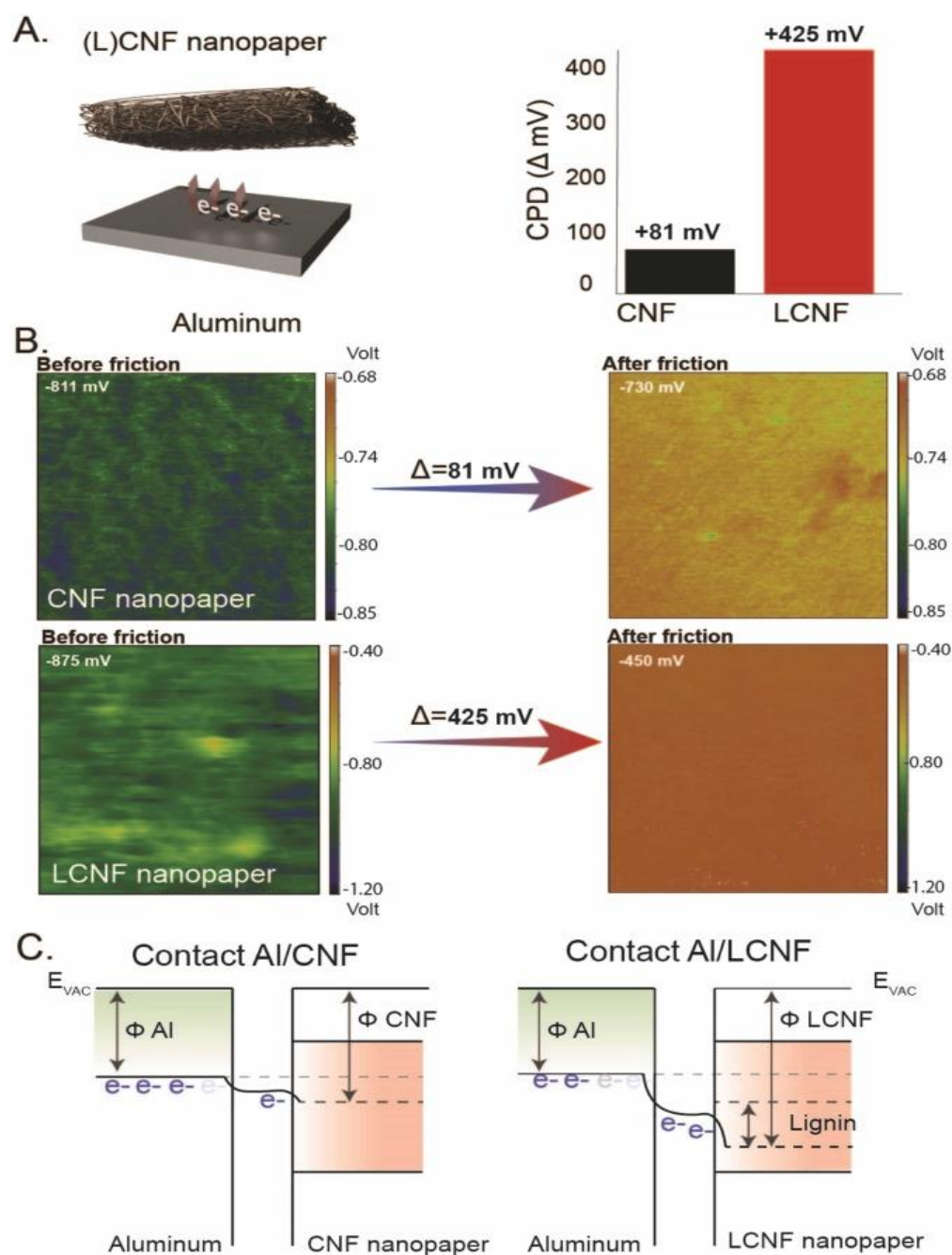


Figure 5.2. (a) Schematic of contact electrification between LCNF (or CNF) nanopaper and aluminum foil and the corresponding CPD values, (b) KPFM surface potential results of CNF and LCNF nanopaper before and after contact electrification with aluminum, (c) Energy band diagram of CNF and LCNF nanopaper during contact electrification with Al.

5.3.3 Triboelectric characteristics of LCNF nanopaper in TENGs

LCNF surface polarizability was further investigated by applying LCNF nanopaper as a tribolayer in TENGs together with several selected materials ranging from tribonegative to tribopositive. Either the LCNF nanopaper or a PTFE film was used as the reference substrate against another triboelectric test material that was placed at the opposite end of the device (**Figure 5.3a**). Operating similar to a typical TENG, LCNF-containing TENGs generated power during a contact/separation cycle via four distinct steps (**Figure 5.3b**). First, the contact between the LCNF nanopaper and the other test material induced a charge transfer between the two materials due to the differences in their work function and electron donating/withdrawing tendency. Second, as the two layers separated, electrons started to flow from the top LCNF (-) electrode to the bottom electrode (+) to produce an electric potential via electrostatic induction. Third, the higher electrical potential was obtained as the triboelectric layers reached the maximum separation distance and the electrical current flow stopped due to the screening out of the triboelectric charges. Lastly, bringing the triboelectric layers closer into contact again lowered the generated electric potential, thereby inducing the flow-back of the electrons to the original electrode. Taking advantage of this contact/separation cycle, electric potential and current were produced periodically as a function of mechanical excitation parameters (such as frequency of contact, loading force during contact, etc.). The voltage and current output of TENGs composed of the LCNF nanopaper and another test material selected from the triboelectric series ranging from highly negative to highly positive (polyethylene terephthalate (PET), Kapton, indium-tin-oxide (ITO), copper (Cu), and aluminum (Al)) was systematically studied. For comparison, TENGs were also made using a PTFE film instead of the LCNF nanopaper with the same set of selected materials as the other tribolayer [414]. The open-circuit output voltage (referred to as voltage subsequently) and short-circuit current (referred to as current subsequently) of the two types of TENG systems were measured at the test frequency and force of 3 Hz and 20.8 N, respectively, and the results are given in **Figure 5.3c** and **Figure 5.3d**. Evidently, higher voltage and current output were obtained for TENGs with LCNF than PTFE for all selected test materials including both highly tribonegative (PET) and highly tribopositive (Al) materials. Using data from a recently published study on the quantification of triboelectric series of polymeric materials, I plotted some of these polymeric materials according to their triboelectric charge density in **Figure 5.3e**.

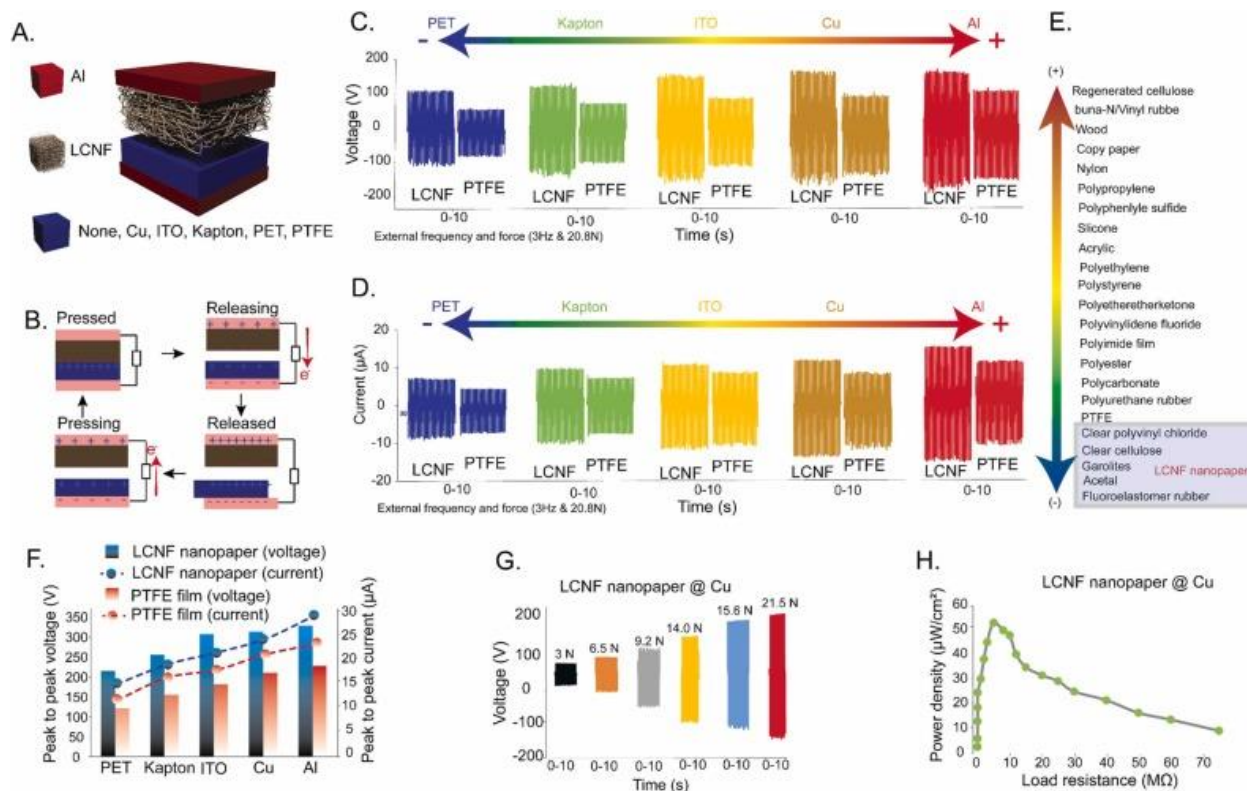


Figure 5.3. (a) Schematic of the LCNF TENG device structure, (b) Steps involved in the power generation of TENGs, (c) Open-circuit voltage output and (d) short-circuit current output of TENGs with LCNF nanopaper compared against that of TENGs with PTFE film as the tribonegative layer, (e) Revised and simplified version of the polymeric triboelectric series according to this test results and literature reference[372], (f) Peak to peak voltage and current of TENGs with either LCNF nanopaper or PTFE film as the tribonegative layer, (g) Effect of contact force on peak to peak open-circuit voltage of TENGs made with LCNF nanopaper and Cu as the two tribolayers, (h) Effect of load resistance on power density of TENGs with LCNF nanopaper and Cu.

It is worth noting that in the referred study these values were generated using a customized setup without verification in TENGs devices, while the results were from side-by-side comparisons of the actual outputs of TENGs made from LCNF vs. PTFE. The test result showed that LCNF was more tribonegative than PTFE as shown in **Figure 5.3e**. Among all materials included in **Figure 5.3e**, LCNF was the only natural material that was tribonegative [372]. Thus, LCNF presented a new green alternative material choice for eco-friendly TENGs. It is important to note that the nanofibrillar nature of LCNF imparted the nanopaper with high surface roughness and porosity (RMS ca. 85.26 nm).

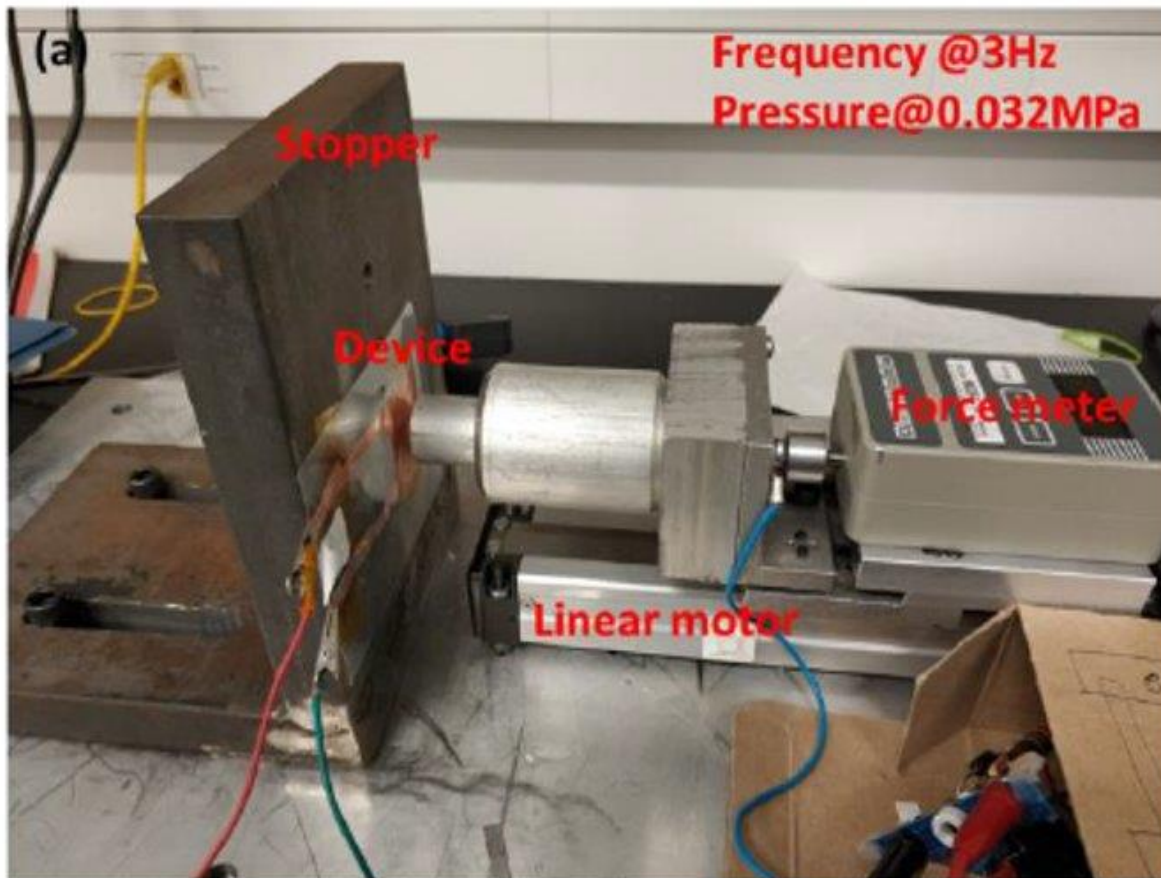


Figure 5.4. a photograph of the TENG characterization set-up, including Stopper, TENG, Linear motor, and force sensor.

Under external force, surface asperities in the nanopaper can deform making contact with the other tribolayers to increase the effective/active contact surface area, and consequently induce more surface charges [415]. Thus, the increase in the voltage and current output of the TENG devices was due to both the tribonegative properties stemming from the natural lignin bound on the surface of the cellulose nanofibrils, and the surface texture of the nanopaper brought by the natural nanofibrillar morphology of LCNF. With the common tribopositive metallic materials (Cu, Al) as the tribopositive layer and LCNF as the tribonegative layer, LCNF TENGs achieved an output voltage of ~ 300 V and ~ 360 V, respectively, which were much higher than that of TENGs with PTFE as the tribonegative layer (~ 200 V for PTFE@Cu TENGs; ~ 260 V for PTFE@Al TENGs) (**Figure 5.3f**). These results clearly demonstrated that the LCNF nanopaper was more tribonegative than the PTFE film. A similar trend

was also observed for the current outputs of the TENGs (**Figure 5.3f**) with 25 μA and 28 μA for the LCNF@Cu and LCNF@Al TENGs and 17 μA and 18 μA for the PTFE@Cu, and PTFE@Al TENGs, respectively. In order to elucidate the role of lignin in inducing triboelectric effect in LCNF nanopaper, “lignin-free”, or pure cellulose nanopaper (CNF) was also used to make TENGs in the same manner as the LCNF nanopaper. The output results of TENGs with CNF were given in **Figure A5.3**. Expectedly, the CNF nanopaper displayed tribopositive behavior. Moreover, TENGs with CNF nanopaper had much lower voltage and current outputs when combined with the same triboelectric layers used in the study. Hence, it was clear that the natural lignin as integral part of LCNF transformed LCNF from tribopositive characteristics of lignin-free CNF to tribonegative responses. Meanwhile, LCNF nanopaper showed a 3–15-fold improvement in storage modulus compared to conventional petroleum-based thermoplastics (polystyrene, polycarbonate, high-density polyethylene, and PTFE) [416–418]. Therefore, wood-derived natural LCNF nanopaper was stronger and more flexible with higher electronegativity than synthetic non-degradable PTFE. The effect of applied force and load resistance on the output voltage of the LCNF@Cu TENG was further studied. As expected, with a higher force applied during contact (from 3 N to 21.5 N), peak to peak voltage increased to ~ 330 V (**Figure 5.3g**). The maximum peak power density of the TENG was $52 \mu\text{W}/\text{cm}^2$ obtained at a load resistance of $8 \text{ M}\Omega$ (**Figure 5.3h**). Overall, LCNF@Cu TENG demonstrated a high output compared to equivalent TENG systems reported in the literature (**Table A5.3**), with an output power exceeding previous unpatterned metal (metal alloys [419] and Au [420])/PTFE systems. Only unpatterned metal TENGs were included in the comparison since it was well known that surface texturing/patterning could drastically change the triboelectric properties of a material [421], and here only used unpatterned metal films in this study. Moreover, the LCNF@Cu TENG devices demonstrated ultra-high performances compared to previously reported TENG systems involving unpatterned metals as the tribopositive layer and CNF-based materials as the tribonegative layers, including > 100 -fold improvement from pristine CNF [411]. Lastly, the LCNF@Cu TENG was able to maintain high performances over long periods of time as demonstrated by the lack of noticeable degradation in the output signal after operating for 72,000 cycles (**Figure A5.4a**), which indicated the excellent long-term stability of the LCNF nanopaper as a high-performance tribonegative material. Moreover, the performances of the LCNF nanopaper/Cu TENG were monitored while varying the temperature and relative humidity levels (%RH) using customized setups. Expectedly, increasing %RH value from 27% to 95% caused 31.4% decrease in peak-to-peak voltage output value of the LCNF nanopaper/Cu TENG (**Figure A5.5 & Table 5.1**).

Table 5.1. LCNF nanopaper/Cu TENG peak to peak voltage outputs at various relative humidity levels.

%RH	Peak to peak voltage (V)	Output reduction (%)
27	78	N/A
40	76	2.6
50	72	7.7
60	68	12.8
70	64	17.9
80	61.5	21.2
90	59	24.4
95	53.5	31.4

Table 5.2. LCNF nanopaper/Cu TENG peak to peak voltage outputs at various temperatures.

Temperature (°C)	Peak to peak voltage (V)	Output reduction (%)
26.5	83.3	N/A
30	82.5	0.9
35	81.2	2.5
40	79.5	4.5
50	78.3	6.0
64	77.7	6.7

It is known that a higher %RH would negatively affect TENG operations. Under high %RH, a thick water layer could form on the surface of the tribolayer which would increase the surface electrical conductivity and the ability to dissipate surface charges to result in a lower TENG voltage output [422]. However, as compared to other pure CNF and CNF-based TENG systems which showed more pronounced reductions (up to 60%) in voltage outputs with the increasing %RH [391, 423-424], the LCNF-based TENG in this study demonstrated better robustness for operation under high %RH levels. Specifically, a CNF/Cellophane TENG previously reported showcased a 32% decrease in the device current output when raising the %RH from 48% to 62% [371]. Similarly, a TENG composed of functionalized CNF/Polyamide demonstrated a 65% decrease in voltage output when increasing the %RH from 30% to 90% [423]. As shown in **Figure A5.6 & Table 5.2**, a slight decrease in the TENG voltage output (ca. 6.8%) was observed when increasing temperature from 26.5 °C to 64 °C, which demonstrated the limited impact of temperature on LCNF TENG operations.

5.3.4 LCNF nanopaper-based cascade-type TENG for self-powering a wireless communication node

The excellent properties of LCNF nanopaper as a tribonegative material for TENGs were further explored to demonstrate the suitability of using this natural material in TENGs for self-powering applications. Usually, self-powering electronics are energy-intensive and require high power output from the energy storage device that drives them. In this regard, a cascade-type TENG (CTENG) was fabricated on a flexible Kapton substrate by using LCNF nanopapers as the tribonegative layers and Al as the tribopositive layers (**Figure 5.5a**). The CTENG consisted of five units of LCNF@Al TENGs connected in parallel was integrated into a wireless communication node (WCN) using an RSL10 Multi-Protocol BLUETOOTH® System-on-Chip with a threshold voltage of 3.1 V and a threshold current of 4.6 mA. The WCN was assembled with an energy management (EM) and a regulation unit to efficiently store the electrical energy in a two-stage charging mechanism [425–429]. The energy regulator unit was a controlled digital switch, which connected the output capacitor to the RF transmitter as soon as its output voltage level reached ~ 3.1 V (common voltage level standard for commercial electronics). The performance of the CTENG was initially tested by verifying the ability of a single LCNF@Al TENG to charge various capacitors (1 μ F, 2.2 μ F, and 4.7 μ F) (**Figure 5.5b**). The device was capable of fast charging the 1 μ F, 2.2 μ F, and 4.7 μ F capacitors up to ~ 3.1 V in 20 s, 40 s, and 90 s, respectively.

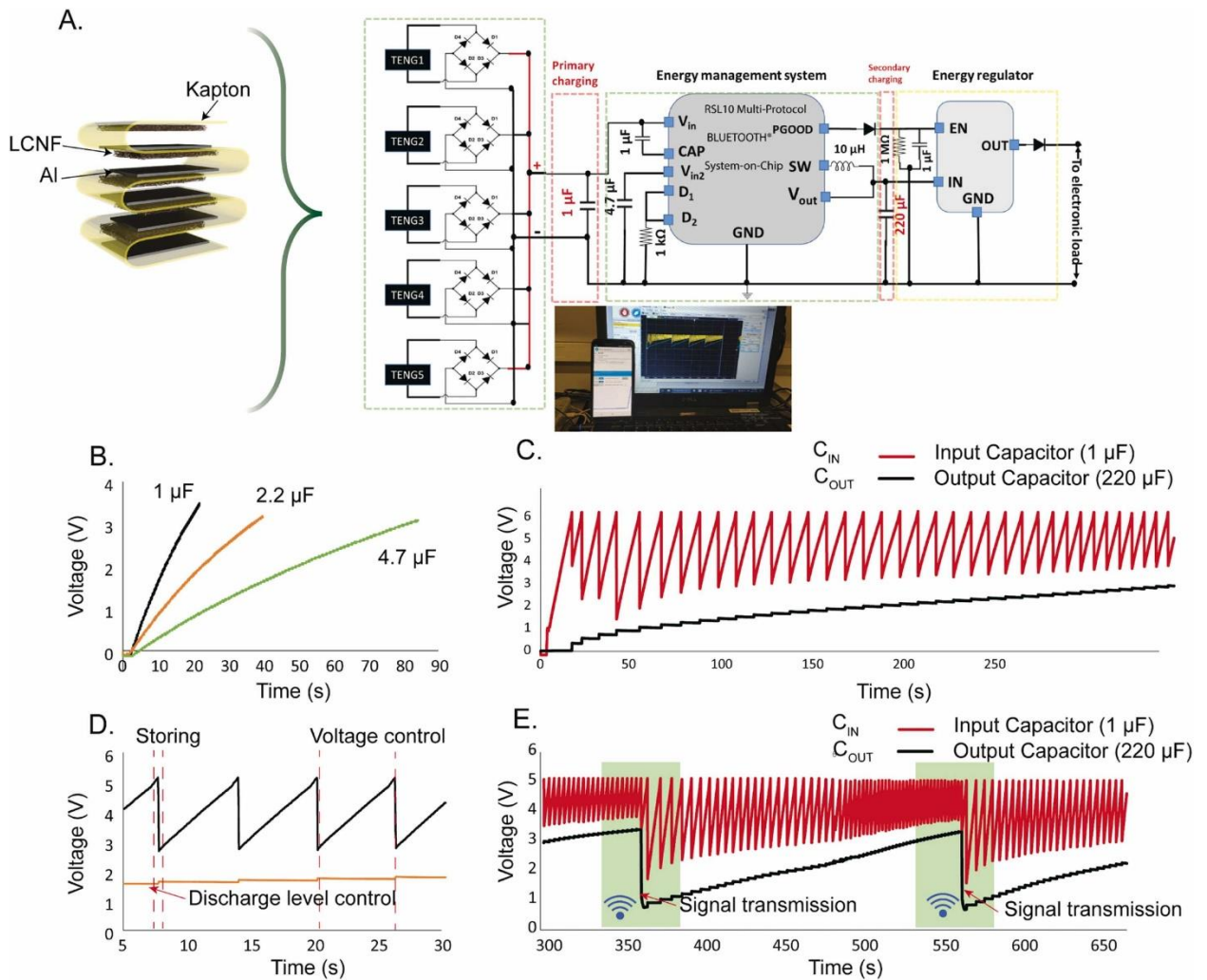


Figure 5.5. LCNF@Al-based CTENG for self-powered wireless communication, (a) Schematic of a LCNF-based cascade type (five units) TENG (CTENG) and a wireless communication node (WCN) comprising of an energy management and regulation system for powering up a radio frequency (RF) transmitter, (b) Charging of different capacitors with the CTENG, (c) Charging of the input and output capacitor units of the WCN by the CTENG, (d) Close up view of the measured voltage-controlled charging waveforms in Fig. 5.4c, (e) Discharging of the output capacitor in the WCN to power-up the RF transmitter indicating each RF transmission.

To power up the RF module, the CTENG output energy (5 LCNF@Al units assembled in parallel) was initially stored in a 1 μF input capacitor (red color charging curve in **Figure 5.5c**) until the capacitor

reached to ~ 6 V. At this point, the buck-converter inside the energy management system switched on to charge the output capacitor of $220 \mu\text{F}$ through an inductor (black charging curve in **Figure 5.5c**). After the input capacitor's voltage level fell between ~ 2.5 – 3 V the buck-converter was turned off and it started charging again to ~ 6 V. This method enabled the efficient transfer of energy from the input to the output capacitors [426]. As the periodic charging process continued, the voltage-level of the output capacitor was kept fixed by an energy regulator to prevent energy consumption by the RF module (**Figure 5.5d**). The voltage of the output capacitor was controlled until it reached ~ 3.1 V, and subsequently the energy was consumed by the RF transmitter via the energy regulator module (**Figure 5.5e**). A RF signal transmission occurred from the built-in antenna in the RF module, where the signal could be further modulated with useful sensory information to realize a self-powered wireless monitoring system for artificial intelligence (AI) technology or internet of things (IoT) [427–430]. The device enabled RF communication after ~ 6 min in the initial charging cycle while only ~ 3 min were sufficient for the subsequent transmission. The longer initial charging time could be explained by the output capacitor charging from an empty state. Following the initial cycle, as the capacitor did not fully discharge (~ 0.9 V level) after powering up the RF module, the subsequent wireless data transmission time was greatly reduced. This demonstration of the integration of LCNF-based CTENG to power a WCN was very exciting as it clearly demonstrated the applicability of a wood-derived, biodegradable, and green lignocellulosic material as a high-performance tribonegative material to enable self-powered wireless electronics.

5.4 Conclusions

In summary, this chapter report a discovery that wood-derived lignocellulosic nanofibrils exhibit pronounced tribonegativity in TENGs, leading to superior output performance (voltage and current) as compared to TENGs with PTFE when paired with various known materials (aluminum, copper, indium-tin-oxide, polyamide, polyethylene terephthalate) operating in the contact-separation mode. The reported results indicated that lignin bound on the surface of the cellulosic nanofibrils induced the increase in the surface polarizability of LCNF nanopaper after friction contact with tribopositive aluminum. LCNF nanopapers were further assembled in a zigzag structure to form a cascade type TENG, which was successfully used as a power source to run a wireless communication node that transmitted a radio-frequency signal every 3 min. Successful application of TENGs made from natural, biodegradable, inexpensive, and renewable lignocellulosic nanofibrils for powering wireless

electronics is significant since it showcases the feasibility of fabricating environmentally friendly disposable electrical energy harvesting devices. This study uncovers a new natural material that can be used as a strong and flexible tribonegative layer in TENGs that are not only more sustainable but also perform better than petroleum-based polymers, including fluorine-containing PTFE. The concept illustrated in this study pinpoints to new possibilities for developing next generation of high-performance sustainable TENGs for energy harvesting and self-powering devices.

Chapter 6

Conclusions and Future Work

6.1. Summary of Contributions

After carefully reviewing the recent progress of organic-inorganic nanomaterials-based flexible NGs for mechanical energy harvesting, the existing problems and challenges in this field were identified. To bridge the gap between the current challenges and practical applications, this research work rationally designed and developed novel organic-inorganic nanomaterials-based NGs aiming for improved output performance and practical applications. Piezoelectric/triboelectric active materials, including organic materials, inorganic materials, and their hybrid were initially studied along with the principle of piezoelectric and triboelectric nanogenerators. Novel and highly piezoelectric active nanocomposites/polymers were explored to enhance the piezoelectric performance. Techniques for surface micro/nanostructure modification of triboelectric materials were developed to achieve improved triboelectric outputs. Taking into account the existing problems, organic-inorganic nanomaterials based nanogenerators with enhanced electrical output performance and desirable flexibility were developed to address the challenges in the development of advanced mechanical energy harvesting technologies and self-powered electronics. By designing and studying flexible NGs with different polymers/organic/inorganic/ nanomaterial structures, ZnO/PVDF porous PENGs, FAPbBr₂I/PVDF based PENGs, FASnBr₃/PDMS based PENGs, and LCNF nanopaper-based TENGs were successfully fabricated and measured, and remarkable electric outputs were obtained. Based on the outcome of this research work, some important conclusions can be drawn.

1. This research began with demonstrating a self-powered wireless sensing system based on a porous PVDF-based PENG, which is prominently anticipated for developing auto-operated sensor networks. The results show that the output of the piezoelectric nanogenerator can be enhanced by adding a piezoelectric polymer matrix (PVDF) with the ZnO nanoparticles. At the same time, the porosity of the film acts as a strain center and can improve the output performance greatly. Porous PVDF film was made from a flexible piezoelectric polymer (polyvinylidene fluoride (PVDF)) and inorganic zinc oxide (ZnO) nanoparticles. The

fabricated porous PVDF-based PENG demonstrates ~ 11 times and ~ 8 times enhancement of output current and voltage, respectively, compared to a pure PVDF-based PENG. The PENG can generate sufficient electrical energy from an automobile car vibration, which reflects the scenario of potential real-life structural health monitoring (SHM) systems.

2. Second, a novel, self-assembled, highly porous perovskite/polymer (polyvinylidene fluoride (PVDF)) composite film was designed and developed for fabricating high-performance piezoelectric nanogenerators (PENGs). The novelty of this work was to develop a single-step fabrication method without HCl etching (to make the film porous). The macroscopic porous structure can significantly enlarge the bulk strain of the piezoelectric composite film, which leads to a 5-fold enhancement in the strain-induced piezo potential. In addition, the novel hybrid halide perovskites (HHP)-Formamidinium lead bromine iodine (FAPbBr₂I) material can improve the conductivity of the final composite film due to its enhanced permittivity, providing a 15-fold amplification of the output current. This P-PENG based on a low-temperature full-solution synthesis approach may initiate a paradigm shift by opening the realms of flexible PENGs as sustainable power sources.
3. Third, an organic-inorganic hybrid perovskites (OIHP) PENG was developed, combining lead-free Formamidinium tin (Sn) halide perovskite (CH(NH₂)₂SnBr₃ (FASnBr₃)) nanoparticles (NPs) and polydimethylsiloxane (PDMS) polymer matrix. Due to the outstanding flexibility and uniform distribution properties, the device demonstrated a maximum piezoelectric peak-to-peak output voltage of 94.5 V_{p-p}, peak-to-peak current of 19.1 μA_{p-p}, and output power density of 18.95 μW/cm² with a tiny force of 4.2 N. It is anticipated that the fabricated FASnBr₃@PDMS nanocomposite PENG not only possesses outstanding performance and reliability but also serves as a stepping-stone towards achieving self-powered Internet of Things (IoT) devices built using environment-friendly perovskite piezoelectric materials.
4. Fourth, a natural wood-derived lignocellulosic nanofibrils (LCNF) tribolayer was employed to replace fluorine-containing petroleum-based polymers as a tribonegative material for TENGs for the first time. The high tribonegativity was due to the presence of natural lignin on the surface of LCNF and LCNF's nanofibril morphology. Assembling LCNF nanopaper as the

tribonegative layers into a cascade TENG that could generate sufficient output power to drive a wireless communication node, capable of sending a radio-frequency signal to a smartphone every 3 min. This study demonstrates the excellent promises of using LCNF to make high-performance and more environmentally friendly wireless self-powered electronics; and pinpoints a new approach for fabricating sustainable triboelectric nanogenerators using natural lignocellulosic materials instead of conventional fluorine-containing petroleum-based polymers as tribonegative layers.

In summary, this thesis has carried out a systematic study on designing, exploring, and developing highly efficient flexible nanogenerators for self-powered wireless electronics. With the combination of highly electroactive nanomaterials with flexible polymer matrix structures, NGs with both high electric output performance and flexibility were successfully obtained. These findings pave the way for the development and innovation of flexible nanogenerators for energy harvesting and self-powered sensing.

6.2. Future Work

Although high-performance flexible NGs of different polymer/organic/inorganic nanomaterials-based structures were successfully designed and developed, there still exist some limitations, and the corresponding recommendations for future study in this field can be summarized as

(1) To fulfill the demands for practical applications, the output performance of the NGs still needs to be further enhanced. One way to enhance the energy efficiency of the polymer/nanomaterials-based NGs is to be extensively studied and adopted active piezoelectric/triboelectric materials. Moreover, the design of NGs should also be further optimized for boosting the electric outputs by maximizing the effective contact area. In addition, cascading the NGs could be a better solution to improve the performance of the individual NGs.

(2) The flexibility of the reported NGs still require to be further improvement. The copper electrodes used in this work are comparatively more rigid and therefore need to find a suitable softer electrode. In addition, it is obvious that the flexibility of the device will reduce when it is encapsulated and protected by a polyester thin film. Therefore, it is extremely necessary to develop and adopt superior encapsulation materials to improve the flexibility and longevity of the device. Moreover, an in-depth investigation is required to ensure that NGs can withstand harsh conditions in practical use.

(3) To develop an inclusive understanding of the piezoelectric polymer characteristics that affect the device performance, such as its molecular weight, crystallinity, piezoelectric phase formation mechanism, and on the crystal grain size in the nanocomposite films can be studied in the future. It is also important to examine whether the origin of enhanced piezoelectricity in organic/inorganic halide perovskite stems from ferroelectricity. Although some current research reports showed the ferroelectricity of some halide perovskite (MAPbI₃, CsPbBr₃, FASnI₃), still more research needs to be done to understand the underline mechanism of ferroelectric-related knowledge in these materials.

(4) The lead (Pb), present in organolead halide perovskite-based PENG devices is very toxic which is a threat to human health and the ecological environment. To avoid toxicity, one solution is to replace the Pb with other nontoxic elements (such as tin (Sn)) to develop Pb-free PENGs. But one of the major challenges related to the Sn-based perovskites is its poor air stability (easy oxidization from Sn²⁺ to Sn⁴⁺), and hence results in rapid degradation of the Sn-based perovskite materials. Therefore, it is an urgent need to find a solution to stable the Sn-based perovskites PENGs which could be a potential research direction in the future.

Letter of Copyright Permission



On the first principle theory of nanogenerators from Maxwell's equations

Author: Zhong Lin Wang
Publication: Nano Energy
Publisher: Elsevier
Date: February 2020

© 2019 Elsevier Ltd. All rights reserved.

Order Completed

Thank you for your order.

This Agreement between University of Waterloo -- Md. Masud Rana ("You") and Elsevier ("Elsevier") consists of your license details and the terms and conditions provided by Elsevier and Copyright Clearance Center.

Your confirmation email will contain your order number for future reference.

License Number 5503230028843 [Printable Details](#)
License date Mar 06, 2023

Licensed Content

Licensed Content Publisher Elsevier
Licensed Content Publication Nano Energy
Licensed Content Title On the first principle theory of nanogenerators from Maxwell's equations
Licensed Content Author Zhong Lin Wang
Licensed Content Date Feb 1, 2020
Licensed Content Volume 68
Licensed Content Issue n/a
Licensed Content Pages 1

Order Details

Type of Use reuse in a thesis/dissertation
Portion figures/tables/illustrations
Number of figures/tables/illustrations 1
Format electronic
Are you the author of this Elsevier article? No
Will you be translating? No

About Your Work

Title Organic-Inorganic Nanomaterial based Highly Efficient Flexible Nanogenerator for Self-powered Wireless Electronics
Institution name University of Waterloo
Expected presentation date Apr 2023

Additional Data

Portions Figure 5

📍 Requestor Location		📄 Tax Details	
Requestor Location	University of Waterloo 200 University Avenue West University of Waterloo	Publisher Tax ID	GB 494 6272 12
	Waterloo, ON N2L 3G1 Canada Attn: University of Waterloo		
\$ Price			
Total	0.00 CAD		
			Total: 0.00 CAD
CLOSE WINDOW		ORDER MORE	

© 2023 Copyright - All Rights Reserved | Copyright Clearance Center, Inc. | Privacy statement | Data Security and Privacy
 | For California Residents | Terms and ConditionsComments? We would like to hear from you. E-mail us at
 customercare@copyright.com



?
Help ▾

🗨️
Live Chat

Publisher: John Wiley and Sons

© 2017 The Authors. Published by WILEY-VCH Verlag GmbH & Co. KGaA, Weinheim

Open Access Article

This is an open access article distributed under the terms of the [Creative Commons CC BY](#) license, which permits unrestricted use, distribution, and reproduction in any medium, provided the original work is properly cited.

You are not required to obtain permission to reuse this article.

For an understanding of what is meant by the terms of the Creative Commons License, please refer to [Wiley's Open Access Terms and Conditions](#).

Permission is not required for this type of reuse.

Wiley offers a professional reprint service for high quality reproduction of articles from over 1400 scientific and medical journals. Wiley's reprint service offers:

- Peer reviewed research or reviews
- Tailored collections of articles
- A professional high quality finish
- Glossy journal style color covers
- Company or brand customisation
- Language translations
- Prompt turnaround times and delivery directly to your office, warehouse or congress.

Please contact our Reprints department for a quotation. Email corporatesaleseurope@wiley.com or corporatesalesusa@wiley.com or corporatesalesDE@wiley.com.

Porosity Modulated High-Performance Piezoelectric Nanogenerator Based on Organic/Inorganic Nanomaterials for Self-Powered Structural Health Monitoring



Author: Md Masud Rana, Asif Abdullah Khan, Guangguang Huang, et al

Publication: Applied Materials

Publisher: American Chemical Society

Date: Oct 1, 2020

Copyright © 2020, American Chemical Society

PERMISSION/LICENSE IS GRANTED FOR YOUR ORDER AT NO CHARGE

This type of permission/license, instead of the standard Terms and Conditions, is sent to you because no fee is being charged for your order. Please note the following:

- Permission is granted for your request in both print and electronic formats, and translations.
- If figures and/or tables were requested, they may be adapted or used in part.
- Please print this page for your records and send a copy of it to your publisher/graduate school.
- Appropriate credit for the requested material should be given as follows: "Reprinted (adapted) with permission from {COMPLETE REFERENCE CITATION}. Copyright (YEAR) American Chemical Society." Insert appropriate information in place of the capitalized words.
- One-time permission is granted only for the use specified in your RightsLink request. No additional uses are granted (such as derivative works or other editions). For any uses, please submit a new request.

If credit is given to another source for the material you requested from RightsLink, permission must be obtained from that source.



Enhanced piezoelectricity in lead-free halide perovskite nanocomposite for self-powered wireless electronics

Author: Md Masud Rana,Asif Abdullah Khan,Weiguang Zhu,Md Fahim Al Fattah,Sathursan Kokilathanan,Shazzad Rassel,Rozenn Bernard,Soraya Ababou-Girard,Pascal Turban,Shuhong Xu,Chunlei Wang,Dayan Ban

Publication: Nano Energy

Publisher: Elsevier


Date: October 2022

© 2022 Elsevier Ltd. All rights reserved.

Journal Author Rights

Please note that, as the author of this Elsevier article, you retain the right to include it in a thesis or dissertation, provided it is not published commercially. Permission is not required, but please ensure that you reference the journal as the original source. For more information on this and on your other retained rights, please visit: <https://www.elsevier.com/about/our-business/policies/copyright#Author-rights>

BACK CLOSE WINDOW



Natural lignocellulosic nanofibrils as tribonegative materials for self-powered wireless electronics

Author: Nicolas R. Tanguy,Masud Rana,Asif A. Khan,Xiao Zhang,Nicole Tratnik,Heyu Chen,Dayan Ban,Ning Yan

Publication: Nano Energy

Publisher: Elsevier

Date: July 2022

© 2022 Elsevier Ltd. All rights reserved.

Journal Author Rights

Please note that, as the author of this Elsevier article, you retain the right to include it in a thesis or dissertation, provided it is not published commercially. Permission is not required, but please ensure that you reference the journal as the original source. For more information on this and on your other retained rights, please visit: <https://www.elsevier.com/about/our-business/policies/copyright#Author-rights>

BACK CLOSE WINDOW

References

- [1] C. Li, R. Cao, X. Zhang, *Appl. Sci.* **2018**, 8, 1–12.
- [2] K. Zhao, Y. Wang, L. Han, Y. Wang, X. Luo, Z. Zhang, Y. Yang, *Nano-Micro Lett.* **2019**, 11, 19.
- [3] G. Chen, Y. Li, M. Bick, J. Chen, *Chem. Rev.* **2020**, 120, 3668–3720.
- [4] Z. L. Wang, W. Wu, *Angew. Chem. Int. Ed.* **2012**, 51, 11700 – 1172.
- [5] F. R. Fan, W. Tang, Z. L. Wang, *Adv. Mater.* **2016**, 28, 4283–4305.
- [6] H. Askaria, E. Hashemia, A. Khajepoura, M. B. Khamessea, Z. L. Wang, *Nano Energy*, **2018**, 53, 1003–1019.
- [7] Y. Suab, X. Wena, G. Zhua, J. Yang, J. Chen, P. Bai, Z. Wu, Y. Jiang, Z. L. Wang, *Nano Energy*, **2014**, 9, 186–195.
- [8] J. A. Paradiso, T. Starner, *IEEE Pervasive Computing*, **2005**, 4, 18-27.
- [9] C. Thomas, M. Greenstone, C. R. Knittel, *Journal of Economic Perspectives*, **2016**, 30, 117-138.
- [10] S. J. Park, S. H. Lee, M. L. Seol, S. B. Jeon, H. Bae, D. Kim, G. H. Cho, Y. K. Choi, *Nano Energy*, **2019**, 55, 115-122.
- [11] H. Tian, S. Ma, H. M. Zhao, C. Wu, J. Ge, D. Xie, Y. Yang, T.L. Ren, *Nanoscale*, **2013**, 5, 8951.
- [12] P. D. Mitcheson, P. Miao, B. H. Stark, E. M. Yeatman, A. S. Holmes, T. C. Green, *Sens. Actuators A Phys.* **2004**, 115, 523.
- [13] M. P. Lu, J. Song, M.Y. Lu, M. T. Chen, Y. Gao, L. J. Chen, Z. L. Wang, *Nano Lett.* **2009**, 9, 1223.
- [14] M. L. Seol, H. Im, D. I. Moon, J. H. Woo, D. Kim, S. J. Choi, Y. K. Choi, *ACS Nano*, **2013**, 7, 10773.
- [15] V. Misra, A. Bozkurt, B. Calhoun, T. Jackson, J.S. Jur, J. Lach, B. Lee, J. Muth, Ö. Oralkan, M. Öztürk, S. Trolier-McKinstry, D. Vashaee, D. Wentzloff, Y. Zhu, *Proc. IEEE.* **2015**, 103, 665–681.
- [16] A. Proto, M. Penhaker, S. Conforto, M. Schmid, *Trends Biotechnol.* **2017**, 35, 610–624.
- [17] T.R. Ray, J. Choi, A.J. Bandodkar, S. Krishnan, P. Gutruf, L. Tian, R. Ghaffari, J.A. Rogers, *Chem. Rev.* **2019**, 119, 5461–5533.

- [18] S. Wang, L. Lin, Z.L. Wang, Triboelectric nanogenerators as self-powered active sensors, *Nano Energy*. **2015**, 11, 436–462.
- [19] H. Zhang, Y. Yang, Y. Su, J. Chen, K. Adams, S. Lee, C. Hu, Z.L. Wang, *Adv. Funct. Mater.* **2014**, 24, 1401–1407.
- [20] K. Il Park, J.H. Son, G.T. Hwang, C.K. Jeong, J. Ryu, M. Koo, I. Choi, S.H. Lee, M. Byun, Z.L. Wang, K.J. Lee, *Adv. Mater.* **2014**, 26, 2514–2520.
- [21] J.H. Bahk, H. Fang, K. Yazawa, A. Shakouri, *J. Mater. Chem. C* **2015**, 3, 10362–10374.
- [22] A.J. Bandodkar, I. Jeerapan, J.M. You, R. Nuñez-Flores, J. Wang, *Nano Lett.* **2016**, 16, 721–727.
- [23] M. Bernechea, N.C. Miller, G. Xercavins, D. So, A. Stavrinadis, G. Konstantatos, *Nat. Photonics*. **2016**, 10, 521–525.
- [24] S. Kim, M.K. Gupta, K.Y. Lee, A. Sohn, T.Y. Kim, K.S. Shin, D. Kim, S.K. Kim, K.H. Lee, H.J. Shin, D.W. Kim, S.W. Kim, *Adv. Mater.* **2014**, 26, 3918–3925.
- [25] X. Pu, M. Liu, X. Chen, J. Sun, C. Du, Y. Zhang, J. Zhai, W. Hu, Z.L. Wang, *Sci. Adv.* **2017**, 3, 1–11.
- [26] S.S. Won, M. Sheldon, N. Mostovych, J. Kwak, B.S. Chang, C.W. Ahn, A.I. Kingon, I.W. Kim, S.H. Kim, *Appl. Phys. Lett.* **2015**, 107, 151101.
- [27] B. Yang, K.S. Yun, *Sensors Actuators, A Phys.* **2012**, 188, 427–433.
- [28] Z. L. Wang, J. Song, *Science*, **2006**, 312, 24.
- [29] F. Fan, Z. Tian, Z. L. Wang, *Nano Energy*, **2012**, 1, 328.
- [30] S. R. Anton, H. A. Sodano, *Smart Mater. Struct.* **2007**, 16, 1-21.
- [31] X. Wang, *Nano Energy*, **2012**, 1, 13–24.
- [32] J. Briscoe, S. Dunn, *Nano Energy*, **2015**, 14, 15–29.
- [33] Z. L. Wang, G. Zhu, Y. Yang, S. Wang, C. Pan, *Materials Today*, **2012**, 15, 532-543.
- [34] Z. L. Wang, J. Chen, L. Lin, *Energy Environ. Sci.* **2015**, 8, 2250-2282.
- [35] R. Hinchet, W. Seung, S. W. Kim, *Chem Sus Chem*, **2015**, 8, 2327 –2344.
- [36] Z. L. Wang, *Faraday Discuss.* **2014**, 176, 447-458.
- [37] M. Ma, Z. Kang, Q. Liao, Q. Zhang, F. Gao, X. Zhao, Z. Zhang, Y. Zhang, *Nano Res.* **2018**, 11, 2951–2969.
- [38] Z. L. Wang, T. Jiang, L. Xu, *Nano Energy*, **2017**, 39, 9–23.
- [39] X. Cao, Y. Jie, N. Wang, Z. L. Wang, *Adv. Energy Mater.* **2016**, 6, 1600665.

- [40] S. Lu, Q. Liao, J. Qi, S. Liu, Y. Liu, G. Zhang, Y. Zhang, *Nano Res.* **2016**, 9, 372.
- [41] Y. Su, K. Gupta, Y. Hsiao, R. Wang and C. Liu, *Energy Environ. Sci.* **2019**, 12, 410.
- [42] X. Yuan, X. Gao, J. Yang, X. Shen, Z. Li, S. You, Z. Wang and S. Dong, *Energy Environ. Sci.* **2020**, 13, 152.
- [43] K. Zhang, S. Wang and Y. Yang, *Adv. Energy Mater.* **2017**, 7, 1601852.
- [44] Y. Qi and M. C. Mcalpine, *Energy Environ. Sci.* **2010**, 3, 1275.
- [45] R. S. Yang, Y. Qin, L. M. Dai and Z. L. Wang, *Nat. Nanotechnology.* **2009**, 4, 34.
- [46] M. Y. Choi, D. Choi, M. J. Jin, I. Kim, S. H. Kim, J. Y. Choi, S. Y. Lee, J. M. Kim and S. W. Kim, *Adv. Mater.* **2009**, 21, 2185.
- [47] Zhu Z. et al., *Adv. Mater.* **2014**, 26, 3788.
- [48] Y. Zi, C. Wu, W. Ding, Z. L. Wang, *Adv. Funct. Mater.* **2017**, 27, 1700049.
- [49] Z. L. Wang, *Nano Energy*, **2020**, 68, 104272.
- [50] Z. L. Wang, *Materials Today*, **2017**, 20, 74.
- [51] Q. Zheng, B. Shi, Z. Li, and Z. L. Wang, *Adv. Sci.* **2017**, 4, 1700029.
- [52] Z. L. Wang, *Adv. Mater.* **2009**, 21, 1311–1315.
- [53] F.R. Fan, W. Tang, Z.L. Wang, *Adv Mater.* **2016**, 28, 4283-4305.
- [54] Y. Lin, J. Song, Y. Ding, S. Lu, Z.L. Wang, Piezoelectric nanogenerator using CdS nanowires, *Appl. Phys. Lett.* **2008**, 92, 022105.
- [55] L. Lin, C. Lai, Y. Hu, Y. Zhang, X. Wang, C. Xu, R.L. Snyder, L. Chen, Z.L. Wang, *Nanotechnology.* **2011**, 22, 475401.
- [56] H. You, X. Ma, Z. Wu, L. Fei, X. Chen, J. Yang, Y. Liu, Y. Jia, H. Li, F. Wang, *Nano Energy.* **2018**, 52, 351-359.
- [57] C. Chang, V.H. Tran, J. Wang, Y. Fuh, L. Lin, *Nano letters.* **2010**, 10, 726-731.
- [58] I. Fujii, K. Nakashima, N. Kumada, S. Wada, *Journal of the Ceramic Society of Japan.* **2012**, 120, 30-34.
- [59] J. Ma, Z. Shi, C. Nan, *Adv Mater.* **2007**, 19, 2571-2573.
- [60] C. Huang, J. Song, C. Tsai, W. Lee, D. Lien, Z. Gao, Y. Hao, L. Chen, Z.L. Wang, *Adv Mater.* **2010**, 22, 4008-4013.
- [61] Z. WANG, *SCIENTIA SINICA Chimica.* **2013**, 43, 759-762.
- [62] X. Wang, J. Song, J. Liu, Z.L. Wang, Direct-current nanogenerator driven by ultrasonic waves, *Science.* **2007**, 316, 102-105.

- [63] Y. Qin, X. Wang, Z.L. Wang, *Nature*. **2008**, 451, 809-813.
- [64] J. Zhang, M. Li, L. Yu, L. Liu, H. Zhang, Z. Yang, *Applied Physics A*. **2009**, 97, 869.
- [65] C. Xu, X. Wang, Z.L. Wang, *J. Am. Chem. Soc.* **2009**, 131, 5866-5872.
- [66] B. Saravanakumar, R. Mohan, K. Thiyagarajan, S. Kim, *RSC Advances*. **2013**, 3, 16646-16656.
- [67] R. Yang, Y. Qin, L. Dai, Z.L. Wang, *Nature nanotechnology*. **2009**, 4, 34.
- [68] Z. Zhou, H. Tang, H.A. Sodano, *Adv Mater*. **2014**, 26, 7547-7554.
- [69] N.R. Alluri, A. Chandrasekhar, V. Vivekananthan, Y. Purusothaman, S. Selvarajan, J.H. Jeong, S. Kim, *ACS Sustainable Chemistry & Engineering*. **2017**, 5, 4730-4738.
- [70] M.H. Malakooti, F. Julé, H.A. Sodano, *ACS applied materials & interfaces*. **2018**, 10, 38359-38367.
- [71] Z. Yang, S. Zhou, J. Zu, D. Inman, *Joule*, **2018**, 2, 642–697.
- [72] Y. You, W. Liao, D. Zhao, H. Ye, Y. Zhang, Q. Zhou, X. Niu, J. Wan, *Science*, **2017**, 357, 306.
- [73] M. T. Todaro, F. Guido, L. Algieri, V. M. Mastronardi, D. Desmaele, G. Epifani, and M. D. Vittorio, *IEEE TRANSACTIONS ON NANOTECHNOLOGY*, **2018**, 17, 02.
- [74] Z. L. Wang, *Nano Today*, **2010**, 5, 540.
- [75] A. I. Hochbaum and P. Yang, *Chem. Rev.* **2010**, 110, 527-546.
- [76] T. I. Lee, S. Lee, E. Lee, S. Sohn, Y. Lee, S. Lee, et al., *Adv. Mater.* **2013**, 25, 2920-2925.
- [77] Z. L. Wang, *Adv. Mater.* **2012**, 24, 4632-4646.
- [78] B. Gil, *Oxford University Press*, **2013**, 18.
- [79] X. Wang, J. Song, F. Zhang, C. He, Z. Hu, and Z. Wang, *Adv. Mater.* **2010**, 22, 2155-2158.
- [80] V. Polyakov, F. Schwierz, F. Fuchs, J. Furthmüller, and F. Bechstedt, *Appl. Phys. Lett.* **2009**, 94, 022102.
- [81] X. Wang, S. Liu, N. Ma, L. Feng, G. Chen, F. Xu, et al., *Appl. Phys. Exp.* **2012**, 5, 015502.
- [82] S. Wang, H. Liu, B. Gao, and H. Cai, *Appl. Phys. Lett.* **2012**, 100, 142105.
- [83] J. Wu, *J. Appl. Phys.* **2009**, 106, 011101.
- [84] G. Liu, S. Zhao, R. D. E. Henderson, Z. Leonenko, E. A. Rahman, Z. Mi, and D. Ban, *Nanoscale* **2016**, 8, 2097.
- [85] S. Zhao, S. Fatholouloumi, K. Bevan, D. Liu, M. Kibria, Q. Li, et al., *Nano lett.* **2012**, 12, 2877-2882.

- [86] S. Zhao, B. Le, D. Liu, X. Liu, M. Kibria, T. Szkopek, et al., *Nano Lett.* **2013**, 13, 5509-5513.
- [87] A. Mahmud, A. A. Khan P. Voss, T. Das, E. Abdel-Rahman and D. Ban, *Adv. Mater. Interfaces* **2018**, 5, 1801167.
- [88] H. Park, C. Ha and J-H. Lee, *J. Mater. Chem. A*, **2020**, 8, 24353-24367
- [89] G.A. Schneider, *Annu Rev Mater Res*, **2008**, 37, 491-538.
- [90] W. Li, Z. Wang, F. Deschler, S. Gao, R. H. Friend and A. K. Cheetham, *Nat. Rev. Mater.*, **2017**, 2, 16099.
- [91] G. Huang, C. Wang, H. Zhang, S. Xu, Q. Xu and Y. Cui, *J. Mater. Chem. A*, **2018**, 6, 2449.
- [92] Y. Li, X. Zhang, H. Huang, S. V. Kershaw and A. L. Rogach, *Mater. Today*, **2020**, 32, 204.
- [93] M. Coll, A. Gomez, E. M. Marsa, O. Almora, G. G. Belmonte, M. C. Quiles, J. Bisquert, *J. Phys. Chem. Lett.* **2015**, 6, 1408.
- [94] Y. J. Kim, T. V. Dang, H. J. Choi, B. J. Park, J. H. Eom, H. A. Song, D. Seol, Y. Kim, S. H. Shin, H. Nah, S. G. Yoon, *J. Mater. Chem. A* **2016**, 4, 756.
- [95] A. A. Khan, G. Huang, M. M. Rana, N. Mei, M. Biondi, S. Rassel, N. Tanguy, B. Sun, Z. Leonenko, N. Ying, C. Wang, S. Xu, D. Ban. *Nano energy*, **2021**. 86, 106039.
- [96] V. Jella et.al, *Nano Energy*, **2019**, 57, 74-93
- [97] R. Ding, H. Liu, X. Zhang, J. Xiao, R. Kishor, H. Sun, B. Zhu, G. Chen, F. Gao, X. Feng, J. Chen, X. Chen, X. Sun and Y. Zheng, *Adv. Funct. Mater.*, **2016**, 26, 7708.
- [98] R. Ding, X. Zhang, G. Chen, H. Wang, R. Kishor, J. Xiao, F. Gao, K. Zeng, X. Chen, X. W. Sun and Y. Zheng, *Nano Energy*, **2017**, 37, 126.
- [99] V. Jella, S. Ippili, J.-H. Eom, J. Choi and S.-G. Yoon, *Nano Energy*, **2018**, 53, 46.
- [100] A. A. Khan, M. M. Rana, G. Huang, N. Mei, R. Saritas, B. Wen, S. Zhang, P. Voss, E.-A. Rahman, Z. Leonenko, S. Islam and D. Ban, *J. Mater. Chem. A*, **2020**, 8, 13619.
- [101] R. Pandey, G. Sb, S. Grover, S. K. Singh, A. Kadam, S. Ogale, U. V. Waghmare, V. R. Rao and D. Kabra, *ACS Energy Lett.*, **2019**, 4, 1004.
- [102] S. Ippili, V. Jella, J. Kim, S. Hong and S.-G. Yoon, *Nano Energy*, **2018**, 49, 247.
- [103] I. Chung, B. Lee and J. Q. He, et al., *Nature*, **2012**, 485, 486
- [104] H.-S. Kim, C.-R. Lee and J.-H. Im, et al., *Sci. Rep.*, **2012**, 2, 591
- [105] A. Abate, Perovskite Solar Cells Go Lead Free, *Joule*, **2017**, 1, 659–664
- [106] S. Chatterjee and A. J. Pal, *J. Mater. Chem. A*, **2018**, 6, 3793–3823

- [107] H. Liu, X. Lin, S. Zhang, Y. Huan, Sh. Huang and X. Cheng, *J. Mater. Chem. A*, **2020**, 8, 19631-19640.
- [108] F. Narita, M. Fox, *Adv. Eng. Mater.*, **2018**, 20, 5.
- [109] X. Yang, G. Hu, G. Gao, X. Chen, J. Sun, B. Wan, Q. Zhang, S. Qin, W. Zhang, C. Pan, Q. Sun, Z. L. Wang, *Adv. Funct. Mater.* **2019**, 29, 1807837.
- [110] Z. W. Xiao, Z. N. Song and Y. F. Yan, *Adv. Mater.*, **2019**, 1803792
- [111] S. Wang, L. Lin, and Z. L. Wang, *Nano Lett.* **2012**, 12, 6339.
- [112] X. Zhang, M. Han, R. Wang, F. Zhu, Z. Li, W. Wang, and H. Zhang, *Nano Lett.* **2013**, 13, 1168.
- [113] C. Wu, A. C. Wang, W. Ding, H. Guo, Z. L. Wang, *Adv. Energy Mater.* **2019**, 9, 1802906.
- [114] Wang, Z.L. *ACS Nano* **2013**, 7, 9533–9557
- [115] Davies, D.K. *J. Phys. D Appl. Phys.* **1969**, 2, 1533–1537
- [116] Zhu, G.; Pan, C.; Guo, W.; Chen, C.Y.; Zhou, Y.; Yu, R.; Wang, Z.L. *Nano Lett.* **2012**, 12, 4960–4965.
- [117] Zhu, G.; Lin, Z.H.; Jing, Q.; Bai, P.; Pan, C.; Yang, Y.; Zhou, Y.; Wang, Z.L. *Nano Lett.* **2013**, 13, 847–853.
- [118] Yun, B.K.; Kim, J.W.; Kim, H.S.; Jung, K.W.; Yi, Y.; Jeong, M.S.; Ko, J.H.; Jung, J.H. *Nano Energy* **2015**, 15, 523–529
- [119] Hu, Y.; Yang, J.; Jing, Q.; Niu, S.; Wu, W.; Wang, Z.L. *ACS Nano* **2013**, 7, 10424–10432.
- [120] Chen, J.; Zhu, G.; Yang, W.; Jing, Q.; Bai, P.; Yang, Y.; Hou, T.C.; Wang, Z.L. *Adv. Mater.* **2013**, 25, 6094–6099.
- [121] Cheng, G.; Lin, Z.H.; Lin, L.; Du, Z.L.; Wang, Z.L. *ACS Nano* **2013**, 7, 7383–7391
- [122] 104. Yang, W.; Chen, J.; Jing, Q.; Yang, J.; Wen, X.; Su, Y.; Zhu, G.; Bai, P.; Wang, Z.L. *Adv. Funct. Mater.* **2014**, 24, 4090–4096
- [123] 105. Lin, Z.H.; Cheng, G.; Lee, S.; Pradel, K.C.; Wang, Z.L. *Adv. Mater.* **2014**, 26, 4690–4696.
- [124] Xie, Y.; Wang, S.; Niu, S.; Lin, L.; Jing, Q.; Yang, J.; Wu, Z.; Wang, Z.L. *Adv. Mater.* **2014**, 26, 6599–6607
- [125] T.; Cheng, G.; Lin, Z.; Du, Z.; Wang, Z.L. *ACS Nano* **2014**, 8, 1932–1939.
- [126] Shi, L.; Dong, S.; Ding, P.; Chen, J.; Liu, S.; Huang, S.; Xu, H.; Farooq, U.; Zhang, S.; Li, S.; et al. *Nano Energy* **2019**, 55, 548–557.

- [127] C. X. Lu, C. B. Han, G. Q. Gu, J. Chen, Z. W. Yang, T. Jiang, C. He, Z. L. Wang, *Adv. Eng. Mater.* **2017**, 19, 1700275.
- [128] J. Wang, C. Wu, Y. Dai, Z. Zhao, A. Wang, T. Zhang, Z. L. Wang, *Nat. Commun.* **2017**, 8, 88.
- [129] X. Chen, K. Parida, J. Wang, J. Xiong, M. F. Lin, J. Shao, P. S. Lee, *ACS Appl. Mater. Interfaces* **2017**, 9, 42200.
- [130] A. Danish, Y. Bin, D. Xiaochao, Y. Hao, Z. Meifang, *Nanotechnology*, **2017**, 28, 075203.
- [131] J. Chen, H. Guo, X. He, G. Liu, Y. Xi, H. Shi, C. Hu, *ACS Appl. Mater. Interfaces* **2016**, 8, 736.
- [132] N. Cui, L. Gu, Y. Lei, J. Liu, Y. Qin, X. Ma, Y. Hao, Z. L. Wang, *ACS Nano*, **2016**, 10, 6131.
- [133] A. Chen, C. Zhang, G. Zhu, Z.L. Wang, *Adv. Sci.* **2020**, 7, 1–25.
- [134] R. Zhang, H. Olin, *EcoMat*, **2020**, 2, 1–13.
- [135] G. Grau, R. Kitsomboonloha, S.L. Swisher, H. Kang, V. Subramanian, *Adv. Funct. Mater.* **2014**, 24, 5067–5074
- [136] W. Lim, E.A. Douglas, S.H. Kim, D.P. Norton, S.J. Pearton, F. Ren, H. Shen, W. H. Chang, *Appl. Phys. Lett.* **2009**, 94, 7–9
- [137] Y.Z. Zhang, Y. Wang, T. Cheng, W.Y. Lai, H. Pang, W. Huang, *Chem. Soc. Rev.* **2015**, 44, 5181–5199
- [138] K.H. Choi, J.T. Yoo, C.K. Lee, S.Y. Lee, *Energy Environ. Sci.* **2016**, 9, 2812–2821
- [139] S. Leijonmarck, A. Cornell, G. Lindbergh, L. Wågberg, *J. Mater. Chem. A.* **2013**, 1, 4671–4677
- [140] L. Hu, H. Wu, F. La Mantia, Y. Yang, Y. Cui, *ACS Nano*, **2010**, 4, 5843–5848
- [141] N.R. Tanguy, K. Khorsand Kazemi, J. Hong, K.-C. Cheung, S. Mohammadi, P. Gnanasekar, S.S. Nair, M.H. Zarifi, N. Yan, *Carbohydr. Polym.* **2021**, 278, 118920,
- [142] Y. Wang, C. Yan, S.Y. Cheng, Z.Q. Xu, X. Sun, Y.H. Xu, J.J. Chen, Z. Jiang, K. Liang, Z.S. Feng, *Adv. Funct. Mater.* **2019**, 29, 1–11
- [143] A. Rida, L. Yang, R. Vyas, M.M. Tentzeris, *IEEE Antennas Propag. Mag.* **2009**, 51, 13–23
- [144] D. Tobjörk, R. Österbacka, *Adv. Mater.* **2011**, 23, 1935–1961
- [145] Y. Bao, R. Wang, Y. Lu, W. Wu, *APL Materials*, **2017**, 5, 074109
- [146] C. Yao, X. Yin, Y. Yu, Z. Cai, X. Wang, *Adv. Funct. Mater.* **2017**, 27, 1–7
- [147] D. Hu, M. Yao, Y. Fan, C. Ma, M. Fan, M. Liu, *Nano Energy.* **2019**, 55, 288–304.

- [148] Z. Pi, J. Zhang, C. Wen, Z. bin Zhang, D. Wu, *Nano Energy*. **2014**, 7, 33–41.
- [149] T. Men, X. Liu, B. Jiang, X. Long, H. Guo, *Thin Solid Films*. **2019**, 669, 579–587.
- [150] J.M. Yun, J.H. Shin, J. Ryu, N.M. Shinde, K.H. Kim, *Adv. Sustain. Syst.* **2018**, 2, 1700133.
- [151] C.K. Jeong, C. Baek, A.I. Kingon, K. Il Park, S.H. Kim, *Small*. **2018**, 14, 1–8.
- [152] G. Liu, E. A. Rahman, D. Ban, *J. Appl. Phys.* **2015**, 118, 094307.
- [153] Y. Mao, P. Zhao, G. McConohy, H. Yang, Y. Tong, and X. Wang, *Adv. Energy Mater.* **2014**, 4, 1301624.
- [154] Qing, X.; Li, W.; Wang, Y.; and Sun, H. *Sensors* **2019**, 19, 545.
- [155] Alibadi, M. H. F.; Khodaei, Z. S. *World Scientific Publishing Europe Ltd. London, UK*, **2018**
- [156] Staszewski, W.; Mahzan, S.; and Traynor, R. *Compos. Sci. Technol.* **2009**, 69, 1678–1685.
- [157] Qiu, L.; Yuan, S.; Boller, C. *Struct. Health Monit.* **2017**, 16, 501–517.
- [158] Le, M. Q.; Capsal, J. F.; Lallart, M.; Hebrard, Y.; Ham, A. V. D.; Reffe, N.; Geynet, L.; and Cottinet, P. J. *Prog. Aerosp. Sci.* **2015**, 79, 147-157.
- [159] Chen, J; Guo, H; Liu, G Xue Wang, X; Xi, Y; Javed, M. S; Hu, C. *Nano Energy* **2017**, 33, 508-514.
- [160] Sun, C.; Shi, J.; Bayerl, D. J.; and Wang, X. *Energy Environ. Sci.* **2011**, 4, 11, 4508–4512.
- [161] Jang, S.; Kim, H.; Kim, Y.; Kang B. J.; and Oh, J. H. *Appl. Phys. Lett.* **2016**, 108, 14, 143901.
- [162] Kumar, C.; Gaur, A.; Tiwari, S.; Biswas, A.; Rai, S. K.; and Maiti, P. *Composites Communications* **2019**, 11, 56–61.
- [163] Won, S. S.; Sheldon, M.; Mostovych, N.; Kwak, J.; Chang, B. S.; Ahn, C. W.; Kingon, A. I.; Kim I. W.; and Kim, S. H. *Appl. Phys. Lett.* **2015**, 107, 20, 202901.
- [164] Huang, L. B.; Xu, W.; Bai, G.; Wong, M. C.; Yang, Z.; Hao, J. *Nano Energy* **2016**, 30, 36–42.
- [165] Xiao, T. X.; Liang, X.; Jiang, T.; Xu, L.; Shao, J. J.; Nie, J. H.; Bai, Y.; Zhong, W.; Wang, Z. L. *Adv. Funct. Mater.* **2018**, 28, 1802634.
- [166] Quan, T.; Wang, Z. L.; and Yang, Y. *ACS Appl. Mater. Interfaces* **2016**, 8, 19573–19578.
- [167] Saha, C. R.; O'Donnell, T.; Wang, N.; McCloskey, P. *Sens. Actuators A Phys.* **2008**, 147, 248-253.
- [168] Beeby, S. P.; Torah, R. N.; Tudor, M. J.; Glynne-Jones, P.; O'Donnell, T.; Saha, C. R.; Roy, S. *J. Micromech. Microeng.* **2007**, 17, 1257-1265.
- [169] Mitcheson, P. D.; Miao, P.; Stark, B. H.; Yeatman, E. M.; Holmes, A. S.; Green, T. C. *Sens. Actuators A Phys.* **2004**, 115, 523-529.

- [170] Tian, H.; Ma, S.; Zhao, H. M.; Wu, C.; Ge, J.; Xie, D.; Yang, Y.; Ren, T. L. *Nanoscale* **2013**, 5, 8951-8957.
- [171] Wang, Z. L.; Song, J. *Science*. **2006**, 312, 242-246.
- [172] Fan, F. R.; Tian, Z. Q.; Wang, Z. L. *Nano Energy* **2012**, 1, 328-334.
- [173] Liu, W.; Wang, Z.; Wang, G.; Liu, G.; Chen, J.; Pu, X.; Xi, Y.; Wang, X.; Guo, H.; Hu, C.; Wang, Z.L. *Nat. Commun.* **2019**, 10, 1426.
- [174] Khan, A. A.; Mahmud, A.; Zhang, S.; Islam, S.; Voss, P.; Ban, D. *Nano Energy* **2019**, 62, 691-699.
- [175] Kang, Y.; Wang, B.; Dai, S.; Liu, G.; Pu, Y.; Hu, C. *ACS Appl. Mater. Interfaces* **2015**, 36, 20469-20476.
- [176] Nie, J.; Ren, Z.; Shao, J.; Deng, C.; Xu, L.; Chen, X.; Li, M.; Wang, Z. L. *ACS Nano* **2018**, 12, 491-499.
- [177] Qin, Z.; Yin, Y.; Zhang, W.; Li, C.; and Pan, K. *ACS Appl. Mater. Interfaces* **2019**, 11, 12452–12459.
- [178] Cao, X.; Zhang, M.; Huang, J.; Jiang, T.; Zou, J.; Wang, N.; Wang, Z. L. *Adv. Mater.* **2018**, 30, 1704077.
- [179] Huang, L. B.; Xu, W.; Zhao, C.; Zhang, Y. L.; Yung, K. L.; Diao, D.; Fung, K. H.; and Hao, J. *ACS Appl. Mater. Interfaces* **2020**, 12, 24030–24038
- [180] Wang, H. S.; Jeong, C. K.; Seo, M. H.; Joe, D. J.; Han, J. H.; Yoon, J. B.; Lee, K. J. *Nano Energy* **2017**, 35, 415-423.
- [181] Li, S.; Wang, J.; Peng, W.; Lin, L.; Zi, Y.; Wang, S.; Zhang, G.; Wang, Z. L. *Adv. Energy Mater.* **2017**, 7, 1602832.
- [182] Chen, J.; Guo, H.; He, X.; Liu, G.; Xi, Y.; Shi, H.; Hu, C. *ACS Appl. Mater. Interfaces* **2016**, 8, 736–744.
- [183] Huang, L. B.; Xu, W.; Tian, W.; Han, J. C.; Zhao, C. H.; Wu, H. L.; Hao, J. *Nano Energy*, **2020**, 71, 104593.
- [184] Zhou, T.; Zhang, C.; Han, C. B.; Fan, F. R.; Tang, W.; and Wang, Z. L. *ACS Appl. Mater. Interfaces* **2014**, 6, 14695–14701.
- [185] Guan, X.; Xu, B.; Gong, J. *Nano Energy*, **2020**, 70, 104516.

- [186] Khan, A. A.; Rana, M. M.; Huang, G.; Mei, N.; Saritas, R.; Wen, B.; Zhang, S.; Voss, P.; Rahman, E-A.; Leonenko, Z.; Islam, S.; and Ban, D. *J. Mater. Chem. A* **2020**, 8, 13619-13629.
- [187] Maity K.; and Manda, D. *ACS Appl. Mater. Interfaces*, **2018**, 10, 18257–18269.
- [188] Hu, C.; Cheng, L.; Wang, Z.; Zheng, Y.; Bai, S.; and Qin, Y, *Small*, **2016**, 12, 10, 1315–1321.
- [189] Lee, E. J.; Kim, T. Y.; Kim, S. W.; Jeong, S.; Choi Y.; and Lee, S. Y. *Energy Environ. Sci.* **2018**, 11, 1425—1430.
- [190] Park, K. I.; Son, J. H.; Hwang, G. T.; Jeong, C. K.; Ryu, J.; Koo, M.; Choi, I.; Lee, S. H.; Byun, M.; Wang, Z. L.; Lee, K. J. *Adv. Mater.* **2014**, 26, 2514–2520.
- [191] Park, K. I.; Xu, S.; Liu, Y.; Hwang, G. T.; Kang, S. J. L.; Wang, Z. L.; Lee, K. J. *Nano Lett.* **2010**, 10, 4939–4943.
- [192] Koka, A.; Sodano, H.A. *Adv. Energy Mater.* **2014**, 4, 1301660.
- [193] Li, J.; Chen, S.; Liu, W.; Fu, R.; Tu, S.; Zhao, Y.; Dong, L.; Yan, B.; and Gu, Y. *J. Phys. Chem. C* **2019**, 123, 11378-11387.
- [194] Park, K. I.; Jeong, C. K.; Ryu, J.; Hwang, G. T.; and Lee, K. J. *Adv. Energy Mater.* **2013**, 3, 12, 1539–1544.
- [195] Yan J.; and Jeong, Y. G. *ACS Appl. Mater. Interfaces*, **2016**, 8, 24, 15700-15709.
- [196] Wu, J. M.; Xu, C.; Zhang, Y.; and Wang, Z. L. *ACS Nano* **2012**, 6, 5, 4335-4340.
- [197] Zhao, C.; Zhang, Q.; Zhang, W.; Du, X.; Zhang, Y.; Gong, S.; Ren, K.; Sun, Q.; Wang, Z. L. *Nano Energy*, **2019**, 57, 440-449.
- [198] Gaur, A.; Shukla, R.; Kumar, B.; Pal, A.; Chatterji, S.; Ranjan R.; and Maiti, P. *Polymer*, **2016**, 97, 362–369.
- [199] Whiter, R. A.; Narayan, V.; and Narayan, S. K. *Adv. Energy Mater.* **2014**, 4, 18, 1400519.
- [200] Paria, S.; Karan, S. K.; Bera, R.; Das, A. K.; Maitra, A.; and Khatua, B. B. *Ind. Eng. Chem. Res.* **2016**, 55, 40, 10671–10680.
- [201] Gaur, A.; Tiwari, S.; Kumar, C.; and Maiti, P. *Nanoscale Advances*, **2019**, 1, 3200-3211.
- [202] Karan, S. K.; Bera, R.; Paria, S.; Das, A. K.; Maiti, S.; Maitra, A.; Khatua, B. B. *Adv. Energy Mater.* **2016**, 6, 1601016.
- [203] Shi, K.; Sun, B.; Huang, X.; Jiang, P. *Nano Energy*, **2018**, 52, 153–162.
- [204] Thakur, P.; Kool, A.; Hoque, N. A.; Bagchi, B.; Khatun, F.; Biswas, P.; Brahma, D.; Roy, S.; Banerjee, S.; Das, S. *Nano Energy*, **2018**, 44, 456–467.

- [205] Chou, X.; Zhu, J.; Qian, S.; Niu, X.; Qian, J.; Hou, X.; Mu, J.; Geng, W.; Cho, J.; He, J.; Xue, C. *Nano Energy*, **2018**, 53, 550-558.
- [206] Lee, G-J. Lee, M-K.; Park, J-J.; Hyeon, D. Y.; Jeong, C. K.; and Park, K-I. *ACS Appl. Mater. Interfaces*, **2019**, 11, 41, 37920–37926.
- [207] Zhong, H.; Xia, J.; Wang, F.; Chen, H.; Wu, H.; Lin, S. *Adv. Funct. Mater.* **2017**, 27, 1604226.
- [208] Chen, X.; Tian, H.; Li, X.; Shao, J.; Ding, Y.; An, N.; Zhou, Y. *Nanoscale*, **2015**, 7, 11536-11544.
- [209] Ghosh, S. K.; Mandal, D. *Nano Energy*, **2018**, 53, 245-257.
- [210] Feng, Y.; Li, W-L.; Xu, D.; Qiao, Y-L.; Yu, Y.; Zhao, Y.; and Fei, W-D. *ACS Appl. Mater. Interfaces*, **2016**, 8, 9231–9241.
- [211] Cha, S. N.; Kim, S. M.; Kim, H.; Ku, J.; Sohn, J. I.; Park, Y. J.; Song, B. G.; Jung, M. H.; Lee, E. K.; Choi, B. L.; Park, J. J.; Wang, Z. L.; Kim, J. M.; Kim, K. *Nano Lett.* **2011**, 11, 5142-5147.
- [212] Bhavanasi, V.; Kusuma, D. Y.; Lee, P. S. *Adv. Energy Mater.* **2014**, 4, 1400723.
- [213] Mao, Y.; Zhao, P.; McConohy, G.; Yang, H.; Tong, Y.; and Wang, X. *Adv. Energy Mater.* **2014**, 4, 130124.
- [214] Yu, Y.; Sun, H.; Orbay, H.; Chen, F.; England, C. G.; Cai, W.; Wang, X. *Nano Energy*, **2016**, 27, 275-281.
- [215] Sun, C.; Shi, J.; Bayerl, D. J.; and Wang, X. *Energy Environ. Sci.* **2011**, 4, 4508-4512.
- [216] Mahmud, A.; Khan, A. A.; Voss, P.; Das, T.; Rahman, E. A.; Ban, D. *Advanced Materials Interfaces*, **2018**, 5, 1801167.
- [217] Chowdhury, A. R.; Abdullah, A. M.; Hussain, I.; Lopez, J.; Cantu, D.; Gupta, S. K.; Mao, Y.; Danti, S.; Uddin, M. J. *Nano Energy*, **2019**, 61, 327-336.
- [218] He, W.; Qian, Y.; Lee, B. S.; Zhang, F.; Rasheed, A.; Jung, J-F.; and Kang, D. J. *ACS Appl. Mater. Interfaces*, **2018**, 10, 44415–44420.
- [219] Mahmud, A.; Khan, A. A.; Islam, S.; Voss, P.; Ban, D. *Nano Energy*, **2019**, 58, 112-120.
- [220] Su, Y. L.; Gupta, K.; Hsiao, Y. L.; Wang, R. C.; and Liu, C. P. *Energy Environ. Sci.* **2019**, 12, 410-417.
- [221] Cai, X.; Lei, T.; Sun, D.; and Lin, L. *RSC Adv.* **2017**, 7, 15382-15389.
- [222] Sui, Y.; Chen, W. T.; Ma, J. J.; Hu, R. H.; and Liu, D. S. *RSC Adv.* **2016**, 6, 7364-7369.

- [223] C. Soci, A. Zhang, B. Xiang, S. A. Dayeh, D. Aplin, J. Park, X. Bao, Y.-H. Lo and D. Wang, *Nano Lett.*, **2007**, 7, 1003
- [224] Y. Qi and M. C. Mcalpine, *Energy Environ. Sci.*, **2010**, 3, 1275
- [225] R. S. Yang, Y. Qin, L. M. Dai and Z. L. Wang, *Nat. Nanotechnol.*, **2009**, 4, 34
- [226] M. Y. Choi, D. Choi, M. J. Jin, I. Kim, S. H. Kim, J. Y. Choi, S. Y. Lee, J. M. Kim and S. W. Kim, *Adv. Mater.*, **2009**, 21, 2185
- [227] T. Xu, X. Ding, Y. Huang, C. Shao, L. Song, X. Gao, Z. Zhang and L. Qu, *Energy Environ. Sci.*, **2019**, 12, 972
- [228] Y. F. Hu, Y. Zhang, C. Xu, L. Lin, R. L. Snyder and Z. L. Wang, *Nano Lett.*, **2011**, 11, 2572.
- [229] C. L. Sun, J. Shi, D. J. Bayerl and X. D. Wang, *Energy Environ. Sci.*, **2011**, 4, 4508
- [230] G.-T. Hwang, H. Park, J.-H. Lee, S. Oh, K.-I. Park, M. Byun, H. Park, G. Ahn, C. K. Jeong, K. No, H. Kwon, S.-G. Lee, B. Joung and K. Jae, *Adv. Mater.*, **2014**, 26, 4880
- [231] S. N. Cha, S. M. Kim, H. Kim, J. Ku, J. I. Sohn, Y. J. Park, B. G. Song, M. H. Jung, E. K. Lee, B. L. Choi, J. J. Park, Z. L. Wang, J. M. Kim, K. Kim, *Nano Lett.* **2011**, 11, 5142
- [232] S. Lu, Q. Liao, J. Qi, S. Liu, Y. Liu, G. Zhang, Y. Zhang, *Nano Res.* **2016**, 9, 372
- [233] J. Li, S. Chen, W. Liu, R. Fu, S. Tu, Y. Zhao, L. Dong, B. Yan, Y. Gu, *J. Phys. Chem. C*, **2019**, 123, 11378
- [234] Z. L. Wang, J. Song, *Science*, **2006**, 312, 242
- [235] Y. Su, K. Gupta, Y. Hsiao, R. Wang and C. Liu, *Energy Environ. Sci.*, **2019**, 12, 410
- [236] Y. Mao, P. Zhao, G. McConohy, H. Yang, Y. Tong, X. Wang, *Adv. Energy Mater.*, **2014**, 4, 1301624
- [237] G. Zhang, P. Zhao, X. Zhang, K. Han, T. Zhao, Y. Zhang, C. K. Jeong, S. Jiang, S. Zhang and Q. Wang, *Energy Environ. Sci.*, **2018**, 11, 2046
- [238] C. R. Bowen, H. A. Kim, P. M. Weaver and S. Dunn, *Energy Environ. Sci.*, **2014**, 7, 25
- [239] D. Chen, K. Chen, K. Brown, A. Hang, J. X. J. Zhang., *Appl. Phys. Lett.*, **2017**, 110, 153902
- [240] Z. Zhang, C. Yao, Y. Yu, Z. Hong, M. Zhi, X. Wang, *Adv. Funct. Mater.* **2016**, 26, 6760

- [241] X. Yuan, X. Gao, J. Yang, X. Shen, Z. Li, S. You, Z. Wang and S. Dong, *Energy Environ. Sci.*, **2020**, 13, 152
- [242] J.-H. Lee, K. Y. Lee, M. K. Gupta, T. Y. Kim, D.-Y. Lee, J. Oh, C. Ryu, W. J. Yoo, C.-Y. Kang, S. -Y. Yoon, J.-B. Yoo, S. -W. Kim, *Adv. Mater.*, **2013**, 26, 765
- [243] J. Zhu, W. Song, F. Ma, H. Wang, *Mater. Res. Bull.*, **2018**, 102, 130
- [244] K. Zhang, S. Wang and Y. Yang, *Adv. Energy Mater.*, **2017**, 7, 1601852
- [245] C.-H. Wang, W.-S. Liao, Z.-H. Lin, N.-J. Ku, Y.-C. Li, Y.-C. Chen, Z. L. Wang, C.-P. Liu, *Adv. Energy Mater.* **2014**, 4, 1400392
- [246] X. Xue, Y. Nie, B. He, L. Xing, Y. Zhang, Z. L. Wang, *Nanotechnology*, **2013**, 24, 22
- [247] Y. Fu, W. Zang, P. Wang, L. Xing, X. Xue, Y. Zhang, *Nano Energy*, **2014**, 8, 34
- [248] S. A. Han, T. -H. Kim, S. K. Kim, K. H. Lee, H. -J. Park, J. -H. Lee, S. -W. Kim, *Adv. Mater.*, **2018**, 30, 1800342
- [249] A. Mahmud, A.A Khan, P. Voss, T. Das, E. Abdel-Rahman, D. Ban, *Adv. Mater. Interfaces*, **2018**, 5, 1801167
- [250] J.H. Jung, M. Lee, J. Hong, Y. Ding, C. Chen, L. Chou, Z.L. Wang, *ACS Nano*, **2011**, 5, 10041
- [251] S. Xu, Y.-W. Yeh, G. Poirier, M. C. Mcalpine, R. A. Register, N. Yao , *Nano Lett.*, **2013**, 13, 2393
- [252] G. Romano, G. Mantini, A. D. Carlo, A. D'Amico, C. Falconi, Z. L. Wang, *Nanotechnology*, **2011**, 22, 465401
- [253] K. I. Park, S. Xu, Y. Liu, G. T. Hwang, S. J. L. Kang, Z. L. Wang and K. J. Lee, *Nano Lett.*, **2010**, 10, 493
- [254] C. K. Jeong, I. Kim, K. I. Park, M. H. Oh, H. Paik, G. T. Hwang, K. No, Y. S. Nam and K. J. Lee, *ACS Nano*, **2013**, 7, 11016
- [255] S. -H. Shin, Y. -H. Kim, M. H. Lee, J. -Y. Jung, J. H. Seol, J. Nah, *ACS Nano*, **2014**, 8, 10844
- [256] C. Baek, J. H. Yun, J. E. Wang, C. K. Jeong, K. J. Lee, K. I. Park and D. K. Kim, *Nanoscale*, **2016**, 8, 17632

- [257] K. I. Park, M. Lee, Y. Liu, S. Moon, G. T. Hwang, G. Zhu, J. E. Kim, S. O. Kim, D. K. Kim, Z. L. Wang and K. J. Lee, *Adv. Mater.*, **2012**, 24, 2999
- [258] C. K. Jeong, K. I. Park, J. Ryu, G. T. Hwang and K. J. Lee, *Adv. Funct. Mater.*, **2014**, 24, 2620
- [259] K. Shi, B. Sun, X. Huang, P. Jiang, *Nano Energy*, **2018**, 52, 153
- [260] S.K. Ghosh, A. Biswas, S. Sen, C. Das, K. Henkel, D. Schmeisser, D. Mandal, *Nano Energy*, **2016**, 30, 30621
- [261] Y.L. Zhao, Q.L. Liao, G.J. Zhang, Z. Zhang, Q.J. Liang, X.Q. Liao, Y. Zhang, *Nano Energy*, **2015**, 11, 719.
- [262] B.S. Lee, J. Yoon, C. Jung, D.Y. Kim, S.Y. Jeon, K.H. Kim, J.H. Park, H. Park, K.H. Lee, Y.S. Kang, J.H. Park, H. Jung, W.R. Yu, S.G. Doo, *ACS Nano*, **2016**, 10, 2617
- [263] E. J. Lee, T. Y. Kim, S. Kim, S. Jeong, Y. Choi and S. Y. Lee, *Energy Environ. Sci.*, **2018**, 11, 1425
- [264] A. Sultana, M. Alam, P. Sadhukhan, U.K.Ghorai, S. Das, T.R. Middy, D. Mandal, *Nano Energy*, **2018**, 49, 380
- [265] R. Ding, X. Zhang, G. Chen, H. Wang, R. Kishor, J. Xiao, F. Gao, K. Zeng, X. Chen, X. W. Sun, Y. Zheng, *Nano Energy*, **2017**, 37, 126
- [266] V. Jella, S. Ippili, J-. H. Eom, J. Choi, S-. G. Yoon, *Nano Energy*, **2018**, 53, 46
- [267] R. Ding, H. Liu, X. Zhang, J. Xiao, R. Kishor, H. Sun, B. Zhu, G. Chen, F. Gao, X. Feng, J. Chen, X. Chen, X. Sun, Y. Zheng, *Adv. Funct. Mater.* **2016**, 26, 7708
- [268] S. K. Ghosh, T. K. Sinha, B. Mahanty, D. Mandal, *Energy Technology*, **2015**, 3, 1190.
- [269] A. Sultana, P. Sadhukhan, M. M. Alam, S. Das, T. R. Middy, D. Mandal, *ACS Applied Materials & Interfaces*, **2018**, 10, 4121
- [270] S. K. Ghosh, T. K. Sinha, B. Mahanty, S. Jana, D. Mandal, *J. Appl. Phys.*, **2016**, 120, 174501
- [271] W. Ma, J. Zhang, S. Chen, X. Wang, *J. Macromol. Sci.*, **2008**, 47, 434
- [272] H.L.W. Chan, M.C. Cheung, C.L. Choy, *Ferroelectrics*, **1999**, 224, 113.
- [273] Q. Zhou, Z. Bai, W. Lu, Y. Wang, B. Zou, H. Zhong, *Adv. Mater.*, **2016**, 28, 9163.

- [274] X. Li, M. Guo and S. Dong, *IEEE Trans. Ultrason. Ferroelectr. Freq. Control*, **2011**, 58, 698
- [275] H.-X. Zou, W.-M. Zhang, W.-B. Li, Q.-H. Gao, K.-X. Wei, Z.-K. Peng, G. Meng, *Smart Materials and Structures*, **2017**, 26, 11
- [276] X. Gao, J. Wu, Y. Yu, Z. Chu, H. Shi and S. Dong, *Adv. Funct. Mater.* **2018**, 28, 1706895
- [277] W. Yang, W. Gong, C. Hou. et al. *Nat Commun.*, **2019**, 10, 5541
- [278] Q. Sun, W. Seung, B.J. Kim, S. Seo, S.-W. Kim, J.H. Cho, *Adv. Mater.*, **2015**, 27, 3411
- [279] Z. L. Wang, J. Chen and L. Lin, *Energy Environ. Sci.*, **2015**, 8, 2250
- [280] W. L. Wang, K. J. Liao, C. G. Hu, S. X. Wang, C. Y. Kong and H. Y. Liao, *Sensors and Actuators A: Physical*, **2003**, 108, 55
- [281] T. Quan, Y. Yang, *Nano Res.*, **2016**, 9, 2226
- [282] W. Seung, H.-J. Yoon, T.Y. Kim, H. Ryu, J. Kim, J. -H. Lee, S. Kim, Y. K. Park, Y. J. Park, S. -W. Kim, *Adv. Energy Mater.* **2017**, 7, 160098
- [283] S. Qin, Q. Zhang, X. Yang, M. Liu, Q. Sun, Z. L. Wang, *Adv. Energy Mater.*, **2018**, 8, 1800069
- [284] J. Luo, Z. Wang, L. Xu, A. Wang, K. Han, T. Jiang, Q. Lai, Y. Bai, W. Tang, F. R. Fan, Z. L. Wang, *Nat Commun.*, **2019**, 10, 5147
- [285] S. Priya, *J Electroceram*, **2007**, 19, 167
- [286] A. A Khan, A. Mahmud, S. Zhang, S. Islam, P. Voss, D. Ban, *Nano Energy*, **2019**, 62, 691
- [287] S. Luo, Y. Shen, S. Yu, Y. Wan, W. Liao, R. Sun and C. Wong, *Energy Environ. Sci.*, **2017**, 10, 137
- [288] A. Jain, P. K. J. , A. K. Sharma, A. Jain, R. P.N , *Polym. Eng. Sci.*, **2015**, 55, 158
- [289] R. Fries, A.J. Moulson, *J. Mater. Sci.: Mater. Electron.* **1994**, 5, 238
- [290] T. Zheng, H. Wu, Y. Yuan, X. Lv, Q. Li, T. Men, C. Zhao, D. Xiao, J. Wu, K. Wang, J. Li, Y. Gu, J. Zhu and S. J. Pennycook, *Energy Environ. Sci.*, **2017**, 10, 52
- [291] S. Sadewasser, T. Glatzel, S. Schuler, S. Nishiwaki, R. Kaigawa and M. C. Lux-Steiner, *Thin Solid Films*, **2003**, 257, 431

- [292] H. Röhm, T. Leonhard, M. J. Hoffmann and A. Colsmann, *Energy Environ. Sci.*, **2017**, 10, 950
- [293] A. D. Schulz, H. Röhm, T. Leonhard, S. Wagner, M. J. Hoffmann, A. Colsmann, *Nat. Mater.*, **2019**, 18, 1050
- [294] A. H. Rahmati, S. Yang, S. Bauer and P. Sharma, *Soft Matter*, **2019**, 15, 127
- [295] A. Kuchler, High Voltage Engineering: Fundamentals-Technology-Applications, *Springer Vieweg*, Berlin, Germany **2018**, p.79
- [296] K. Wang, Y. Hou, B. Poudel, D. Yang, Y. Jiang, M.-G. Kang, K. Wang, C. Wu, S. Priya, *Adv. Energy Mater.*, **2019**, 9, 1901753
- [297] G. J. Aubrecht, Energy: Physical, Environmental, and Social Impact, *Pearson Education, London* **2006**
- [298] C. Beggs, Energy: Management, Supply and Conservation, *Elsevier, Oxford* **2002**
- [299] J. C. Shin, P. K. Mohseni, K. J. Yu, S. Tomasulo, K. H. Montgomery, M. L. Lee, J. A. Rogers, X. Li, *ACS Nano*, **2012**, 6, 11074.
- [300] Y. Yang, W. Guo, K. C. Pradel, G. Zhu, Y. Zhou, Y. Zhang, Y. Hu L. Lin , Z. L. Wang , *Nano Lett.* **2012**, 12, 2833.
- [301] J. Huang, X. Yang, J. Yu, J. Han, C. Jia, M. Ding, J. Sun, X. Cao, Q. Sun, Z. L. Wang, *Nano Energy*, **2020**, 69, 104419.
- [302] A. Ghaderiaram, A. Bazrafshan, K. Firouzi, M. Kolahdouz, *Nano Energy*, **2021**, 87, 106170,
- [303] Y. Hu, J. Yang , Q. Jing , S. Niu , W. Wu , Z. L. Wang , *ACS Nano*, **2013**, 7 , 10424 .
- [304] S. Xu, Y.-W. Yeh, G. Poirier, M. C. Mcalpine, R. A. Register, N. Yao, *Nano Lett.* **2013**, 13, 2393.
- [305] P. Jiao & A. H. Alavi, *International Materials Reviews* **2021** 66:6, 365-393.
- [306] K. Barri, P. Jiao, Q. Zhang, J. Chen, Z. L. Wang, A. H. Alavi, *Nano Energy* **2021**, 86, 106074.
- [307] C. Pan, J. Zhai and Z. L. Wang, *Chem. Rev.*, **2019**, 119, 9303
- [308] W. Wang, J. Zhang, Y. Zhang, F. Chen, H. Wang, M. Wu, H. Li, Q. Zhu, H. Zheng, and R. Zhang, *Appl. Phys. Lett.* **2020**, 116, 023901.
- [309] S. Hajra, A. M. Padhan, M. Sahu, P. Alagarsamy, K. Lee, H. J. Kim, *Nano Energy*, **2021**, 89, 106316.
- [310] C. R. Bowen, H. A. Kim, P. M. Weaver and S. Dunn, *Energy Environ. Sci.*, **2014**, 7, 25

- [311] Z. L. Wang, *Nano Energy*, **2020**, 68, 104272.
- [312] Y Chen, G. Gao, J. Zhao, H. Zhang, J. Yu, X. Yang, Q. Zhang, W. Zhang, S. Xu, J. Sun, Y. Meng, Q. Sun. *Adv. Funct. Mater.* **2019**, 29, 1900959.
- [313] Z. L. Wang and J. Song, *Science*, **2006**, 312, 242
- [314] C. H. Wang, W. S. Liao, Z. H. Lin, N. J. Ku, Y. C. Li, Y. C. Chen , Z. L. Wang , C.-P. Liu, *Adv. Energy Mater.* **2014**, 4, 1400392.
- [315] K. Kapat, Q.T.H. Shubhra, M. Zhou, S. Leeuwenburgh, *Adv. Funct. Mater.*, **2020**, 1909045.
- [316] H. Liu, X. Lin, S. Zhang, Y. Huan, Sh. Huang and X. Cheng, *J. Mater. Chem. A*, **2020**, 8, 19631-19640.
- [317] F. Narita, M. Fox, *Adv. Eng. Mater.*, **2018**, 20, 5.
- [318] X. Yang, G. Hu, G. Gao, X. Chen, J. Sun, B. Wan, Q. Zhang, S. Qin, W. Zhang, C. Pan, Q. Sun, Z. L. Wang, *Adv. Funct. Mater.* **2019**, 29, 1807837.
- [319] A. A. Khan, G. Huang, M. M. Rana, N. Mei, M. Biondi, S. Rassel, N. Tanguy, B. Sun, Z. Leonenko, N. Ying, C. Wang, S. Xu, D. Ban. *Nano energy*, **2021**. 86, 106039.
- [320] L. K. Park, S. Xu, Y. Liu, G. T. Hwang, S. J. Kang, Z. L. Wang, K. J. Lee, *Nano Lett.* **2010**, 10, 4939.
- [321] X. Niu, W. Jia, S. Qian, J. Zhu, J. Zhang, X. Hou, J. Mu, W. Geng, J. Cho, J. He and X. Chou, *ACS Sustainable Chem. Eng.*, **2018**, 7, 979.
- [322] N. R. Alluri, A. Chandrasekhar, V. Vivekananthan, Y. Purusothaman, S. Selvarajan, J. H. Jeong and S.-J. Kim, *ACS Sustainable Chemistry & Engineering*, **2017**, 5, 4730.
- [323] K. Y. Lee, D. Kim, J.-H. Lee, T. Y. Kim, M. K. Gupta and S.-W. Kim, *Adv. Funct. Mater.*, **2014**, 24, 37.
- [324] A. Garg, D.C. Agrawal, *Mater Sci Eng B*, **2001**, 86, 134-143.
- [325] S.L.S. Lucato, D.C. Lupascu, J. Rödel., *J Am Ceram Soc*, **2000**, 83, 424-426.
- [326] Close T. Sluka, K.G. Webber, E. Colla, D. Damjanovic *Acta Mater*, **2012**, 60, 5172-5181.
- [327] G.A. Schneider, *Annu Rev Mater Res*, **2000**, 37, 491-538.
- [328] W. Li, Z. Wang, F. Deschler, S. Gao, R. H. Friend and A. K. Cheetham, *Nat. Rev. Mater.*, **2017**, 2, 16099.
- [329] G. Huang, C. Wang, H. Zhang, S. Xu, Q. Xu and Y. Cui, *J. Mater. Chem. A*, **2018**, 6, 2449.
- [330] Y. Li, X. Zhang, H. Huang, S. V. Kershaw and A. L. Rogach, *Mater. Today*, **2020**, 32, 204.
- [331] B. Wang, X. Xiao, T. Chen, *Nanoscale*, **2014**, 6, 12287.

- [332] M. Coll, A. Gomez , E. M. Marza , O. Almora , G. G. Belmonte , M. C. Quiles , J. Bisquert , *J. Phys. Chem. Lett.* **2015**, 6, 1408.
- [333] Y. J. Kim, T. V. Dang, H. J. Choi , B. J. Park , J. H. Eom , H. A. Song , D. Seol , Y. Kim , S. H. Shin , H. Nah , S. G. Yoon , *J. Mater. Chem. A*, **2016**, 4, 756.
- [334] R. Ding, H. Liu, X. Zhang, J. Xiao, R. Kishor, H. Sun, B. Zhu, G. Chen, F. Gao, X. Feng, J. Chen, X. Chen, X. Sun and Y. Zheng, *Adv. Funct. Mater.*, **2016**, 26, 7708.
- [335] R. Ding, X. Zhang, G. Chen, H. Wang, R. Kishor, J. Xiao, F. Gao, K. Zeng, X. Chen, X. W. Sun and Y. Zheng, *Nano Energy*, **2017**, 37, 126.
- [336] V. Jella, S. Ippili, J.-H. Eom, J. Choi and S.-G. Yoon, *Nano Energy*, **2018**, 53, 46.
- [337] A. A. Khan, M. M. Rana, G. Huang, N. Mei, R. Saritas, B. Wen, S. Zhang, P. Voss, E.-A. Rahman, Z. Leonenko, S. Islam and D. Ban, *J. Mater. Chem. A*, **2020**, 8, 13619.
- [338] R. Pandey, G. Sb, S. Grover, S. K. Singh, A. Kadam, S. Ogale, U. V. Waghmare, V. R. Rao and D. Kabra, *ACS Energy Lett.*, **2019**, 4, 1004.
- [339] S. Ippili, V. Jella, J. Kim, S. Hong and S.-G. Yoon, *Nano Energy*, **2018**, 49, 247.
- [340] I. Chung, B. Lee and J. Q. He, et al., *Nature*, **2012**, 485, 486
- [341] H.-S. Kim, C.-R. Lee and J.-H. Im, et al., *Sci. Rep.*, **2012**, 2, 591
- [342] A. Abate, Perovskite Solar Cells Go Lead Free, *Joule*, **2017**, 1, 659–664
- [343] S. Chatterjee and A. J. Pal, *J. Mater. Chem. A*, **2018**, 6, 3793–3823
- [344] Z. W. Xiao, Z. N. Song and Y. F. Yan, *Adv. Mater.*, **2019**, 1803792
- [345] X. Liu, Y. Wang, T. Wu, X. He, X. Meng, J. Barbaud, H. Chen, H. Segawa, X. Yang, & L. Han, *Nature Comm.*, **2020**, 11, 2678.
- [346] Q. Zhang, L. Chu, F. Zhou, W. Ji and G. Eda, *Adv. Mater.*, **2018**, 30, 1704055.
- [347] S. Yang, W. Niu, A. L. Wang, Z. Fan, B. Chen, C. Tan, Q. Lu and H. Zhang, *Angew. Chem. Int. Ed.*, **2017**, 56, 4252.
- [348] X. Fu, S. Jiao, Y. Jiang, L. Li, X. Wang, C. Zhu, C. Ma, H. Zhao, Z. Xu, Y. Liu, W. Huang, W. Zheng, P. Fan, F. Jiang, D. Zhang, X. Zhu, X. Wang and A. Pan, *ACS Appl. Mater. Interfaces*. **2020**, 12, 2884.
- [349] Mark T. Weller, Oliver J. Weber Jarvist M. Frost and Aron Walsh., *Phys. Chem. Lett.* **2015**, 6, 16, 3209–3212
- [350] W. Rehman, R. L. Milot, G. E. Eperon, C. Wehrenfennig, J. L. Boland, H. J. Snaith, M. B. Johnston, L. M. Herz, *Adv. Mater.* **2015**, 27, 7938.

- [351] J. Dai, H. G. Zheng, C. Zhu, J. F. Lu, C. X. Xuc, *J. Mater. Chem. C* **2016**, 4, 4408.
- [352] N. Arora, M. I. Dar, M. Hezam, W. Tress, G. Jacopin, T. Moehl, P. Gao, A. S. Aldwayyan, B. Deveaud, M. Grätzel, M. K. Nazeeruddin, *Adv. Funct. Mater.* **2016**, 26, 2846.
- [353] A. A. Zhumekenov, M. I. Saidaminov, M. A. Haque, E. Alarousu, S. P. Sarmah, B. Murali, I. Dursun, X.-H. Miao, A. L. Abdelhady, T. Wu, O. F. Mohammed, O. M. Bakr, *ACS Energy Lett.* **2016**, 1, 32.
- [354] P.J. Goodhew, J. Humphreys, R. Beanland, *Electron Microscopy and Analysis*, third ed., *Taylor & Francis, New York*, **2001**.
- [355] Cheema SS, Kwon D, Shanker N, Dos Reis R, Hsu SL, Xiao J, Zhang H, Wagner R, Datar A, McCarter MR, Serrao CR, Yadav AK, Karbasian G, Hsu CH, Tan AJ, Wang LC, Thakare V, Zhang X, Mehta A, Karapetrova E, Chopdekar RV, Shafer P, Arenholz E, Hu C, Proksch R, Ramesh R, Ciston J, Salahuddin S. *Nature*. **2020**, 580 (7804), 478-482.
- [356] Xue, F., Hu, W., Lee, K.-C., Lu, L.-S., Zhang, J., Tang, H.-L., Han, A., Hsu, W.-T., Tu, S., Chang, W.-H., Lien, C.-H., He, J.-H., Zhang, Z., Li, L.-J., Zhang, X., *Adv. Funct. Mater.* **2018**, 28, 1803738.
- [357] Lauren M. Garten, David T. Moore, Sanjini U. Nanayakkara, Shyam Dwaraknath, Philip Schulz, Jake Wands, Angus Rockett, Brian Newell, Kristin A. Persson, Susan Trolier-McKinstry, David S. Ginley. *Sci. Adv.* **2019**, 1, 5
- [358] Y. Mao, P. Zhao, G. McConohy, H. Yang, Y. Tong, and X. Wang. *Adv. Energy Mater.* **2014**, 4, 130124.
- [359] H. Han, C. Voisin, S. Guillemet-Fritsch, P. Dufour, C. Tenailleau, C. Turner and J. C. Nino, *J. Appl. Phys.*, **2013**, 113, 024102.
- [360] M. M. Rana, A. A. Khan, G. Huang, N. Mei, R. Saritas, B. Wen, S. Zhang, P. Voss, E. A. Rahman, Z. Leonenko, S. Islam, and D. Ban, *ACS Appl. Mater. Interfaces*, **2020**, 12, 42, 47503–47512
- [361] W. Zhang, H. Yang, Li Li, S. Lin, P. Ji, C. Hu, D. Zhang, Y. Xi, *Nanotechnology*, **2020**, 31, 385401.
- [362] N. Wang, W. Dou, S. Hao, Y. Cheng, D. Zhou, X. Huang, C. Jiang, X. Cao, *Nano Energy*, **2019**, 56, 868.
- [363] Y. Han, C. Gao, H. Zhu, S. Chen, Q. Jiang, T. Li, M. Willander, X. Cao, N. Wang, *Nano Energy*, **2015**, 13, 405

- [364] Y. Xi, J. Song, S. Xu, R. Yang, Z. Gao, C. Hu and Z. L. Wang, *J. Mater. Chem.*, **2009**, **19**, 9260
- [365] S. Hao, J. Jiao, Y. Chen, Z. L. Wang, X. Cao, *Nano Energy*, **2020**, **75**, 104957
- [366] F. Yi, Z. Zhang, Z. Kang, Q. Liao, Y. Zhang, *Adv. Funct. Mater.* **2019**, **29**, 1–16,
- [367] W.G. Kim, D.W. Kim, I.W. Tcho, J.K. Kim, Y.K. Choi, *ACS Nano* **2021**, **15**, 258–287.
- [368] S. Wang, L. Lin, Z.L. Wang, *Nano Lett.* **2012**, **12**, 6339–6346.
- [369] F.R. Fan, Z.Q. Tian, Z. Lin Wang, *Nano Energy*, **2012**, **1**, 328–334
- [370] F.R. Fan, L. Lin, G. Zhu, W. Wu, R. Zhang, Z.L. Wang, *Nano Lett.* **2012**, **12**, 3109–3114.
- [371] C. Wu, A.C. Wang, W. Ding, H. Guo, Z.L. Wang, *Adv. Energy Mater.* **2019**, **9**, 1–25
- [372] H. Zou, Y. Zhang, L. Guo, P. Wang, X. He, G. Dai, H. Zheng, C. Chen, A.C. Wang, C. Xu, Z.L. Wang, *Nat. Commun.* **2019**, **10**, 1–9.
- [373] Z.L. Wang, *Rep. Prog. Phys.* **2021**, **84**, 096502.
- [374] A. Chen, C. Zhang, G. Zhu, Z.L. Wang, *Adv. Sci.* **2020**, **7**, 1–25.
- [375] R. Zhang, H. Olin, *EcoMat*, **2020**, **2**, 1–13.
- [376] G. Grau, R. Kitsomboonloha, S.L. Swisher, H. Kang, V. Subramanian, *Adv. Funct. Mater.* **2014**, **24**, 5067–5074
- [377] W. Lim, E.A. Douglas, S.H. Kim, D.P. Norton, S.J. Pearton, F. Ren, H. Shen, W. H. Chang, *Appl. Phys. Lett.* **2009**, **94**, 7–9
- [378] Y.Z. Zhang, Y. Wang, T. Cheng, W.Y. Lai, H. Pang, W. Huang, *Chem. Soc. Rev.* **2015**, **44**, 5181–5199
- [379] K.H. Choi, J.T. Yoo, C.K. Lee, S.Y. Lee, *Energy Environ. Sci.* **2016**, **9**, 2812–2821
- [380] S. Leijonmarck, A. Cornell, G. Lindbergh, L. Wågberg, *J. Mater. Chem. A.* **2013**, **1**, 4671–4677
- [381] L. Hu, H. Wu, F. La Mantia, Y. Yang, Y. Cui, *ACS Nano*, **2010**, **4**, 5843–5848
- [382] N.R. Tanguy, K. Khorsand Kazemi, J. Hong, K.-C. Cheung, S. Mohammadi, P. Gnanasekar, S.S. Nair, M.H. Zarifi, N. Yan, *Carbohydr. Polym.* **2021**, **278**, 118920,
- [383] Y. Wang, C. Yan, S.Y. Cheng, Z.Q. Xu, X. Sun, Y.H. Xu, J.J. Chen, Z. Jiang, K. Liang, Z.S. Feng, *Adv. Funct. Mater.* **2019**, **29**, 1–11
- [384] A. Rida, L. Yang, R. Vyas, M.M. Tentzeris, *IEEE Antennas Propag. Mag.* **2009**, **51**, 13–23
- [385] D. Tobjörk, R. Österbacka, *Adv. Mater.* **2011**, **23**, 1935–1961

- [386] H. Oh, S.S. Kwak, B. Kim, E. Han, G.H. Lim, S.W. Kim, B. Lim, *Adv. Funct. Mater.* **2019**, 29, 1904066
- [387] P. Cui, K. Parida, M.F. Lin, J. Xiong, G. Cai, P.S. Lee, *Adv. Mater. Interfaces* **2017**, 4, 1-7
- [388] C. Zhang, X. Lin, N. Zhang, Y. Lu, Z. Wu, G. Liu, S. Nie, *Nano Energy*, **2019**, 66, 104126
- [389] H.Y. Mi, X. Jing, Q. Zheng, L. Fang, H.X. Huang, L.S. Turng, S. Gong, *Nano Energy*, **2018**, 48, 327-336
- [390] Z. Bai, Y. Xu, Z. Zhang, J. Zhu, C. Gao, Y. Zhang, H. Jia, J. Guo, *Nano Energy*, **2020**, 75, 104884
- [391] R. Zhang, C. Dahlström, H. Zou, J. Jonzon, M. Hummelgård, J. Örtengren, N. Blomquist, Y. Yang, H. Andersson, M. Olsen, M. Norgren, H. Olin, Z.L. Wang, *Adv. Mater.*, **2020**, 32, 1-8
- [392] Y. Bao, R. Wang, Y. Lu, W. Wu, *APL Materials*, **2017**, 5, 074109
- [393] C. Yao, X. Yin, Y. Yu, Z. Cai, X. Wang, *Adv. Funct. Mater.* **2017**, 27, 1-7
- [394] B. Dudem, S.A. Graham, R.D.I.G. Dharmasena, S.R.P. Silva, J.S. Yu, *Nano Energy*, **2021**, 83, 105819.
- [395] N. Wang, Y. Zheng, Y. Feng, F. Zhou, D. Wang, *Nano Energy*, **2020**, 77, 105088.
- [396] T. Charoonsuk, S. Pongampai, P. Pakawanit, N. Vittayakorn, *Nano Energy*, **2021**, 89, 106430.
- [397] R.J. Ross, *Wood Handbook: Centennial Edition*, **2010**.
- [398] B. Thomas, M.C. Raj, B.K. Athira, H.M. Rubiyah, J. Joy, A. Moores, G.L. Drisko, C. Sanchez, *Chem. Rev.* **2018**, 118, 11575-11625.
- [399] C.J. Biermann, *Handb. Pulping Papermak*. **1996**.
- [400] S.S. Nair, P.Y. Kuo, H. Chen, N. Yan, *Ind. Crops Prod.* **2017**, 100, 208-217.
- [401] S.S. Nair, N. Yan, *Cellulose* **2015**, 22, 3137-3150.
- [402] Y. Huang, Q. Feng, C. Ye, S.S. Nair, N. Yan, *Prog. Org. Coat.* **2020**, 138, 105210.
- [403] Y. Huang, S.S. Nair, H. Chen, B. Fei, N. Yan, Q. Feng, *ACS Sustain.Chem. Eng.* **2019**, 7, 15607-15616.
- [404] H. Chen, S.S. Nair, P. Chauhan, N. Yan, *Chem. Eng. J.* **2019**, 360, 393-401.
- [405] J.A. Sirviõ, M.Y. Ismail, K. Zhang, M.V. Tejesvi, A. "Amm"al"ã, *J. Mater. Chem. A.* **2020**, 8, 7935-7946.
- [406] N.R. Tanguy, H. Wu, S.S. Nair, K. Lian, N. Yan, *Chem Sus Chem*, **2021**, 14, 1057-1067.
- [407] K. Li, D.W. Reeve, *J. Wood Chem. Technol.* **2004**, 24, 183-200.
- [408] O. Derkacheva, D. Sukhov, *Macromol. Symp.* **2008**, 265, 61-68.

- [409] C.M. Ewulonu, X. Liu, M. Wu, H. Yong, *J. Bioresour. Bioprod.* **2019**, 4, 3–10.
- [410] E. Rojo, M.S. Peresin, W.W. Sampson, I.C. Hoeger, J. Vartiainen, J. Laine, O. J. Rojas, *Green. Chem.* **2015**, 17, 1853–1866.
- [411] H.J. Kim, E.C. Yim, J.H. Kim, S.J. Kim, J.Y. Park, I.K. Oh, *Nano Energy*, **2017**, 33,130–137.
- [412] H. Ryu, J.H. Lee, T.Y. Kim, U. Khan, J.H. Lee, S.S. Kwak, H.J. Yoon, S.W. Kim, *Adv. Energy Mater.* **2017**, 7, 1–6.
- [413] L.H. Lee, *J. Electro*, **1994**, 32, 1–29.
- [414] G. Khandelwal, N.P. Maria Joseph Raj, S.J. Kim, *Adv. Energy Mater.* **2021**, 11, 1–32.
- [415] A. Ahmed, I. Hassan, A.M. Pourrahimi, A.S. Helal, M.F. El-Kady, H. Khassaf, R. B. Kaner, *Adv. Mater. Technol.* **2020**, 5, 1–20.
- [416] J.A. Molefi, A.S. Luyt, I. Krupa, *J. Mater. Sci.* **2009**, 45, 82–88.
- [417] K.C.M. Nair, S. Thomas, G. Groeninckx, *Compos. Sci. Technol.* **2001**, 61, 2519–2529.
- [418] A. Arribas, F.J. Carrio, *Eur. Polym. J.* **2008**, 44, 968–977.
- [419] K. Xia, Z. Xu, Z. Zhu, H. Zhang, Y. Nie, *Nanomaterials*, **2019**, 9.
- [420] P. Bai, G. Zhu, Y.S. Zhou, S. Wang, J. Ma, G. Zhang, Z.L. Wang, *Nano Res*, **2014**, 7, 990–997.
- [421] H.S. Wang, C.K. Jeong, M.H. Seo, D.J. Joe, J.H. Han, J.B. Yoon, K.J. Lee, *Nano Energy*, **2017**, 35, 415–423.
- [422] V. Nguyen, R. Yang, *Nano Energy*, **2013**, 2, 604–608.
- [423] S. Nie, Q. Fu, X. Lin, C. Zhang, Y. Lu, S. Wang, *Chem. Eng. J.* **2021**, 404, 126512.
- [424] I. Kim, H. Jeon, D. Kim, J. You, D. Kim, *Nano Energy*, **2018**, 53, 975–981.
- [425] M. Li, Y. Jie, L.H. Shao, Y. Guo, Wang, Z.L. Wang, *Nano Res*, **2019**, 12,1831–1835.
- [426] F. Xi, Y. Pang, G. Liu, S. Wang, W. Li, C. Zhang, Z.L. Wang, *Nano Energy*, **2019**, 61, 1–9.
- [427] M.M. Rana, A.A. Khan, G. Huang, N. Mei, R. Saritas, B. Wen, S. Zhang, P. Voss, E. Abdel-Rahman, Z. Leonenko, S. Islam, D. Ban, *ACS Appl. Mater. Interfaces*, **2020**, 12, 47503–47512.
- [428] A.A. Khan, M.M. Rana, G. Huang, N. Mei, R. Saritas, B. Wen, S. Zhang, P. Voss, E. A. Rahman, Z. Leonenko, S. Islam, D. Ban, *J. Mater. Chem. A* **2020**, 8, 13619–13629.
- [429] A.A. Khan, A. Mahmud, S. Zhang, S. Islam, P. Voss, D. Ban, *Nano Energy*, **2019**, 62, 691–699.
- [430] Z. Zhou, K. Chen, X. Li, S. Zhang, Y. Wu, Y. Zhou, K. Meng, C. Sun, Q. He, W. Fan, E. Fan, Z. Lin, X. Tan, W. Deng, J. Yang, J. Chen, *Nat. Electron.* **2020**, 3, 571–578.

Appendices

Appendix for Chapter 2

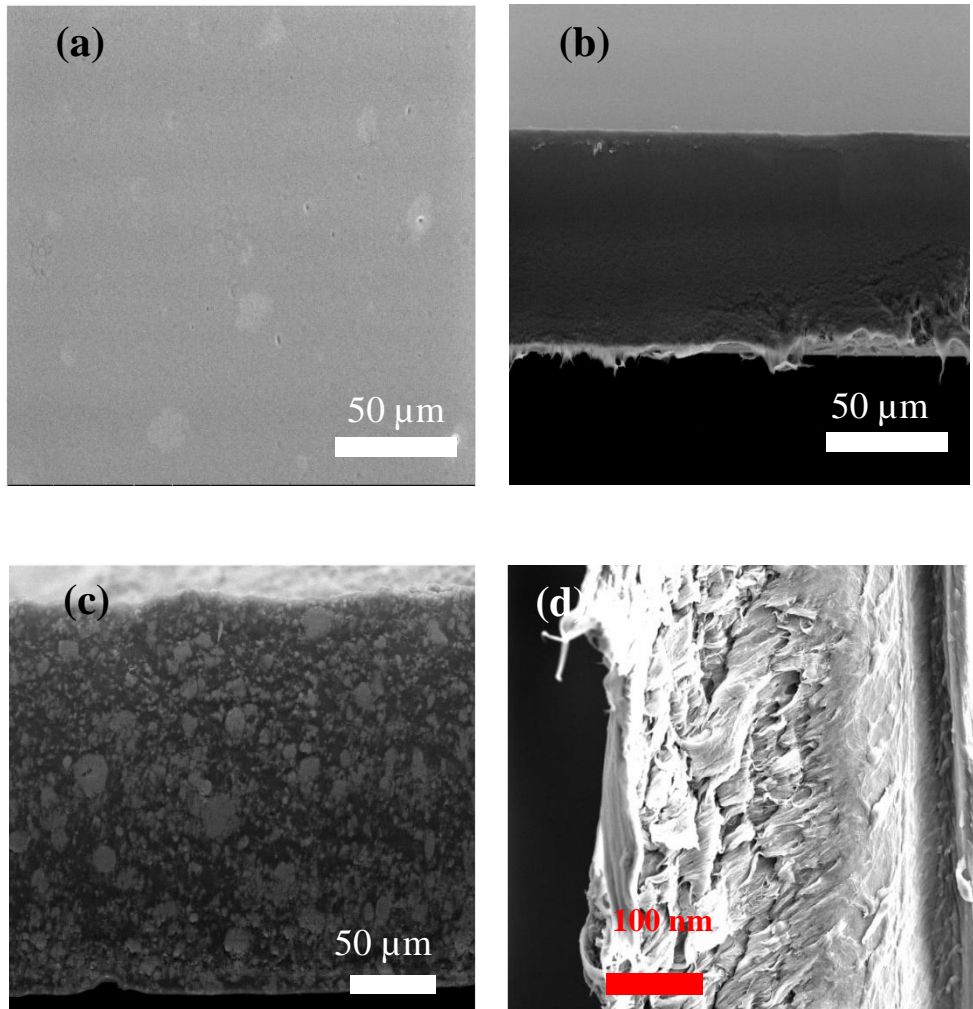
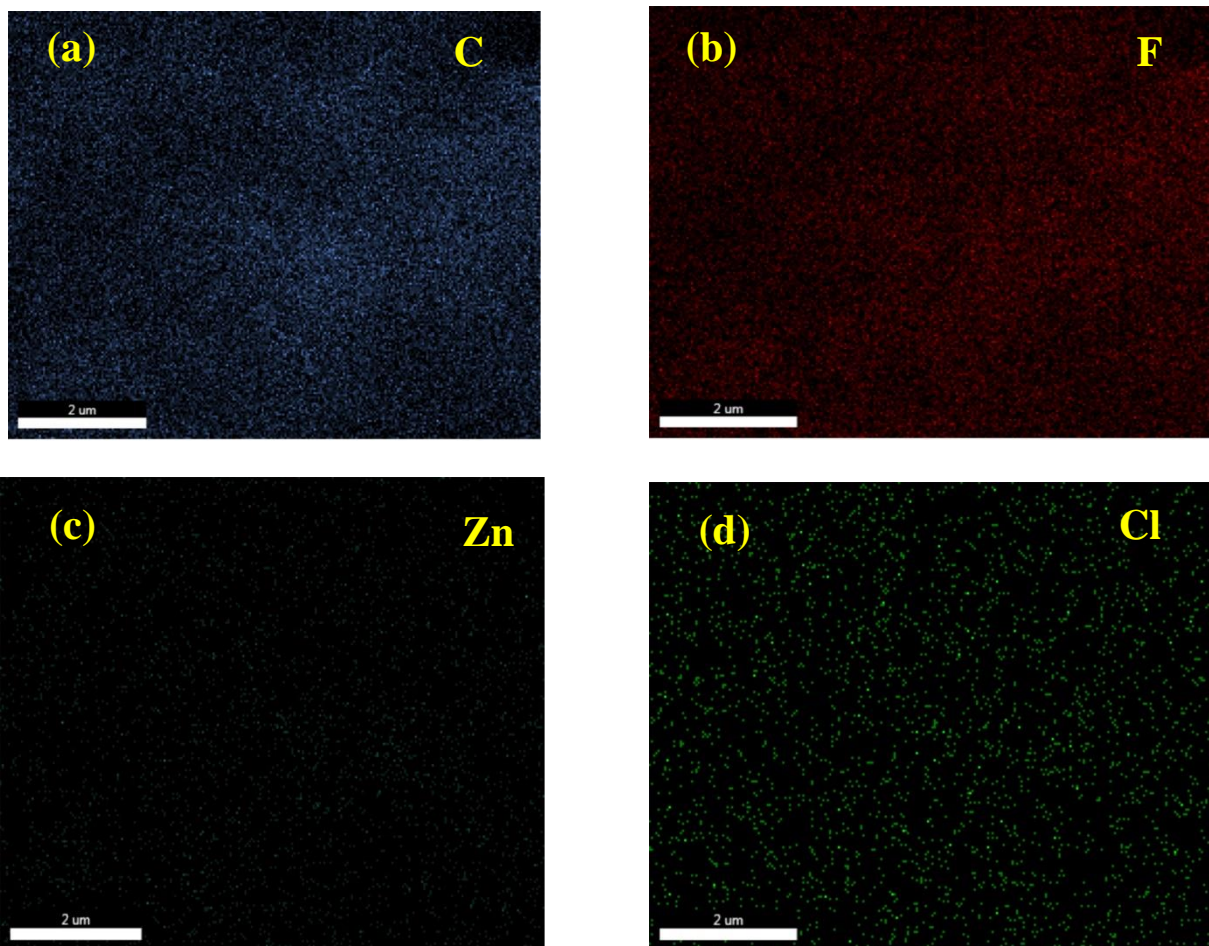


Figure A2.1. The characterization of the pure and porous PVDF film. scanning electron microscope (SEM) images of the pure PVDF film (a) Plane view SEM (b) Cross-sectional SEM, annealed at 75°C, the SEM image indicates that the surface of the pure PVDF is uniform for both cases (c) distributed ZnO NPs on the surface of the PVDF matrix. (c) the cross-sectional SEM image of the PVDF mixed with ZnO NPs, The SEM image indicates that nanoparticles are not uniformly distributed rather accumulated in different positions of the PVDF film. This creates pores of different sizes after an etching process. (d) Cross-sectional SEM image of the porous PVDF film after the etching of the ZnO NPs



(e)

Element	Weight %	Atomic %	Net Int.
C K	68.46	77.69	731.4
F K	30.73	22.05	458.3
ZnL	0.29	0.06	2.4
ClK	0.51	0.20	5.8

Figure A2.2. Element mapping of (a) Carbon (C); (b) fluorine (F); (c) Zinc (Zn); (d) Chlorine (Cl); in porous PVDF thin film for a specific region of interest. (e) compare the quant results of elements in the porous film.

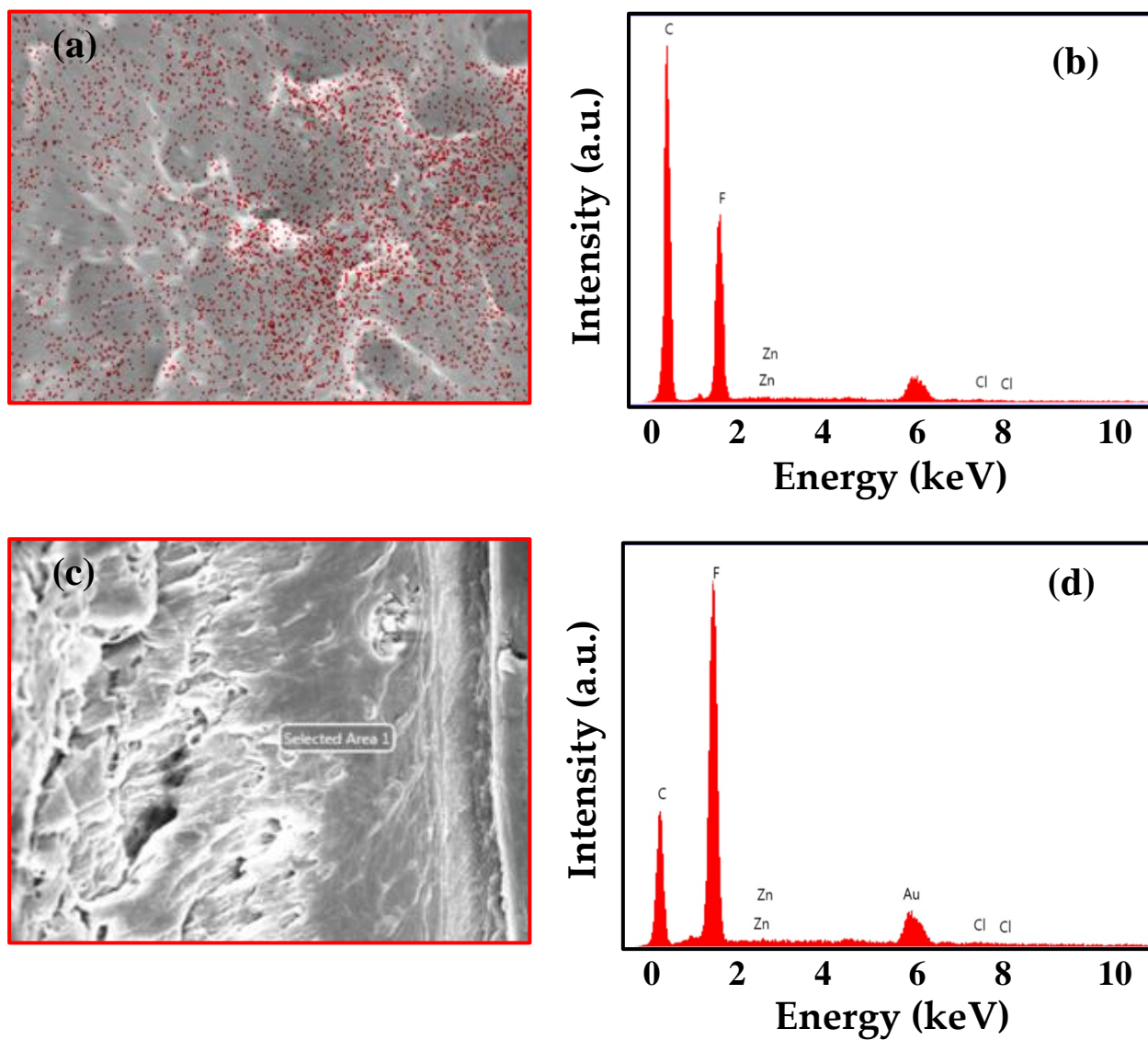


Figure A2.3. (a) The selected area of top surface SEM of nanoporous PVDF film; (b) EDS spectrum of the nanoporous PVDF film of image (a); (c) Selected area of cross-sectional SEM of nanoporous PVDF film; (d) EDS spectrum of the nanoporous PVDF film of image (c);

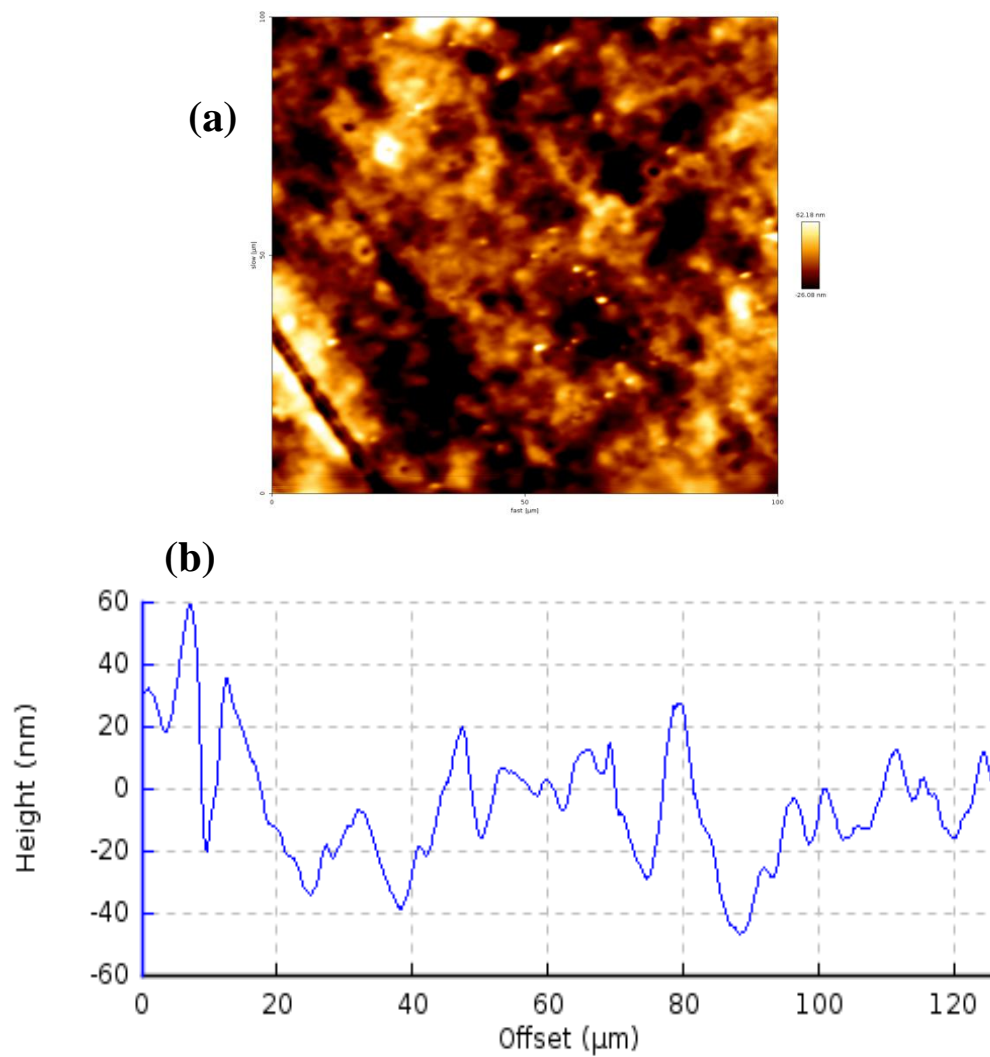


Figure A2.4. The characterization of the porous PVDF film (a) the atomic force microscopy (AFM) image of porous PVDF surface (b) measured surface roughness of porous PVDF (~100 nm)

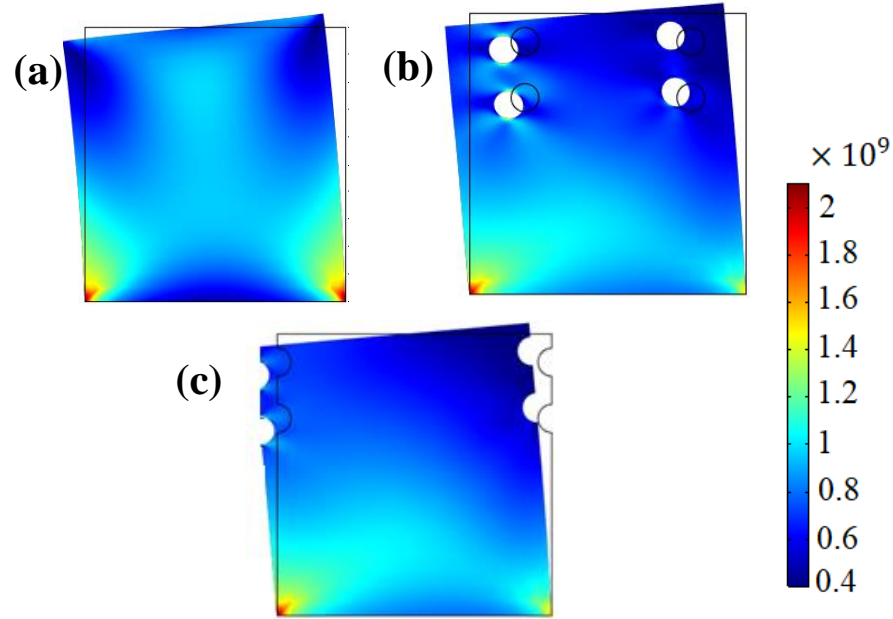


Figure A2.5. Strain distribution in the porous PVDF with varying porosity under a lateral bending force of 2GPa (a) pure (0%) PVDF (b) porous PVDF with inner pores only, and (c) porous PVDF with only surface pores. **The scale bar is the same for all profiles from (a–c).**

Supporting note A2.1: Here a PVDF piezoelectric polymer is used to study the simple cases of the porous structure, where a square (100nm \times 100nm) 2D model is developed. To make the structure porous, we then intentionally incorporate inner and surface circular nano-pores, with a pore size of 5 nm radius. Here we summarize a comparison between three basic models that included a non-porous (pure) PVDF, a porous PVDF with surface pores, and a porous PVDF with inner pores only, with different porosity concentration, having spatially uniform pore distributions. To study the piezoelectricity of the porous structure a lateral bending force of 2 GPa is uniformly applied on the side surface. **Figure A2.6a-c** shows the simulation results, revealing the piezopotential is substantially modified due to the presence of pores. More specifically, the piezopotential increases proportionally with the degree of porosity, which is represented by the brightness of color grading. The potential is raised by 39.45 % (10.9 V to 15.2 V) when the porosity increases from zero to 3.9 % if pores are on the surface and the potential is raised by 31.19 % (10.9 V to 14.3 V) when the porosity increases from zero to 7.85 % if pores are inside (**Figure A2.6d**).

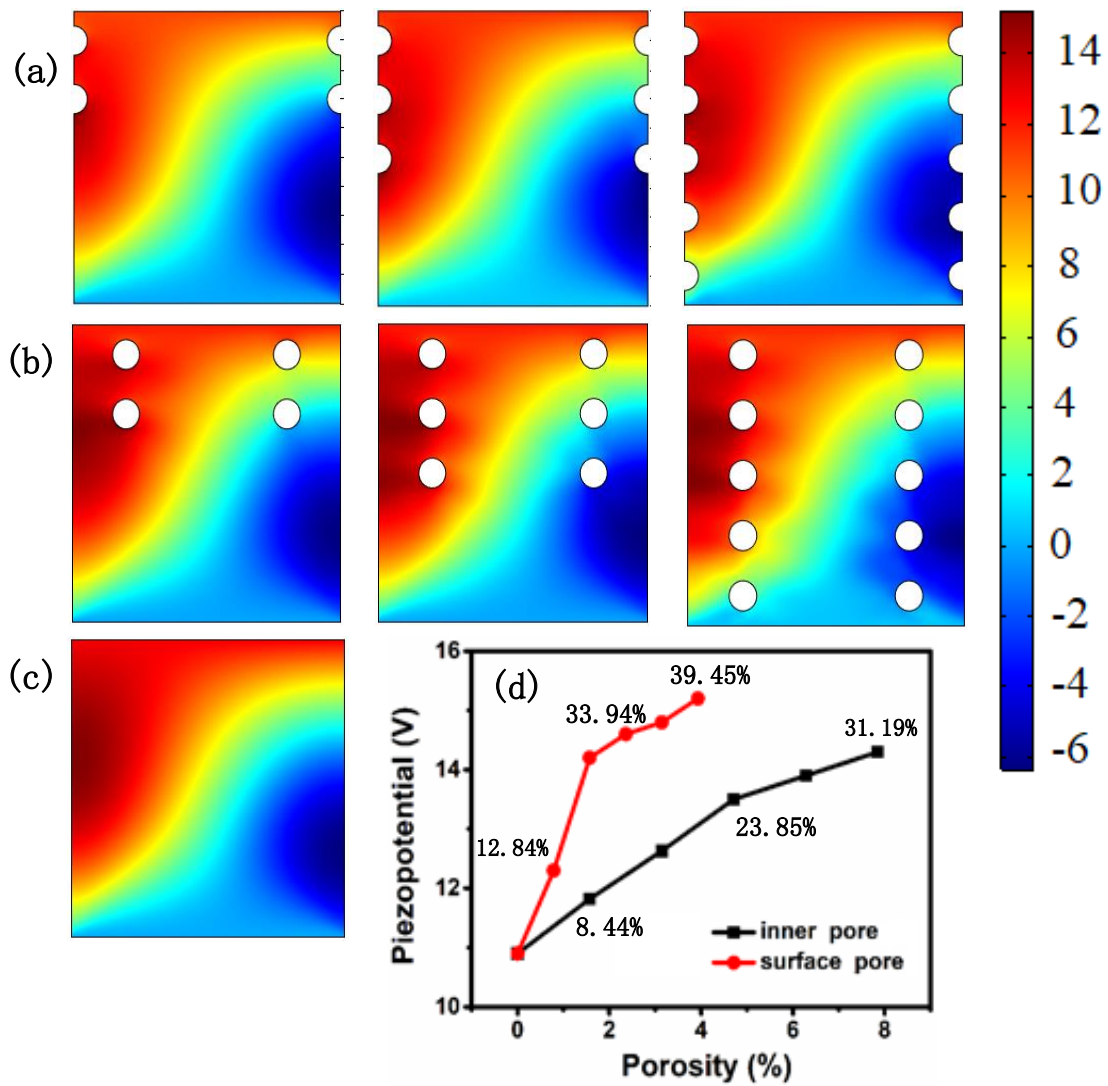


Figure A2.6. Piezopotential distribution in the porous PVDF model with varying porosity percentages under lateral bending force (a) with surface pores only, (b) with only inner pores, and (c) a non-porous PVDF. Same scale bar for (a–c) (d) comparison of piezopotential as a function of porosity.

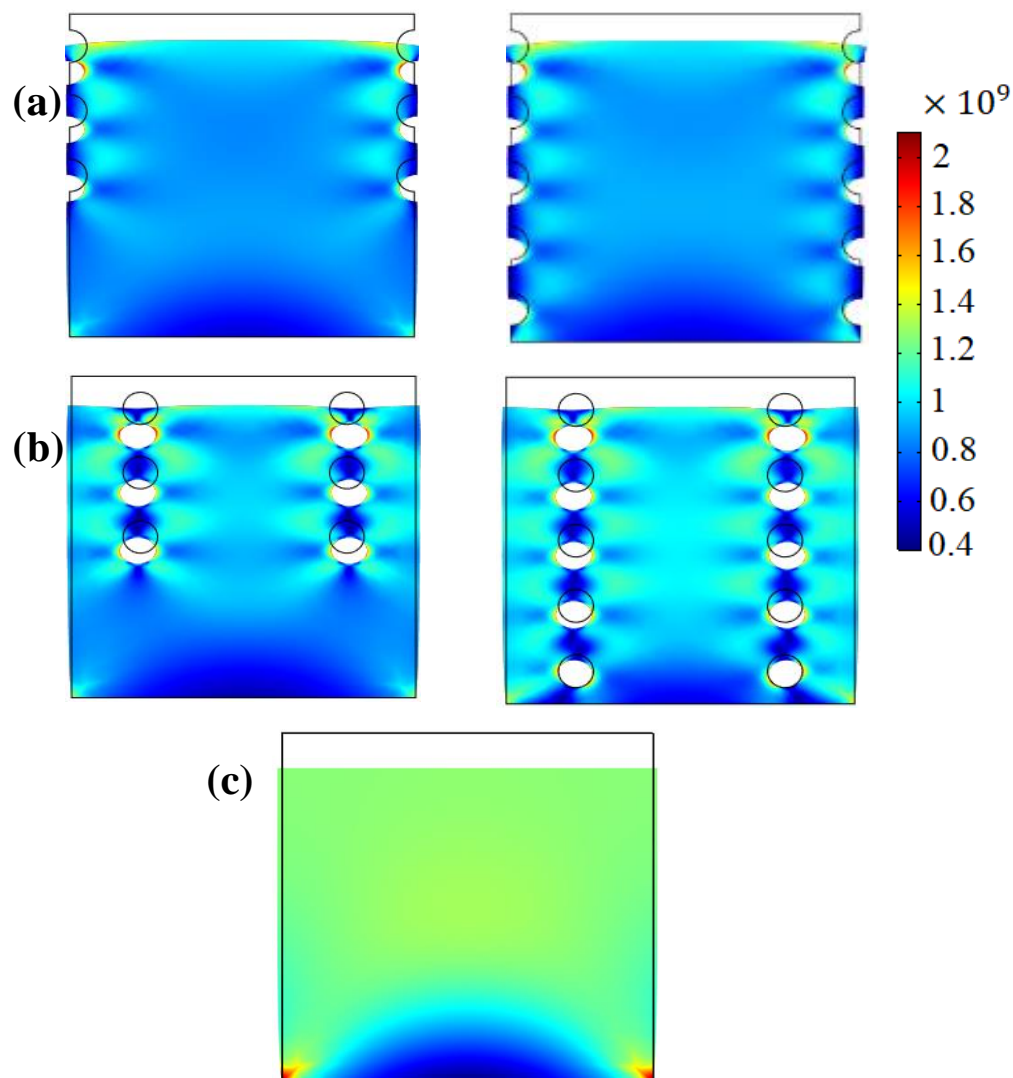


Figure A2.7. Strain distribution in the porous PVDF with varying porosity under a vertical compressive force of 2 GPa (a) porous PVDF with only surface pores, (b) porous PVDF with inner pores only, and (c) pure PVDF, the scale bar is the same for all profiles from (a–c).

Supporting note A2.2:

As shown in **Figure A2.7a** for surface pores and **Figure A2.7b** for inner pores, when the compressive force is applied, the stress of pores deformed asymmetrically. The strain concentration near both sides of the pores is much more significantly visualize which indicates tensile strain creation at both sides of

the pores compared to its bulk counterpart (**Figure A2.7c**). As discussed earlier that the piezopotential is the result of combined dipole moments that form due to the displacement of positive and negative charge centers upon application of external stress, these dipole moments add together and provide the positive and negative piezopotential. This localized strain of higher magnitude induces higher potential, which adds up and enhances the bulk piezopotential.

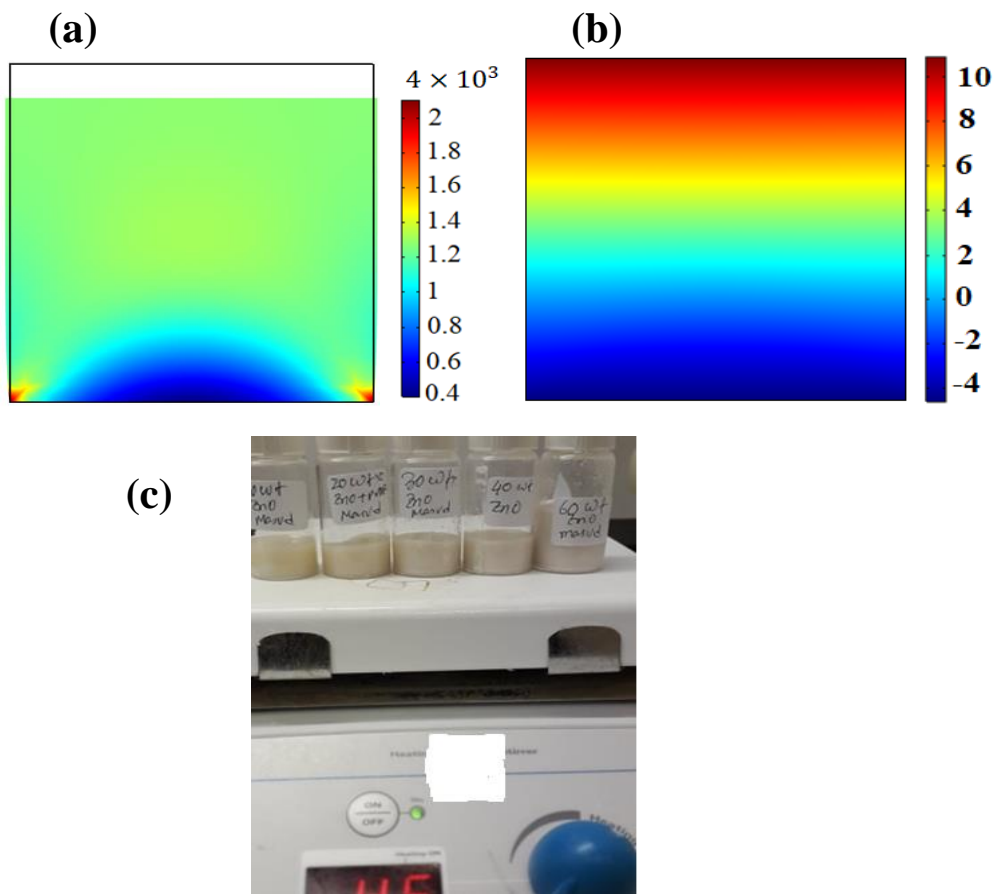


Figure A2.8. (a) Stress distribution for pure PVDF film (b) potential distribution for pure PVDF film where the peak output voltage is 10.9 volt, (c) prepared solution of PVDF-ZnO with a ZnO mass ratio of 0 to 60 wt. % (0 and 50 wt. % are not shown here).

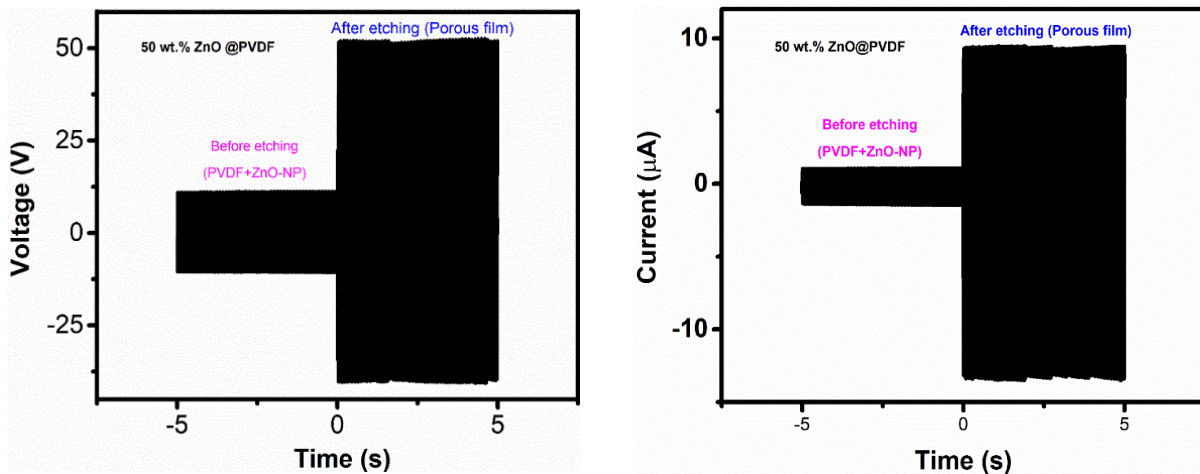


Figure A2.9. Comparison of the electrical output performance for 50 wt. % of ZnO-NP-based PVDF porous and nonporous film. (a) Output voltage (b) output current.

Table A2.1: Comparison of percentage increases of piezopotential with porosity

Lateral Bending force					
Surface Pore Condition			Inner Pore condition		
% of Porosity	Piezo-potential (V)	% of Voltage increase	% of Porosity	Piezo-potential (V)	% of Voltage increase
0	10.9	-	0	10.9	-
0.79	12.3	12.84	1.57	11.82	8.44
1.57	14.2	30.27	3.14	12.63	15.87
2.36	14.6	33.94	4.71	13.50	23.85
3.14	14.8	35.79	6.28	13.90	27.52
3.93	15.2	39.45	7.85	14.30	31.19

Compressive force					
Surface Pore Condition			Inner Pore condition		
% of Porosity	Piezo-potential (V)	% of Voltage increase	% of Porosity	Piezo-potential (V)	% of Voltage increase
0	46.6	-	0	46.6	-
0.79	47.2	1.29	1.57	47.8	2.58
1.57	47.7	2.36	3.14	49.1	5.36
2.36	48.2	3.43	4.71	50.3	7.94
3.14	48.7	4.51	6.28	51.6	10.73
3.93	49.3	5.79	7.85	53	13.73

% of porosity Calculation for Inner pore

Radius of pore = 5 nm

Area of pore = $3.1416 \times 25 = 78.54 \text{ nm}^2$

Area of PVDF = 10000 nm^2

% of porosity in the PVDF = $(78.54/10000) \times 100 \% = .79 \%$ for a single pore

For surface pore, this will be half as the surface contain only the half portion of the circle.

References for Table 2.1

- [1] Pi, Z.; Zhang, J.; Wen, C.; Zhang, Z-B.; Wu, D., *Nano Energy* **2014**, 7, 33-41.
- [2] W. S. Jung, W. S.; Lee, M. J.; Kang, M. K; Moon, H. G.; Yoon, S. J.; Baek, S. H., *Nano Energy* **2015**, 13, 174-181.
- [3] Yang, L.; Zhao, Q.; Chen, K.; Ma, Y.; Wu, Y.; Ji, H.; and Qiu, J., *ACS Appl. Mater. Interface* **2020**, 12, 11045-11054.
- [4] Alluri, N. R.; Saravanakumar, B.; Kim, S. J., *ACS Applied Materials & Interfaces* **2015**, 7, 9831-9840.

- [5] Thakur, P.; Kool, A.; Hoque, N. A.; Bagchi, B.; Khatun, F.; Biswas, P., *Nano Energy* **2018**, 44, 456-467.
- [6] Kar, E.; Bose, N.; Dutta, B.; Banerjee, S.; Mukherjee, N.; Mukherjee, S. *Energy Conversion and Management* **2019**, 184, 600-608.
- [7] Karan, S. K.; Bera, R.; Paria, S.; Das, A. K.; Maiti, S.; Maitra, A, *Advanced Energy Materials* **2016**, 6, 1601016.
- [8] Saravanakumar, B.; Soyoon, S.; Kim, S. J., *ACS Applied Materials & Interfaces* **2014**, 6, 13716-13723.
- [9] Jeong, C. K.; Baek, C.; Kingon, A. I.; Park, K. I.; Kim, S. H., *Small* **2018**, 14, 1704022.
- [10] Yaqoob, U.; Uddin, A. S. M. I.; Chung, G. S., *Applied Surface Science* **2017**, 405, 420-426.
- [11] Maity, K.; Mandal, D. *ACS Applied Materials & Interfaces* **2018**, 10, 18257-18269.
- [12] Soin, N.; Shah, T. H.; Anan, S. C.; Geng, J.; Pornwannachai, W.; Mandal, P., *Energy & Environmental Sci.* **2014**, 7, 1670-1679.
- [13] Dutta, B.; Kar, E.; Bose, N.; Mukherjee, S., *ACS Sustainable Chemistry & Engineering* **2018**, 6, 10505-10516.
- [14] Zhang, C.; Fan, Y.; Li, H.; Li, Y.; Zhang, L.; Cao, S., *ACS Nano* **2018**, 12, 4803-4811.
- [15] Li, J.; Chen, S.; Liu, W.; Fu, R.; Tu, S.; Zhao, Y., *The Journal of Physical Chemistry C* **2019**, 123, 11378-11387.

Appendix for Chapter 3

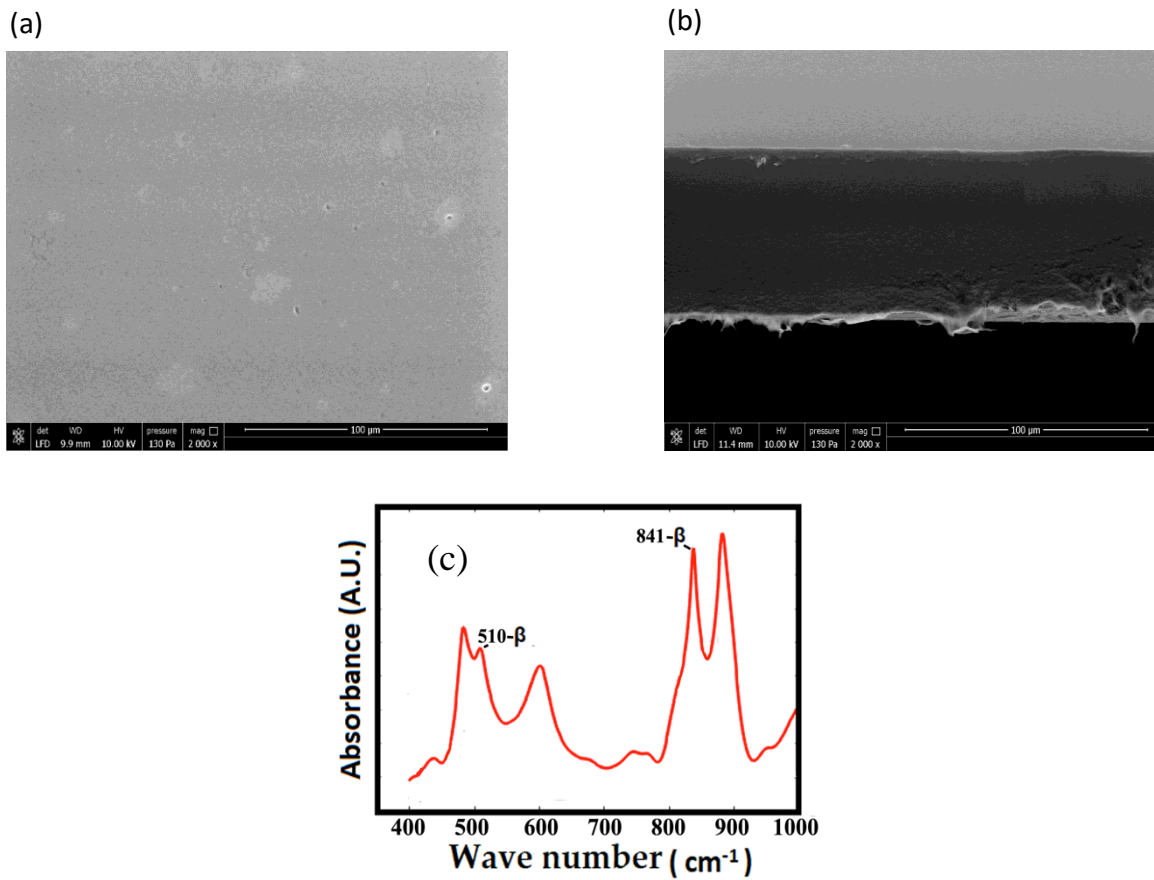


Figure A3.1. The characterization of the pure PVDF film. Scanning electron microscopy (SEM) image of (a) top surface of the pure PVDF (annealed at 75 °C) (b) the cross section of the pure PVDF film. The SEM images indicate that the surface of the pure PVDF is uniform (c) FTIR spectrum of the PVDF film is indicating the β -phase formation (corresponding absorptions at the wavenumbers of 510 cm^{-1} , and 841 cm^{-1}).

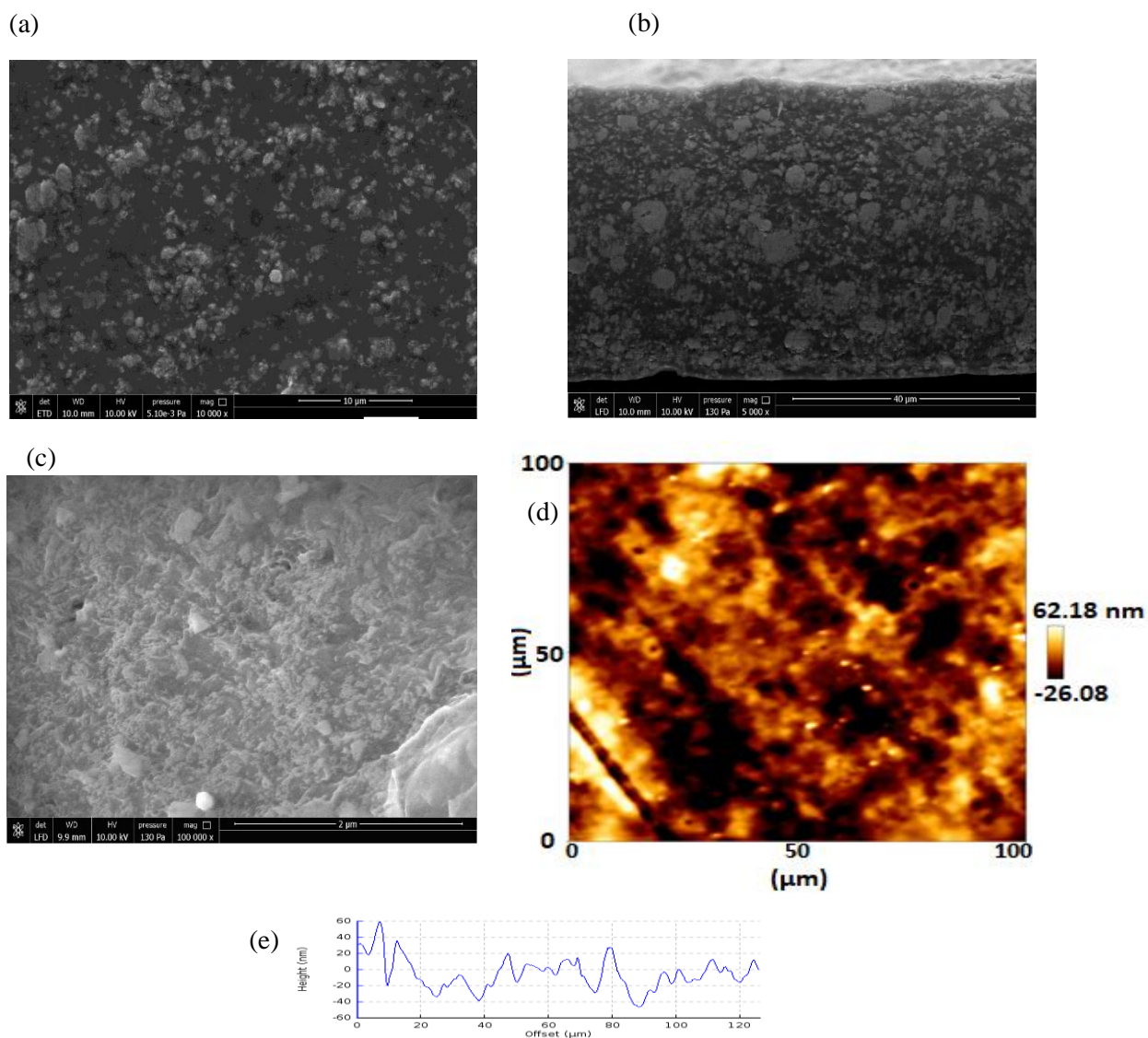


Figure A3.2. The characterization of the porous PVDF film (a) top surface SEM image of the PVDF loaded with ZnO nanoparticles (NPs) with a diameter of 35-45 nm (b) cross sectional SEM image of the PVDF loaded with ZnO NPs. The SEM images are indicating that nanoparticles are not uniformly distributed rather accumulated in different positions of the PVDF film. This creates pores of different sizes after an etching process (c) top surface SEM image of the porous PVDF film obtained after the etching of ZnO NPs by 37 wt. % hydrochloric acid (HCl) (d) atomic force microscopy (AFM) image of the porous PVDF surface (e) measured surface roughness of the porous PVDF (≈ 100 nm)

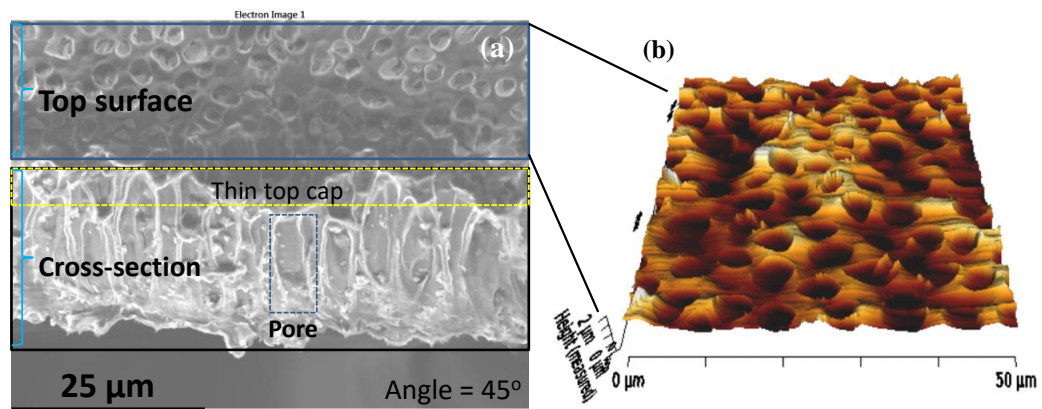


Figure A3.3. The morphology of pore structures in the P-PNGs (a) cross-sectional SEM image of the FAPbBr₂I@PVDF film shows that the pores with a length of 20-25 μm are regularly distributed here (b) surface topography of the FAPbBr₂I@PVDF film from the AFM image illustrates that the diameter of the pores are approximately 3-5 μm.

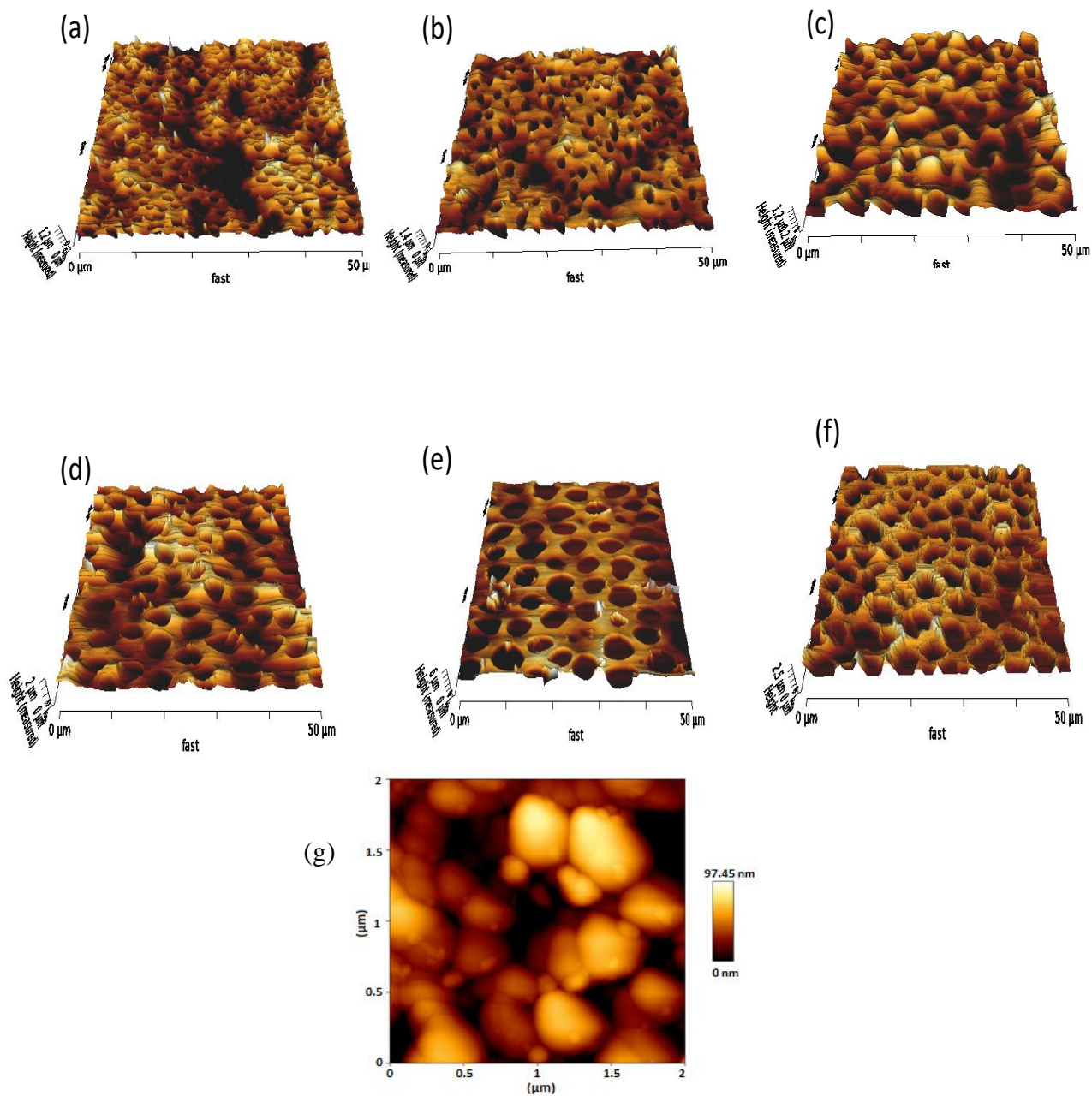


Figure A3.4. The atomic force microscopy (AFM) images of PVDF-FAPbBr₂I film with different mass ratios (wt. %) of FAPbBr₂I precursor in 10 wt. % PVDF solution (a) 5 wt. % (b) 10 wt. % (c) 15 wt. % (d) 20 wt. % (e) 25 wt. % (f) 30 wt. %. This AFM images clearly indicates the gradual increase in the pores size (diameter of up to 7 μm at 30 wt. % FAPbBr₂I) with the increase of FAPbBr₂I concentration. Interestingly the pores are generated almost in the nature of a periodic array throughout the entire film (g) grain boundary topology of FAPbBr₂I NPs (≈ 100 nm).

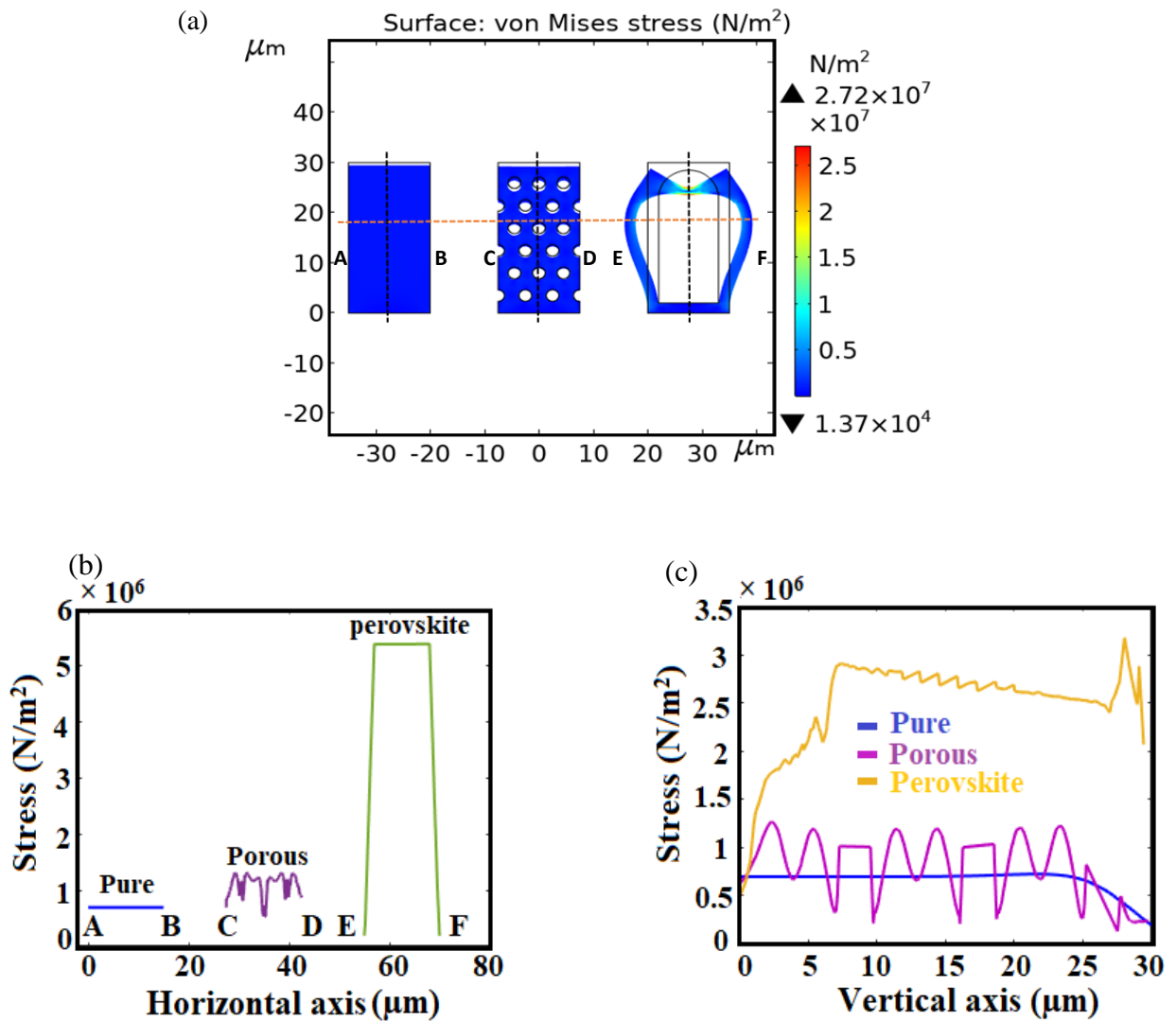


Figure A3.5. (a) Finite element simulation of the pure, the circular porous and the highly porous perovskite-polymer films under a compressive pressure of 800 kpa. The mechanical stress is calculated (b) along the horizontal axis (A-F) (c) along the vertical axis, which clearly shows a higher stress in the film with a porous structure than the non-porous (pure) film. The stress distribution is disrupted by the presence of pores inside the film and further increases with the porosity.

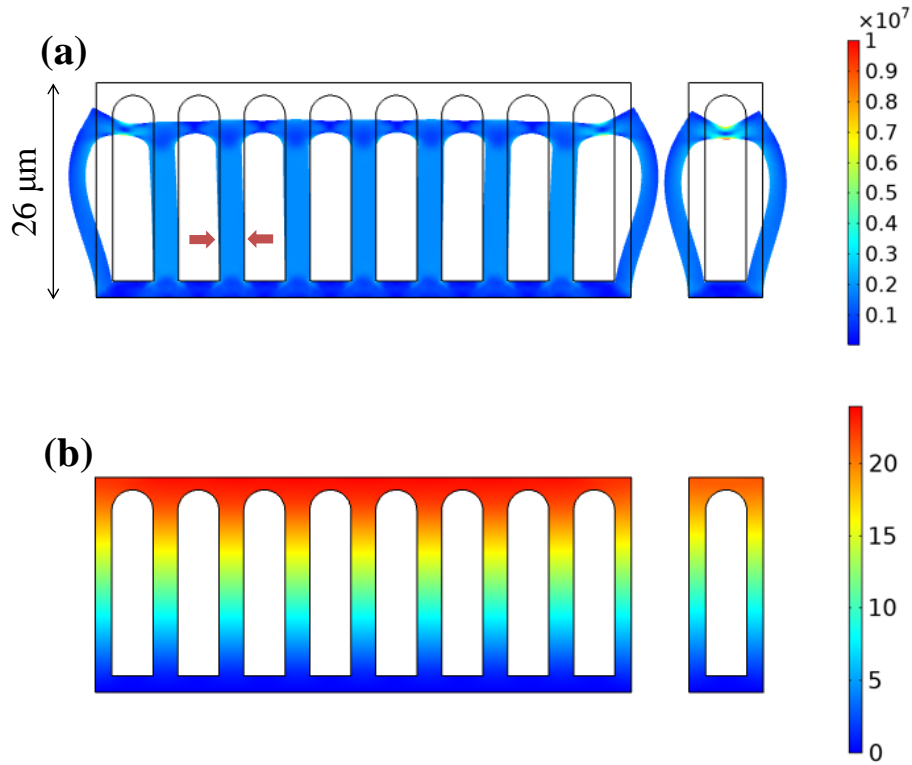


Figure A3.6. A comparison of piezo-potential distribution for porous FAPbBr₂I@PVDF (20 wt. %) film with the presence of a single and an array of pore (8 pores) structures. The shape of the pores has been optimized from the observation of cross-section SEM image of the composite film. (a) Mechanical stress distribution of the film with the array of pores (left) and the film with a single pore (right) structure. The arrows are indicating the amplified stress on the sidewall of each pore. (b) The piezo-potential distribution is higher in the film with the presence of a large number of pore structures (left).

Supporting Note A3.1: Relationship between the piezoelectric charge coefficient and the strain

The behavior of self-assembled porous perovskite-PVDF nanogenerator (NGs) can be analyzed by the fundamental piezoelectric equations. For the composite porous film in both mechanical and electrically equilibrium condition (no external force & no free charge density), the coupled constitutive law is,

$$\sigma_{ij} = C_{ijkl}^E S_{kl} - e_{nij} E_n \quad (1)$$

$$D_m = e_{mkl} S_{kl} + k_{mn}^\epsilon E_n \quad (2)$$

Here, σ_{ij} and S_{kl} are the stress and strain, E_n and D_m are the electric field and electric displacement, respectively; and C_{ijkl}^E , e_{mkl} , and k_{mn}^ε are the elastic (under a constant field), piezoelectric and dielectric tensor (under a constant stress).

For our P-PNG model, electric displacement (D_m) is strain (S_{kl}) dependent. As there is no applied electric field, equation (2) can be written as,

$$D_m = e_{mkl}S_{kl} \quad (3)$$

Therefore, the electric displacement across the device thickness direction (along 3-axis) is,

$$D_3 = e_{3kl}S_{kl} \quad (4)$$

For the P-PNG model, according to the simulation, not only the strain S_{33} along the 3-axis is contributing to the electric-displacement, a significant amount of strain S_{31} along 1-axis is influencing the net electric displacement D_3 . As a result, the equation (4) turns into,

$$D_3 = e_{333}S_{33} + |e_{331}|S_{31} \quad (5)$$

Here, $D_3 = Q/A = CV/A$ (Q is charge, C is the device capacitance, V is the output voltage from device, A is the electrode area) S_{33} can be written as, $S_{33} = z/t$ (t is the device thickness, and z is the displacement along 3-axis); And $S_{31} = x/w$ (w is the device width, and x is the displacement along 1-axis).

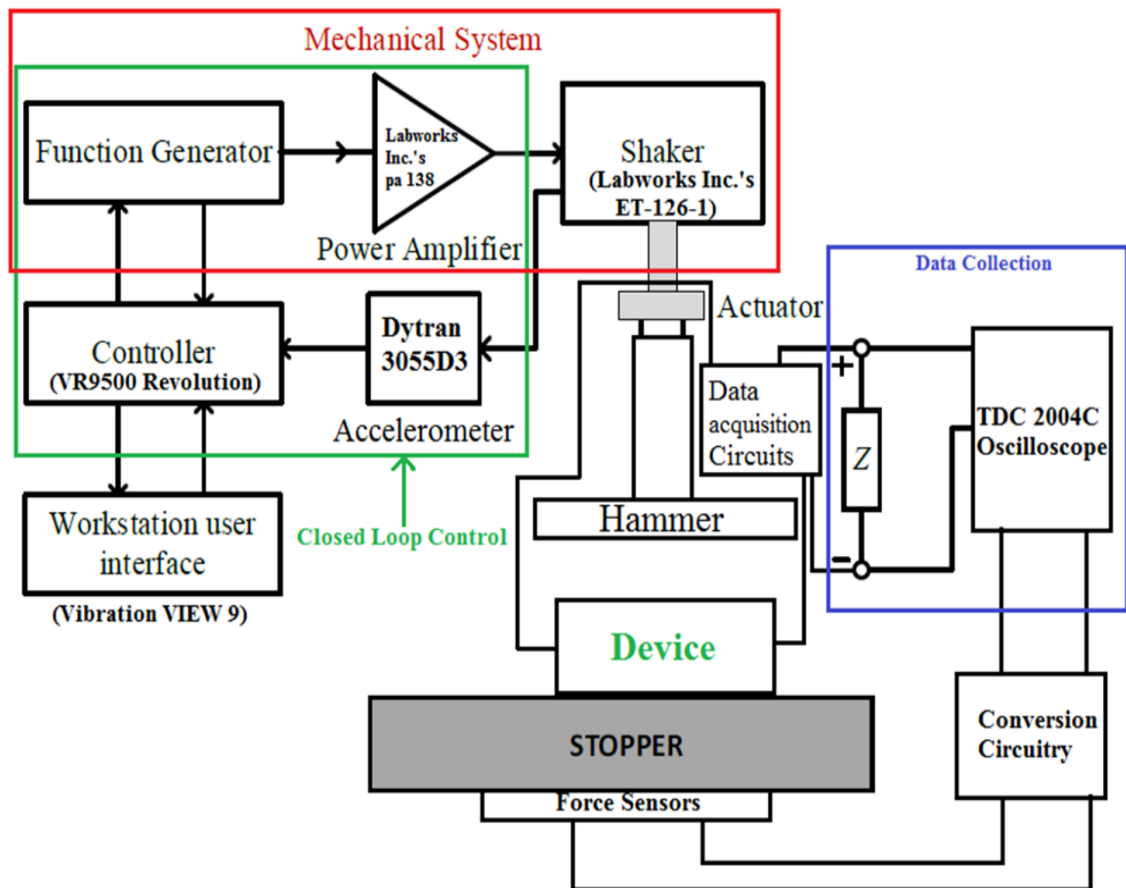


Figure A3.7. A characterization system [64] of energy harvester. The controller unit is operated by a workstation interface (Vibration View 9). The controller unit (VR 9500) generates different control signals which are amplified by a power amplifier (Lab Works Inc.'s pa 138) to feed an electrodynamic shaker (ET-126-1) to control its motion. An accelerometer (3055D3) provides the feedback signal from the shaker to the controller unit which can take actions if there are any faults. The shaker is mechanically coupled with a metallic hammer to characterize the energy harvesting devices. The output from the devices is measured and viewed by an oscilloscope.

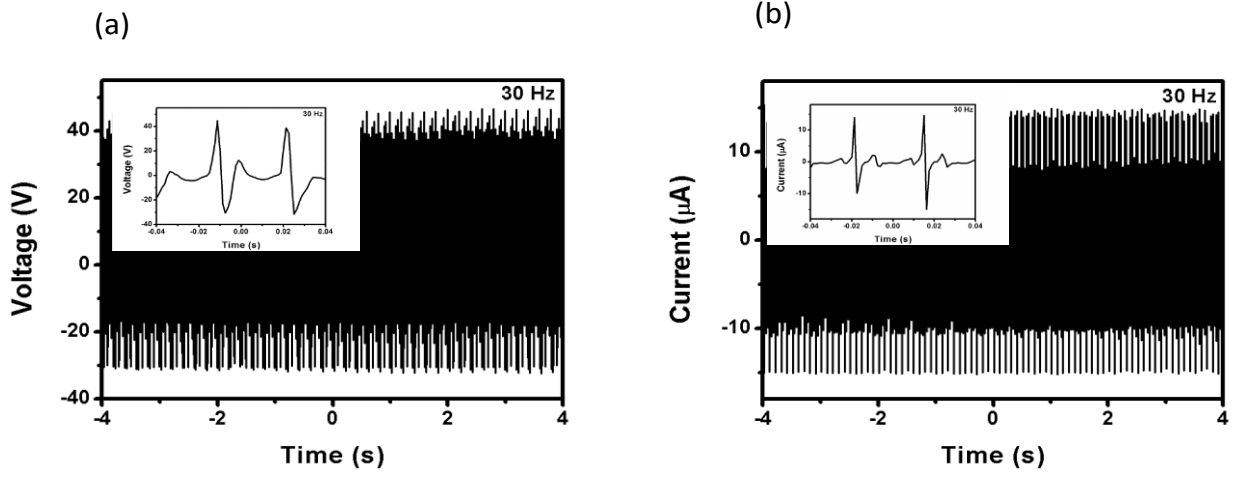


Figure A3.8. Output performance of the P-PNGs. (a) output voltage and (b) current of the P-PNG at 30 Hz and 2G acceleration with an applied load of 138 gram (g).

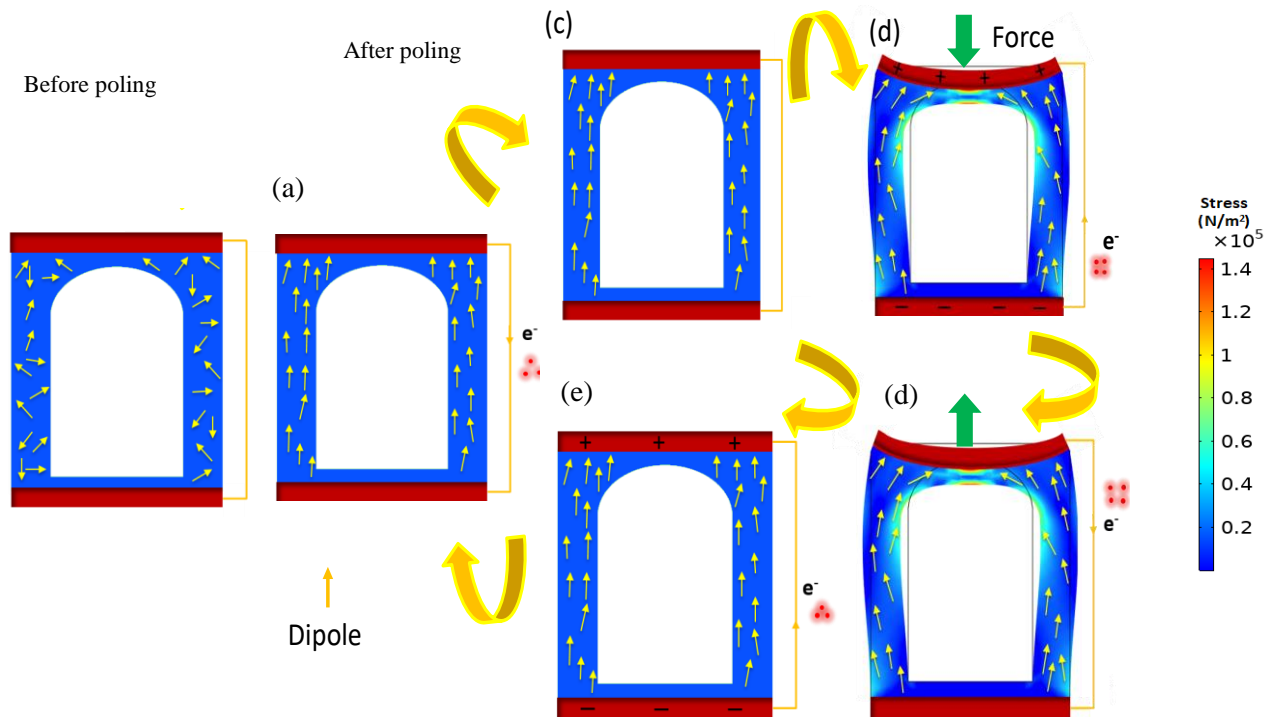


Figure A3.9. Schematics of energy generation mechanisms of the P-PNGs based on distributed stress profile.

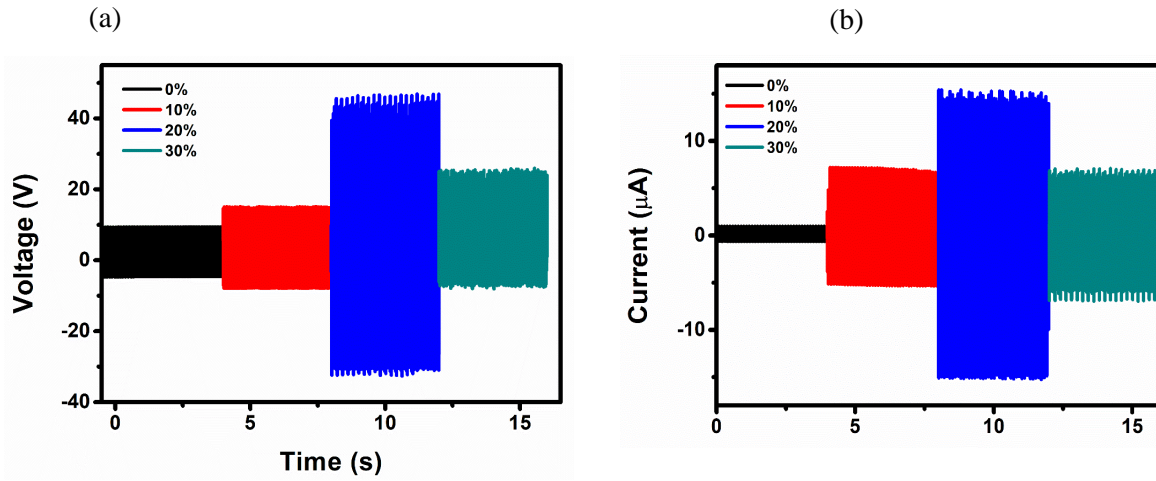


Figure A3.10. Variation of output voltage (left) and output current (right) of the P-PNGs with different FAPbBr₂I mass ratios (0 wt.%, 10 wt.%, 20 wt.%, 30 wt. %). The maximum output voltage (85 V) and current (30 μA) was obtained for 20 wt. % FAPbBr₂I@PVDF composites. The output voltage and current increases up to the mass ratio of 20 wt.%, and then decreases afterwards. The higher mass ratio of FAPbBr₂I (> 20 wt. %) will generate very large pores to greatly reduce PVDF per unit volume and create more defects.

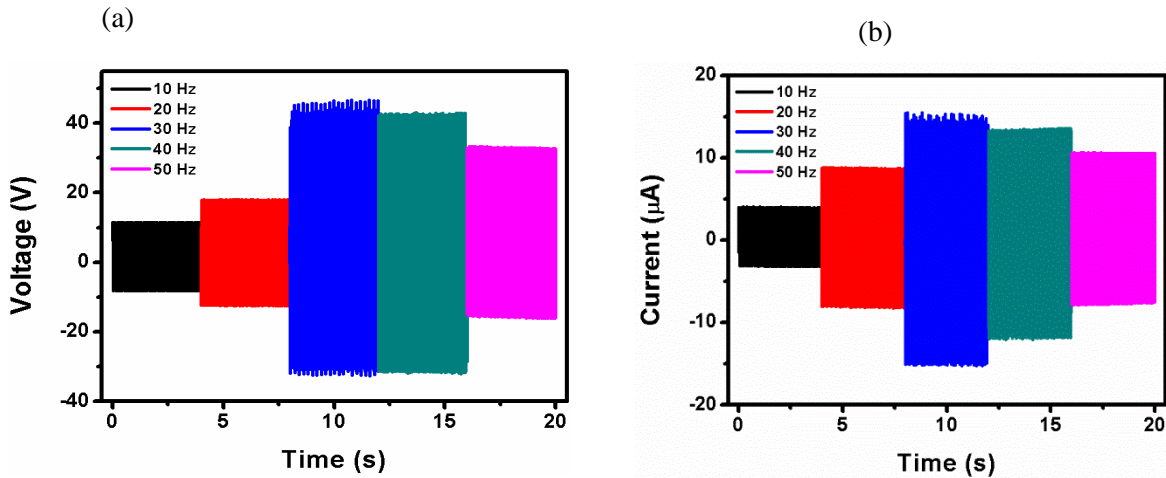
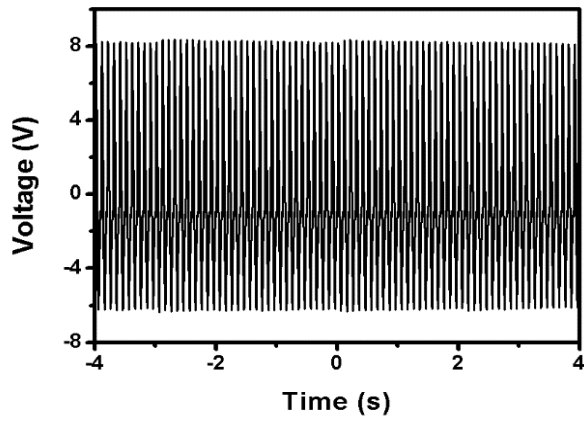


Figure A3.11. Frequency dependent (10-50 Hz) output voltage (left) and output current (right) of the 20 wt. % FAPbBr₂I@PVDF based P-PNGs, when the acceleration is fixed at 2G. The maximum output voltage and output current at 30 Hz frequency was 85 V and 30 μA, respectively. As the frequency increases the strain rate rises and causing the increase in the output voltage and current. The gradual decrease in the output at higher frequencies (> 30 Hz) corresponds to the reduction of impact on the device by the 138-gram (g) proof mass.

(a)



(b)

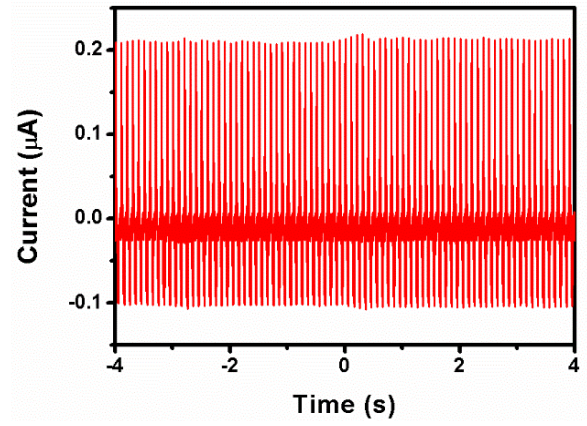


Figure A3.12. Flexibility test of the P-PNGs at 10 Hz and 2G acceleration when a periodic bending force was applied from an electrodynamic shaker. The generated (a) output voltage (b) output current of 14 V and 0.3 μA , respectively, depicts the performance of the P-PNG during the bending condition.

Table A3.1 A Comparison of output performance of the state-of-the-art PNG devices

Active material of PNGs	Film thickness (μm)	Applied force (N)/pressure (Mpa)	Frequency (Hz)	Output voltage (V)	Output current (μA)/current density ($\mu\text{A}/\text{cm}^2$)	References
FaPbBr ₃ -PDMS	150	0.5 Mpa	7	8.5	3.8 $\mu\text{A}/\text{cm}^2$	267
NaNbO ₃ -PDMS	100	[-]	<1	3.2	0.072 μA	250
PMN-PT-PDMS	150	Hand-tapping	5	7.8	2.29 μA	251
FAPbBr ₃ -PVDF	120	0.5 Mpa	5	30	6.2 $\mu\text{A}/\text{cm}^2$	265
MAPbBr ₃ -PVDF	[-]	Finger tapping	2	5	0.06 μA	264
MAPbI ₃ -PVDF	6	0.5 Mpa	5	17.8	2.1 $\mu\text{A}/\text{cm}^2$	266
PZT-NH ₂ /SM	200	[-]	<1	65	1.6 μA	263
FAPbBr₂I-PVDF	30	1.35 N	30	85	30 μA	This work

Appendix for Chapter 4

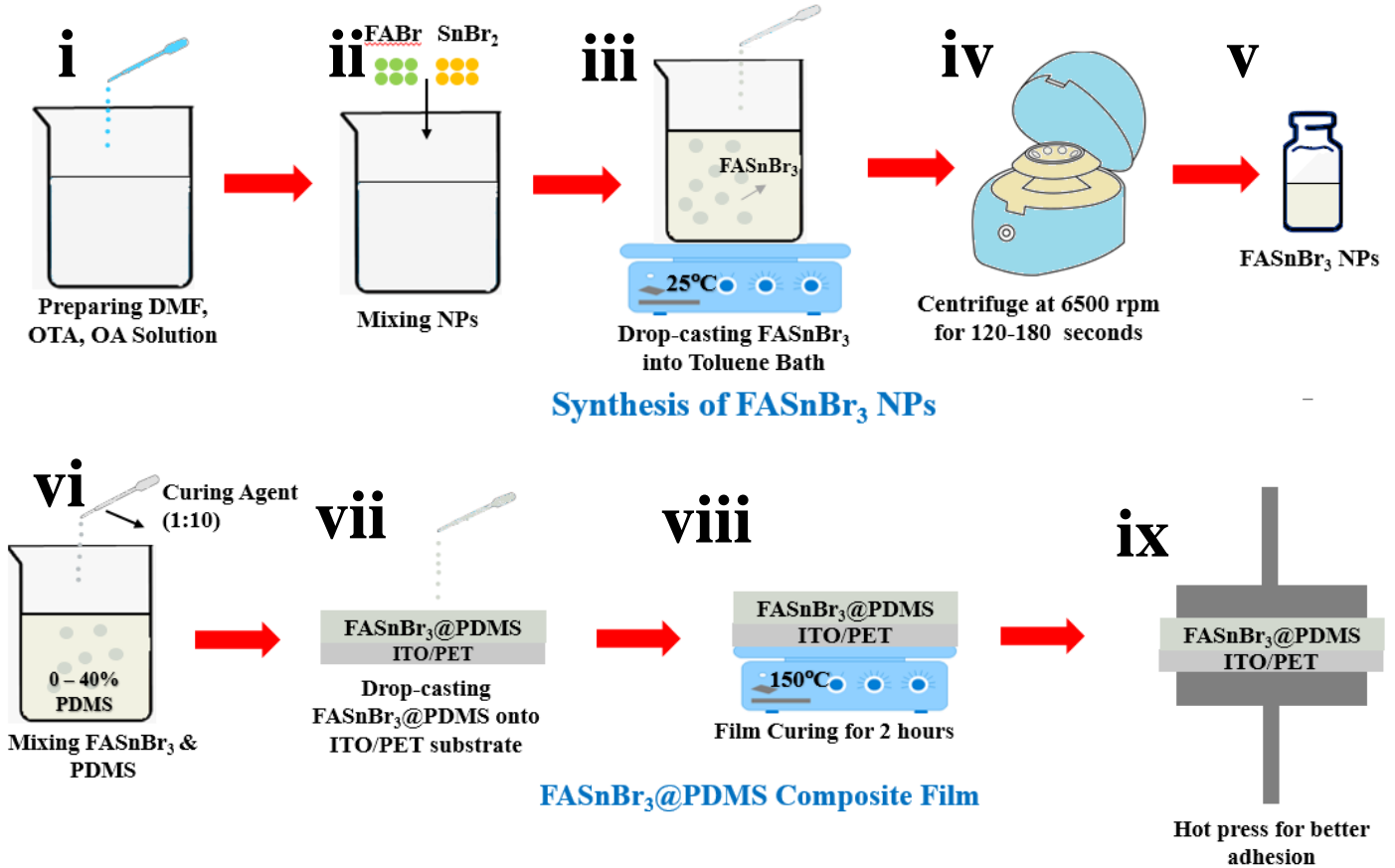


Figure A4.1a. (i-v) Step by step synthesis process of FASnBr_3 NPs. (vi-ix) Details of FASnBr_3 @PDMS composite film preparation.

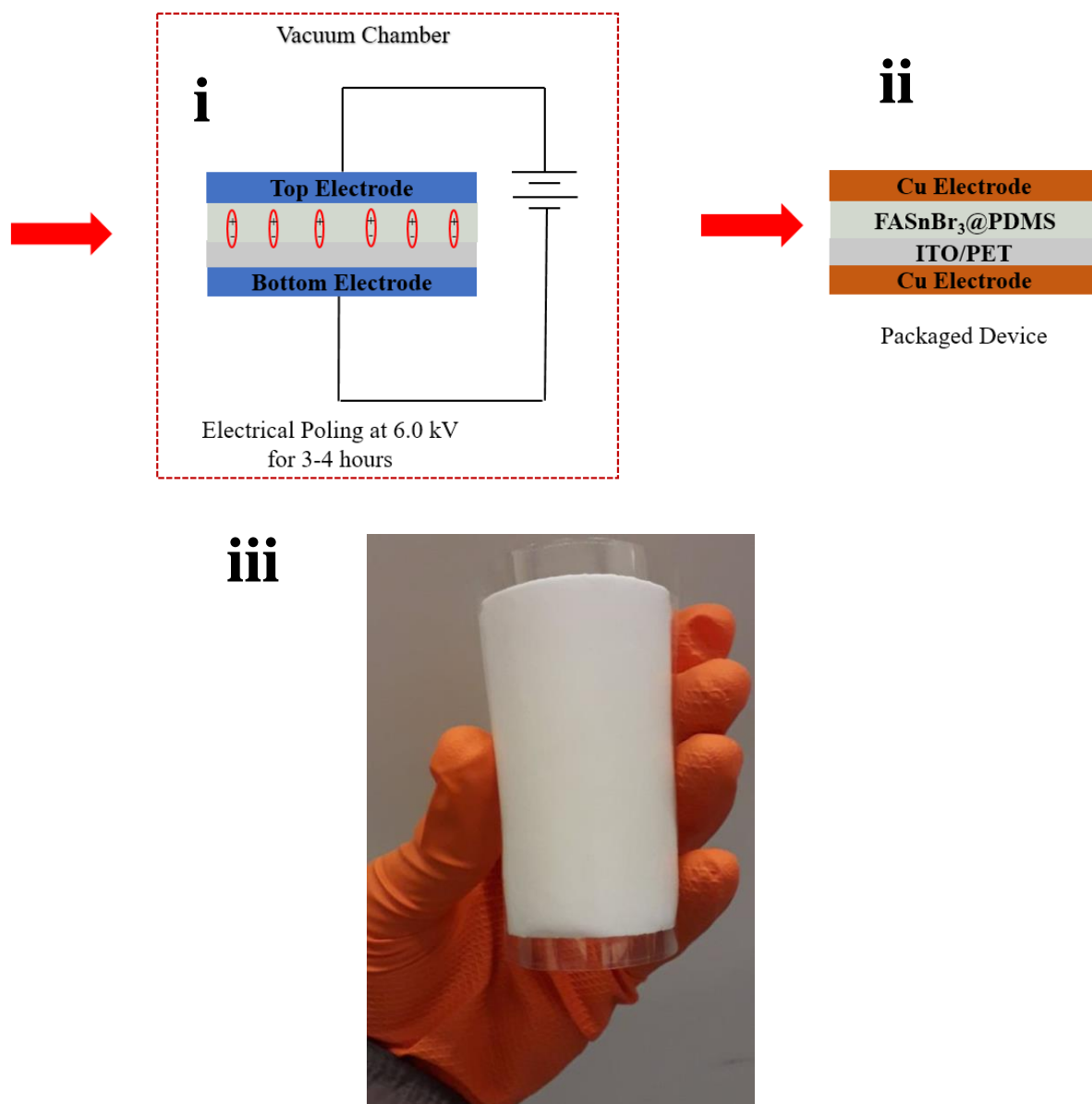


Figure A4.1b. (i) Electrical polling of the composite film at 6kV for 3-4 hours (ii) Schematic of packaged device with different layers (iii) Original fabricated composite film

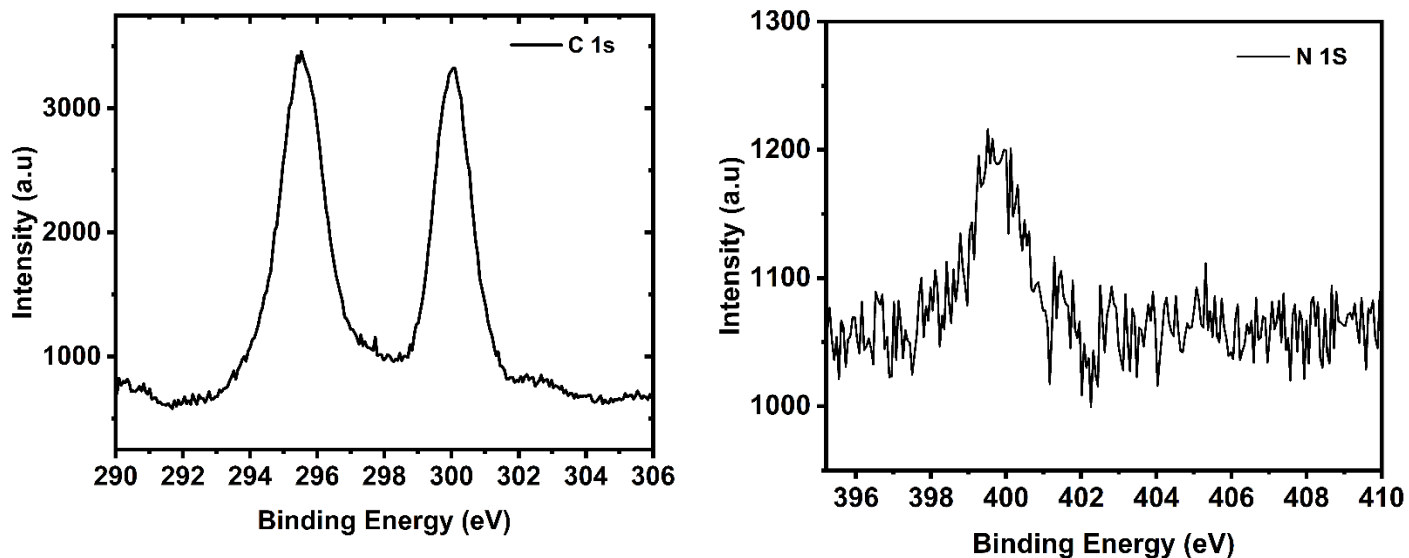


Figure A4.2. XPS spectra of C1s and N1s

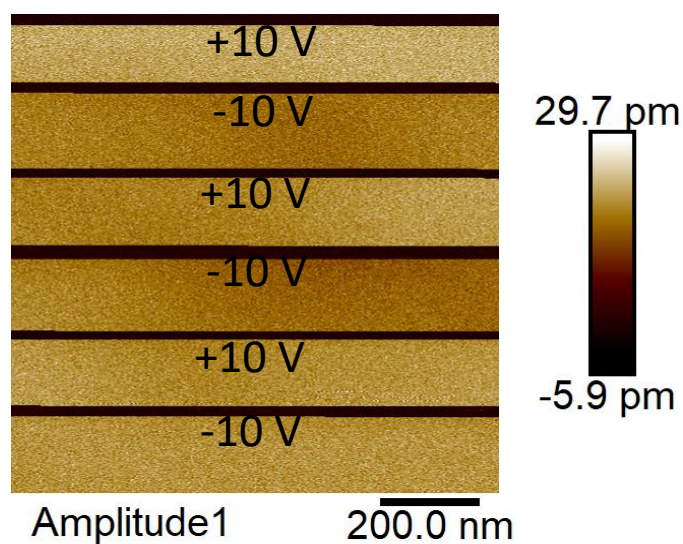


Figure A4.3. Verification of polling effect to confirm the dipole formation inside the composite NPs

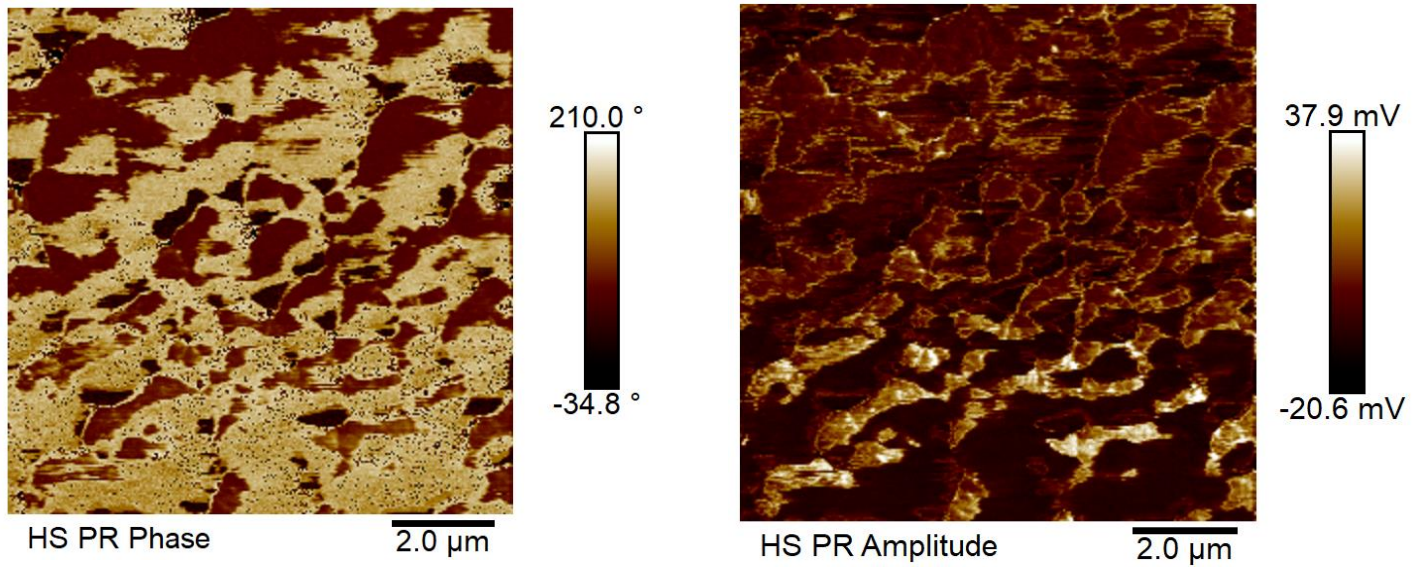


Figure A4.4. (a) Lateral PFM amplitude and (b) Lateral phase images of the FASnBr_3 NPs, the weak signals obtained in the L-PFM images indicates the weak polarization magnitudes in that direction.

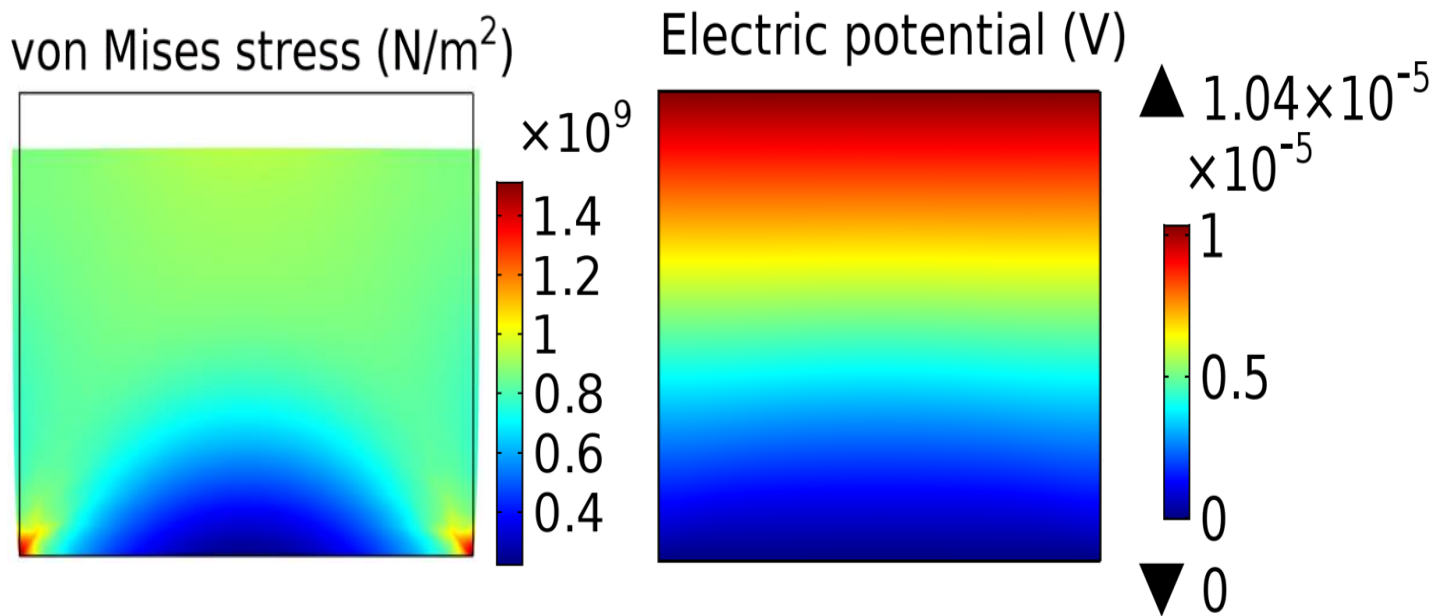


Figure A4.5. (a) the strain distribution of pure PDMS matrix, (b) the piezopotential distribution of pure PDMS matrix.

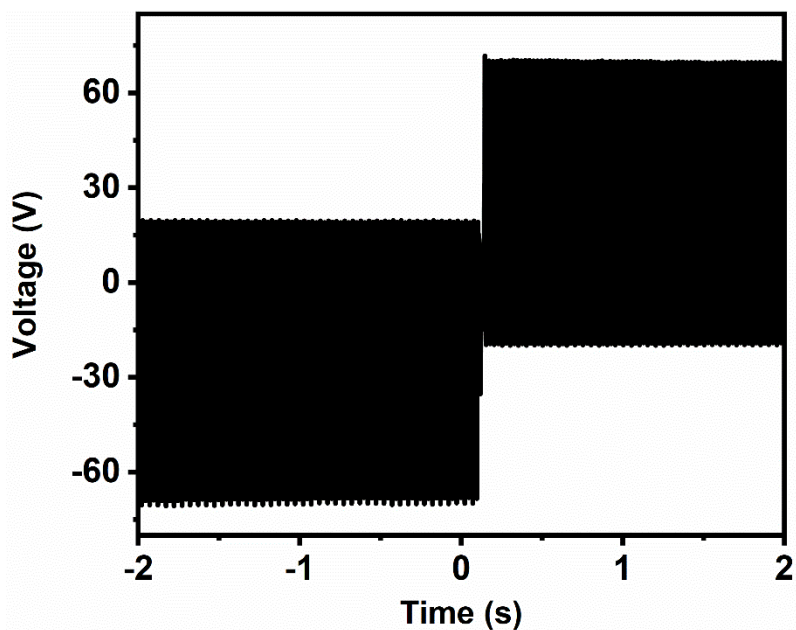


Figure A4.6. polarity switch testing of open circuit voltage to confirm piezoelectricity

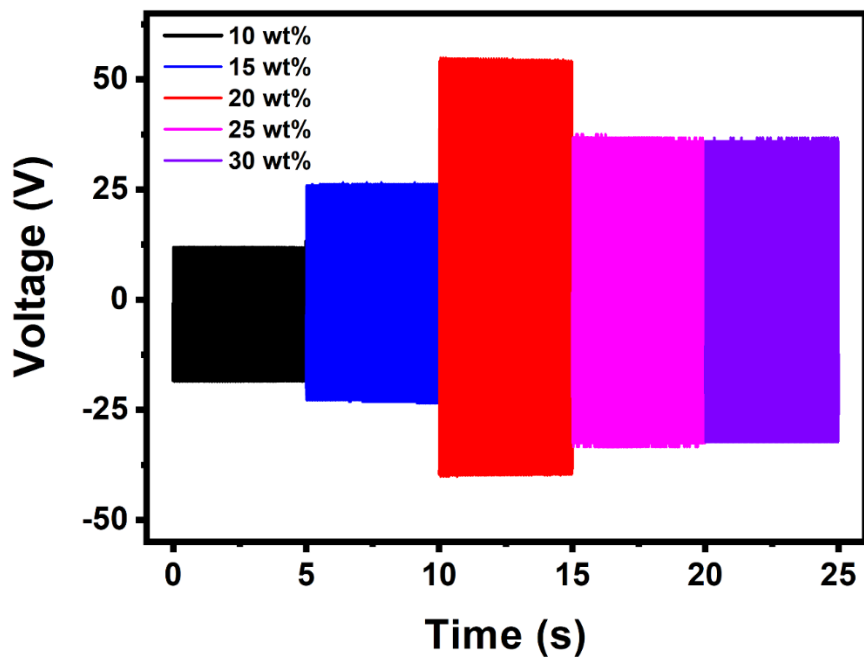


Figure A4.7. Measured electrical output performance of FASnBr₃@PDMS PENG device: (a) the measured open-circuit voltage of composite FASnBr₃@PDMS PENG when FASnBr₃ mass fraction increased from 10 wt. % to 30 wt. %, with a frequency of 40Hz.

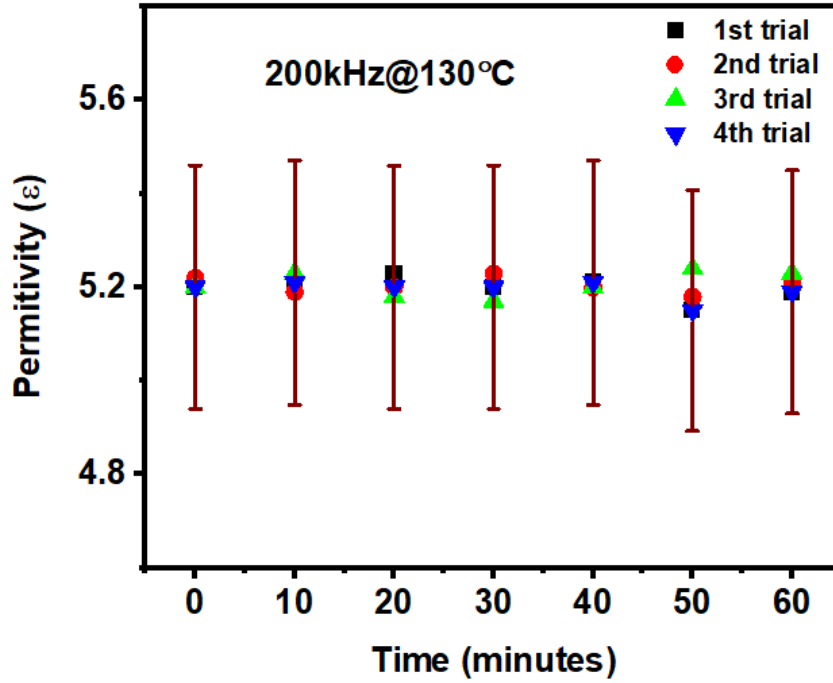


Figure A4.8. Thermal stability of the relative permittivity is measured for one hour at 130 °C, and 200 kHz for the 20 wt. % FASnBr₃@PDMS composite film. The relative permittivity showed a negligible change in their values.

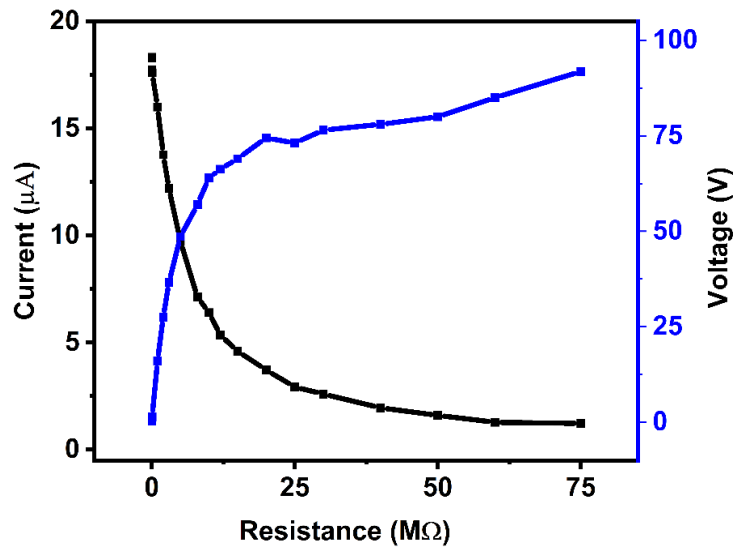


Figure A4.9. Load resistance dependent voltage and current measurement.

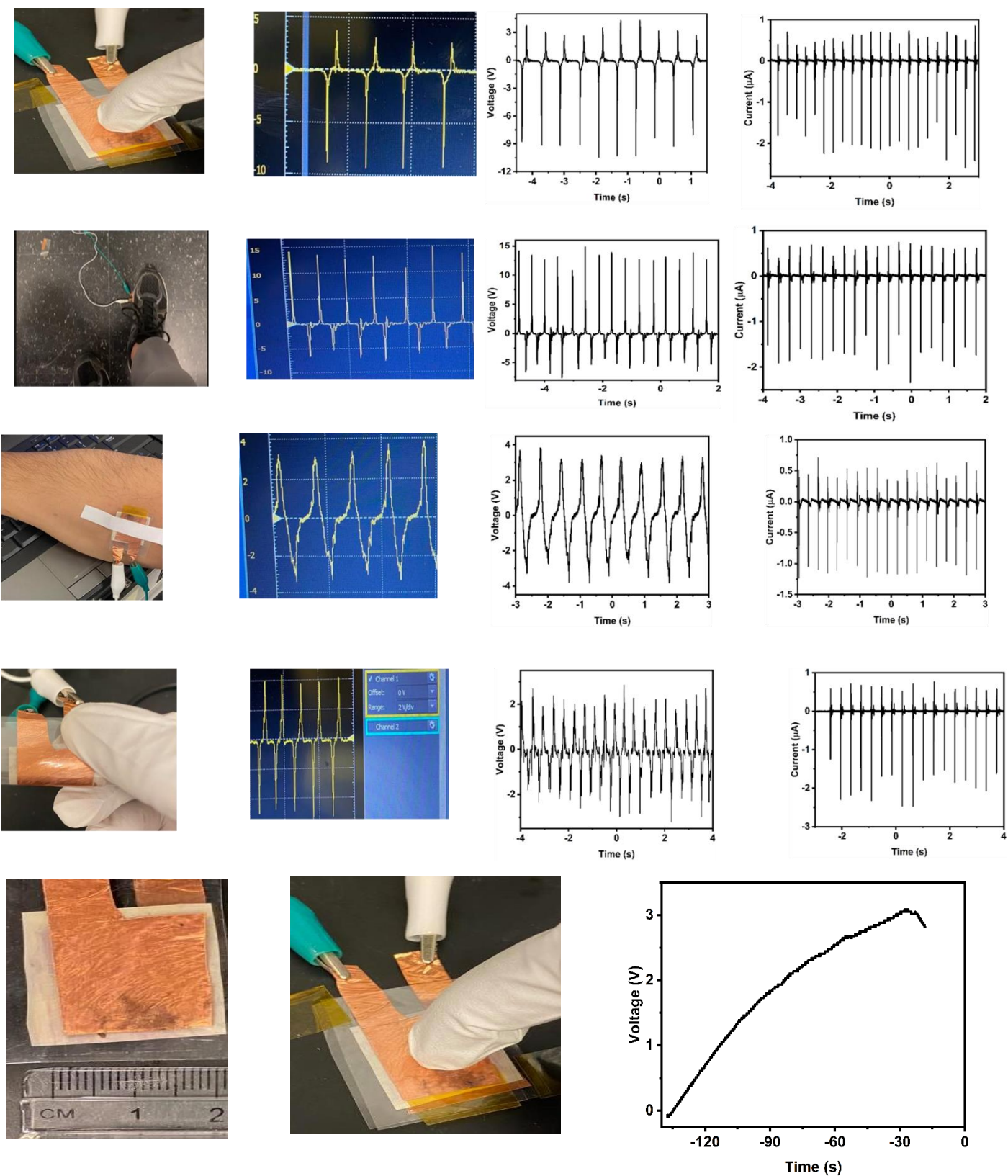


Figure A4.10. Energy harvesting from (i) Single finger tapping (ii) Foot stepping (iii) Hand gesture (iv) bending the device (v) device size (vi) charging by using only finger tapping.

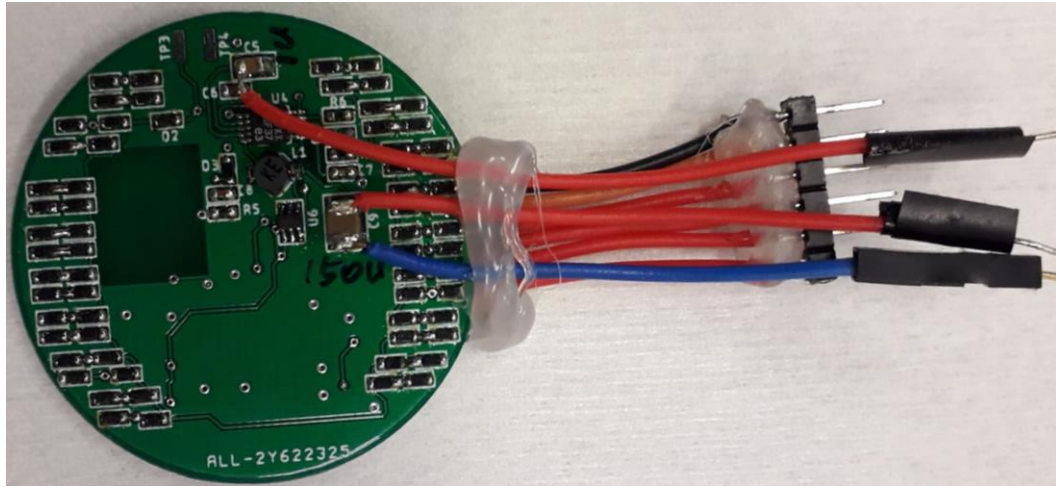


Figure A4.11. Custom made wireless signal transmission circuit

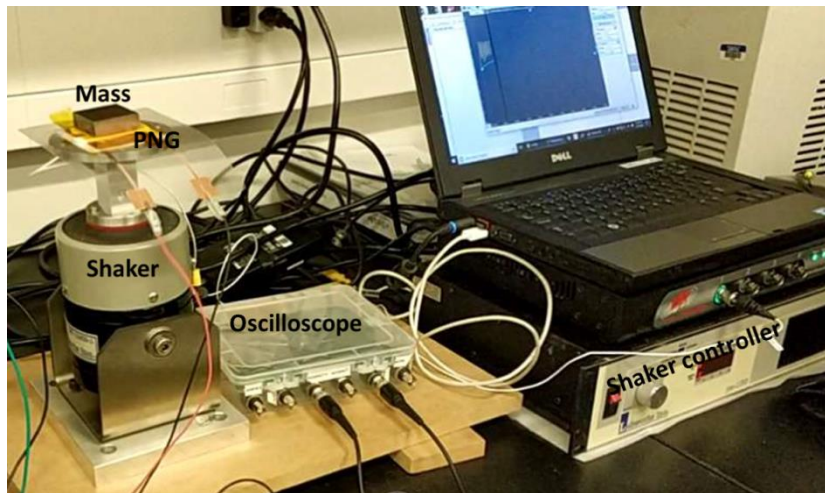


Figure A4.12. a photograph of the PENG characterization set-up, including mass, PENG, electrodynamic shaker, oscilloscope, shaker controller and the control software.

Table A4.1 output performance comparison of PENGs based on PDMS.

Piezoelectric Materials	Pressure (MPa)	V _{oc} (V)	J _{sc} (μA/cm ²)	Power density (μW/cm ²)	Growth Temperature	Ref.
BCZT	0.085	30	0.6	N/A	high	4
BaTiO ₃	0.002	2.7	0.26	0.12	high	5
ZnSnO ₃	rolling tire	20	1	N/A	high	6
BiFeO ₃	0.01	3	0.25	N/A	high	7
PMN-PT	tapping	7.8	4.6	N/A	high	8
Sm-PMN-PT	0.35	60	0.85	11.5	high	9
KNN-BNZ-AS-Fe	0.0625	52	1.2	N/A	high	10
FAPbBr ₃	0.5	8.5	3.8	12	low	11
MAPb _x Fe _(1-x) I ₃	0.5	7.3	0.88	N/A	low	12
(ATHP) ₂ PbBr ₂ Cl ₂	4.66 kPa	74	6.5 μA	1.7	low	13
FASnBr₃	4.2 N	94.5	19.1 μA	18.95	low	This work

- [1] C. Zhang, J. Chen, S. Wang, L. Kong, S. W. Lewis, X. Yang, A. L. Rogach, G. Jia, *Adv. Mater.* **2020**, 32, 2002736.
- [2] W. Liu, J. Zheng, S. Cao, L. Wang, F. Gao, K. C. Chou, X. Hou, W. Yang, *Inorg. Chem.* **2018**, 57, 1598.
- [3] Y. Tong, E. Bladt, M. F. Aygüler, A. Manzi, K. Z. Milowska, V. A. Hintermayr, P. Docampo, S. Bals, A. S. Urban, L. Polavarapu, J. Feldmann, *Angew. Chem., Int. Ed.* **2016**, 55, 13887.
- [4] X. Gao, M. Zheng, X. Yan, J. Fu, M. Zhu and Y. Hou, *J. Mater. Chem. C*, **2019**, 7, 961.

- [5] J. Yan and Y. G. Jeong, *ACS Appl. Mater. Interfaces*, **2016**, 8, 15700.
- [6] K. Y. Lee, D. Kim, J.-H. Lee, T. Y. Kim, M. K. Gupta and S.-W. Kim, *Adv. Funct. Mater.*, **2014**, 24, 37.
- [7] X. Ren, H. Fan, Y. Zhao and Z. Liu, *ACS Appl. Mater. Interfaces*, **2016**, 8, 26190.
- [8] S. Xu, Y. W. Yeh, G. Poirier, M. C. McAlpine, R. A. Register and N. Yao, *Nano. Lett.*, 2013, 13, 2393.
- [9] Y. Zhang, C. K. Jeong, J. Wang, H. Sun, F. Li, G. Zhang, L.-Q. Chen, S. Zhang, W. Chen and Q. Wang, *Nano Energy*, 2018, 50, 35.
- [10] M. Wu, T. Zheng, H. Zheng, J. Li, W. Wang, M. Zhu, F. Li, G. Yue, Y. Gu and J. Wu, *J. Mater. Chem. A*, 2018, 6, 16439.
- [11] R. Ding, H. Liu, X. Zhang, J. Xiao, R. Kishor, H. Sun, B. Zhu, G. Chen, F. Gao, X. Feng, J. Chen, X. Chen, X. Sun and Y. Zheng, *Adv. Funct. Mater.*, 2016, 26, 7708.
- [12] S. Ippili, V. Jella, J. Kim, S. Hong and S.-G. Yoon, *Nano Energy*, 2018, 49, 247.
- [13] A. A. Khan, G. Huang, M. M. Rana, N. Mei, M. Biondi, S. Rassel, N. Tanguy, B. Sun, Z. Leonenko, N. Ying, C. Wang, S. Xu, D. Ban., *Nano energy*, 2021. 86, 106039

Appendix for Chapter 5

Supporting note A5.1

Both CNF and LCNF nanopapers contained C=O and OH-C=O moieties that can be the product of side reactions taking place during the nanofibrillation step (**Figure 5.1b**, **Figure A5.1a**). The harsh conditions during the fibrillation step causes the formation of highly reactive free radicals that can lead to a decrease in the cellulose crystallinity and degree of polymerization [1]. The higher content of C=O moieties (ca. 13.55 %) observed in CNF as compared to LCNF (ca. 4.81%) (**Table A5.1**) indicated that a greater extent of side reactions (i.e. oxidation, recombination, cross-linking) took place during CNF production. This outcome may be explained by the radical scavenging capabilities of lignin, [2] which in this case may have mitigated some of the side reactions during nanofibrillation process [3]. Interestingly, smaller diameters were measured for the unbleached (ca. 16 nm) nanofibrils as compared to the bleached (ca. 30 nm) ones. This could be explained by the radical scavenging ability of lignin on the nanofibrils that mitigated side reactions during production, including cross-linking between the cellulose nanofibrils [3]. SEM cross-section images displayed the anticipated layered structures for the CNF nanopapers, while it was not evident for LCNF nanopaper (**Figure 5.1e**). The mechanical properties of the nanopapers, discussed here in terms of storage and loss moduli, are shown in **Figure A5.2a-b**. This results indicated that the lignin bound on the surface of the nanofibrils reduced the mechanical properties of the LCNF nanopaper as compared to CNF nanopaper, which may be explained by the lower amount of cellulose in LCNF, which impedes the formation of intra- and inter-molecular hydrogen bonds between nanofibrils that could reduce the mechanical performance of the LCNF nanopapers [3-5]. Despite the hydrophobic nature of lignin, LCNF nanopaper had a lower water contact angle (67°) than the pristine CNF one (85°) (**Figure 5.1f & Figure A5.2c**), which conflicts with observations in previous studies [3, 4, 7]. It is argued that the observed outcome can be explained by the differences in both nanopapers' surface roughness and porosities. As previously discussed, CNF can form abundant hydrogen bonds inter and intra nanofibrils that enable packing tightly and a smoother surface. This assembly can reduce the number of hydroxy moieties available for instantaneous interaction with water during testing, therefore leading to a high instantaneous water contact angle on the surface of the nanopaper. In comparison, the large surface roughness and pores on the LCNF nanopaper surface together with the limited inter-nanofibrils interactions due to lignin presence could facilitate the accommodation of water droplets on the surface and result in a lower water contact angle.

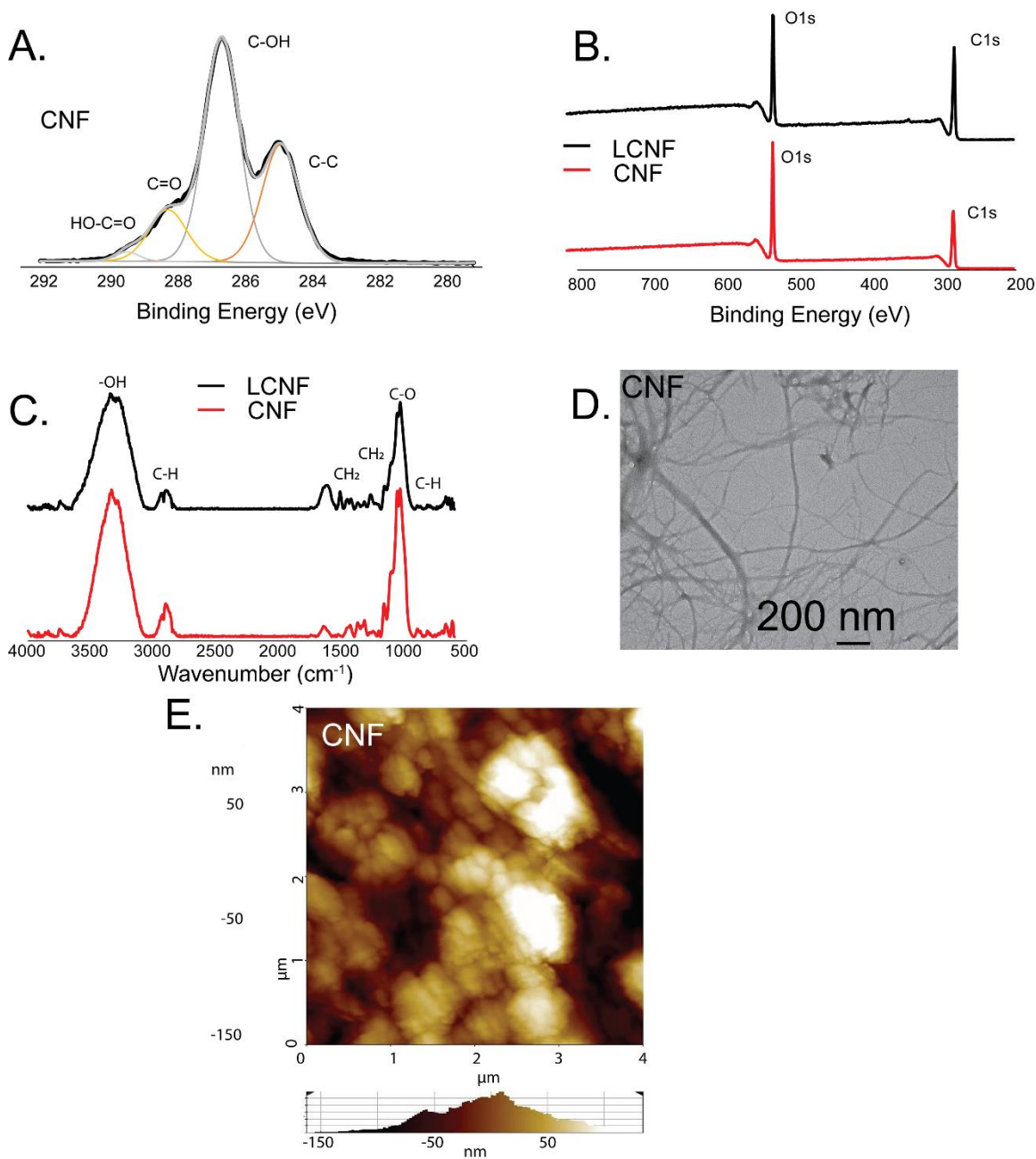


Figure A5.1. a. XPS C 1s deconvoluted spectra of CNF nanpaper, b. XPS survey and c. ATR spectrum, d. TEM image of CNFs, e. AFM results of CNF film.

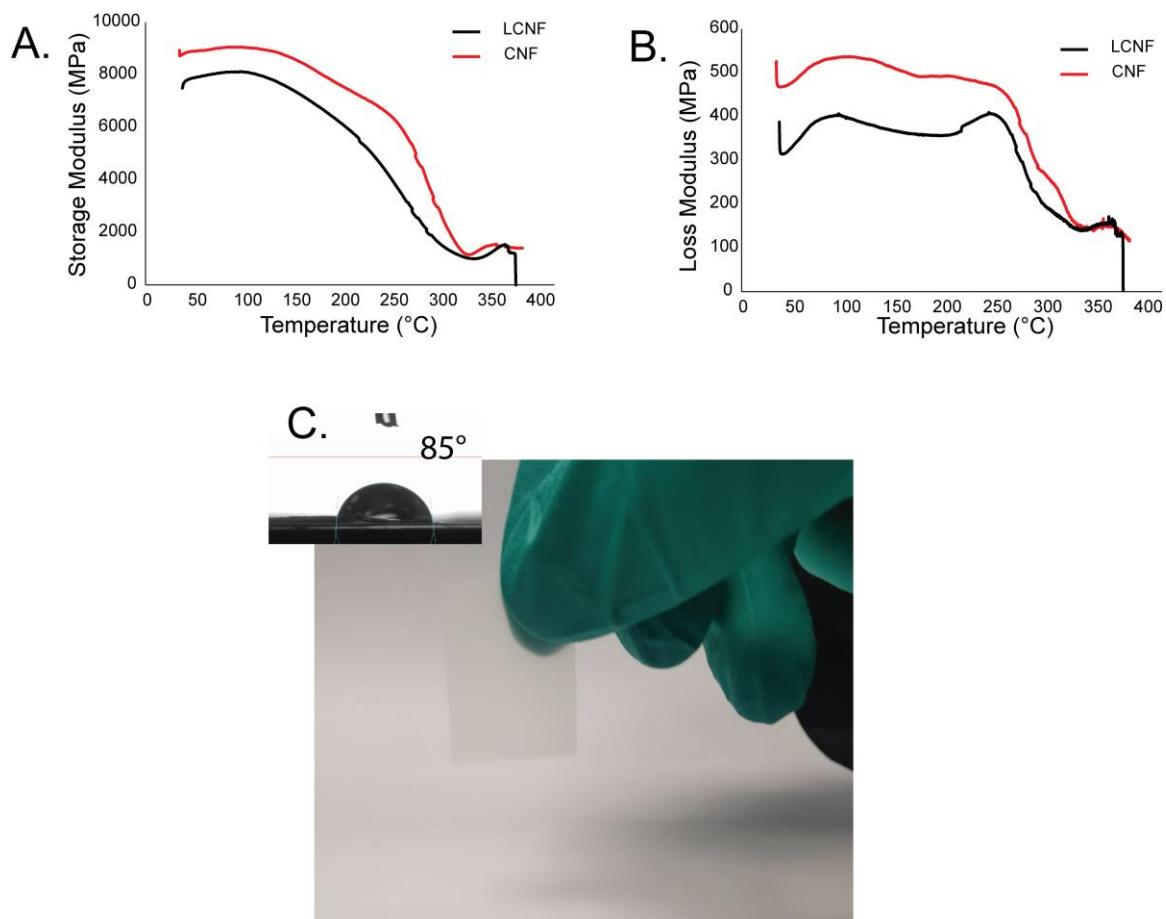


Figure A5.2. DMA results of CNF and LCNF film a. Storage modulus and b. loss modulus, c. photo of CNF film and associated contact angle results.

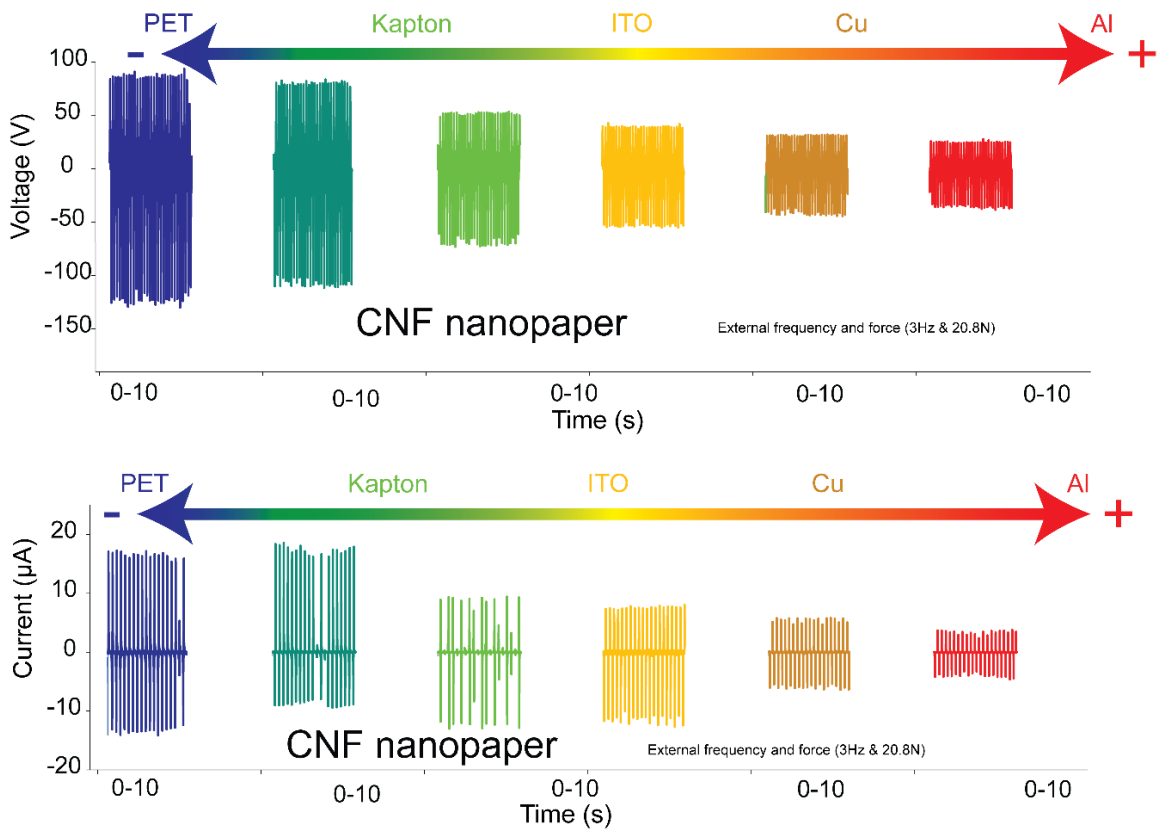


Figure A5.3. Open-circuit voltage and short-circuit current between CNF nanopaper and various materials.

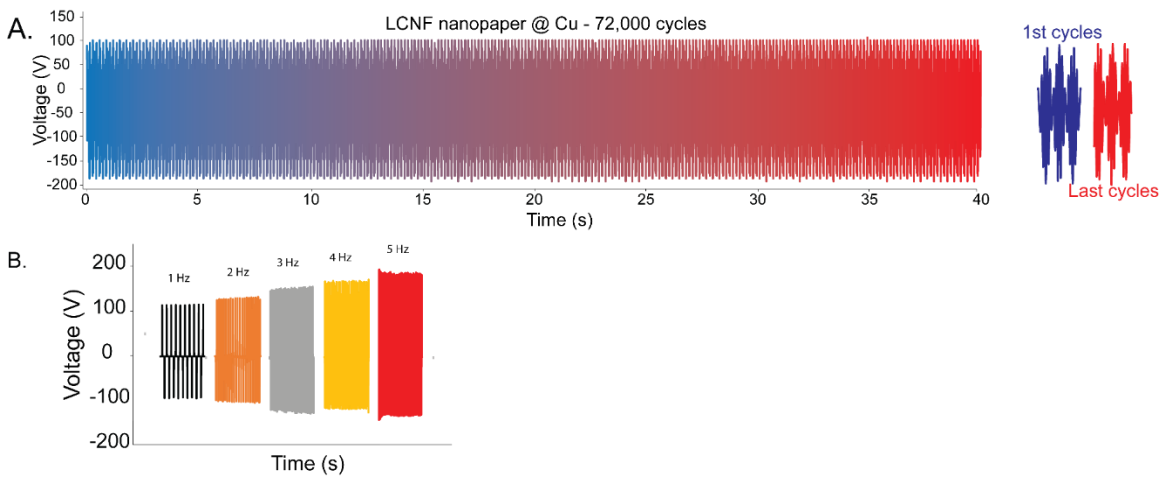


Figure A5.4. a. Reliability testing of the output voltage of LCNF nanopaper/Cu TENG (30 Hz, 4.2 N), b. Open circuit voltage of LCNF nanopaper/Cu at different test frequencies.

External frequency and force (3Hz & 13N)

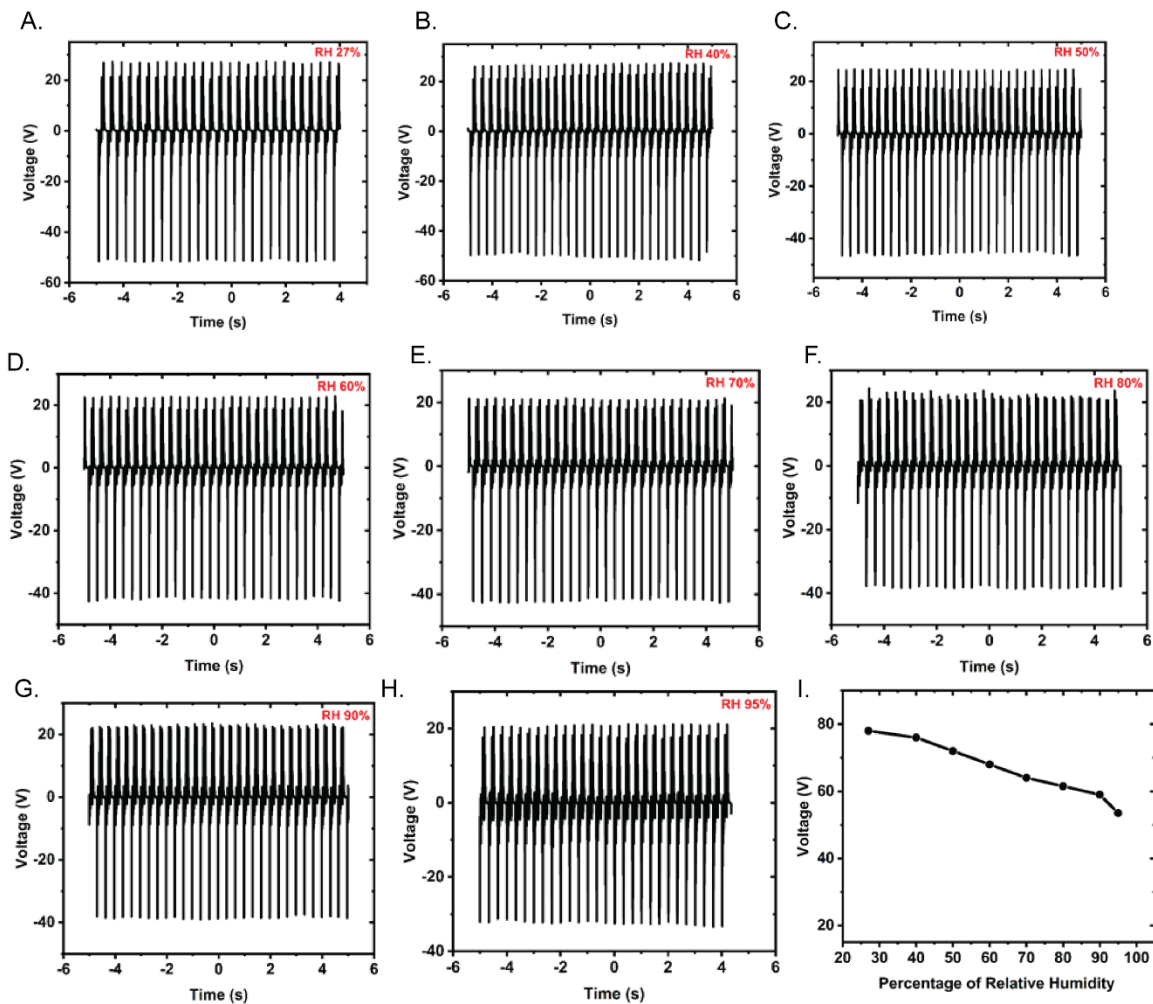


Figure A5.5. Output voltage of LCNF nanopaper/Cu TENG at various %RH levels, a) 27%, b) 40%, c) 50%, d) 60%, e) 70%, f) 80%, g) 90%, h) 95%, and i) TENG voltage outputs plotted against RH levels.

External frequency and force (5Hz & 13N)

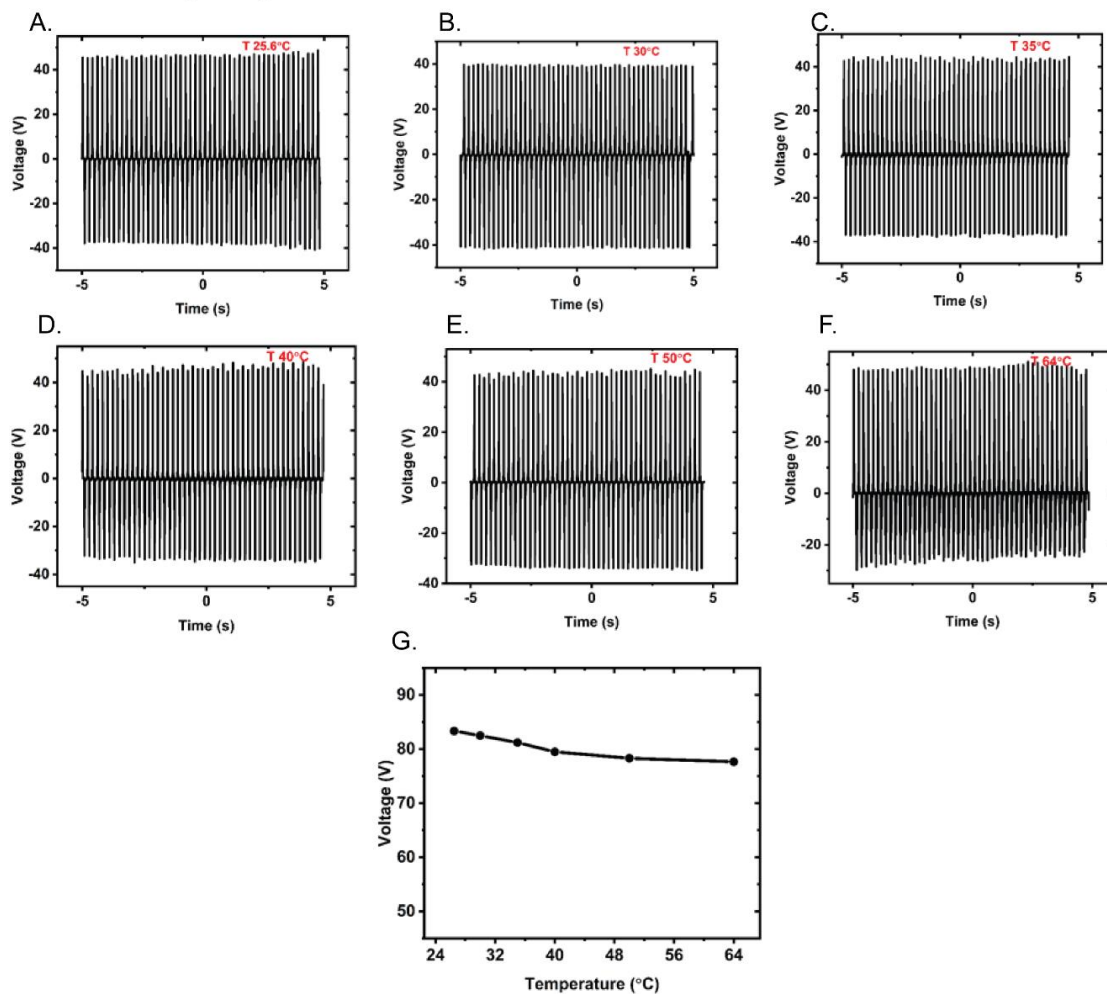


Figure A5.6. Output voltage of LCNF nanopaper/Cu TENG at various temperatures, a) 25.6°C, b) 30°C, c) 35°C, d) 40°C, e) 50°C, f) 64°C, g) TENG voltage outputs against temperature.

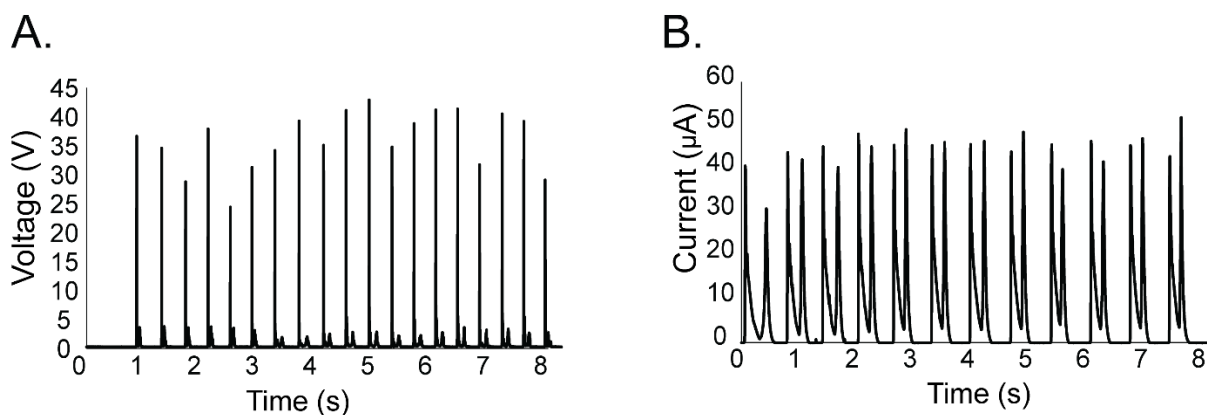


Figure A5.7. Rectified voltage a. and current b. output of LCNF/Al based cascade-type TENG (CTENG) device.

Table A5.1. X-ray photoelectron spectroscopy (XPS) peak positions data for C 1s line of nanopapers. Band C 1s was deconvoluted into five peaks.

Sample type	Component Assignment	Peak BE (eV)	Atomic Conc. (%)
CNF	C-C	284.83	30.93
	C-OH	286.58	54.04
	C=O	288.18	13.55
	OH-C=O	289.38	1.49
LCNF	C-C	284.68	66.44
	C-OH	286.48	26.84
	C=O	287.98	4.81
	OH-C=O	288.98	1.91

Table A5.2. X-ray photoelectron spectroscopy (XPS) survey results. Atomic concentration of carbon and oxygen in CNF and LCNF nanopapers.

Sample type	Component	Peak BE (eV)	Atomic Conc. (%)
CNF	C	286.25	62.3
	O	532.98	37.7
LCNF	C	292.58	69.2
	O	538.58	30.8

Table A5.3 Comparison of output performances of TENGs using unpatterned metal as the tribopositive layer

Tribopositive layer (+)	Tribonegative layer (-)	Output power density	Short-circuit current density	Open-circuit voltage	Conditions	Ref
Nickel	Nitro CNF	0.09 W/m ²	1.2 μ A/cm ²	35 V	3 N & 5 Hz	⁸
Cu	CNF	0.0048 W/m ²	0.44 μ A/cm ²	13 V	16.8 N & 1 Hz	⁹
Cu-Ni alloy	PTFE	45 μ W/cm ²	1 μ A/cm ²	196.8 V	NA & 6 Hz	¹⁰
Au*	PTFE	10 μ W/cm ²	0.20 μ A/cm ²	45 V	NA	¹¹
Cu	LCNF	52 μ W/cm ²	11.1 μ A/cm ²	300 V	20.8 N & 5 Hz	**

* Piezo-tribo configuration

** This work

References

- [1] Nair, S. S.; Zhu, J. Y.; Deng, Y.; Ragauskas, A. J. *J. Nanoparticle Res.* **2014**, *16* (4), 2349. <https://doi.org/10.1007/s11051-014-2349-7>.
- [2] Dizhbite, T.; Telysheva, G.; Jurkjane, V.; Viesturs, U. C. *Bioresour. Technol.* **2004**, *95* (3), 309–317.
- [3] Rojo, E.; Peresin, M. S.; Sampson, W. W.; Hoeger, I. C.; Vartiainen, J.; Laine, J.; Rojas, O. J. *Green Chem.* **2015**, *17* (3), 1853–1866.
- [4] Sirviö, J. A.; Ismail, M. Y.; Zhang, K.; Tejesvi, M. V.; Ämmälä, A. *J. Mater. Chem. A*, **2020**, *8*, 7935–7946.
- [5] Ewulonu, C. M.; Liu, X.; Wu, M.; Yong, H. *J. Bioresour. Bioprod.* **2019**, *4* (1), 3–10.
- [6] Nair, S. S.; Yan, N. *Cellulose* **2015**, *22*, 3137–3150.
- [7] Visanko, M.; Sirviö, J. A.; Piltonen, P.; Sliz, R.; Liimatainen, H.; Illikainen, M., *Cellulose* **2017**, *24* (10), 4173–4187.
- [8] Li, M.; Jie, Y.; Shao, L. H.; Guo, Y.; Cao, X.; Wang, N.; Wang, Z. L., *Nano Res.* **2019**, *12*, 1831–1835.
- [9] Kim, H. J.; Yim, E. C.; Kim, J. H.; Kim, S. J.; Park, J. Y.; Oh, I. K., *Nano Energy* **2017**, *33*, 130–137.
- [10] Xia, K.; Xu, Z.; Zhu, Z.; Zhang, H.; Nie, Y., *Nanomaterials* **2019**, *9* (5).
- [11] Bai, P.; Zhu, G.; Zhou, Y. S.; Wang, S.; Ma, J.; Zhang, G.; Wang, Z. L. *Nano Res.* **2014**, *7* (7), 990–997.